



Explorations of turtle cortex function through molecular, optogenetic and electrophysiological techniques

Dissertation
for attaining the PhD degree
of Natural Sciences

submitted to the Faculty of Biological Sciences
of the Johann Wolfgang Goethe University
in Frankfurt am Main
by

Lorenz Pammer
from Vienna

Frankfurt am Main 2017
D30

Accepted by the Faculty of Biological Sciences of the Johann Wolfgang Goethe University as a dissertation.

Dean:
Prof. Dr. Sven Klimpel

Expert assessors:

Prof. Gilles Laurent
Neural Systems and Coding
Max Planck Institute For Brain Research, Frankfurt am Main

Prof. Dr. Manfred Kössl
Department Cell Biology and Neuroscience
Johann Wolfgang Goethe University, Frankfurt am Main

Date of the defense:

Contents

Abstract	i
Zusammenfassung	v
Abbreviations	xiii
1 Introduction	1
1.1 The complexity of multi-scale problems	3
1.1.1 Comparing cortical circuits: details vs. computational principles	4
1.1.2 Theta-band activity in mammalian navigation circuits	5
1.1.3 Normalizing gain-control circuits	6
1.2 Reptiles in comparative neuroscience	8
1.2.1 Phylogenetic position of turtles	11
1.2.2 Simplicity & preparatory advantages	12
1.2.3 Reptilian behavior	14
1.2.4 Phenomena for comparisons	14
1.3 Turtle dorsal cortex	18
1.3.1 Connectivity of the visual system	18
1.3.2 Cytoarchitecture of cortex	20
1.3.3 Evoked activity	23
1.3.4 Oscillatory activity	26
1.4 Motivation & objectives	29
1.4.1 Questions	29
1.4.2 Experiments	30
1.5 Conclusion	32
2 Materials & Methods	33
2.1 General methods	33
2.1.1 Turtles	33
2.1.2 Mice	33
2.2 Viral Material	33

2.2.1	Adeno Associated Virus	33
2.2.2	Lentivirus	34
2.2.3	Rabies virus	35
2.2.4	AAV-SL1	35
2.3	Neurophysiology	35
2.3.1	Slab preparation	35
2.3.2	Patch-clamp	36
2.3.3	Multi electrode recordings	37
2.3.4	Pharmacology	38
2.3.5	Spike Sorting	38
2.3.6	SIF measurement	39
2.3.7	Estimation of spike source location	40
2.3.8	Dendrogram & SIF Clustering	41
2.3.9	SIF calculation from anatomy of reconstructed neurons	41
2.3.10	Mean Oscillation Cycle	41
2.4	Optogenetics	42
2.4.1	Light delivery	43
2.5	Histology	44
2.5.1	Perfusion, sectioning, mounting	44
2.5.2	Staining methods	44
2.5.3	BABB clearing	46
2.5.4	Imaging	46
2.5.5	Reconstruction of neuronal morphologies	47
2.5.6	Alignment of cell to MEA	47
3	Olfactory stimulation software	49
3.1	Requirements	50
3.2	Olfactometer	50
3.3	Olfactometer Control	52
3.4	I/O	55
3.5	"smell" structure	55
3.6	Odor library	56
3.7	Protocols	58
3.8	Scripting	59
3.9	For developers	60
3.10	Conclusions	61

CONTENTS

4 Genetic tools in reptiles: Results	63
4.1 Gene delivery	64
4.1.1 Viral injection surgeries	64
4.1.2 Adeno Associated Virus	66
4.1.3 Lentivirus	70
4.1.4 Rabies virus	72
4.1.5 AAV-SL1	73
4.2 Gene expression	80
4.2.1 High yield promoters	81
4.2.2 Cell type-specific promoters	82
4.2.3 Cre lox system	86
4.3 Organotypic cortical slab preparation	87
4.4 Immediate early genes	89
5 Neurophysiology in the cortical slab	93
5.1 Whole cortex preparation	95
5.2 Extracellular spread of action potential	98
5.3 Extracellular detection of synaptic potentials	99
5.4 Estimating neuronal morphology from SIFs	105
5.5 Cellular features from MEA signals	109
6 Dynamical activity in cortical circuits	111
6.1 Controlling activity with light	113
6.2 Activity by cell type	114
6.2.1 LII/III Pyramidal cells	115
6.2.2 LIII Interneurons	116
6.2.3 LI Interneurons	118
6.3 Potential circuit mechanism for oscillations	119
6.4 Controlling oscillatory phase & frequency	121
6.5 Spatiotemporal control of oscillations	124
7 Discussion	127
7.1 Genetic Tools	127
7.1.1 Viruses	127
7.1.2 Promoters	129
7.2 Neurophysiology	130
7.2.1 Detecting synaptic events with extracellular electrodes	131
7.2.2 Extensions	132
7.2.3 Advantages & applications	133

7.3	Optogenetic manipulation of neural dynamics	134
7.3.1	Dissection of cortical oscillations	135
7.3.2	Controlling cortical dynamics	140
7.4	Conclusion	143
	Declaration	167
	Acknowledgments	169
	Curriculum Vitae	171

Abstract

The objectives of this thesis were to understand how distinct classes of cell types interact to shape oscillatory activity in cortical circuits of the turtle. We chose the turtle cortex as a model system for cortical computations for two reasons. One is that the phylogenetic position of turtles makes their cortex functionally and anatomically particularly interesting. The second is that reptilian brains present several unique experimental advantages. Turtles have a three-layered cortex that forms the dorsalmost part of their pallium and receives direct input from visual thalamus. Thus turtle cortex, while sharing several features with mammalian cortices, constitutes a simpler system for studying cortical computations and dynamics. Freshwater turtles are semiaquatic species, that dive for hours and hibernate for months without breathing. Their brains are adapted to these behaviors so that they can operate under severe anoxia. This property allows for *ex vivo* whole-brain and whole-cortex (“cortical slab”) preparations *in vitro*, enabling the use of many sophisticated techniques for monitoring activity in parallel.

I thus set out to utilize the advantages of our model system, by using optogenetic methods to reliably evoke oscillations in an *ex vivo* whole-cortex preparation while observing activity in parallel with planar multi-electrode arrays (MEA), linear silicon depth-electrodes and patch-clamp recording techniques. This required several technical aspects to be solved.

Prior work in turtle cortex (Prechtl, 1994; Prechtl et al., 1997; Senseman and Robbins, 2002) indicated that visual stimuli evoke complex activity patterns (e. g. wave patterns) in dorsal cortex. The goal was to examine these dynamics in detail and to provide mechanistic explanations for them whenever possible. The recent advent of optogenetics, the development of microelectrode arrays, and the possibility to combine these techniques with classical electrophysiological approaches on a resistant, accessible and stable preparation led me to explore a number of technical avenues.

First I had to establish gene delivery methods in reptiles. I settled on recombinant viruses, and show results from several serotypes of *adeno-associated virus* (AAV),

lentivirus and *rabies virus*. I report successful gene expression of genes of interest with several subtypes of AAV, including the commonly used AAV2/1 and AAV2/5 serotypes. Second I had to find promoters enabling global and cell-type specific gene expression in reptiles. Ubiquitous high-yield promoters such as CAG/CB7 or CMV drive high levels of expression in turtles; cell-type specific promoters such as hSyn (expression limited to neurons) and CaMKIIa (expression limited exclusively or mostly to excitatory neurons) appear similarly biased in turtles. Other cell-type specific promoters reported in the literature (fNPY, fPV, fSST) failed to express in turtles.

A second major aspect of my work focused on electrophysiological recordings using microelectrode arrays and the interpretation of extracellular signals recorded from cortex in *ex vivo* preparations. We observed that spike signals produced by pyramidal and inhibitory neurons were very often followed by a slower potential. We identified these slower potentials as reflections of synaptic currents, and thus of the axonal projections of the neurons, at least within the deep layers of cortex. This also resulted in a means to classify neurons as excitatory or inhibitory with much higher reliability than classical methods (e. g. spike width).

The final aspect of my work concerns the use of optogenetics to dissect the mechanisms of cortical oscillations and wave propagation. I show that oscillations can be induced by light in turtle cortex after transfection with AAV2/1 carrying the gene for channelrhodopsin 2 (ChR2). By using the CaMKIIa promoter, ChR2 induced currents are limited to LII/III excitatory cells; we can therefore control excitatory drive to cortical networks. If this drive is strong enough, layer III inhibitory interneurons are recruited and fire in a concerted fashion, silencing the excitatory population. The visually evoked 20 Hz oscillations observed in chronically recorded animals (Schneider, 2015) or in anaesthetized animals (Fournier et al., in press) thus appear to result from a feedback loop between E and I cells within layers II & III. Details of these interactions are being investigated but - layer I interneurons, by contrast, do not seem to be involved. By pulsing light I could control the frequency of the oscillations within a range of several Hz around the natural oscillation frequency. Above this range, cortex could only follow the stimulus at a fraction ($1/2$, $1/3$,...) of the light pulse frequency. Using a digital micromirror device, I limited activation of the cortical networks spatially, enabling the study of wave propagation in this system.

Reptilian cortex offers a relatively simple model system for a reductionist and comparative strategy on understanding cortical computations and dynamics. Turtle dorsal cortex could thus give fundamental insights to the primordial organiza-

tional, computational and functional principles of cortical networks. These insights are relevant to our understanding of mammalian brains and may prove valuable to decipher fundamental questions of modern neuroscience.

Zusammenfassung

Die grundsätzliche Fragestellung dieser Dissertation ist, wie unterschiedliche neuronale Zellklassen interagieren, um oszillatorische Aktivität in kortikalen Netzwerken der Schildkröte zu erzeugen. Als Modellsystem kortikaler Rechenoperationen wählten wir die Schildkröte aus zwei Gründen: Zum einen ist ihr Kortex aufgrund ihrer phylogenetischen Position funktionell und anatomisch besonders interessant, zum anderen bieten Reptiliengehirne einige experimentelle Vorteile. Schildkröten haben einen dreischichtigen Kortex, der den dorsalsten Teil ihres Palliums bildet und direkten visuell-thalamischen Input erhält. Das heißt, dass der Schildkrötenkortex Eigenschaften des Säugetierkortex teilt, aber ein einfacheres System zur Erforschung kortikaler Rechenoperationen und Dynamiken bietet. Wasserschildkröten sind semiaquatische Tiere, die ohne zu atmen stundenlang tauchen und monatelang Winterschlaf halten können. Ihr Hirn hat sich diesen Verhaltensweisen angepasst, um auch unter starkem Sauerstoffmangel operieren zu können. Diese Eigenschaft ermöglicht es, *ex vivo* Präparationen vom gesamten Hirn mit sensorischen Organen oder dem gesamten Kortex mehrere Tage *in vitro* zu halten, was den parallelen Einsatz komplexer Experimentalmethoden erlaubt. Vorangegangene Arbeiten zeigten, dass visuelle Stimulation im dorsalen Kortex komplexe Aktivitätsmuster (Oszillationen und kortikale Wellen) hervorruft (Prechtl, 1994; Prechtl et al., 1997; Senseman and Robbins, 2002). Wenn gewisse Funktionen oder neuronale Rechenoperationen in Nervensystemen weit verbreitet sind, kann man von kanonischen Operationen sprechen. Oszillationen und neuronale Aktivitätswellen sind exemplarische allgegenwärtige Phänomene neuronaler Netzwerke und eignen sich daher für einen vergleichenden Forschungsansatz (Ermentrout and Kleinfeld, 2001).

Wie alle biologischen Organe sind Gehirne das Resultat langer evolutionärer Prozesse. Eine evolutionäre oder vergleichende Perspektive auf Hirnfunktionen kann in zumindest zweifacher Hinsicht informativ sein: mechanistisch, durch die Identifikation vererbter Merkmale; und algorithmisch, durch Aufzeigen ähnlicher Lösungen für gleiche Problemstellungen. Vergleiche decken die Essenz einer Operation auf und identifizieren sowohl Rechenoperationen als auch algorithmische

Lösungen unabhängig von der spezifischen Implementierung (Marr and Poggio, 1976; Marr, 1982). Anstatt zu synthetisieren (Douglas and Martin, 2004), folgte ich einem Ansatz, der ausgehend von emergenten funktionalen Eigenschaften zu den zugrundeliegenden Mechanismen führt, um so gemeinsame Prinzipien der Rechenoperationen herauszuarbeiten (Hemberger et al., 2016). Die erfolgreichen Untersuchungen von Geräuschlokalisierung, „spike-timing-dependent plasticity“ und „looming“-kodierenden visuellen Neuronen bestätigen den Nutzen komparativer Arbeitsweisen, die neuronale Rechenoperationen als Ausgangsbasis für vergleichende Studien wählen (Konishi, 1991; Gabbiani et al., 2002; Sun and Frost, 1998; Cassenaer and Laurent, 2007; Markram et al., 1997b; Borst and Helmstaedter, 2015).

Reptilien und Schildkröten als Modellsystem

Der Säugetierkortex bleibt, obwohl es sich um das wissenschaftlich meistuntersuchte Hirnareal handelt, weitgehend unverstanden. Seine sechs Schichten, die modulare Architektur, die kanonischen Netzwerke (Douglas and Martin, 2004), die unzähligen Zelltypen (Petilla Interneuron Nomenclature Group et al., 2008) und die komplexen Rechenoperationen führten zu zahllosen phänomenologischen Beobachtungen, aber wenigen Prinzipien, von denen sich eine vertikal-integrierte Theorie ableiten ließe. Reduktionismus und Vergleich können sich unter diesen Herausforderungen als hilfreich erweisen. Amniotische Wirbeltiere (Säugetiere, Reptilien, Vögel) entstammen einem gemeinsamen Vorfahren, der vor 320 Millionen Jahren lebte. Innerhalb dieser Gruppe wurden die Säuger neurowissenschaftlich mit Abstand am meisten erforscht. Die evolutionäre Position von Reptilien macht diese allerdings zu einem attraktiven Modellsystem, um neuronale Netzwerkfunktionen und deren Evolution in Wirbeltieren zu erforschen – auch im Hinblick auf Säugetiere. Die grundlegenden Teile des Palliums sind konserviert und diese homologen Areale beinhalten auch den zerebralen Kortex, der spätestens im gemeinsamen Vorfahren von Sauropsiden und Theropsiden (den Vorfahren der Säugetiere) entstanden ist (Naumann et al., 2015). Vielmehr scheint der Neokortex der Säugetiere durch die Expansion einer kleinen Region des ancestralen dorsalen Palliums entstanden zu sein, dem Homolog des dorsalen Reptilienkortex (Aboitiz and Zamorano, 2013; Naumann et al., 2015; Montiel et al., 2016; Laurent et al., 2016; Tosches et al., submitted).

In Reptilien besteht der gesamte zerebrale Kortex weiterhin aus nur drei Schich-

ten, vergleichbar mit der Struktur des Allokortex in Säugetieren, und der dorsale Kortex ist ein primäres sensorisches Areal mit direkten thalamischen Eingängen (Desan, 1984; Jones and Peters, 1990). Genetische Untersuchungen von Einzelzellen belegen keine direkten Homologien zwischen den drei Schichten des Reptilienkortex und den definierten Schichten des Säugerkortex. Allerdings existieren Pyramidenzellen der Schildkröte mit genetischen Profilen von höherschichtigen und tieferschichtigen Säugerpyramidenzellen, sowie direkt-homologe inhibitorische Zelltypen (Tosches et al., submitted).

Reptiliengehirne sind somit viel einfacher aufgebaut als Säugerhirne, und sie teilen sowohl anzebrale Neuroanatomie, wie auch die funktionelle und strukturelle Spezialisierung der Hirnregionen und emergente kortikale Netzwerkdynamiken. Der dorsale Kortex der Schildkröte stellt daher ein einfacheres Experimentalsystem dar, um fundamentale organisatorische, rechnerische und funktionelle Prinzipien kortikaler Netzwerke zu untersuchen.

Ein weiterer Vorteil besteht in der aussergewöhnlichen Möglichkeit, *ex vivo* Präparationen experimentell zu nutzen. Wasserschildkröten sind wechselwarme Tiere, die während der kalten Monate unter Wasser Winterschlaf halten. Unter diesen anoxischen Bedingungen wechselt das Gewebe in einen Zustand geringen Energieverbrauchs, nutzt die anaerobe Glykolyse, eine extrazelluläre Pufferung von Milchsäure und wirkt Sauerstoffradikalen entgegen. Aufgrund dieser Fähigkeit, Sauerstoffmangel standzuhalten, bleiben *in vitro* Präparationen des Schildkrötengehirns über mehrere Tage hinweg am Leben und zeigen spontane neuronale Aktivität (Belkin, 1963; Hounsgaard and Nicholson, 1990; Bickler and Buck, 2007). Kortikale „slab“-Präparationen halten das intrakortikale Netzwerk intakt. Die „whole-brain“-Explantation bewahrt die lokale und weitreichende neuronale Konnektivität, erlaubt realistische sensorische Stimulation und eine hohe Zugänglichkeit der stabilen Präparation (Mori et al., 1981b; Mori et al., 1981c; Mori et al., 1981a; Hounsgaard and Nicholson, 1990; Kriegstein, 1987; Ariel, 2005).

Resultate

Uns fehlt bisher ein datenfundierte Verständnis für die Bedeutung von neuronalen Aktivitätswellen in Hinblick auf Algorithmen und Rechenoperation, und ein zufriedenstellendes mechanistisches Verständnis von Oszillationen in intakten kortikalen Netzwerken (Bartos et al., 2007; Atallah and Scanziani, 2009). Ich nutzte daher die Vorteile unseres Modellsystems, um mit Hilfe optogenetischer Verfahren

zuverlässig Oszillationen in *ex vivo* Präparationen des gesamten Kortex auszulösen, während diese parallel mit Multielektrodenarrays und patch-clamp Techniken gemessen wurden. In einer Serie von Experimenten untersuchte ich im Detail aus der Literatur bekannte kortikale Dynamiken der Schildkröte, wie Oszillationen und Aktivitätswellen, und lege mechanistische Erklärungen für diese Phänomene vor (Pechtl, 1994; Pechtl et al., 1997; Senseman and Robbins, 2002). Das jüngste Aufkommen der Optogenetik, die Entwicklung von Mikroelektrodenarrays, die Möglichkeit, diese Techniken mit klassischen elektrophysiologischen Methoden zu kombinieren und in einer widerstandsfähigen, zugänglichen und stabilen Präparation einzusetzen, erforderte zunächst die Entwicklung der technischen Voraussetzungen für dieses neue Modellsystem.

Genetische Werkzeuge

Um optogenetische Manipulationen zu ermöglichen, musste ich erst Methoden zum Gentransfer in Reptilien etablieren. Ich wählte rekombinante Viren, entwickelte ein Operationsprotokoll für virale Injektionen und organotypische kortikale „slab“-Kulturen. Ich zeige Resultate von mehreren Serotypen von *Adenoassoziierten Viren* (AAV), ferner des *Tollwut-* und *Lentivirus*. Ich berichte erfolgreiche Genexpression mit Hilfe von mehreren Subtypen von AAV, unter anderen den weitverbreiteten AAV2/1 und AAV2/5 Serotypen. *Lentivirus*, von Interesse wegen seiner Kapazität, größere Mengen an genetischem Material zu tragen, und seiner kürzeren Expressionslatenz in Säugern, scheint in Schildkröten nicht funktional zu sein. Das *Tollwutvirus* wurde getestet, weil es die Fähigkeit besitzt, transsynaptisch-retrograd zu infizieren, scheint aber ebenfalls nicht in der Lage zu sein, neuronales Gewebe der Schildkröten zu infizieren (Luo et al., 2008). Als Alternative präsentiere ich einen kürzlich publizierten, gentechnisch veränderten AAV – AAV-SL1 (auch rAAV2-retro bezeichnet) – der erfolgreich axonale Nervenenden in Reptilien infizieren kann (Tervo et al., 2016).

Im zweiten Schritt mussten Promotoren gefunden werden, die globale und zelltypspezifische Genexpression in Reptilien erlauben. Ubiquitäre hochexprimierende Promotoren wie CAG/CB7 und CMV bewirken hohe Expressionsraten in Schildkröten. Zelltypspezifische Promotoren wie hSyn (Expression beschränkt auf Nervenzellen) und CaMKIIa (Expression beschränkt auf exzitatorische Neurone) scheinen in Schildkröten vergleichbare Eigenschaften wie bei Säugern zu besitzen. Weitere in der Literatur dokumentierte zelltypspezifische Promotoren (fNPY, fPV, fSST) wurden erfolgreich getestet (Nathanson et al., 2009).

Kartierung synaptischer Projektionen

Ein zweiter Teil dieser Arbeit behandelt elektrophysiologische Messungen mit Mikroelektrodenarrays (MEA) und die Interpretation solcherart gewonnener extrazellulärer Signale in *ex vivo* Kortexträparationen (Shein-Idelson et al., 2017). Um eine detaillierte Beschreibung neuronaler Aktivität während kortikaler Dynamiken zu ermöglichen, prüften wir, wie viel Information aus extrazellulären Aufnahmen über jede aktive Zelle extrahierbar ist. Diese Aufnahmetechnik nutzt Elektroden mit größeren Durchmessern (100 μm) und niedrigeren elektrischen Impedanzen (50 $\text{k}\Omega$) als Tetroden, der standardmäßigen Aufnahmetechnik in intaktem Gewebe. Dadurch erlauben MEAs die simultane Untersuchung von Hunderten einzelner Zellen (typischerweise zwischen 250 und 1200). Wir beobachteten, dass Aktionspotentiale von Pyramiden- und inhibitorischen Zellen sehr häufig von langsameren Potentialen gefolgt werden. Wir identifizierten diese langsameren Potentiale als Signaturen synaptischer Ströme und somit von axonalen Projektionen der Neurone. Das gibt uns auch die Möglichkeit, extrazellulär abgeleitete Neurone als exzitatorisch oder inhibitorisch zu identifizieren, und zwar mit viel höherer Zuverlässigkeit als durch klassische Methoden (z.B. Aktionspotentialbreite). Für den Großteil jeder einzelnen sortierten „Unit“ lassen sich somit zusätzlich zur Position des Zellkörpers, ein morphologischer Imprint (axonale Projektionen) und der Zelltyp bestimmen. Ich zeige auch, dass dieser Ansatz in akuten kortikalen Hirnschnitten der Maus, und somit in Säugern, erfolgreich ist.

Kortikale Dynamiken

Der letzte Aspekt der Arbeit betrifft die Untersuchung von Mechanismen kortikaler Oszillationen und der Ausbreitung neuronaler Aktivitätswellen durch optogenetische Methoden. Oszillationen können durch Lichtstimulation des Schildkrötenkortex hervorgerufen werden, nachdem dieser mit Channelrhodopsin 2 (lichtabhängiger Kationenkanal) tragendem AAV2/1 transfiziert wurde. Durch Verwendung des CaMKIIa Promoters werden ChR2-induzierte Ströme auf exzitatorische Zellen der Schichten II/III beschränkt. Das erlaubt es die Aktivität (exzitatorischer „Drive“) im kortikalen Netzwerk zu kontrollieren. Intrazelluläre Messungen elektrophysiologisch und morphologisch charakterisierter Zellen zeigen, dass bei ausreichendem „Drive“ inhibitorische Interneurone der Schicht III rekrutiert werden, welche zeitlich abgestimmt feuern und dadurch die exzitatorische Population inhibieren. Visuell evozierte 20 Hz Oszillationen, wie sie in chronisch abgeleiteten Tieren beobachtet werden (Schneider, 2015; Fournier et al., *in press*), scheinen

somit durch eine Feedback-Schleife zwischen exzitatorischen und inhibitorischen Zellen der Schichten II & III hervorgerufen zu werden. Details dieser Interaktionen werden untersucht, aber Interneurone der Schicht I scheinen im Gegensatz nicht involviert zu sein. Durch das Pulsen von Licht konnte ich die Frequenz und Phase der hervorgerufenen Oszillationen innerhalb einer gewissen Bandbreite um die natürliche Oszillationsfrequenz kontrollieren. Oberhalb dieser Bandbreite konnte das kortikale Netzwerk nur Subharmonischen der Lichtpulsfrequenz folgen. Durch die Erweiterung eines Mikroskops mit einem Mikrospiegelaktor konnte der Lichtstimulus zeitlich und räumlich kontrolliert werden, um neuronale Wellen zu untersuchen. Eine Stimulation des gesamten Kortex resultierte in simultaner Aktivierung und gleichphasigen Oszillationen im erfassten Areal. Bei der Aktivierung einer Subregion verhielten sich die Dynamiken ähnlich: die Aktivität setzte simultan ein, Oszillationen waren phasengleich und breiteten sich nicht von der stimulierten Region ausgehend wellenförmig aus. Eine tonische Aktivierung der Zellpopulationen der Schichten II & III reicht also nicht aus, damit das intrakortikale Netzwerk wellenförmige Aktivitätsausbreitung zeigt. Inhibitorische Zellen der Schicht I könnten eine kritische Rolle im funktionalen Mechanismus spielen.

Fazit

Optogenetische Methoden eröffnen interessante Möglichkeiten für die Erforschung neuronaler Netzwerke, für die Untersuchung des Wechselspiels zwischen Neuronentypen und für die Aufklärung der funktionellen Bedeutung neuronaler Netzwerkphänomene (Deisseroth, 2011; Yizhar et al., 2011). Der Einsatz dieser Technologie mit einer Präzision, die der Komplexität neuraler Prozesse gerecht wird, bleibt jedoch weiterhin eine Herausforderung (Peron and Svoboda, 2011). Neue Entwicklungen könnten helfen, diese Herausforderungen zu bewältigen. Die Zugänglichkeit der Schildkröten-ex vivo-Präparation, mit der relativen Einfachheit des Kortex, macht die Schildkröte zu einem exzellenten Modellsystem, um diese technischen Verfeinerungen zu verwerten. Der Reptilienkortex bietet sich somit für eine reduktionistische und vergleichende Strategie mit dem Ziel des Verständnisses kortikaler Rechenoperationen und Dynamiken an. Der dorsale Kortex der Schildkröte kann somit fundamentale Einsichten zu den primordialen organisatorischen, rechenoperativen und funktionellen Prinzipien kortikaler Netzwerke liefern. Diese Erkenntnisse sind aufgrund der evolutiven Verwandtschaft relevant für unser Verständnis von Säugergehirnen und könnten sich als wertvoll erweisen, um fundamentale Fragen der modernen Neurowissenschaft zu entschlüsseln.

Abbreviations

A1	Primary auditory cortex	IT	Inferior temporal cortex
AAV	Adeno associated virus	L1/LI	first, most dorsal cortical layer
AL	Antennal lobe	L2/LII	second cortical layer
AP	Action potential	L3/III	third, most ventral cortical layer
APV	2-amino 5-phosphonovalerate	LC	Lateral cortex
CAG	Cytomegalovirus-immediate early enhancer β -actin promoter	LFP	Local field potential
CaMKIIa	Calmodulin dependent protein kinase IIa	LGN	lateral geniculate nucleus
Chr2	Channelrhodopsin 2	M1	Primary motor cortex
CMV	Cytomegalovirus	MC	Medial cortex
CNQX	6-cyano-7-nitroquinoxaline-2,3-dione	MEA	Multi electrode array
CSF	Cerebro spinal fluid	MFC	Mass flow controller
CTB	Cholera toxin subunit B	NMDA	N-methyl-D-aspartate
DC	Dorsal cortex	NeuN	Neuronal nuclei
DMD	Digital micro-mirror device	NT	Nucleus rotundus
DMSO	Dimethyl sulfoxide	OB	Olfactory bulb
DVR	Dorso ventricular ridge	PFA	Paraform aldehyde
EGFP	Enhanced green fluorescent protein	PT	Pallial thickening
EPSC	Excitatory post synaptic current	RT	Room temperature
EPSP	Excitatory post synaptic potential	S1	Primary somatosensory cortex
EYFP	Enhanced yellow fluorescent protein	SC	Subcutaneous
FEF	Frontal eye fields	SIF	Spike induced field
GABA	gamma-Aminobutyric acid	SNR	Signal to noise ratio
Gbx2	Gastrulation brain homeobox 2	TTX	Tetrodotoxin
GBZ	Gabazine	V1	Primary visual cortex
HRP	Horse radish peroxidase	V _m	Membrane potential
hSyn	human Synapsin-1 promoter	VSD	Voltage sensitive dyes
IEG	Immediate early gene	WCPC	Whole cell patch-clamp Woodchuck hepatitis virus
IM	Intra muscular	WPRE	posttranscriptional regulatory element
IN	Interneuron		
IPSP	Inhibitory post synaptic potential		
IPSC	Inhibitory post synaptic current		

Chapter 1

Introduction

Brains, like all biological organs, are the result of long evolutionary processes. An evolutionary or comparative perspective on brain function can be informative on at least two levels: the mechanistic, by identifying inherited features (e. g. , molecular components); and the algorithmic, by pointing to similar forms of solutions to common problems (e. g. , circuit graphs, cellular operations, etc.). Of particular interest are cases where common algorithms are not inherited, but rather result from evolutionary convergence. Those instances, clear evidence for which is still admittedly rare, may point to the essence of an operation, identifying both computation and algorithmic solutions, independently of implementation. A comparative approach to understanding brains as information processing systems thus meets David Marr's classical distinction between levels of understanding ([Marr and Poggio, 1976](#); [Marr, 1982](#)).

An evolutionary approach to brain function requires comparisons. One great practical difficulty in this exercise lies in defining the objects of these comparisons (Figure 1.1). Should they be gene or protein sequences, spatio-temporal gene expression patterns, cell morphologies, architectonics, connectivity graphs, gross structural features, biophysical and synaptic characteristics, emergent properties (e. g. , travelling waves, consciousness), or functional consequences (e. g. , gain control), to take but a few examples? In other words, what are the relevant dimensions? At a time when modern technology takes us from an artisanal to an industrial phase of neurobiological investigation, do we acquire all data that can be had, on the premise that any data are useful? If so, should we (and if so, how?) harmonize data acquisition, archiving and cataloguing? Or do we make some wise operational choices? If so, which ones? These questions are very important if we wish, for example, to cluster and compare datasets. The answers depend much on how we conceive of "understanding the brain". Understanding implies reducing the description, i. e. , throwing away. But what can we throw away?

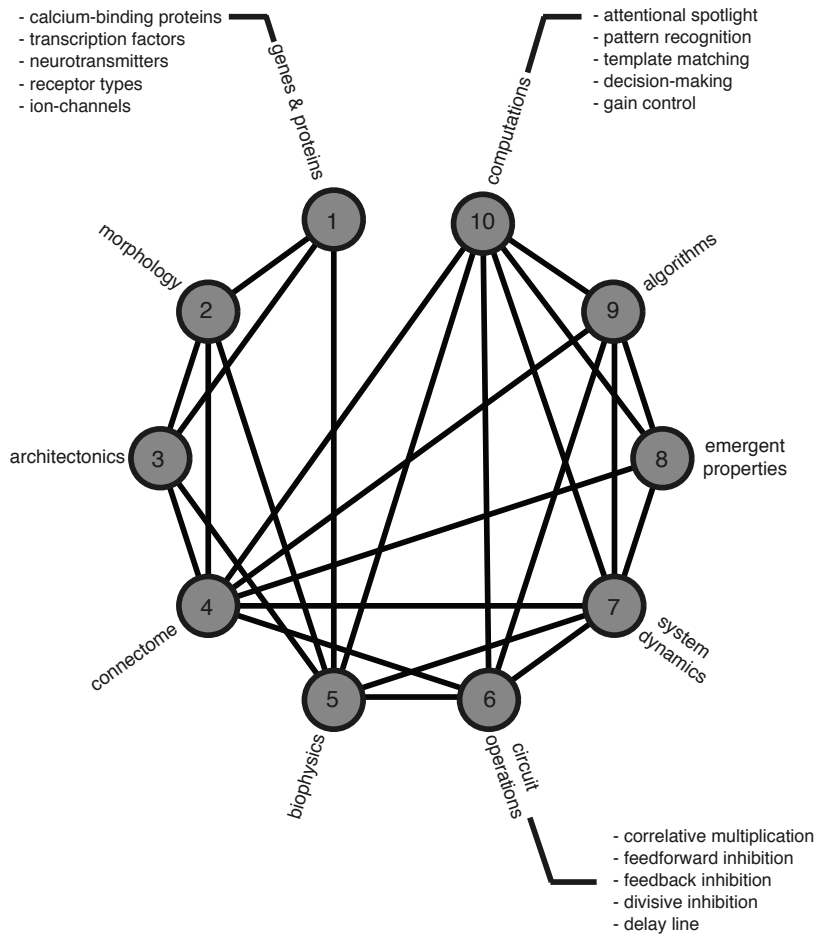


Figure 1.1: Comparing brains or circuits is a challenging multi-scale problem. This circular diagram illustrates some important features of neural systems and some of the possible mappings between them. Nodes 1 to 10 are meant to represent different levels of analysis, from the molecular to the computational. Each node represents a large class of descriptors, that can be more or less independent of one another. Take genes and proteins (node 1) for example: a neuron becomes sensitive to certain external cues through the expression of the appropriate receptors. These cues then shape morphology (node 2), e.g. guide the axon or constrain dendritic branching during development. Further subdivisions are given for nodes 1, 6 and 10. Not depicted here is the fact that there usually exist many possible mappings between pairs of nodes. For example, a given computation may result from several biophysical or circuit implementations, which may themselves result from several molecular/developmental histories. The challenge is to uncover, through these comparisons and linkages, some overarching principles of brain function.

How do we know a priori? A comparative approach is thus useful also in that it forces us to identify, or at least be explicit about, the features and dimensions that should matter to reach a functional understanding.

This introduction deals with general problems Neuroscience faces today in the first part. It will then discuss reptiles as a class of vertebrates whose study might

shed light on some of these questions. The research presented in this thesis was performed in one such reptile species - the yellow and red eared sliders, a freshwater turtle species. Thus the third part will introduce and characterize the turtle's dorsal cortex, where all experiments have been carried out. Finally the motivation and objectives for the particular experiments will be argued in the final part. This introduction draws heavily from four resources: a review written by me in collaboration with Mike Hemberger and Gilles Laurent a book chapter on reptilian cortex by the lab (Laurent et al., 2016) and two further published sources from our colleagues of the Laurent laboratory - the PhD thesis of Dr. Ingmar Schneider (Schneider, 2015) and a review on the reptilian brain (Naumann et al., 2015).

1.1 The complexity of multi-scale problems

The multilevel organization of the brain makes it difficult to define precisely meaningful entities for comparisons (Figure 1.1). The outcome of a comparison (for example, across cell types or circuits) depends on the features selected and on their relative weightings. Results based on some features or dimensions may not map clearly onto classifications based on other dimensions. In addition, classification and feature profiles themselves may change with developmental time or brain state (Steriade, 2004). In some cases, these parametric variations may be linked to the homeostatic stabilization of some high-level set point, itself often unknown. If so, the parametric variations are only sets of solutions to a larger overarching goal (Prinz et al., 2004; Marder and Taylor, 2011), but not necessarily interesting in and of themselves. In other cases, they may underlie true state transitions, and thus be critical to a functional understanding. Finally, the variability of data collected across hundreds of laboratories using many finicky techniques makes comparability a central problem of neuroscience. How then do we deal with comparative outcomes that are based on these data? Industrial scale initiatives, such as those of the Allen Institute (Tasic et al., 2016; Lein et al., 2007; Oh et al., 2014), strive towards explicit standardization. But is the time ripe for worldwide standardization?

1.1.1 Comparing cortical circuits: details vs. computational principles

Cortical microcircuits are particularly difficult to compare (across brain areas as well as across animal species), in great part because we still understand little about them and the coding principles that they express. (It is useful to remember here that we know the architecture of cerebellum in exquisite detail in many vertebrate species, but still understand little about its operations.) Cortical neurons probably have no single “role” in a circuit, and defining precisely what a circuit consists of is, when one thinks hard about it, not at all clear. We are naturally drawn to the neuron as a scale for study and comparison, but is it always the right one? Add to these observations the fact that activity-dependent plasticity rules can constantly alter circuit constituents and one realizes the complexity of the challenge (Markram et al., 1997b; Holtmaat and Svoboda, 2009).

How then can we proceed? The synthesizing approach of certain anatomists led to the concept of a canonical circuit that, repeated throughout cortical areas, implements some computational primitive (Douglas and Martin, 2004). This is a powerful operational idea for it means that if we understood the canonical circuit, say of visual neocortex, we could understand the rest of the neocortical sheet. Recent work, however, highlights interesting differences across primary sensory cortices (Medini, 2011; Sharma et al., 2000), raising some doubt about the prospect of identifying equivalent operations and circuits across cortical areas that process primary visual, auditory or somatosensory information (V1, S1, A1), recognize abstract visual objects (IT), plan- or execute eye movements (FEF, M1) or motivate behaviors (cingulate cortex). Furthermore recent work on orientation selectivity in visual cortex indicates profound inter-species differences in the organization of maps (pinwheels vs. “salt and pepper”) in visual cortex (Ohki et al., 2006; Kaas, 2008; White et al., 2001; Kaschube et al., 2010). While these results raise some doubt about the idea of a ‘canonical’ cortical circuit, the different architectures recently uncovered may ultimately reveal even more powerful organizing principles, of which pinwheels and salt-and-pepper architectures would be only two examples (Reichl et al., 2012).

A different style of comparative approach rather proceeds from the emergent functional properties back towards underlying mechanisms. For example, looming-sensitive visual neurons with similar response dynamics have been described in very distant species such as pigeons and locust (Gabbiani et al., 2002; Sun and Frost, 1998). This identifies these dynamics as a potentially key property

in circuits that mediate collision avoidance, although these circuits are totally unrelated (thalamic nucleus rotundus in birds, lobula optic lobe in insects). Similarly, spike-timing-dependent plasticity rules have been found in insects (Cassenaer and Laurent, 2007) as well as vertebrates (Markram et al., 1997b; Bell et al., 1997) and early visual pathways in the retinae of vertebrates and flies (Borst and Helmstaedter, 2015; Silies et al., 2014; Wernet et al., 2014) increasingly appear to operate according to similar principles. These examples confirm the essential value of a comparative approach, based on computation, as beautifully illustrated in the classical comparison of sound localization circuits in the barn owl and jamming-avoidance circuits in the electric fish *Eigenmannia* (Konishi, 1991). These studies all identify common computational principles that were reached through evolutionary convergence and thus may often rely on different mechanisms. Hence, while exhaustive mechanistic descriptions (e. g. , (Oh et al., 2014; Lein et al., 2007; Tasic et al., 2016; Markram et al., 2015)) have undeniable value, it is not entirely clear that they are the most efficient path towards computational understanding. We believe that comparative computational work has an essential role to play in identifying those principles (without minimizing the importance of mechanistic detail).

1.1.2 Theta-band activity in mammalian navigation circuits

The hippocampus and entorhinal cortex offer an excellent case study for the value of a comparative approach. While these brain areas and their role in spatial navigation have been studied for decades in rats (O'Keefe and Conway, 1978), it is only recently that their operations have been examined in flying mammals such as the Egyptian fruit bat (Ulanovsky and Moss, 2007; Geva-Sagiv et al., 2015), an animal with long-range foraging behavior and challenging navigational requirements. Place cells, grid cells, border cells and head-direction cells all appear to exist in both rats and bats (O'Keefe and Conway, 1978; Ulanovsky and Moss, 2007), even though place fields are 2-dimensional in rats and 3-dimensional in flying bats. Interesting inter-species differences occur, however, in the collective neural dynamics that accompany these mapping properties. Whereas high-frequency ripple oscillations are seen in both rats and bats (Ulanovsky and Moss, 2007; Yartsev et al., 2011), theta range oscillations in bats are different from those seen in rodents: for example, they occur only in short (1 to 2 s) bouts during echolocation, their spectral peak is small and they are accompanied by a large delta-band component. In addition, theta rhythmicity is absent in the firing patterns of place cells in the bat, during any mode of behavior examined (Buzsáki,

2002; Ulanovsky and Moss, 2007; Yartsev et al., 2011). These findings appear to relativize the role of theta as a fundamental or necessary phenomenon linked to spatial navigation and are relevant for primate studies also, where intermittent theta oscillations have also been observed (Stewart and Fox, 1991).

Several computational models, developed for spatial representation by place and grid cells in rats, are impacted by these findings. Oscillatory interference models propose that interference between somatic and dendritic theta-band oscillations in single neurons transforms a temporal oscillation into a spatially periodic grid (Burgess et al., 2007; Blair et al., 2007; Hasselmo et al., 2007). While this model received support from intracellular recordings of place cells (Harvey et al., 2009), the recent results in bats suggest that it may not be a general model for representing space (or for the encoding and retrieval of memories) (though see (Barry et al., 2012)). Alternative models based on attractor dynamics (Domnisoru et al., 2013), however, can account for the bat data. If the different roles of theta in rodents and bats are confirmed, one would like to know how they evolved, and when. These results emphasize the observation that solutions to fundamental and common computational problems are not necessarily unique, and that understanding the diversity of these solutions should also be an important goal of modern neuroscience.

1.1.3 Normalizing gain-control circuits

It is increasingly clear that microcircuits in the brain carry out a number of essential functions, such as gain control, filtering, amplification, exponentiation, association, and coincidence detection, to take but a few examples. They can also serve to constrain and define trajectories in neural space, a property now observed in olfactory as well as motor systems (Mazor and Laurent, 2005; Churchland et al., 2012).

Normalization is a special case of a gain control operation and is well illustrated by recent studies in invertebrates (*Drosophila* antennal lobe and locust olfactory system) (Papadopoulou et al., 2011), early vertebrates (zebrafish olfactory bulb) and mammals (retina and neocortex). While these examples are all interesting, meaningful comparisons between them are sometimes difficult. In *Drosophila* and zebrafish, the computation is essential and low-level (odor concentration normalization), and the algorithmic and mechanistic details very well understood (Wilson, 2011; Hong and Wilson, 2013). In mammalian V1, by contrast, details on implementation are still fragmentary, but the computations accomplished of greater

operational scope (Carandini and Heeger, 2012).

The antennal lobe (AL) of *Drosophila* and olfactory bulb (OB) of zebrafish perform a normalization of responses to a range of odor concentrations, as well as normalizing single glomerular responses to global AL/OB activity. In mammalian V1, "response normalization" (Albrecht and Hamilton, 1982) usually describes operations whereby responses to a particular feature of visual space (e. g. , spatial position and orientation) are suppressed by stimuli with a broader feature range (Busse et al., 2009). Phenomena described as response normalization are, for instance, cross-orientation suppression (Carandini et al., 1997) and surround suppression where the suppressive field covers a larger area than the summation field (Cavanaugh et al., 2002). Algorithmic and mechanistic implementations are now well understood in the *Drosophila* and zebrafish early olfactory systems (Asahina et al., 2009). High gain for weak signals in *Drosophila* is implemented by high-quantal EPSPs, high basal release rate (Kazama and Wilson, 2008), and olfactory receptor neuron (ORN) convergence on projection neurons (PNs) (Kazama and Wilson, 2009; Gouwens and Wilson, 2009). Gain reduction for strong signals, by contrast, relies on fast vesicle depletion (hence strong short term depression) at the ORN-PN synapse (Kazama and Wilson, 2008). Adaptive homeostatic mechanisms appear to be involved also, whereby μ -EPSCs are tuned to PN input resistance (Kazama and Wilson, 2008). In both zebrafish and *Drosophila*, unspecific "lateral" inhibition is established via interneurons that receive inputs from many (in some cases almost all) glomeruli; thus, PN responses are controlled adaptively when other glomeruli are co-activated. The effect of this normalizing inhibition grows almost linearly with the magnitude of the entire network's activity (Olsen and Wilson, 2008; Olsen et al., 2010; Zhu et al., 2013; Hong and Wilson, 2013) . In both systems, one observes electrical coupling of interneurons to PNs/mitral cells, contributing to normalization by spike synchronization and shunting (Yaksi and Wilson, 2010; Zhu et al., 2013). Interesting differences exist, however, such as the site of interneuron action: presynaptic in *Drosophila* (Olsen et al., 2010) but postsynaptic (on mitral cells) in the zebrafish olfactory bulb (Zhu et al., 2013).

In mammalian V1, details on mechanistic implementation are less exhaustive and the evidence originates mainly from slice work (Rothman et al., 2009). It has been suggested that GABAergic inhibition plays little or no role in normalization such as contrast saturation or cross orientation suppression (Katzner et al., 2011), though it might be involved in surround suppression. Evidence for shunting in-

hibition is also unclear (Isaacson and Scanziani, 2011). Only the timing of the divisive signals involved in normalization offers some clues as to their origin: for cross orientation suppression they match that of LGN (Freeman et al., 2002) suggesting a feed-forward arrangement. By contrast, signals from a broader region of visual space as in surround suppression resemble V1 responses (Bair et al., 2003), suggesting a feedback arrangement. Recent results nicely show that layer 6 modulates the gain of visual responses via intracortical disinaptic inhibition (Bortone et al., 2014; Olsen et al., 2012).

1.2 Reptiles in comparative neuroscience

While the previous chapters formulated a framework for evolutionary and comparative neuroscience, this chapter will focus on reptiles and specifically turtles as model systems for this line of research.

About 320 million years ago (MYA), the amnion developed in so called amniotes. This embryo-protecting membrane allowed these ancestors of mammals, reptiles and birds, to invade non-aquatic habitats. Within this group of amniotes by far the most neuroscientific research has been directed towards mammals. The evolutionary position of reptiles however makes them an attractive model system to study neural circuit function and their evolution in vertebrates, also in regard to mammals.

To compare different vertebrate species meaningfully, a look into embryogenesis is often required, as it is not in adults but rather during early development (the “phylogenic stage”) when their similarities are most pronounced. This fact is also observable when comparing transcriptomes across species. Transcription factor co-expression in embryogenesis allows the identification of homologous brain regions and shows that major subdivisions of the brain are conserved across vertebrates. Despite the heterogeneity of adult brains, the basic division of the pallium in a lateral, ventral, medial and dorsal part, during development are conserved and substantiated by transcription data (Medina and Abellán, 2009) (Figure 1.2). These homologues include the cerebral cortex, a subregion of the telencephalon, which expresses transcription factors as Pax6, Emx1 and Tbr1 during development of all vertebrates (Fernandez et al., 1998; Moreno et al., 2010).

From these findings we can conclude that cortex appeared at the latest in the common precursor to sauropsids and theropsids (the mammalian ancestor) and

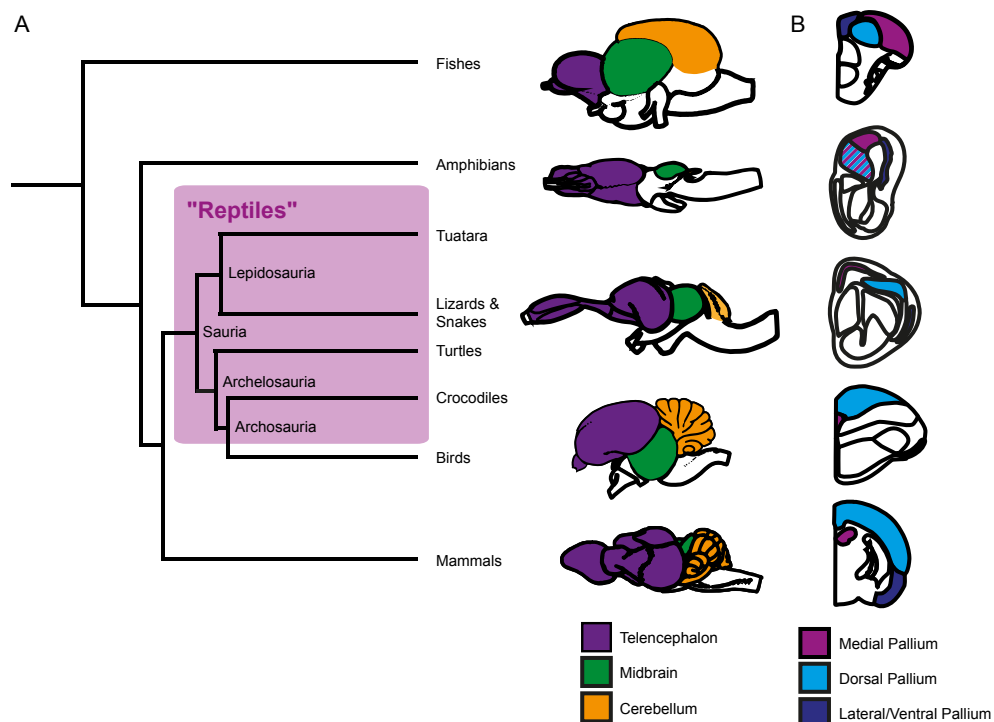


Figure 1.2: Brains in vertebrate phylogeny **A** Phylogenetic tree of vertebrates (shaded area encompassing reptiles). The origin of amniotes is 320 million years ago. On the right, schematic illustrations show brains (lateral view, anterior left) of vertebrate representatives: from top to bottom, a fish (knife-fish), an amphibian (tiger salamander), a reptile (monitor lizard), a bird (pigeon) and a mammal (hedgehog tenrec). Colors indicate major subdivisions present in all species albeit in different proportions. **B** Corresponding transverse sections of the brain's right hemisphere, however from different representatives: zebrafish, frog, lizard, pigeon and rat. Colors indicate conserved pallial subdivisions. From Naumann et al. (2015) adapted from Nieuwenhuys et al. (1998).

not in mammals. Furthermore given the architectural similarities of adult brain structures and developmental characteristics one can speak of a general vertebrate Bauplan with conserved basic functional organization (processing and storage of sensory input in the telencephalon; motor control in basal ganglia, etc.) (Medina and Abellán, 2009).

To conclude while reptilian brains are much simpler than mammalian brains both share ancestral neuroanatomy. The similarity of structural and functional specialization of brain regions, makes reptiles a promising model system to answer fundamental questions of modern neuroscience.

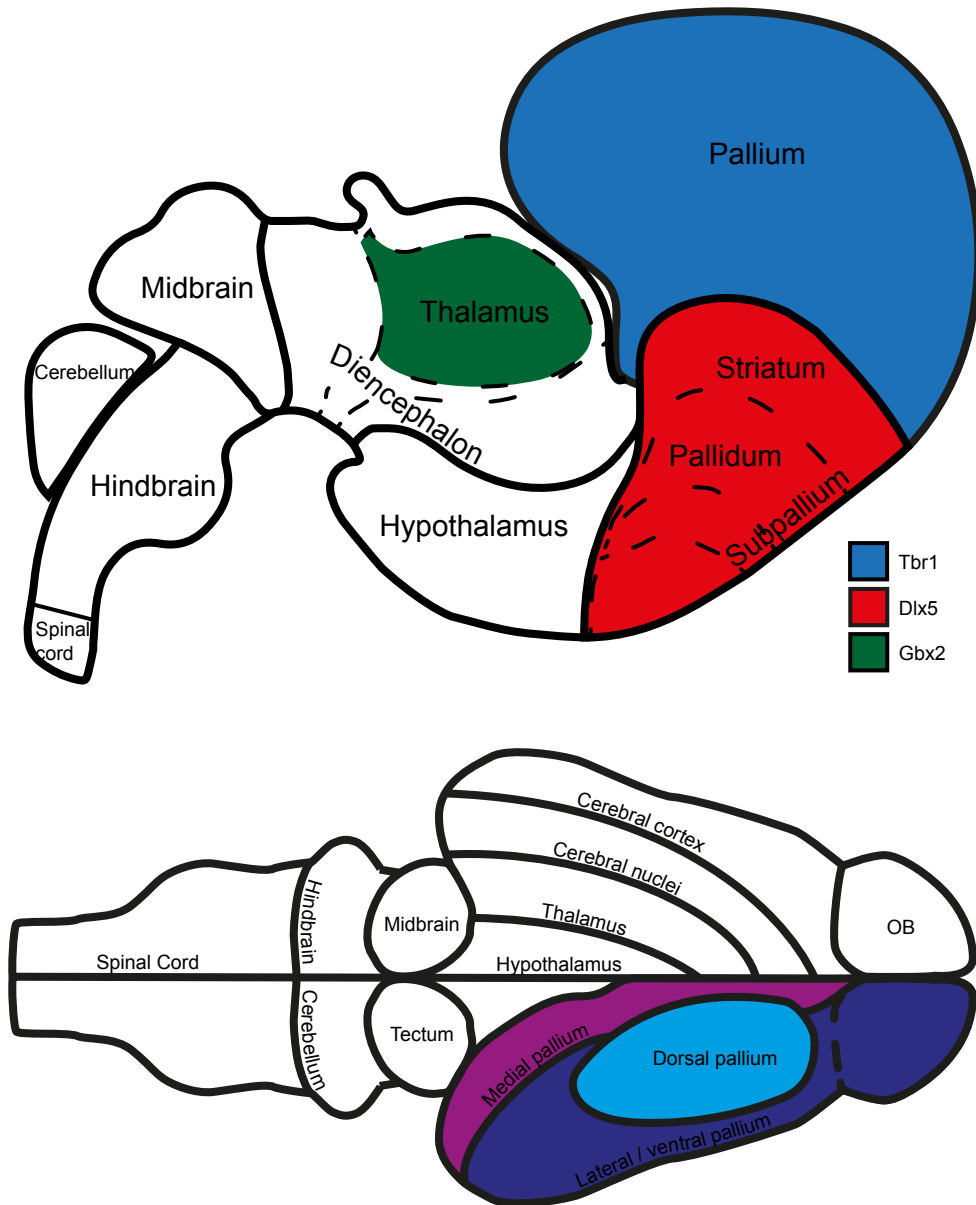


Figure 1.3: Bauplan of the vertebrate brain. Development and adult. Top: Schematic drawings of vertebrate brain regions during development. Colors indicate expression of a selection of transcription factors (Tbr1, Dlx5 and Gbx2) delineating brain regions during development. These major subdivisions become further refined in adults. Bottom: Schematic of the major subdivisions present in all vertebrates exemplified in the adult turtle brain. Different combinatorial expression of molecular markers during development segregate lateral and medial pallium. Delineation of lateral and ventral pallium is an active research topic and thus treated as a single region in the figure. From Naumann et al. (2015) adapted from Puelles et al. (2013) and Swanson (2011).

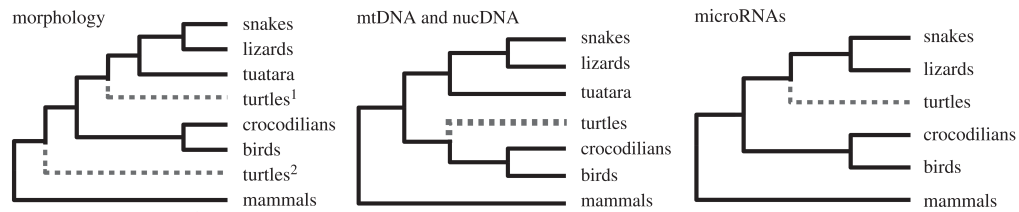


Figure 1.4: Left: Cladogram based on morphological data. Turtles branch most basally from the reptilian lineage (Lee, 1997; Rieppel, 1999). Middle: Based on molecular data, a turtle-archosaur group was suggested (Hedges and Poling, 1999; Zardoya and Meyer, 1998; Shedlock et al., 2007). Right: Based on miRNA loci, turtles are a sister group of Leosauria (Lyson et al., 2012). Adapted from Crawford et al. (2012). Genomic data dates the sauropsid - therapsid (branch including mammals) divergence to approximately 315 million years ago. Sauropsid lines giving rise to birds and turtles diverged 275 MYA, and Testudines developed 212 MYA (Wang et al., 2011).

1.2.1 Phylogenetic position of turtles

Modern reptiles are a class of more than 10,000 species defined in part by exclusion (paraphyletic grouping). While mammals and birds are considered to be a clade they are in fact subclades of Amniota. Reptiles however are comprised of a diverse group of amniote species that are neither mammals nor birds, including sphenodonts, lizards, snakes, crocodilians and turtles. Despite these weaknesses in terms of phylogenetic accuracy, reptiles have evolutionary, anatomical, developmental, physiological and functional features in common (Butler and Hodos, 2005; Bruce, 2006; Northcutt, 2013).

Also in terms of phylogeny there are uncertainties. In particular there is currently no consensus about the exact position of turtles in amniote phylogeny (Figure 1.4). While they were traditionally considered to be the most "primitive" reptile, this view has been challenged recently in light of new data. Depending on the choice of technical approach (morphologic, genomic, transcriptomic) and depending on the interpretation of data, currently three grouping schemes are the result (Lee, 1997; Hedges, 2012). (1) As the turtle skull has no temporal opening (anapsid condition) while other reptiles and mammals have one (diapsid condition), the classic view holds the hypothesis that turtles diverged early to form a sister group to all other sauropsida. This was challenged in light of new fossil finds, which show that the closed skull of turtles evolved from a diapsid condition (Schoch and Sues, 2015). This led to a repositioning and placement among the diapsid sauropsids (Rieppel and deBraga, 1996; Rieppel, 1999). (2) Based on microRNA transcriptomics turtles are a sister group to Squamata (snakes and lizards) (Lyson et al., 2012) (3) Based on mitochondrial and nuclear genomics from 32 turtle species, they are placed as a sister group to the Archosauria (dinosaurs

and modern birds and crocodiles) (Zardoya and Meyer, 1998; Hedges and Poling, 1999; Crawford et al., 2012; Crawford et al., 2015). This model is consistent with stratigraphic and geographic distributions of fossils (Figure 1.4).

While turtles might not anymore be considered to form the closest surviving relative to arche-amniotes and thus closest to the origin of cortex, they do certainly represent a group of species with a far simpler cortex than mammals.

1.2.2 Simplicity & preparatory advantages

The previous chapter proposed turtles as a model system for neuroscience because of their evolutionarily proximity to the stem ancestor of all amniotes, including mammals, whereas in this chapter two further reasons for establishing the turtle model are dealt with: (i) The relative simplicity of the turtle cortex with its three layers and clear lamination (Desan, 1984; Jones and Peters, 1990). (ii) The major experimental advantage of the turtle brain being highly resistant to anoxia (Belkin, 1963; Hounsgaard and Nicholson, 1990; Bickler and Buck, 2007).

While fish, amphibians and birds also have a pallium, among vertebrates it's only reptiles and mammals who have a cerebral cortex with clear layering. In reptiles this cortex consists of three layers, comparable to the structure of the mammalian allocortex (Naumann et al., 2015; Laurent et al., 2016). These evolutionary considerations formed the consensus in the field, that a layered proto-cortex existed in the common ancestors to reptiles and mammals. This structure was then in turn secondarily lost in the course of avian evolution. A comparison of amniote forebrains is illustrated in (Figure 1.2).

The reptilian cortex is subdivided into a medial cortex (also referred to as hippocampus), a lateral cortex (homologue to the mammalian piriform cortex), and a dorsal cortex receiving multimodal sensory information (in turtles particularly visual). Hardly any evidence exists on the other hand for motor and somatosensory cortical areas. The number of cortical subdivisions is much smaller than for example in rodents or primates, a simplicity, which is advantageous to understand the primary function of cortex. Currently this seems to be rather general associative functions than sensory or motor processing. The three-layered reptilian dorsal cortex just like the six-layered mammalian isocortex develops from the dorsal pallium (Aboitiz et al., 2002a). It is generally believed that reptilian cortex main cell layer (L2) corresponds to the deep output layers of mammalian neocor-

tex, while the layers L2-4 are hypothesized to be evolutionarily later additions. Reptilian L1 corresponds to mammalian LI (Aboitiz et al., 2002b). Mammalian paleo- and archicortices (pyriform cortex and hippocampus) are particularly similar to reptilian cortex in cellular properties and architectonics, clearly arguing for a common ancestral brain area in early amniote evolution (Medina and Abellán, 2009).

Fresh-water turtles are ectotherms who in the cold months go into hibernation. During this period they are submerged in deep oxygen-poor water up to several months. Turtles evolved several physiological adaptations to anoxic conditions. Mechanisms of anoxia resistance include a reduction of energy consumption by reducing membrane permeability via the inactivation of ionic pumps as well as voltage-gated (Na^+ channels, Ca^+ activated K- channels) and ligand gated ion channels (AMPA and NMDA receptors). NMDA receptor opening times are reduced by 65 % within 60 min of anoxia and NMDA currents are silenced via the cytosolic release of Ca^{2+} from Mitochondrial stores. Besides a reduction in energy consumption, oxygen-independent ways of ATP production have to be used. Under anoxic conditions turtle tissue uses anaerobic glycolysis for energy production and extracellular buffering of lactic acid (the product of anaerobic glycolysis). While in mammals reoxygenation of hypoxic tissue results in cell damage through reactive oxygen species (ROS), turtles upregulate nitric oxides and its metabolites to counteract ROS. Surprisingly turtles remain responsive to visual stimuli during hibernation, suggesting the maintenance of basic visual functionality. Due to this capacity to resist anoxia, *in vitro* preparations of the turtle brain remain vital and spontaneously active for several days after tissue extraction and can be stored overnight in a refrigerator at 3 to 5 °C (Houngaard and Nicholson, 1990). This fact allows the system to be studied in various degrees of reduction and led to the development of cortical slab and whole-brain explant preparations (Mori et al., 1981b; Mori et al., 1981c; Mori et al., 1981a; Houngaard and Nicholson, 1990; Kriegstein, 1987; Ariel, 2005). The whole-brain preparation preserves local- and long-range neuronal connectivity, permits realistic sensory stimulation (eg. olfactory or visual) and allows high accessibility of the preparation (OB, all telencephalic regions, thalamus and basal pallium). Due to the lack of respiration and animal movement the preparation is extremely stable. These features allow a range of possible preparations from *in vivo* awake recordings, to isolated and perfused heads, eye- or nose-attached whole-brain explants, dorsal cortical slabs (keeping intracortical networks intact) and slice preparations.

1.2.3 Reptilian behavior

Reptiles are endemic to all continents and oceans, living in a wide spectrum of habitats. They show complex natural behaviors such as long range navigation across the ocean for homing, showing high nest-site fidelity (Lohmann et al., 2001; Roth and Krochmal, 2015). Also in a laboratory setting they can learn to navigate mazes, and perform behavioral tasks akin to mammals (Wilkinson et al., 2009). Turtles thus constitute an interesting model organism in which to scientifically explore navigation.

The hippocampus is critical for map-like or relational memory representations of allocentric space, where objects are represented in relation to other objects. Hippocampus lesions impair animal performance in a subset of spatial navigation tasks (in particular place learning). This is the case in mammals as well as in reptiles when targeting medial cortex, the hippocampal homologue. In one such exemplary lesion study, turtles failed in place learning tasks which required allocentric space learning, while visual discrimination capability remained intact. This indicates medial cortex role in map-like memory representations of the environment comparable to mammalian hippocampus (Rodríguez et al., 2002b; Rodríguez et al., 2002a).

Against common preconceptions reptiles do exhibit interesting social behaviors. Several lizard species for example exhibit pair bonding, parental care and play behaviors. Others construct and maintain an interconnected network of tunnels being similar to the social complexity of mole rats (Northcutt, 2013; McAlpin et al., 2011). Thus, not only offer reptiles an interesting possibility for uncovering mechanistic aspects of cortical circuits, but they allow to study the entire spectrum from cellular to behavioral neuroscience.

1.2.4 Phenomena for comparisons

Recent trends in neuroscience have narrowed the scope of comparative neuroscience, notably through the progressive elimination of "model systems" that were key to the development of modern molecular, developmental and functional neuroscience. While the fantastic opportunities offered by modern molecular biology entirely justify the use of selected organisms (e. g. , for their genetic advantages), I argued that a diversity of model systems is essential if we wish to identify the brain's computational principles. It is through comparisons that we can hope to

separate mechanistic details (results of each organism's specific history) from functional principles, those that will hopefully one day lead to a theory of the brain. In this chapter I describe two exemplary features of neural circuits suitable for comparative research with the turtle model system.

Travelling waves

An example of an emergent property several neural systems have converged to are travelling waves. They are seen in invertebrate sensory areas (molluscan olfactory lobe) (Ermentrout and Kleinfeld, 2001), reptilian cortex (turtle dorsal cortex) (Prechtl et al., 1997; Prechtl et al., 2000), rat hippocampus (Lubenov and Siapas, 2008) and mammalian visual neocortex (V1) (Massimini et al., 2004; Sato et al., 2012).

In cat V1 travelling waves are seen during sensing of weak-contrast or small stimuli (Sato et al., 2012; Benucci et al., 2007). While direct data to describe mechanistic implementation is missing, some conclusions can be drawn from propagation speeds. With a propagation speed of 0.3 m s^{-1} in anesthetized V1 (Benucci et al., 2007) the propagation mechanism is likely to be passive transmission along horizontal fibers (Hirsch and Gilbert, 1991). In awake V1 transmission is significantly slower with 0.1 m/s , arguing for active recurrent mechanisms (Petersen et al., 2003; Harris and Thiele, 2011). While we lack any data-corroborated understanding of algorithmic or computational significance of travelling waves, further work is necessary to disseminate whether there is common functionality.

Turtle visual cortex offers a promising system to uncover and integrate mechanistic to computational descriptions, because of robustness of the phenomenon and accessibility of the *ex vivo* whole-brain preparation (Prechtl et al., 1997; Prechtl et al., 2000). Using VSD recordings visually evoked responses were shown to exhibit a spatiotemporal wave pattern in the *ex vivo* whole-brain preparation (Prechtl et al., 1997; Senseman and Robbins, 1999; Senseman, 1999; Senseman and Robbins, 2002). Looming visual stimuli consistently evoked responses in dorsal cortex with multiple frequency components exhibiting different spatiotemporal gradients. These include wave-patterns such as plane, spiral-like and more complex forms. Phase gradients of low frequency (around 5 Hz) oscillations propagate in parallel to the afferent thalamo-cortical fibers, the propagation speed of 0.01 m s^{-1} argues for active propagation mechanisms (unpublished data). At higher frequencies (around 18 Hz) phase gradients are perpendicular.

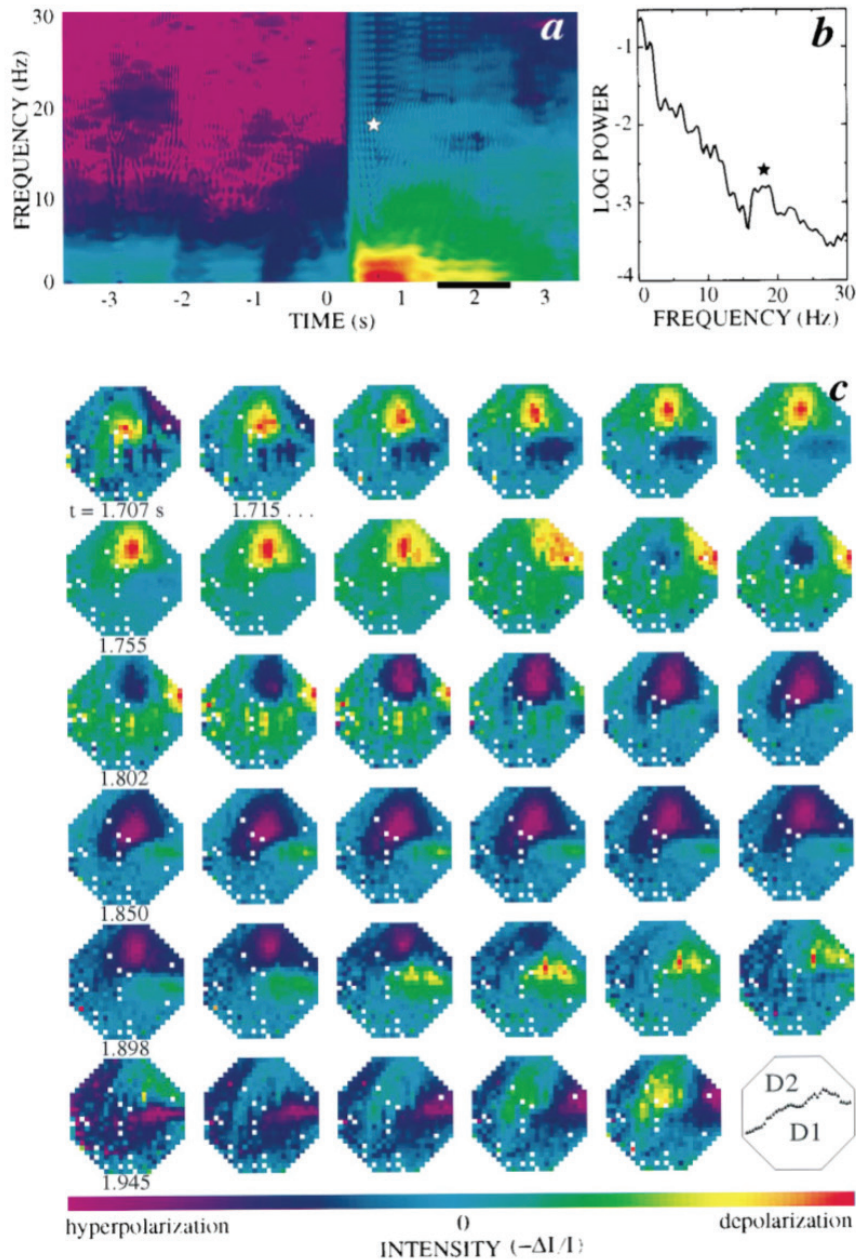


Figure 1.5: The spatiotemporal optical signal. **A** The average of the power spectra for 72 pixels over the most active part of cortex (logarithmic plot, red maximum, purple minimum values). Star indicates the stimulus-induced band at 18 Hz. **B** The spectrum for a 1 s interval (bar in A). **C** The broad-band filtered optical data, normalized for every frame, frames progressing from top left to bottom right (large stimulus-induced depolarization was removed with a median filter). Note the propagation of the signal. Figure from Prechtl et al. (1997) (Prechtl et al., 1997).

Sleep

Sleep is a common phenomenon across the animal kingdom (Cirelli, 2009). Taking such an emergent property and comparing what neuronal elements give rise

to it promises to be very informative. An example is the recent finding that sleep rhythms in lizards are highly similar to the ones found in mammals.

Mammalian sleep consists of at least two alternating brain states, rapid eye movement sleep (REMS) and non-REM or slow-wave sleep (SWS). Both states show characteristic LFP oscillations in multiple brain regions. These sleep rhythms are controlled by brainstem nuclei, primordial networks likely conserved through evolution. Widespread neuromodulatory projections from brainstem for example coordinate REMS/SWS transitions. One outcome of such coordinated interactions - correlated activity between hippocampus and cortex - was implicated in memory transfer and consolidation during sleep. The mechanisms, however, by which hippocampal- and cortical activity become coordinated during sleep remain elusive.

Behavioral and electrophysiological signatures of mammalian REMS and SWS are present in reptiles. A recent study recorded hippocampus-like sleep patterns from the lizard DVR, an area without obvious hodologic or architectonic similarity to hippocampus. Lizards show robust behavioral sleep and prominent LFP oscillations correlated with REMS and SWS that include sharp wave ripple (SWR) complexes. Furthermore, cortical activity is correlated to DVR activity during SWRs. A multi-level comparison using sleep as a common denominator raises the question of the deviations (from our current understand) we do or do not tolerate. Some variations of the fine temporal details may well be due to poikilothermic lifestyle (ripple frequency, beta instead of theta oscillations).

Comparative work in this direction promises to be revealing on several levels. Future work may clarify whether DVR is functionally analog to mammalian hippocampus. Optimistically DVR may even reveal alternative ways to represent space or to consolidate memories. In contrast to hippocampus, sensory inputs reach DVR via thalamic nuclei. A short path from sensory experience to memory may help us to understand the operational logic of primordial neural memory systems. On the mechanistic scale such work promises to further uncover primordial sleep patterns, their control and underlying neuronal circuits. Along the way we may identify cellular- or circuit properties common to hippocampus and DVR that facilitate inclusion in global network dynamics. Candidates are cellular resonance properties, shared signal transduction pathways initiated by neuromodulators or common local and long range connectivity rules.

1.3 Turtle dorsal cortex

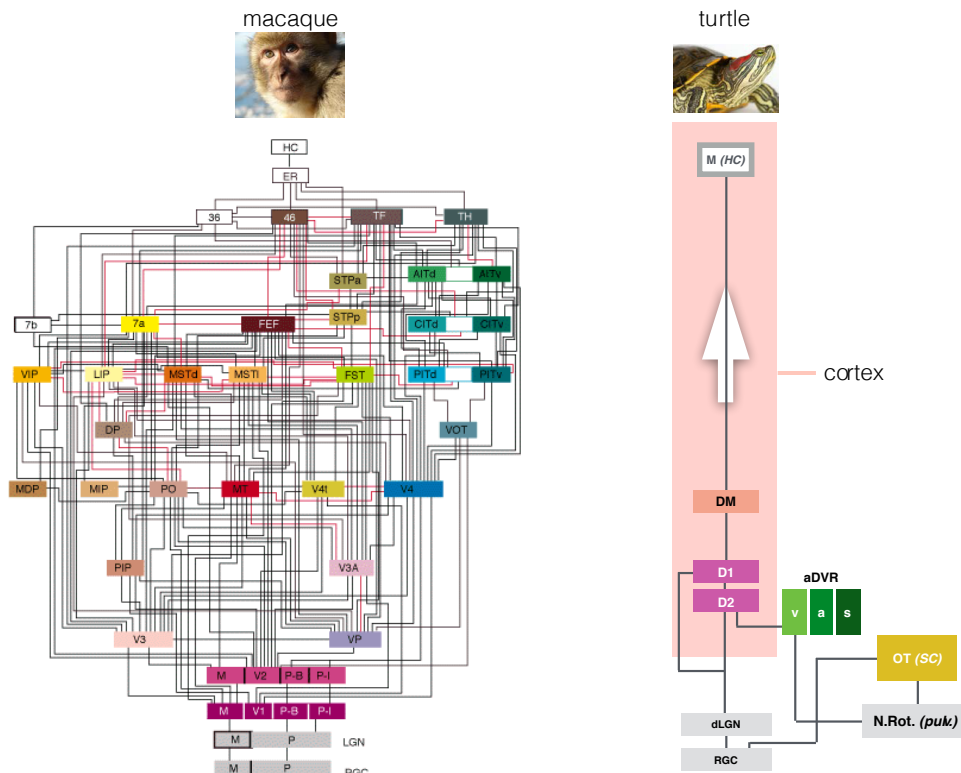
In the last chapter I argued why this lab has chosen the turtle as a model system. To recapitulate the main points. (1) turtles are non-avian sauropsids, (2) cortex of non-avian sauropsids is a sheetlike layered structure and (3) its cytology seems more simple than in lacertians (Smeets et al., 1986), (4) turtles have a high degree of anoxia-resistance (Belkin, 1963; Hounsgaard and Nicholson, 1990; Bickler and Buck, 2007), which makes them attractive for *in vitro* studies.

In this chapter a more detailed description of one turtle cortical region - the dorsal cortex - will be provided, as all experiments presented in this thesis have been carried out in this structure. Dorsal cortex is of particular interest for three reasons. (1) A simple three-layered cortical sheet (2) Direct input of visual thalamic afferent fibers, similar to mammalian V1 (3) The cortical area with best experimental accessibility *in vivo* and *in vitro*.

1.3.1 Connectivity of the visual system

In turtles as in mammals, visual signals travel from the retina to cortex via a thalamic relay. For a description of anatomy and processing in the turtle retina see the two reviews (Granda and Dvorak, 1977; Ammermüller and Kolb, 1996). For the purpose of this overview it should just be noted that the turtle retina does not have a fovea but rather an elongated strip of high ganglion cell density oriented along the nasotemporal axis and slightly dorsal of the meridian which is called the visual streak (Peterson and Ulinski, 1979).

Retinal ganglion cells (RGC) send their axon as part of the optic nerve towards central brain areas. After the majority of fibers cross the optic chiasm (a small fraction runs to the ipsilateral side) they project onward in two major pathways. The retinogeniculocortical pathway leads to the dorsolateral geniculate nucleus (dLGC) of the thalamus, from where the signals are passed on to the dorsal cortex via the lateral forebrain bundle. The second being the retinotectofugal pathway, where RGC axons directly project to the optic tectum. The optic tectum's circuits are important for processing visual information. Outputs of these computations are then relayed further to the nucleus rotundus of the thalamus, and from there onward to the anterior parts of the dorsoventricular ridge (DVR) a subcortical structure, which itself sends projections to dorsal cortex (Kosareva, 1967; Bass and Northcutt, 1981; Ulinski and Nautiyal, 1988). The dLGC of each hemisphere



Felleman and van Essen, 1991

Figure 1.6: Visual circuits in monkey and turtle. Graphic depiction of known visual cortical circuits in macaque (left) and turtle (right). Left panel shows connections between multiple areas involved in macaque vision. Right: Arrow indicates direction of information flow. Retinal ganglion cells (RGC), dorsal lateral geniculate nucleus (dLGN), nucleus rotundus "pulvinar" (N.Rot.), optic tectum (OT) anterior dorsal ventricular ridge (aDVR) with visual (v), auditory (a) and somatosensory (s), dorsal cortex areas D1 and D2, dorsomedial cortex (DM), medial cortex "hippocampus" (M). From Naumann et al. (2015). Adapted from Felleman and van Essen (1991), by permission of Oxford University Press. Monkey photo: RedCoat, Wikimedia Commons; turtle photo: Eurogroup for Animals.

receives inputs from RGCs of the entire contralateral retina as well as from RGCs located in ventrotemporal regions of the ipsilateral retina and thus does not receive inputs from ipsilaterateral regions of highest ganglion cell density (visual streak). The terminals of ganglion cell axons originating from the frontal visual field (temporal retina) are located in the caudal parts of dLGC, while RGCs from the caudal visual field (nasal retina) terminate in the rostral parts of dLGC (Ulinski and Nautiyal, 1988).

As briefly noted above the geniculocortical projections which originate from thalamic neurons in the dLGC travel along the ipsilateral lateral forebrain bundle and terminate in the dorsal cortex (Mulligan and Ulinski, 1990). In the dorsal

cortex the fibers enter laterally and project dorsally in an orderly fashion through cortex along so-called "iso-azimuth lamellae" (strips of projections corresponding to a particular azimuth in the visual field) along the rostrocaudal axis. Another organizing principle is that neurons from rostral dLGC project to caudal cortex and caudal dLGC neurons to rostral cortex. Axons from the dLGC form synaptic connections in the upper 100 μm of dorsal cortical L1. They synapse mainly on the spiny dendrites of cortical pyramidal neurons and smooth dendrites of subpial interneurons. Interneurons receive - on average - six times more thalamic inputs than pyramidal cells (Smith et al., 1980). Retinogeniculate and geniculocortical projection maps combined suggest a representation of visual space in a stripe-wise manner in turtle dorsal cortex. Resolving azimuth, discarding elevation, nasal segments of visual space would be represented in rostral parts, temporal visual space in caudal parts of dorsal cortex. Colleagues in this lab are conducting tracing experiments at this moment to reproduce these projection patterns.

1.3.2 Cytoarchitecture of cortex

As described above, mammals and reptiles share pallial modules, the turtle cerebral cortex being similar to mammalian archi- and paleocortices (i. e. pyriform cortex and hippocampal formation). Furthermore they appear to have cortical cell types in common. This suggests that fundamental building blocks of cortical circuits developed early in amniote evolution. As in mammals, the reptilian cortex is comprised of excitatory glutamatergic neurons and inhibitory GABAergic interneurons, with a common developmental origin - excitatory neurons from multipotent cortical progenitors, inhibitory neurons are born in the subpallium and migrate to cortex. Reptilian cortices comprise three layers, the cell layer (layer II, L2), dorsally the molecular layer (layer I, L1) and the subcellular layer (layer III, L3). It has been suggested that layer II of turtle cortex corresponds to the deep output layers of mammalian neocortex. L1 is a mix of thalamic and cortico-cortical input, and therefore considered to be equivalent to mammalian L1. The argument is that in the course of mammalian evolution new intermediate cell layers were incorporated into isocortex as its input point (layer 4 in neocortex) and internal circuitry. The fact that reptilian subpallial cells transplanted into mammalian embryos generate GABAergic interneurons which populate only the deeper cortical layers added support to this hypothesis (Naumann et al., 2015; Laurent et al., 2016). Recent molecular studies however seem to contradict this model. Lizard cortical neuroblasts generate neurons expressing upper layer molecular markers, in a similar developmental sequence to mammals (Naumann et al., 2015; Laurent

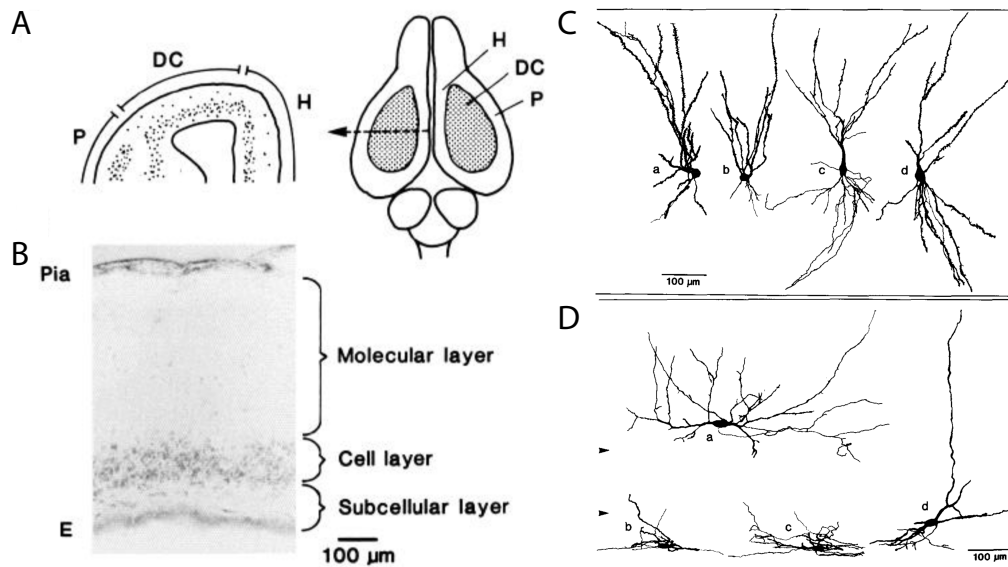


Figure 1.7: **A** Schematic of a transverse section (left) and a dorsal view (right) of a turtle brain showing dorsal cortex (DC), lateral or piriform cortex (P), and medial cortex (H). The position of the section is marked with a broken-line arrow. **B** Cresyl violet stained transverse section of DC with the three layers labeled. Pia surface and ependymal layer (E) labeled. Panels **C** and **D** show reconstructions of golgi-stained pyramidal (**C**) and inhibitory cells (**D**) in 50 µm thick sections of turtle dorsal cortex. Lines at top and bottom represent the pial (top) and ependymal (bottom) surface of cortex. **C** Cells a and b typical for medial area, c and d typical for lateral dorsal cortex (note the difference in basal dendrites). **D** Cells b and c typical for LIII interneurons with dendrites restricted to the subcellular layer. Cell d shows an occasional exception. Cell a is a typical LI interneuron, fusiform in shape with long aspiny dendrites. Arrowheads indicate the extent of the pyramidal cell layer. Adapted from Connors and Kriegstein (1986).

et al., 2016). Thus at this moment no clear understanding of the relationships between the cell types of reptilian dorsal cortex and mammalian neocortex exist, but it is possible that the reptilian cortex represents a simpler ancestral form of the mammalian neocortical networks.

On the level of macroscopic neuroanatomical features turtle cerebral cortex is divided into lateral, dorsal, dorsomedial and medial cortical areas (Desan, 1984). Traditionally dorsal cortex was further subdivided into a lateral and medial region, denoted as D2 and D1 respectively. The border being defined by a fall off in cell density of L2 and thickening of L3 towards D2 (Desan, 1984). Furthermore dLGC afferents who enter cortex ventrolaterally project medially through PT into D2 and are considered to terminate at the D1/D2 border (Mulligan and Ulinski, 1990). Unpublished results of this lab however indicate that thalamic afferents project well into what would be considered D1.

Layer 1 of dorsal cortex consists of incoming thalamic afferent fibers in the

superficial 100 μm (Smith et al., 1980), the apical dendrites of the pyramidal-like cells of layer II and sparsely interspersed interneurons. These interneurons are GABAergic and were divided into two classes (a) subpial cells with dendrites running in parallel to the pial surface and co-localizing with fascicles of the geniculate afferents. Physiologically they show spike-rate adaptation. (b) Stellate cells in the lower two thirds of L1 with smooth or sparsely spiny dendrites extending across all layers (Colombe et al., 2004). Physiologically they are fast spiking with no frequency adaptation.

Layer 2 contains densely packed principal neurons, which are excitatory pyramidal cells, with spiny dendrites extending towards the pia (Mazurskaya et al., 1966). Morphologically they are most similar to mammalian hippocampal excitatory neurons. They have little to no basal dendrites, and several densely spiny primary apical dendrites, differing from the single long apical dendrite with a proximal tuft of neocortical pyramidal neurons. Physiologically they show frequency adaptation (Connors and Kriegstein, 1986; Kriegstein and Connors, 1986). Widespread cell-physiological phenomena are found in turtle neurons as well. Such as active membrane properties in turtle pyramidal neurons which enable the backpropagation of somatic spikes as well as dendritic spikes that propagating towards the soma where they lead to full-blown somatic APs. Voltage-gated influx and activity dependent release of Ca^{2+} from internal stores. As in mammalian pyramidal cells, turtle pyramidal cell excitatory synapses are glutamatergic, inhibitory ones rely on GABA_A and GABA_B (Kriegstein and Connors, 1986; Larkum et al., 2008).

Layer 3 contains mostly interneurons, as well as the axons and basal dendrites of L2 pyramidal cells. Interneurons are GABAergic, have horizontal aspiny dendrites, are fast spiking and show no frequency adaptation. (Mazurskaya et al., 1966; Connors and Kriegstein, 1986; Kriegstein and Connors, 1986).

Upon brief electrical stimulation of afferents to dorsal cortex, stellate cells receive long-lasting input of excitatory postsynaptic potentials (EPSPs) and fire action potentials themselves. Pyramidal cells on the other hand receive short-latency EPSPs for a brief period which is followed by long-lasting inhibition (Kriegstein and Connors, 1986). Similar effects were observed during light evoked responses of cells in an *ex vivo* whole-brain preparation. Pyramidal cells received excitation and inhibition in parallel for about 50 to 100 ms. Inhibition, however, outlasts excitation by another 100 to 500 ms (Kriegstein, 1987). Kriegstein and Connors thus proposed a basic circuit design where (i) both pyramidal cells and L1 interneurons receive excitatory afferent input, (ii) pyramidal cells excite each other and L3 interneurons, (iii) L3 INs in turn mediate feedforward and feedback inhib-

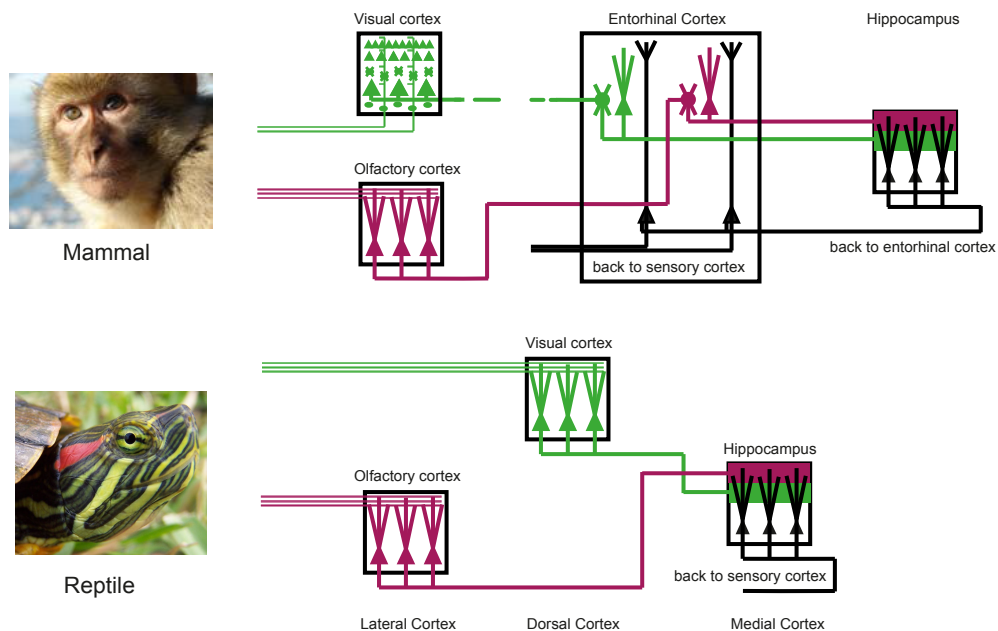


Figure 1.8: Comparison of circuit motifs between reptile and mammal cortex. Despite a much greater simplicity of the reptilian cortex, sensory processing ends in the same target area - the hippocampus or medial cortex. Furthermore, reptilian cortical architecture is more similar across sensory modalities and regions (medial, dorsal, lateral), suggesting more general computations being performed in the different modalities. From Naumann et al (2015), adapted from: Igarashi et al. (2014). Monkey photo: RedCoat, Wikimedia Commons; turtle photo: Eurogroup for Animals.

ition onto pyramidal cells (Kriegstein and Connors, 1986).

1.3.3 Evoked activity

Early studies using electrical stimulation in three sensory pathways showed spatial segregation of evoked activity of different sensory modalities in cortex. While visual, auditory and somatosensory responses were most pronounced in the anterior regions, olfactory responses were strongest in posterior and lateral sections. Also multi-unit activity in pallial thickening (PT) showed activity upon stimulation of single as well as multiple sensory modalities (Mazurskaya et al., 1966). Also response amplitude and latency depended on light intensity and wavelength, with a preference at 646 nm (Zagorul'ko, 1968).

Prominent features of mammalian primary visual cortex (V1) include a precise retinotopic representation of visual space and spatial selectivity of V1 neurons (Hubel and Wiesel, 1959). Are these organization principles similar in turtle dorsal

cortex? One could expect similar properties as V1 from the fact that dorsal cortex sit at the same processing stage. So far this seems not to be the case however, in fact turtle dorsal cortex exhibits quite different characteristics. In immobilized awake turtles, stimulation of retinal quadrants results in activity of specific but extensive regions of the turtle pallium (Mazurskaya, 1973a; Mazurskaya, 1973b). Visual activity along the nasotemporal axis of cortex corresponds to the nasotemporal axis of the visual field while the lateromedial axis of cortex represents the dorsoventral axis of the visual field (Mazurskaya, 1973b). Neurons have extensive receptive fields which cover the entire visual field and preferentially respond to motion and novelty (Mazurskaya, 1973b). Given the retinotopic organization of thalamic inputs described in chapter 1.3.1 (afferent projections from dLGC mirror the nasotemporal axis of the retina) these physiological results are surprising. The experiments with which these results were obtained, were coarse, but what is clear is that turtle dorsal cortex shows many fundamental deviations from mammalian V1.

Visually evoked population activity in the dorsal cortex shows interesting dynamical properties. In awake turtles moving visual stimuli evoked field potential responses in form of a slow (1 to 5 Hz) surface potential, as well as sustained synchronous activity in the form of coherent, spindle-like 15 to 25 Hz oscillations in the dorsal cortex and anterior DVR (Prechtl, 1994; Prechtl, 1995). Using simultaneous recordings of local field potentials and current source density analysis the observed oscillations were demonstrated to be caused by local, intracortical current sources (Mitzdorf, 1985). Thus the phase gradients were proposed to be generated by coupled oscillators in the cortical network (Prechtl et al., 2000). Also using voltage sensitive dye recordings (VSD) a dominant rostrocaudal propagation (Figure 1.5C) of flash-evoked activity was observed (Prechtl et al., 1997; Senseman, 1999; Senseman and Robbins, 1999). This allowed the authors to identify the location of primary (Desan's D/D2) and secondary (Desan's DM/D1) visual areas of dorsal cortex (Desan, 1984; Senseman and Robbins, 2002).

To summarize both groups report rostrocaudal and to weaker lateromedial spread of activity upon visual stimulation, however with propagation velocities differing by one order of magnitude. The available results are thus difficult to reconcile and the functional role of the observed propagating waves in visual processing remains unknown.

In a recent project in this laboratory Dr. Ingmar Schneider recorded visually-evoked responses from awake red-eared sliders (*Trachemys scripta elegans*) using

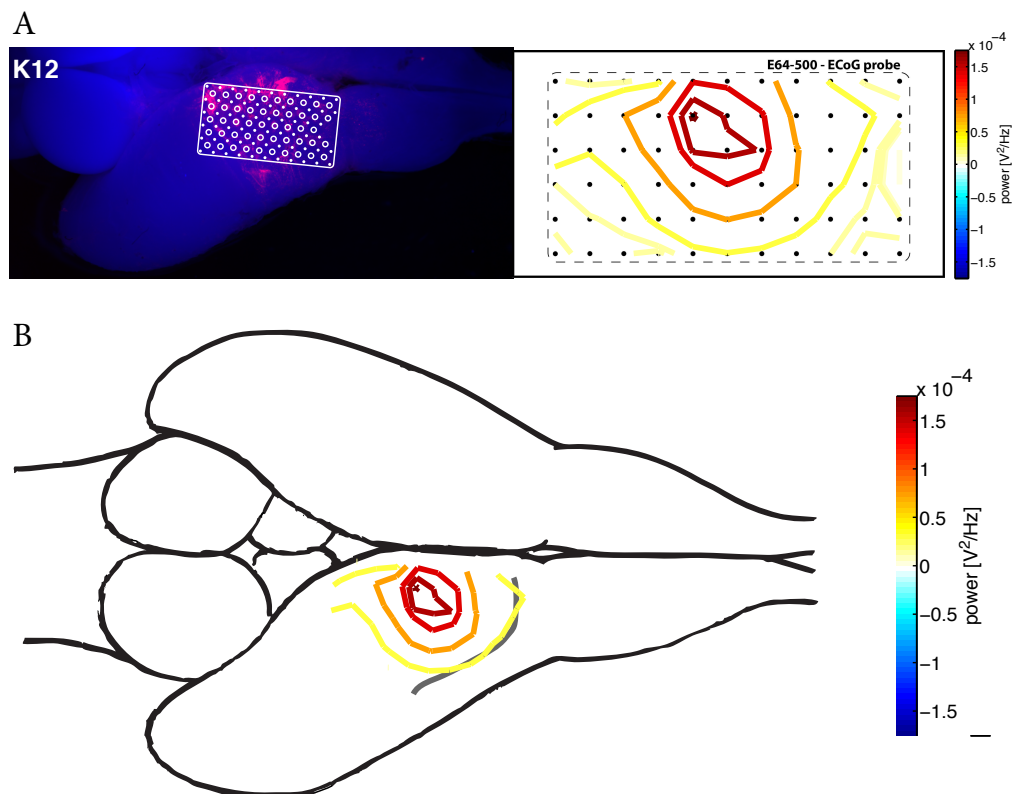


Figure 1.9: Co-registration of physiological data obtained in awake *in vivo* visual stimulation and anatomical data showing the site of maximum visually-evoked activity in turtle dorsal cortex. **A** Left: Fluorescent photograph of the brain of one turtle superimposed with the reconstructed location of the electrode grid measuring an electrocorticogram. Right: Spatial representation of the peak in natural-scene-evoked oscillatory power (filtered between 15 to 35 Hz). Distance between two recording sites (black dots) is 500 μ m. **B** Consensus location of visual stimulus-evoked oscillatory activity superimposed on a schematic of the turtle brain. Figure from the thesis of Ingmar Schneider (2015) (Schneider, 2015).

chronically implanted, high-density surface electrode grids covering large areas of dorsal cortex. Stimuli, probing a wide range of visual statistics, covered extensive parts of visual space. The evoked activity was located consistently in the same position of dorsal cortex with a preference for natural scenes (Figure 1.9). Furthermore they consisted of coherent oscillations in the 15 to 35 Hz range with a rostrocaudal phase gradient, confirming and extending earlier results. Thus, spatio-temporal features of visual stimuli influence cortical response dynamics (Schneider, 2015).

In summary, our current knowledge about anatomy and physiology of the turtle visual cortex is very limited. The literature is scarce, dated and a substantial fraction is methodologically dubious. No data-substantiated statements on computational functions of the described structures can be made at this point. What

one can say with confidence is that dorsal cortex is not functionally equivalent to the presumed mammalian counterpart V1. The absence of retinotopy, wide receptive fields and increased responses to natural vs. matched control stimuli all argue against a common functionality. Rather a similarity to non-retinotopic mammalian associative cortex might be suggested.

The goal of this lab is to establish the computations performed by the cortical regions of the turtle brain and characterize their mechanistic implementation, this will require substantial parallel efforts in the fields of anatomy, physiology, behavior and computational modeling.

1.3.4 Oscillatory activity

Periodic signals of brain activity (neuronal oscillations) are a ubiquitous phenomenon in neural systems. Neuronal oscillations are observed over a wide range of frequencies and are correlated with various brain states (Laurent, 2002; Buzsáki and Draguhn, 2004; Singer, 2013; Buzsáki, 2006). The frequency of the oscillation is determined by the time constants of the parts that make of the network. These periodic signals are termed neuronal oscillations and are an inherent feature of recurrent neuronal networks, and the frequency is determined by the time constants of its constituents. Since the first report of rhythmic brain activity in the 8 to 12 Hz range (alpha rhythm) by Hans Berger in human subjects (Berger, 1929), neural oscillations have been found across the animal kingdom (Adrian, 1950; Vanderwolf, 1969; Gray and Singer, 1989; Gelperin and Tank, 1990; Kreiter and Singer, 1992; Laurent and Naraghi, 1994; Prechtl, 1994; Fries et al., 2001). Oscillations can synchronize neuronal populations locally and over large distances. Extracellular field potential recordings integrate electric activity dominated by input currents around the recording electrode. If activity is synchronized the field potential oscillates. While single pyramidal neurons often show temporally random firing patterns, the same neuron might participate in oscillatory activity of synchronized ensembles. Inhibitory interneurons support the coordination of coactive excitatory neurons (Klausberger and Somogyi, 2008; Lasztoczi and Klausberger, 2014; Hu et al., 2014). Additional synchronization results from electrical coupling via gap junctions.

The proposed functional roles of oscillatory activity are many. In the following paragraphs I present four which have been of major consideration in the neuroscientific community - input selection, phase information, long range synchronization and memory consolidation.

Input selection

Neurons have temporal filtering properties resulting from the interaction between high pass voltage-gated currents and low pass capacitance and leak conductance filters. Depending on the properties of these components a given neuron can exhibit resonator (band-pass), notch (band-stop) or subthreshold oscillator filtering properties. Filtering properties not only allow cells to respond preferentially to presynaptic inputs of a certain frequency, but also to bias responses to local and afferent inputs depending on the phase of the simultaneous local network oscillations. For pyramidal cells oscillations amount to rhythmic inhibition during transient excitation. While receiving phase-locked somatic inhibition these pyramidal cells are highly unlikely to be brought to threshold of AP firing. This thus constitutes a mechanism to allow the network to effectively temporally gate information flow, synchronizing ensembles and resulting in discrete temporal windows of input integration for its constituent neurons.

Oscillations are also important within the concept of Hebbian learning, where synapses between simultaneously active neurons within the oscillation cycle are strengthened (Markram et al., 1997b; Bi and Poo, 1998; Cassenaer and Laurent, 2007; Cassenaer and Laurent, 2012). As an example the time a pyramidal cell of the hippocampus fires relative to the phase of the theta oscillation determines whether synapses undergo long term potentiation or depression (LTP or LTD) (Huerta and Lisman, 1995).

Representation by phase information

Network oscillations introduce a reference clock, which has further implications for coding information (Hopfield, 1995). In this manner action potential timing in relation to the phase of the ongoing oscillation is indicative of excitatory drive. The greater the drive the earlier the firing within a window of opportunity. Place cells in hippocampus fire progressively earlier within each successive theta cycle as an animal moves through the cell's place field - with firing at the trough of the theta oscillation in the center of the place field (O'Keefe and Recce, 1993; Kamondi et al., 1998).

Long range synchronization

Network oscillations allow the phase-synchronization of separate but connected neuronal assemblies when the frequencies of these coupled oscillators are similar. This synchronization is required for meaningful interactions between these distributed networks (Womelsdorf et al., 2007). Oscillations in the gamma frequency range seem to be particularly involved in this phenomenon in visual cortices of mice (Nase et al., 2003), cats (Gray and Singer, 1989; Gray et al., 1989), and macaques (Kreiter and Singer, 1992). Theories of the brain requiring precise temporal codes in action potential firing are debated, with a central counter argument being the high amount of variability and irregular interspike intervals frequently seen (Shadlen and Newsome, 1994). Alternatively noisy rate codes are proposed to encode information as being more robust to temporal jitter (Shadlen and Movshon, 1999; London et al., 2010). As always biology may not follow one proposed model, but these might co-exist.

Memory consolidation

Place cell assemblies and theta oscillation in the hippocampus and entorhinal cortex of rodents are re-active during slow-wave and REM sleep phases following behavioral tasks where they had been active (Wilson and McNaughton, 1994; Louie and Wilson, 2001). This is to say that the content of these oscillations reflects spike sequence patterns created by prior waking experience. Thus oscillatory activity during sleep is thought to be involved in the consolidation and combination of replayed waking experiences and their transfer from hippocampus to neocortex by means of synaptic modifications (Buzsáki et al., 1992; Siapas and Wilson, 1998; Wilson, 2002).

A particularly well established case of the functional role of oscillations are in the odor-evoked oscillations (20 Hz) in insect olfactory circuits. In honeybees oscillations and spike timing are necessary for fine sensory discrimination (Stopfer et al., 1997). In locusts they are involved in information transfer from the antennal lobe to the mushroom body and the sparsening of kenyon cell responses and thus support correlation codes and sparse coding schemes (Perez-Orive et al., 2002). Furthermore spike timing dependent coding mechanisms based on these oscillations lead to the stabilization of odor representations in the mushroom body of locusts (Cassenaer and Laurent, 2007; Cassenaer and Laurent, 2012).

Also the networks of turtle dorsal cortex spontaneously and upon stimulation exhibit around 20 Hz oscillatory activity (Prechtl, 1994), which furthermore show a phase gradient across the mediolateral axis of cortex (Prechtl et al., 2000). Mechanisms and functional significance of these oscillations were uninvestigated and unknown. This thesis hopes to start targeting these questions.

1.4 Motivation & objectives

Before beginning to describe the motivations for the specific line of work presented in these pages, the questions and the experiments, it is important to note the context. The onset of this thesis was also the beginning of this laboratory in its current form - in the Max Planck Institute for Brain Research in Frankfurt working on turtle and later lizard cortices. In the beginning the scientifically most fruitful approaches to this new model systems had to be established and necessitated flexibility and resulting shifts of focus.

1.4.1 Questions

At the beginning I planned to research olfactory coding in nose attached whole-brain explant preparations, which then shifted to probing dynamics in the dorsal cortex. Thus this thesis has two independent parts. The first part described in the first results chapter concerns the work on olfaction. While the obtained results are too preliminary to discuss, a software I developed for controlling an olfactometer was finished and is presented in chapter 3. The other chapters concern the work to characterize dynamics in turtle dorsal cortex. I will elaborate on the motivation for this part.

Why research cortical dynamics? The fundamental goal was to understand how distinct classes of cell types interact to shape oscillatory activity in cortical circuits of the turtle. Prior work in turtle cortex (Prechtl, 1994; Prechtl et al., 1997; Senseman and Robbins, 2002) indicated that visual stimuli evoke complex activity patterns (e. g. wave patterns) in dorsal cortex. If certain functions are prevalent throughout nervous systems, one can speak of canonical computations. Oscillatory dynamics and travelling waves are exemplary ubiquitous phenomena in neural networks and thus lend itself to an comparative approach. They are seen in invertebrate sensory areas (molluscan olfactory lobe) (Ermentrout and Kleinfeld, 2001), reptilian cortex (turtle dorsal cortex) (Prechtl et al., 1997; Prechtl et al.,

2000), rat hippocampus Lubenov:2008em and mammalian visual neocortex (V1) (Massimini et al., 2004; Sato et al., 2012; Benucci et al., 2007). Comparing microcircuit function shaped by convergent evolution allows one to differentiate between algorithmic and computational aspects and in this case of a canonical computation (see section 1.1.1).

Why investigate this phenomena in turtles? While we lack any data-corroborated understanding of algorithmic or computational significance of travelling waves, and no satisfying mechanistic understanding of oscillations in intact cortical circuits (Bartos et al., 2007; Atallah and Scanziani, 2009) the turtle offers a promising system to address these questions. This is because it allows using an *ex vivo* whole-cortex preparation where the entire intracortical network stays intact. In this preparation we optogenetically evoked reliable oscillations while observing these dynamics in detail to provide mechanistic explanations where possible. To observe we used in parallel planar multi-electrode arrays (MEA), linear silicon depth-electrodes and patch-clamp recording techniques. The recent advent of optogenetics, the development of microelectrode arrays, and the possibility to combine these techniques with classical electrophysiological approaches on a resistant, accessible and stable preparation led me to explore a number of technical avenues.

While the previous chapters of this introduction deal in detail with the advantages of comparative research in reptilian cortices and our resulting choice of model systems, certain problems do come with this choice. One being, that very little technical expertise on experimentation in this model system has been accumulated in the community. The other regarding that turtles with a generation time of about 10 years are peculiarly unsuited for genetic manipulations in the course of one PhD thesis. Alternative routes had to be followed to allow manipulation of cortical dynamics.

1.4.2 Experiments

Thus before acquiring data, several technical methods had to be established or transferred to turtles. To allow optogenetic manipulation, methods for gene delivery and expression had to be found.

For gene delivery viral methods seemed most promising. Their wide use in mammals results in availability of most genetic tools in these vectors. This necessitated first the development of a viral injection surgery protocol (section 4.1.1) and or-

ganotypic slab cultures (section 4.3) for testing. We then tested different recombinant viruses in turtles (section 4.1). Namely numerous *adeno-associated virus* serotypes to find the most efficient tropism for turtle neurons. *Lentivirus* because of its larger genetic carrying capacity and faster expression. And last *rabies virus* and *AAV-SL1* because of their capacity to infect axonal nerve endings (Luo et al., 2008). In a preparation which allows unparalleled accessibility to a brain with an intact processing cascade, from sensory organs to hippocampal equivalents, the identifiability of distantly connected cells promises experiments previously impossible in vertebrates. For instance parallel patching of connected cell pairs in different brain regions during sensory processing are conceivable. Finally promoters were tested to enable global and cell-type specific gene expression (section 4.2).

To enable a detailed description of neural activity during cortical dynamics, we examined how much information we can extract from extracellular recordings about each active cell (section 5.3). The fact that we used MEAs merited this approach. The reason being that this recording technique makes use of large diameter electrodes (100 μm) with low electrical impedances (50 $\text{k}\Omega$) (see section 2.3.3) compared to prevalent tetrode techniques normally used in intact tissue. In this detailed inquiry we observed that spike signals produced by pyramidal and inhibitory neurons were very often followed by a slower potential. We identified these slower potentials as reflexions of synaptic currents, and thus of the axonal projections of the neurons, at least within the deep layers of cortex. This also gives us a means to classify neurons as excitatory or inhibitory with much higher reliability than classical methods (e. g. spike width).

After these technical developments it was possible to target the final aspect of my work (section 6.1). To begin to develop a mechanistic understanding how the individual elements of the turtle cortical circuits interact to shape cortical oscillations and wave propagation. I show that oscillations can be induced by light in turtle cortex after transfection with *AAV2/1* carrying the gene for channelrhodopsin 2 (ChR2). By using the *CaMKIIa* promoter, ChR2-induced currents are limited to LII/III excitatory cells; we can therefore control excitatory drive to cortical networks. If this drive is strong enough, layer III inhibitory interneurons are recruited and fire in a concerted fashion, silencing the excitatory population. The visually evoked 20 Hz oscillations observed in chronically recorded animals (Schneider, 2015) or in anaesthetized animals thus appear to result from a feedback loop between E and I cells within layers II & III. Details of these interactions are being

worked out but - layer I interneurons, by contrast, do not seem to be involved. By pulsing light I could control the frequency of the oscillations within a certain range of the natural oscillation frequency. Above this range, cortex could only follow light pulse frequency at a fraction ($1/2$, $1/3$, etc.) of the light pulse frequency. Using a digital micromirror device, I have been able to limit activation of the cortical networks spatially, enabling the study of wave propagation in this system.

1.5 Conclusion

Six hundred million years of metazoan evolution have generated many solutions to comparable neurobiological challenges, all constrained by the common physics of our environment. Comparative approaches, though often considered quaint relics of musty 19th-century museum systematics, are essential to modern neuroscience in a number of ways. For example, one can exploit them to gain historical or evolutionary insight into the progressive elaboration of complex circuits, such as cortical networks in amniotes (Fournier et al., 2015). Alternatively, informed comparisons can help us separate implementation details - interesting in and of themselves but also essential for practical applications, such as in human and animal medicine - from computational and algorithmic principles, those that will ultimately help us derive a theory of the brain. One added benefit of diverse experimental approaches is that they keep revealing surprises. For example, insects appear to possess a navigation system not without resemblance with the head direction system of mammals (Seelig and Jayaraman, 2013; Seelig and Jayaraman, 2015). Insects also probably generate internal models of prey motion and steering maneuvers (Mischiati et al., 2015), not unlike vertebrates do (Körding and Wolpert, 2006). In short, comparative approaches may, in many cases, allow us to identify general principles of circuit function, just as they have in past decades with basic biophysical and synaptic functions.

Chapter 2

Materials & Methods

2.1 General methods

2.1.1 Turtles

All experimental procedures were performed according to German animal welfare guidelines. Wild-type turtles (*Trachemys scripta elegans* and *Chrysemys picta bellii*) of either sex, 200 to 500 g were obtained from an open-air breeding colony (NASCO Biology, WI, USA) and housed in a state-of-the-art animal facility.

2.1.2 Mice

All experimental procedures were performed according to German animal welfare guidelines. For experiments testing *rabies virus* we used adult (>P60) mice (C57BL/6, n=2) in the laboratory of Dr. Ilka Diester at the Ernst Strüngmann Institute in Frankfurt. Mice were housed in cages containing tunnels and bedding material.

2.2 Viral Material

2.2.1 Adeno Associated Virus

We received recombinant *adeno-associated virus* (AAV) as a gift from Dr. Boris Zemelman, Dr. Edward Callaway or purchased them from the University of Pennsylvania Vector core.

To research the specificity of the CaMKII α promoter we used AAV2/1-CaMKII-EGFP-WPRE-RBG abbreviated as

AAV2/1-CaMKII α -EGFP (concentration 3.665×10^{13} GC ml $^{-1}$) (Yizhar et al., 2011).

To establish infectious properties of different AAV serotypes we used AAV2/1-CB7-CI-mCerulean-WPRE-rBG (AAV2/1-CB7-mCerulean), AAV2/2-CB7-CI-eGFP-rBG (AAV2/2-CB7-EGFP), AAV2/5-CB7-CI-eGFP-WPRE-rBG (AAV2/5-CB7-EGFP), AAV2/6-CMV-PI-eGFP-WPRE-bGH (AAV2/6-CMV-EGFP), AAV2/7-CB7-CI-eGFP-rBG (AAV2/7-CB7-EGFP), AAV2/8-CMV-TurboRFP-WPRE-rBG (AAV2/8-CMV-turboRFP), AAV2/9-CB7-CI-mCherry-WPRE-RBG (AAV2/9-CB7-mCherry). Three different viruses were mixed for each injection. The mixture ratio was determined so that each individual virus was present at a final concentration of 3×10^{12} GC ml⁻¹ (Yizhar et al., 2011).

For optogenetics experiments three viruses were used AAV2/1-CAG-hChr2(H134R)-mCherry-WPRE-SV40 based on the Addgene plasmid 20938M (AAV2/1-CAG-hChr2(H134R)-mCherry), AAV2/1-CamKII α -hChr2(H134R)-mCherry-WPRE-hGH, Addgene 26975 (AAV2/1-CamKII α -hChr2(H134R)-mCherry) and AAV2/1-CamKII α -hChr2(H134R)-eYFP-WPRE-hGH based on Addgene 26969P (AAV2/1-CamKII α -hChr2(H134R)-eYFP). Several batches of virus were used, concentration ranged from 6×10^{12} to 2.48×10^{13} GC ml⁻¹ (Yizhar et al., 2011).

To test Fugu promoters as a means to achieve interneuron specific expression, we received the following constructs for the three Fugu derived promoters fNPY, fSST and fPV as a gift from the laboratory of Dr. Edward Callaway. AAV2/1-fNPY-bGlob-GFP-bGH, AAV2/1-fPV-bBGlob-GFP-bGH, AAV2/1-fSST-bGlob-RFP-bGH, AAV2/1-fSST-bGlob-GFP-bGH (Nathanson et al., 2009).

Cre-lox was tested using a 1:1 mixture of AAV2/1-CAG-Cre virus and AAV2/1-CAG-Flex-tdTomato-WPRE (final concentration 2.94×10^{12} GC ml⁻¹). The mixture was injected.

2.2.2 Lentivirus

Lentivirus was purchased from the University of Pennsylvania vector core. For experiments to test lentivirus infectious properties in turtles we used VSVG-HIV-SIN-Syn-ChR2(H134R)-eYFP.WPRE based on the Addgene plasmid 20945 (concentration 8.87×10^{10} GC ml⁻¹).

2.2.3 Rabies virus

Aliquots of *rabies virus* (Callaway, 2008; Wickersham et al., 2007; Wickersham et al., 2006) were obtained as a gift from the Dr. Karl-Klaus Conzelmann laboratory. Two types of *rabies virus* were injected into turtles. *SAD-deltaG-eGFP(SAD G)* and *SAD-deltaG-mCherry(SAD G)* (Ginger et al., 2013). In mice we injected *SAD-deltaG-eGFP(SAD G)*. Injections were as described in chapter 4.1.1), incubation times before perfusion was 7 days (Niedworok et al., 2012). Virus concentration were not determined.

2.2.4 AAV-SL1

AAV-SL1 (also referred to as *rAAV2-retro*) was a gift from the laboratories of Dr. Alla Karpova, Dr. Loren Looger of Janelia Farm Research Campus and Dr. David Schaffer at UC Berkeley. At the time of experimental use *AAV-SL1* had not yet been published (Tervo et al., 2016). *AAV-SL1* is a novel serotype of AAV differentiated by a novel capsid protein. To create *AAV-SL1* the gene coding the capsid protein of *AAV2/2* was engineered (Luo et al., 2008) into several variants. These variants were then screened for the property of retrogradely infecting neurons. This property arises from the virus' tropism for infecting neuronal axons. *AAV-SL1* shows these retrograde infective properties.

To test the potential retrograde properties of *AAV-SL1*, we injected a mixture of *AAVSL1-CAG-EGFP* and *AAV2/1-CB7-Cl-mCerulean-WPRE-rBG (AAV2/1-CB7-mCerulean)* (concentration of both 3×10^{12} GC ml⁻¹). To characterize retrograde properties of *AAV-SL1* against a known standard, we used the standard retrograde tracing technique of Cholera Toxin subunit B. Thus the injected mixture also contained CTB-Alexa555 (1 %, Life Technologies (Dederen et al., 1994; Trojanowski, 1983; Trojanowski et al., 1982; Wan et al., 1982).

2.3 Neurophysiology

2.3.1 Slab preparation

Turtles were anesthetized using Ketamine (23 mg kg⁻¹, IM) and dexmedetomidine (75 µg kg⁻¹, IM). After loss of the corneal reflex, turtles were decapitated and the heads rapidly transferred into cooled turtle Ringer solution (96.5 mm NaCl, 2.6 mm KCl, 4 mm CaCl₂, 2 mm MgCl₂, 31.5 mm NaHCO₃, 20 mm glucose, pH

7.4) aerated with carbogen gas (95 %-O₂ / 5 %-CO₂). The skull was opened to access the dorsal surface of the brain and dura mater and arachnoid were carefully removed.

Cortical slabs were prepared with iridectomy scissors after two transverse sections of the cortical sheet: (1) slightly posterior to the anterior pole of the cortex; (2) 3 to 5 mm caudally of the first incision. In addition two parasagittal sections: (1) along the medial-dorsal cortex border medially; (2) just medial to the olfactory cortex laterally, where dorsal cortex joins the DVR. Slabs exceeding 4 mm (A-P direction) were often cut in half. Experiments were performed with slabs of both anterior and posterior portions of dorsal cortex.

To penetrate the turtle pia mater (a peculiarly resilient structure) with a patch pipette, we ablated the pia by pulsing a UV laser (7000 pulses of 14.5 kV at 200 Hz, Ex5 Excimer, GAM Laser Inc., FL, USA) spot (300 to 400 μm diameter) onto the pia. UV excimer lasers, commonly used in ophthalmology surgeries, remove superficial layers without damaging underlying tissue with high precision (on the order of several micrometers).

During all experiments tissue was superfused with oxygenated turtle Ringer kept at a temperature of 25 °C with an inline temperature controller (CL-200A, Warner Instruments, CT, USA).

2.3.2 Patch-clamp

For all experiments in chapter 5, long-shank patch pipettes (8 to 12 M Ω) were pulled from borosilicate glass capillaries (outer/inner diameter 1.5 mm/0.86 mm; Sutter Puller P1000). We used a blind-patching approach, by penetrating the tissue in areas where the UV-Laser treatment had removed the pia. UV-laser holes in the pia were identified for tissue penetration based on an autofluorescence signal. Upon >10% increase of the initial pipette resistance, positive pressure was released to achieve a Giga-Ohm seal (success rate 80%). Patching pyramidal cells through the pia required penetration depths of up to 400 μm . Therefore, L2 pyramidal cells were patched blindly, and L1 interneurons under visual guidance. After establishing the Giga-Ohm seal, a pneumatic device (Sigmann Elektronik, Manual Sealsucker) was used to open the membrane with defined vacuum pulses (400 to 600 mbar, 230 ms) and to establish whole-cell configuration. Cells were held for at least 30 minutes to insure filling with biocytin.

In another configuration of slab patching experiments (used in all optogenetic experiments), cells of Layer II and III were patched under visual guidance from the ventricular side of cortex using pipettes of lower impedances (4 to 7 M Ω). The ependymal side of the slab could be penetrated by applying high pressure (up to 100 mbar) to the pipette.

Pipettes were filled with internal solution (140 mm K-gluconate, 4 mm NaCl, 14 mm Phosphocreatine, 10 mm HEPES, 4 mm Mg-ATP, 0.3 mm Na-GTP, 4 mg ml⁻¹ Biocytin, 0.015 mm Alexa-594 or Alexa-488). All patching was done on an upright Olympus BX61WI microscope with a 40x water immersion objective.

To induce spikes in the patched cell we injected rectangular current pulses (duration 2 s) of amplitudes which would induce action potentials firing at roughly the rate of 7 Hz.

Patched cells were judged to be excitatory or inhibitory based on spike width (at 25 °C excitatory cells greater, interneurons lesser than 2 ms). In electrophysiological protocols testing adaptation of a high frequency spike train interneurons either sustained high frequency spiking, were weakly adapting or non-adapting. Excitatory cells fired lower frequency spike trains and were always adapting.

2.3.3 Multi electrode recordings

After preparation (section 2.3.1), the slab was placed on the multi electrode array (MEA) equipped with a custom-made chamber with the ventricular side down, facing the electrodes. For experiments with channelrhodopsin-infected slabs the pial side faced the electrodes unless otherwise indicated.

Sixty, 120 or 250-channels extracellular electrophysiological recording systems (Multichannel Systems, MEA1060, MEA2100, MEA256) were used with glass embedded titanium-nitrate electrode arrays with 10 or 30 μ m electrode diameter and 40 or 100 μ m electrode spacing (120MEA100/30iR-ITO, 256MEA100/30iR-ITO, 60MEA100/30iR-ITO, 60HexaMEA40/10iR-ITO, Multichannel Systems, Germany). Electrodes are plated with ITO and typically have impedances of 50 k Ω . To insure good contact between electrodes and tissue a nylon mesh on a 200 to 500 μ m-thick spacer (similar to a slice grid) was used. For experiments combining patching of deep Layer III interneurons with parallel MEA recordings, slabs were placed pial side down in a bath chamber, flexible MEAs (FlexMEA, Multichannel Sys-

tems, Germany) with electrodes embedded in polyimide foil were placed on the ventricular surface and held in place with a regular grid for brain slices. Patching was performed through one of several 30x70 μm holes in the polyimide foil.

2.3.4 Pharmacology

To increase spontaneous firing rates without causing synchronized activity or epileptic events we used carbachol (5 to 20 μm) (Konopacki et al., 1987; Tateno et al., 2005). To block GABAA receptors we used gabazine (5 μm), excitatory currents were blocked with APV (NMDA receptor antagonist; 75 μm) and CNQX (AMPA receptor antagonist; 20 μm). All pharmacological agents were added to the superfusate.

2.3.5 Spike Sorting

Spike sorting was developed by Mark Shein Idelson (unpublished). Spikes were detected from band-pass filtered (200 to 250 Hz) voltage traces using a floating threshold (updated every 2 min) of 5 standard deviations over the mean for spikeless recording segments. Spike-less segments (20 ms binning) were selected if their kurtosis was ≤ 3 . Spike segment were characterized by higher values (corresponding to super Gaussian distributions). Spike time was determined from the minima of the Gaussian-convoluted ($\sigma = 0.3$ ms) spike waveform. To avoid multiple detection of spikes on several electrodes, we rejected spikes if, within 0.5 ms of a spike's occurrence, a spike with a larger minimum was detected in one of the 4 nearest channels. Each spike was associated with the electrode (spike channel) in which the spike voltage deviation was the greatest.

Spike features were extracted from 5 ms spike waveforms (upsampled to 60kHz and starting 2ms before spike peak time) on all electrodes with distances ≤ 150 μm from the spike channel. Waveforms were decomposed using the Haar wavelets (4 levels). The distribution of wavelet coefficients over all spikes was used to select the 30 coefficients that best discriminated between spikes according to their non-Gaussianity using the Lilliefors modification of the Kolmogorov-Smirnov test (Quiroga et al., 2004). Finally, 6 coefficients per spike were selected by taking the first six (maximally variable) component.

For each electrode, spike features were clustered using modified mean shift clustering as introduced by Marre et al. (Marre et al., 2012). Some of the clusters

were subsequently merged to avoid over-clustering. For every pair of clusters, the spikes belonging to both clusters were projected on the line connecting the two cluster centers and their distributions along this line were calculated. Clusters were merged if the probability in the interval $[l-\sigma_1/2, l+\sigma_2/2]$ was > 0.19 , where l is the intersection point of the two distributions (the point where the integral over one distribution minus the integral of the other changes sign), and σ_i is the standard median deviation of cluster i . Spikes in each cluster were averaged to form spike templates and the standard deviation of this mean template was calculated using $\sigma/\sqrt{n+1}$, where n is the number of averaged spikes and σ the standard deviation.

In some cases, the site at which the spike of one neuron was the largest varied due to local noise (e. g. , if the neuron was located in between two electrodes). This resulted in more than one template for that neuron. Such templates were merged as follows:

First, templates were aligned by using the lag of their cross-correlation maxima. Next, samples exceeding 4 standard deviations of the mean in both templates were selected. Finally, templates were merged if $(M_1-M_2)^2/(\sigma_1^2+\sigma_2^2)>0.1$, where M and σ are the mean and standard deviation of the selected samples. After merging, all detected spikes were fitted to one of the templates according to the minimal Minkowski distance (order 2) between the spike and all time-shifted template versions (-0.5 to 0.5 ms, 0.3 ms intervals).

2.3.6 SIF measurement

Raw segments around the spike times of sorted units (100 ms-long traces starting 20 ms before spike peak time) were extracted and averaged. For every electrode, traces were smoothed and the baseline was estimated and subtracted from the traces to remove slow drifts. Both baseline and smoothed traces were calculated using a weighted cubic spline with weights (w) described as follows:

$$\begin{cases} w = 1 - \exp\left(-\left(\frac{t-t_0}{2a}\right)^2\right), & \text{if } t > t_0 \\ w = 0, & \text{otherwise.} \end{cases}$$

For baseline calculation we used $t_0=50$ and $a = 7$; for smoothing we used $t_0 = -3$

and $a = 21$. In both cases spike peak was at $t = 0$. In simple cases where less than 20% of the electrodes showed a baseline shift of at least $20 \mu\text{V}$, we set the baseline to be a constant function estimated from the median over the potential during 10 to 20 ms before spike peak.

SIF polarity was calculated as follows. We first correlated the baseline-subtracted averaged raw waveforms (BSWF) with the different SIF templates (Fig. 3 and supplementary Fig. 3) during a time segment of 5 to 30 ms post spike peak and over electrodes with distances of up to $290 \mu\text{m}$ from that of spike peak. Next, SIFs were determined as excitatory if more than half of the electrodes showed greater correlation with the excitatory template; there were determined as inhibitory otherwise.

To determine the spatial distribution of SIFs, the peak potential (minimum for excitatory cells and maximum for inhibitory cells) was extracted from the BSWF and interpolated over the array with a 2 dimensional spline ($10 \mu\text{m}$ resolution). The SIF vector was calculated from the triangulated spike-source position to the peak of the interpolated SIF. SIFs with peaks outside the array area or within an inner band of up to $50 \mu\text{m}$ from the array edges were rejected.

2.3.7 Estimation of spike source location

Triangulation of spike-source location (putative spike-initiation zone and/or soma) was performed on averaged (over all spikes of a given neuron) high-pass filtered spike waveforms (5 ms window, starting 2 ms before spike peak) with distances of up to $150 \mu\text{m}$ for the spike-peak electrode (electrode with the largest spike amplitude). The potential V_i at peak time was extracted from all electrodes (at positions r_i) and the triangulated position r_0 was optimized (Lagarías et al., 1998) by minimizing the mean square error:

$$\sum_i (V_i - V_0 e^{-\frac{|\vec{r}_i - \vec{r}_0|}{\lambda}})^2$$

with the constraints that (i) the z position is between 0 and $200 \mu\text{m}$ from the electrode surface and (ii) V_0 is larger than the potential on the maximal electrode.

2.3.8 Dendrogram & SIF Clustering

For each neuron, the baseline-subtracted averaged raw waveforms (BSWF) recorded from the electrode with the largest SIF was used for clustering. The Pearson correlation matrix between all BSWF pairs was evaluated. This correlation matrix was clustered into two main groups using agglomerative clustering (Ward linkage method over Euclidean distances). SIF templates were extracted by averaging BSWFs within each group. SIFs from single units with average spike amplitude $< 5 \mu\text{V}$, with $n < 100$ detected spikes or with $SNR < 0.5$ were rejected. SNR was defined as the root mean square of the ratio between the average and standard deviation of all spike samples and all spikes in electrodes with distances $< 150 \mu\text{m}$ from the spike-peak electrode.

2.3.9 SIF calculation from anatomy of reconstructed neurons

The SIF recorded on the MEA was estimated from the reconstructed neuron, using volume conductance theory (Rall, 1962) to estimate the potential in space due to individual current point sources located along the reconstructed axon ($10 \mu\text{m}$ spacing). To account for the boundary conditions created by the MEA and the ringier solution surrounding the cortex, we used an approximation based on the method of images (Ness et al., 2015). For simplicity, we assumed the current sources to be uniformly distributed along the axon with current density I [A/m]. To account for return currents we placed, for each source, an additional source with an opposite charge $50 \mu\text{m}$ above the cell layer. By fitting the estimated to the measured potentials we could estimate I for every neuron; a typical value was $1 \text{ pA } \mu\text{m}^{-1}$ of axon.

2.3.10 Mean Oscillation Cycle

To compare the shape and relative timing of the oscillation cycles in multiple cells patched in parallel and the MEA, I calculated a "mean oscillation cycle" as follows.

One patch recording was chosen as a reference; during the period of one light stimulation (2 s) a Hilbert transform was calculated on this trace. From the resulting Hilbert envelope the phase angle was computed. Peak times of the phase angle were detected. Time windows ($\pm 150 \text{ ms}$) centered around these peak times

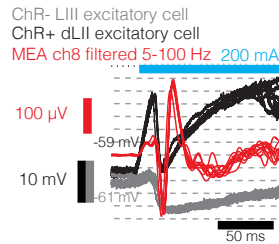


Figure 2.1: Parallel patch-clamp recording of two pyramidal cells and LFP recording with MEA (red trace). Ten trials are superimposed. The V_m of one cell (black trace) shows sharp depolarization immediately after light onset and is thus judged ChR+. The other cell (grey trace) depolarizes so weakly it is judged ChR2-.

were used to extract recording traces of all parallel recordings from patch-clamp and MEA. All resulting traces of each oscillation cycle in the 10 repetitions of light stimulation were averaged for each recording type and plotted.

2.4 Optogenetics

For the optogenetic experiments, the protein channelrhodopsin-2 (ChR2) was expressed in cortical cells (Nagel et al., 2002; Nagel et al., 2003; Boyden et al., 2005). ChR2 is a microbial rhodopsin and ion channel, whose gene was isolated from *Chlamydomonas reinhardtii*, maximally activated by light at 470 nm resulting in rapid depolarization and repolarization of neurons expressing it. The H134R variant of ChR2 was used yielding larger photocurrents relative to wild-type ChR2 (Nagel et al., 2005; Gradinaru et al., 2007), and well suited for ms-precision in the activation of neurons (Zhang et al., 2010; Deisseroth, 2011; Yizhar et al., 2011).

ChR2 was under the control of a CAG or CaMKIIa promoter, delivered with AAV2/1 virus and visualized by the a fluorescent protein tag (mCherry, EYFP) (Yizhar et al., 2011). See section 2.2 for a detailed description of the viruses used. Experiments were done within 48 h after preparation.

Patched cells were judged to be ChR2-positive or -negative based on visual inspection of fluorescence under the microscope and subsequent analysis of the timing of light-evoked depolarization (see Figure 2.1). ChR2-negative cells depolarized about 8 to 15 ms after light onset (reflecting indirect activation via connected ChR2+ cells), whereas ChR2+ cells depolarized immediately upon light onset (the membrane potential crossing of 3 standard deviations within around

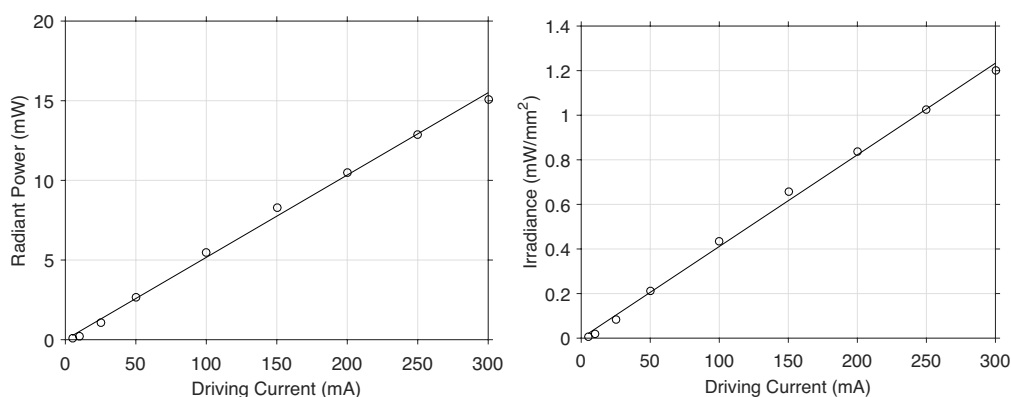


Figure 2.2: Graphs show linear correspondence between electric current driving the LED of the PlexBright light stimulation system and its light output. Left graph shows light power measured at a distance of 3 mm from the tip of the optic fiber, corresponding to the distance between fiber tip and slab during experiments (radiant power in mW). Right graph shows surface power density (irradiance in mW/mm^2) in the illuminated area of the slab (12.6 mm^2). Circles indicate measured light at a given driving current, the line a fitted linear regression.

one 1 ms).

2.4.1 Light delivery

For delivery of light to tissue (slab or whole-brain preparations) in the described optogenetic experiments (chapter 6) two types of light sources were used.

(a) A PlexBright optogenetic stimulation system (Plexon Inc, Texas, USA) under the control of the Radiant control software was used, allowing light delivery with submillisecond precision. In short this system consists of a LED driver unit with real-time control of light output, triggered externally by TTL pulses to synchronize intracellular and extracellular recordings with the light stimulus. The driver controls an LED emitting light with a wavelength of 465 nm. Maximum driving current was 300 mA. The tip of a 0.5 m-long fiber-optic cable attached to the LED was placed into the bath, 2 to 4 mm from the specimen. The tip of the fiber was oriented such that the light beam was centered onto the region of Chr2 expression. Emitted light power ranged from 0.2 to 15 mW. In the results section driving current (in the range 5 to 300 mA) is given. Calibration is given in Figure 2.2.

(b) For experiments that required spatiotemporal control of light delivery, a custom-made system was constructed on an inverted microscope. A digital micromirror device (DMD) DLP LightCrafter4500 (Texas Instruments, Texas, USA) producing approximately 150 lumens at 15-W LED power consumption was attached with

appropriate lenses to the light port of an Olympus IX73. A set of Matlab functions, the “psychtoolbox” (Brainard, 1997; Pelli, 1997), was used to control the DMD and synchronize data acquisition with light stimulation. This setup allowed us to deliver light with a resolution of 912 x 1140 pixels in the field of view (corresponding to submicron resolution with a 20x objective) with a temporal precision of 17 ms. The experimental setup with the DMD was developed in collaboration with Mark Shein-Idelson.

2.5 Histology

2.5.1 Perfusion, sectioning, mounting

Turtles were anaesthetized as in 2.3.1. After decapitation the carotid arteries were exposed, intravenous needles for premature infants (Braun, Germany) were inserted and 30 ml of PBS was perfused through each hemisphere to remove blood from the brain, followed by 25 ml of fixative. For all histological procedures the fixative was 4% PFA (heated to 72 °C prior to usage then cooled on ice), except for GABA antibody (polyclonal anti-GABA, guinea pig, Novus Biologicals / Anti-GABA antibody, rabbit, Sigma). For GABA antibody staining, the brain was additionally perfused with 0.5% glutaraldehyde.

The brains were removed from the skull and kept for 24 h in 4% PFA at 4 °C, then transferred for at least 12 h in 30% Sucrose for cryoprotection.

The brain (from the olfactory bulb to the posterior end of cortex) was embedded in Tissue-Tek (Sakura, Japan) and frozen onto the specimen-table. Sectioning was performed on a cryotome (Zeiss, Germany) with a section thickness ranging typically from 40 to 70 µm.

2.5.2 Staining methods

Immunohistochemistry on brain sections

The sections (40 to 70 µm) were collected in 48-well plates with 500 µL PBS per well. In sections for horse radish peroxidase (HRP)-based staining, endogenous peroxidase was quenched in 3% H₂O₂. To block unspecific binding sites the sections were gently shaken overnight in 200 to 250 µL blocking solution. Blocking solution contained 5% BSA (Carl Roth) in PBS.

The primary antibody was applied in 200 to 300 μL solution in a cold-room for 72 h. Antibody concentrations in PBS with 2 % BSA and 1 % Triton were 1:1000 for NeuN AB (Merck Millipore, Anti-NeuN monoclonal mouse antibody, MAB377), 1:3000 for NPY AB, 1:3000 for GABA_B AB (polyclonal anti-GABA, Guinea Pig, Novus Biologicals / Anti-GABA antibody, rabbit, Sigma), 1:250 for Somatostatin AB, 1:500 for c-Fos (Santa Cruz Biotech), 1:500 for Egr1 (Santa Cruz Biotech), 1:250 for Arc (Santa Cruz Biotech). Finally sections were washed in 1 % Triton in PBS 2-3 times for 1 h each.

Alexa-conjugated or biotinylated (for IEGs) secondary antibody was applied in 200 to 300 μL solution per well overnight at room temperature at a dilution of 1:1000 in PBS with 2 % BSA and 1 % Triton. Sections were then washed in PBS 2 times for 1 h each and finally mounted on gelatine-coated microscope slides (Fisherbrand Superfrost) using DAKO mounting medium and glass coverslips.

All solutions contained 0.05 % Thimerosal.

Staining following electrophysiology

Images of tissue and electrodes were taken directly after preparation, during recording and after biocytin staining for later spatial alignment. For registration with confocal images of the tissue we added the vascular stain Isolectin-IB4 (either applied intravenously during the preparation or directly into the recording chamber at the end of the experiment; 0.01 mg mL^{-1}) (Ernst and Christie, 2006) .

After an experiment, the tissue was fixed for 24 hours in 4 % PFA (PFA heated to 72°C prior to use then cooled on ice). For experiments performed with whole-brain preparations, the cortical slab was subsequently removed from the rest of the brain for further processing.

We immunostained cortical slabs following a protocol adapted from published whole-mount immunohistochemistry method (Sillitoe and Hawkes, 2002)(Sawada and Sun, 2010). Tissue was post-fixed overnight in Dent's fixative (methanol:DMSO = 4:1) at room temperature (RT), followed by Dent's bleach (methanol:DMSO:H₂O₂ = 4:1:1) also overnight at RT. The tissue was then rehydrated in 50 % and 15 % Methanol in PBS for 90 min each and subsequent overnight incubation in PBSBT at 4°C . The slabs remained for 72 h at RT in primary antibody specific to neurons (Merck Millipore, monoclonal mouse Anti-NeuN antibody, 1:100) and calbindin-positive interneurons (Swant, polyclonal rabbit anti-calbindin antibody, 1:100) diluted in PBS containing 10 % goat serum, 0.1 % Triton and 5 % DMSO. After rinsing with PBSBT, we incubated for another 48 h in secondary antibody (Life

Technologies, donkey Alexa Fluor 568 anti-rabbit, 1:200; donkey Alexa Fluor 488 anti-mouse, 1:200). Finally the tissue was stained with DAPI.

Biocytin staining

To visualize neuronal morphologies we used a common biocytin staining procedure (Helmstaedter et al., 2008; Lübke et al., 2003; Markram et al., 1997a; Stuart et al., 1993). Briefly, after recordings slices were fixed at 4 °C for at least 24 h in 100 mm PB, pH 7.4, containing 4 % paraformaldehyde (4 % PFA). After extensive rinsing in PB and quenching of endogenous peroxidase in 3 % H₂O₂, turtle cortical slabs were incubated in 2 % Triton X-100 solution for permeabilization and after PB rinsing, incubated in 1 % Triton X-100 containing avidin-biotinylated horseradish peroxidase (ABC-Elite; Camon, Wiesbaden, Germany). We used 3,3-diaminobenzidine (DAB) as a chromogen for visualizing dendritic and axonal arborization. Slabs were then placed in Mowiol (Carl Roth, Germany) or further processed for tissue clearing with benzyl alcohol-benzyl benzoate (BABB, see section 2.5.3).

2.5.3 BABB clearing

We cleared the slabs using the benzyl alcohol-benzyl benzoate (BABB) method (Dodt et al., 2007). We dehydrated the tissue with an increasing ethanol series (30 %, 50 %, 70 %, 80 %, 96 %) gently shaking the tissue in glass vials on a shaker for one hour at each step, followed by an overnight incubation in 100 % ethanol. The slabs were then incubated for 2 hour in Methanol, followed by a benzylalcohol - benzylbenzoate mixture (1:2) for a minimum of 48 hours. After clearing, the tissue was stored in darkness in the BABB solution at 4 °C.

BABB clearing had no deleterious effect on Biocytin and Isolectin-IB4 (Ernst and Christie, 2006) staining.

2.5.4 Imaging

Imaging of histological sections and whole cortical slab mounts was performed using a laser scanning confocal microscope (LSM710, LSM880, Zeiss). For sections with immediate-early-gene staining and those with EGFP expression under a CaMKIIa promoter, we used a laser scanning automated microscope (Pannoramic

Midi, 3D Histech).

2.5.5 Reconstruction of neuronal morphologies

Biocytin-stained neurons in cortical slabs were reconstructed with the aid of NeuroLucida software (MicroBrightField) using a Zeiss Axiophot microscope with a 63x Zeiss objective. Cell bodies, dendrites and axons are identified in the reconstruction. The ependymal surface of the slab was also reconstructed. Resulting reconstructions were read into MATLAB and were the basis for further morphological analyses.

2.5.6 Alignment of cell to MEA

To allow coregistering morphologies of the reconstructed biocytin-labelled patched neurons to the spatial distribution of the electrophysiological signals recorded on the 2D microelectrode array (section 5.5) a set of Matlab functions were used to perform a linear transformation for rotation, translation, scaling and reflection. The MSAC algorithm (M-estimator Sample Consensus, (Torr and Zisserman, 2000)) was used to calculate the linear transformation based on N ($N > 6$) manually selected points in each set of images. Three steps, each yielding a matrix for spatial transformation, were followed to allow the final transformation.

1. Registration of cell morphology to the fixed slab.
Photographs were taken of the slab after fixation, biocytin staining and clearing. Picking landmarks on the neuron clearly identifiable both in the photograph and the reconstruction (cell body, ends, forks and unique bends of the dendrites) allowed to calculate a transformation matrix from the neuronal morphology to the global photograph of the fixed slab.
2. Registration of the fixed slab to the live slab.
During the experiment images were taken of the slab on the MEA. These images showed both the pial surface of the slab and the electrodes of the MEA. Thus picking landmarks identifiable both in the photograph of the fixed slab and the slab on the MEA (edges and blood vessels) allowed to calculate a second transformation matrix.
3. Registration of the slab during the experiment to the MEA electrodes.
The images during the experiment showed the physical electrodes of the

MEA. For the last transformation, the location of the physical electrodes in the images were assigned to the electrode layout for analysis.

Combining the resulting three transformation matrices resulted in a global transformation matrix, which enabled us to project the reconstructed neuron morphology on the MEA, retaining the relative spatial arrangement of the neuron and the recording electrodes during the experiment and thus, to assign MEA signals recorded from specific electrodes to particular regions of the recorded neuron.

Chapter 3

Olfactory stimulation software

Even though olfactory research has become a major area in neuroscience there is at present no general-purpose software for the delivery of olfactory stimuli, as there exists for vision with the psychophysics toolbox (Brainard, 1997; Pelli, 1997). Therefore solutions are often idiosyncratic and usually not flexible enough for new tasks or extensions. They are also often not published, leading to a multiplication of coding effort within the community.

The goal of *olfStim* is to start bridging this gap and provide scientists with a core set of functionalities solving basic olfactory stimulation needs. We constructed a modular software architecture written in the widely used MATLAB programming language. For more specialized needs users can combine existing modules and write extensions. *olfStim* is open source, available at no cost and hosted on the collaborative coding platform github, which will hopefully lead to a collaborative effort in expanding its functionality.

olfStim can currently be used in combination with the LASOM olfactometer control board, sold by RPMetrix (<1500 USD). All interactions with the LASOM board are executed from one library of functions and one library of scripts. Hence if a different control board is needed (e. g. Arduino processor), new libraries can be added and used.

olfStim, in combination with LASOM board and the necessary valves and mass flow controllers, offers a versatile and inexpensive solution to the technical needs of scientists in the field of olfaction research.

olfStim is hosted on github <https://www.github.com/lorenzpammer/olfstim>, available either as a standard bundled download or via the recommended method using git (<http://git-scm.com/>). Git is a widely used version control system and

offers many advantages such as enabling users to update *olfStim* to new versions, while keeping personalization of the software intact, allowing rollback to a previous working version, etc..

Detailed description of *olfStim*'s features and usage can be found in the Documentation file on the web page. *olfStim* is available under a creative commons license.

3.1 Requirements

olfStim requires a basic Matlab installation (R2008a and higher, Mathworks, Natick, MA, USA) and runs as a collection of functions and scripts. No commercial toolbox or external function is required.

olfStim runs on any standard personal computer with a USB 2.0 port, and works with 32bit versions of Windows XP and Windows 7. The limitations of possible operating systems are due to the executables communicating directly with the LASOM olfactometer control boards. All other functions of *olfStim* run on any machine with the necessary Matlab installation (Windows, Linux or Mac).

3.2 Olfactometer

The design of the olfactometer hardware (Figure 3.1) comes from Dmitry Rinberg and his laboratory. For a detailed description of the hardware components and construction, please refer to *olfStim*'s documentation included in the *olfStim* package.

Briefly, vials pierced with two tubes, one for gas inflow and one for outflow, are partially filled with odorants and connected to valve manifolds (Figure 3.1). In the ground state one nitrogen gas line joins an air gas flow after passing through an empty "dummy" vial. Dedicated mass flow controllers (MFC) regulate the flow rate of each gas. For odor presentation the ratio between nitrogen and air gas flow is set to the desired odor concentration. The opening of two valves gating the odorant-containing vial and the simultaneous closing of the dummy vial gating valves routes the nitrogen flow through the odorant vial. After passing through the odorant vial the odorized nitrogen joins the air-flow. Thus the air stream from the olfactometer carries odorant. For actual odorant presentation to the subject, the final valve, a two three-way valve (two inputs, two outputs, swapping the outputs) is powered, switching the gas flow to the experimental subject from clean air

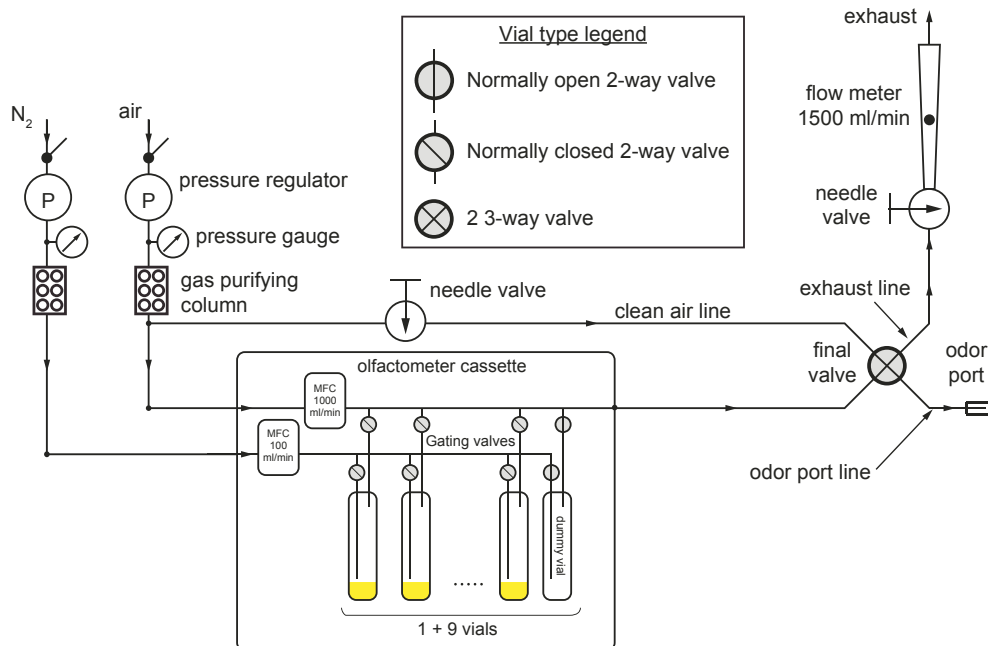


Figure 3.1: Olfactometer hardware design was developed in the laboratory of Dmitry Rinberg. Two gas supplies (around 2 bar), one with Nitrogen the other with pressurized air, are first routed through gas purifying columns (Drierite, OH, USA), ensuring clean and dry gas and are connected to the inlets of two IQ+flow mass flow controllers (Bronkhorst, Netherlands). The gas exits the MFCs with a defined flow rate and enters the solenoid valve manifolds (NRResearch, NJ, USA) included in the olfactometer cassette. Two of these valves gate a vial, which is prepared with two tubes, one for gas inflow and one for outflow. The tubes are partially filled with odorants. In the ground state the nitrogen gas flow joins the air gas flow after passing through a normally open valve and the empty "dummy" vial. The opening of two valves gating the odorant-containing vial and the simultaneous closing of the dummy vial gating valves routes the nitrogen flow through the odorant vial. For odor presentation the ratio between nitrogen and air gas flow is adapted to the desired odor concentration. After passing through the odorant vial the odorized nitrogen joins the air-flow. Thus the air stream from the olfactometer cassette is carrying odorant. For the actual odorant presentation to the subject, the final valve, a 2 three-way valve (NRResearch, NJ, USA) is powered, which results in replacing the gas flow in the odor port line to the subject from clean air (supplied by the clean air line) with the odor-containing air from the olfactometer cassette. It also results in routing the clean air to the exhaust line (in the ground state the air from the olfactometer cassette is routed to the exhaust line). The needle valve in the exhaust line allows to match the resistance of the exhaust line to the resistance of the odor port line. This is important to avoid unexpected jumps in flow rate with inaccurate odor concentrations when switching the final valve to present the odor. At the end of the presentation the gating valves and the final valve are switched back to their initial state. This ensures rapid onsets and offsets of odors, precise concentrations and minimal (cross)contamination. Using the LASOM control board, nine to fourteen odors are organized into one "olfactometer cassette" (Figure 3.2, 3.3). Every cassette has its own LASOM board, MFCs and valve manifolds. By combining multiple of these cassettes up to 100 odorants can be added to the olfactometer and are available for use in experiments.

with the odorant-containing air. At the end of the presentation the gating valves and the final valve are switched back to their initial state. This ensures rapid odor pulse onsets and offsets, precise concentrations and minimal (cross)contamination during odor presentation (Figure 3.2, 3.3).

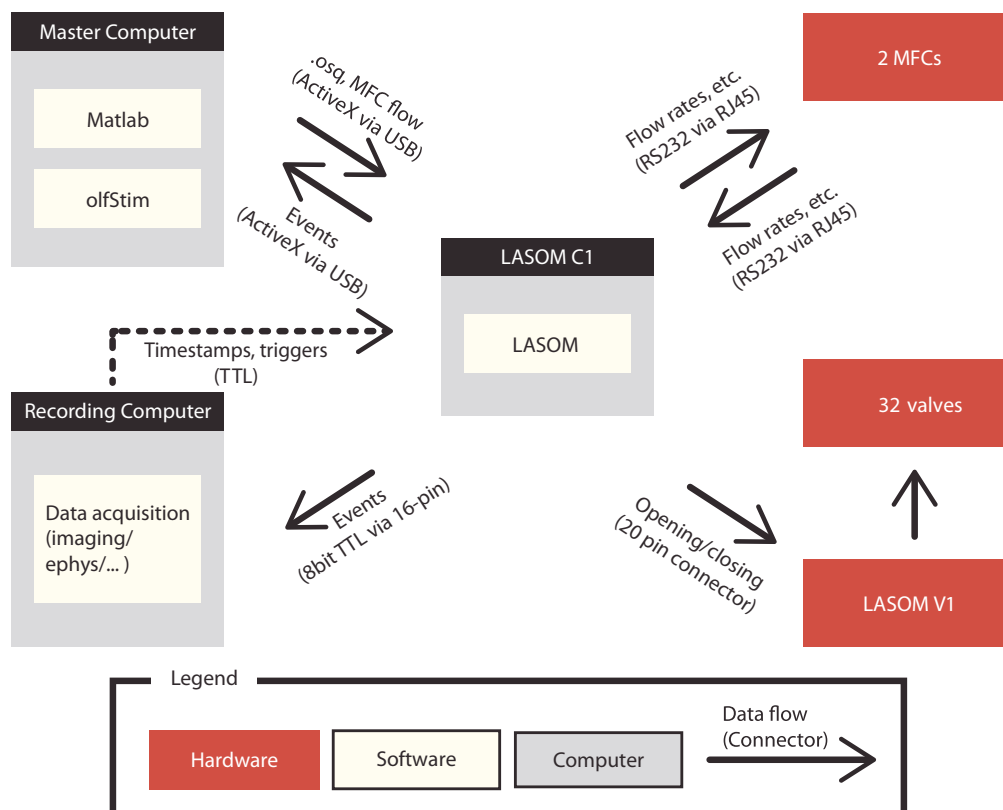


Figure 3.2: *olfStim* interacts with the olfactometer on a trial by trial basis. The graphic shows the interactions between the components of a simple olfactometry experiment. *olfStim* runs in Matlab on the master computer, which is connected to the olfactometer (LASOM C1) via USB. *olfStim* initiates a trial in two steps once the user specified the trial parameters and starts the trial. First it constructs a script in the sequencer-language of the control board's microprocessor and transmits this sequencer code (.lsq files) via ActiveX. Second it sets the flow rates of the MFCs. The sequence code contains all the instructions for the respective trial except setting the MFC flow rates. Thus it contains all the time-critical commands, such as valve actions, timestamps, responses to external triggers, etc. After transmission, *olfStim* sends commands via ActiveX to LASOM to start executing of the sequencer code by the LASOM control unit, which results in a temporally precise sequence of events such as valve-opening and closing (via the LASOM V1 valve board) and digital triggers (pins on LASOM C1). Other devices can be synced to the actions of the olfactometer via these digital triggers.

3.3 Olfactometer Control

olfStim is fundamentally designed to function in a trial-based regime. In each trial one odor can be presented with one concentration. Odor concentrations are measured in fraction of saturated head-space. It is possible to present the same odor at the same concentration several times within one trial, by repeated switching of the final valve. It is however not possible to present several odorants or change concentrations within one trial. This is because, in such a regime, cross-contamination or inaccurate concentrations would be unavoidable. The duration



Figure 3.3: **A** Sequence of events during a typical trial. The GUI allows the user to set the total flow rate of the presented odorant and the times of several valve actions. Writing a vector (multiple numbers surrounded with brackets) in the field results in multiple instances of the valve-opening or closing in one trial at the defined times. Name, number and default values of these valve actions can be defined in configuration files. In this example the times of opening and closing valves gating the odorant, the final valve gating the line to the animal and several custom valves can be set. **B** Another GUI component allows the user to add I/O actions to the current trial. Available I/O actions enable the user to start real time execution of the sequencer by external triggering and controlling 3 digital output lines. Custom I/O actions can be defined, ranging in complexity from controlling a certain digital trigger to sequences of code allowing closed loop experiments. **C** The GUI visualizes the sequence of events during one trial. Lines denote the open (high) and closed (low) state of the valve stars denote onset times of digital outputs. The broken line denotes the end of the trial (time of the last action).

of the inter-trial period should be chosen to allow for clearing of the tubes from residual odors of the previous trial, at least 5 seconds.

olfStim's main functionality lies in its ease of use for olfactometer control, ensuring accuracy in concentration and time course. To achieve this, the typical events contained in a trial are as follows.

olfStim creates a set of commands for the microprocessor of the olfactometer controller (e. g. LASOM), reflecting the user's choices for the trial. This set of commands is written in a language appropriate for the microprocessor (eg, the *lsq* language) and transmitted to LASOM using an activeX command over USB 2.0 (Figure 3.2, 3.3).

Once this sequence has been transmitted, an *olfStim* Matlab function, via an activeX command, sets the target flow rates of the two mass flow controllers (Figure 3.2, 3.3). The target flow rates follow from the user's definition of total gas flow rate to the subject and the desired concentration of the odor. The range of possible flow rates depends on the specifications of the MFCs and desired odor

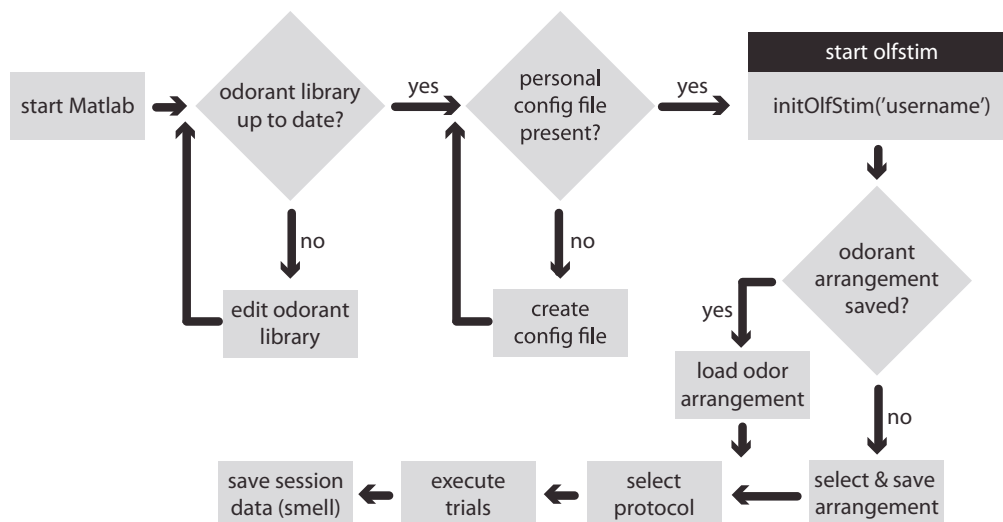


Figure 3.4: Flowchart describing a typical sequence of actions and events during an experimental session using *olfStim*. At first use of *olfStim* or when the user wants to use a novel odorant, the odorant library has to be edited. Every user of the olfactometer can create its own configuration file, otherwise the defaults will be used. The configuration file defines which valves are connected to the olfactometer, their names, and default settings as well as the digital I/O actions. *olfStim* is then started from the Matlab command line. First the arrangement and properties of the odorants has to be entered (Figure 3.5), then a protocol selected. A protocol is a collection of functions, which define the look and components of the GUI and the processes governing trial execution in order to optimize the functionality of *olfStim* for certain types of experiments. At this point odor stimulations can be performed as governed by the protocol. At the end of the experiment all the data can be saved into a mat structure called *smell*.

concentration; in the described setup, they range from 30 to 1500 ml/min. *olfStim* gives warnings if desired concentrations or flow rates cannot be achieved accurately. The MFCs' flow rates stabilize after roughly 1 second, implying that odor presentation to the animal should be delayed for at least 2 seconds after setting MFC flow rates.

After setting the MFC flow rates, *olfStim* via activeX causes the olfactometer controller to start executing the transmitted sequence, such as opening and closing of valves, and sending or waiting for triggers (Figure 3.2, 3.3).

Every odor presentation involves the following sequence of events. The N₂ stream is routed through the odor vial, resulting in the line from the olfactometer to the final valve filling up with odor-carrying air. The final valve routes the odor to an exhaust, while the experimental subject still receives clean air through a parallel line, also routed through the final valve towards the subject. After flow rate stabilization, the concentration of odor leaving the olfactometer is constant. At this point the final valve can be switched, and the odorant-carrying air is presented to the subject (Figure 3.1).

Mass flow controller flow rates are monitored and stored continuously and warnings are issued at relevant deviations from target rates to a log panel of the GUI (Figure 3.6).

The flow-rate stabilization period results in one limitation: *olfStim* needs time (on the order of seconds) between the command for odor-delivery and actual presentation. Hence closed loop two choice experiments for example cannot be performed with sub-second precision with one olfactometer. A solution would require two olfactometers.

3.4 I/O

For many applications it is necessary to trigger or record precise time stamps of olfactometer actions with external devices. *olfStim* allows a simple form of digital input/output triggers. To add trigger actions, the user has to do two things: Save a block of sequencer code (language for the olfactometer controller) to a designated folder and create an entry in *olfStim*'s configuration file.

Once accomplished, the actions will be available in the I/O GUI as well as for scripting and can be placed at one or multiple time points within the sequence of actions (3.3B).

3.5 "smell" structure

The *smell* structure serves two purposes. First it contains all relevant information for every trial of an olfactory stimulus presentation session. These instructions are provided by the user through the GUI interface or the scripting protocols and are then used by *olfStim*'s functions, for the execution of each trial. Additionally, during the execution of each trial, some trial-related data are stored in *smell* such as the measured flow rate of the mass flow controllers over time, user's notes, logs, etc. Thus after finishing one session of odor presentation, the *smell* structure contains all relevant data for every trial and will typically be saved as a .mat file by the user. In addition it is saved automatically after each trial to avoid data loss during crashes. The final *smell* structure is useful for later analyses.

Data contained in *smell* are: Information associated with the presented odorant in the odor library (see below), time of presentation, target odor concentration,

target flow rates of the mass flow controllers, actual mass flow controller flow rates, user's notes, valves opening and closing times, inter-trial intervals, names of experimenter and animal, command file for sequencer, digital triggers.

3.6 Odor library

An olfactory-research lab typically uses an assortment of different odors for experiments. The same odors, however, are used across several experiments. In such a regime *olfStim*'s odor library targets two problems. First keeping track of the position of a given odorant in the olfactometer. Second facilitating analysis by storing all odor-related information for every trial of an experiment.

The odor library is a text file, which the user has to populate with the information on every odorant to be used in experiments. Typically the odor library contains descriptions of all odorants used in the lab for odor presentations (Figure 3.5).

The following fields describing every odorant are available now (they can be expanded or reduced as desired):

Common name of the odorant, IUPAC name, CAS number, producing company, odorant purity, state of matter, odorant dilution, dilution medium, default concentration at presentation, vapor pressure, odorant position in olfactometer, whether the odorant should be used during the experiment.

Required fields are: Common name of odorant, odorant dilution, position in the olfactometer, whether odorant should be used.

At the start of an experiment, the user must enter information about odorant arrangement (which odorants are loaded into which position of the olfactometer) (Figures 3.4, 3.5). This can be done via a GUI which opens at the beginning of a session or can be called directly with:

```
odorSelectionGui
```

This GUI (Figure 3.5) accesses the odor library and the user can choose odors from the odor library for every position in the olfactometer. Once the odorants in the olfactometer have been entered into the GUI, a .mat odor library file can be saved containing the provided information. For later experiments, the file can be loaded. This relieves the user of having to enter the information manually every

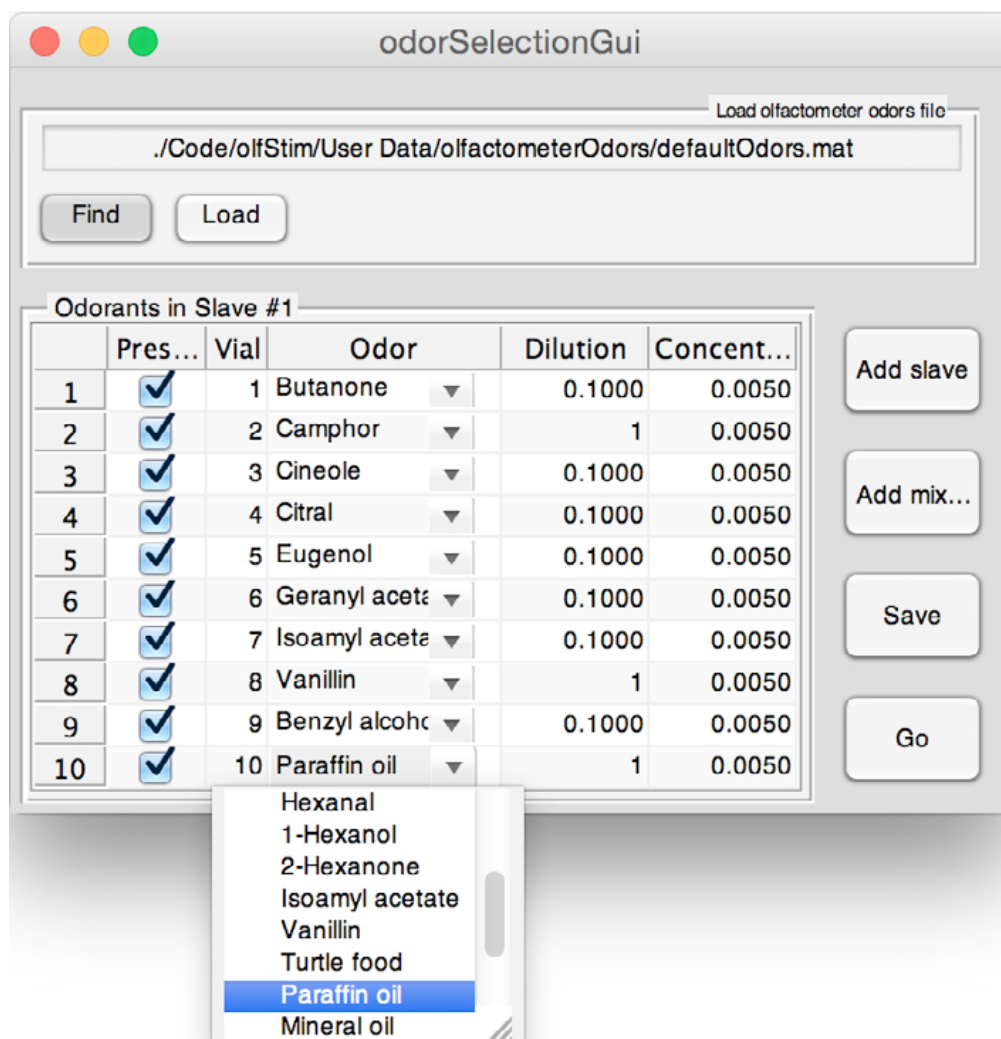


Figure 3.5: GUI to select and specify olfactometer odorants from the odor library. Each row in the GUI represents one vial position in the olfactometer. For every position the user can choose one odor from the drop down menu, which features all odorants of the the odor library. Dilution and default concentration at presentation ("concentration") are extracted from the odor library as well, but can be changed manually. The checkboxes in the leftmost column define whether the odorant should be used in the session. The "add slave" button adds another table of vial positions in case more than one olfactometer cassette is used. The save button allows to save the current user defined arrangement of odorants in the olfactometer for later use and this arrangement can be loaded by using the top panel "Load olfactometer odors file".

time, as odorants are typically not exchanged for every experiment.

Fields that can be altered from the odor selection GUI are: odorant dilution, default concentration at presentation, position in the olfactometer, whether the odorant should be used.

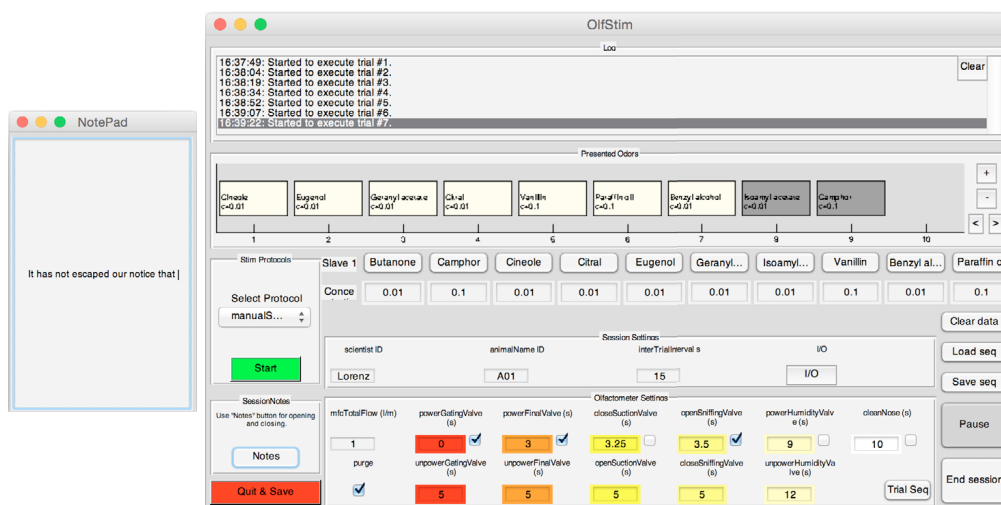


Figure 3.6: Example of a typical use situation of the GUI in the manualProgrammingStim protocol.

If odorant dilution in the vial has been set correctly in the odorant Library or the odorSelectionGui, *olfStim* will automatically adjust the flow rates accordingly.

3.7 Protocols

A protocol is a collection of functions that define the look and components of the GUI (Figure 3.6) and the processes governing trial execution. The protocols are introduced to optimize the functionality of *olfStim* for certain types of experiments. *olfStim* offers several protocols used in the Laurent lab, able to deal with many odor presentation needs.

The *manualStim* stimulation protocol is simple and a good starting point to test the olfactometer but also for exploratory experiments. It allows one to set the concentration of the odor presentation, control the total flow rate and the opening and closing times of all relevant valves. Every odor that has been defined in the odorSelectionGUI will show up in form of a button, where vial numbers ascend from left to right. Beneath every odor button a concentration field is present. In the concentration field one can set the concentration at which the odor will be presented. If the dilution of the odorant in the vial has been set correctly in the odorant library or the odorSelectionGui, *olfStim* will automatically adjust the flow rates accordingly to reach the desired concentration.

Pressing the odor button will start the trial. Executed trials are shown in the pro-

gress panel. During a trial, the users can enter notes which will be saved to the *smell* structure.

All features of the *manualStim* protocol are also available in the *manualProgrammingStim* (Figure 3.6), with the additional feature of creating sequences of odor presentations with definable inter-trial intervals. It is also possible to load and save a *smell* structure as a template for a sequence of odor presentation trials.

Using the *protocolsSJ_stim* interface, complex presentation patterns and protocols can be created and executed based on a hierarchical organization. The smallest unit is a trial in which a single odor can be presented once or multiple times at a fixed concentration. The temporal behavior of all valves can be controlled and the trial start can optionally be delayed until an external trigger is received. Several trials can be combined into sequences with waiting periods as specified in the trial definitions. Each sequence is sent as one block to the olfactometer, ensuring perfect temporal accuracy during execution. Trials and sequences can further be combined to create protocols. Each unit in a protocol is executed as a block, with Matlab taking care of the timing between units. Execution is possible at each level (i. e. each trial, sequence or protocol can be directly executed). In addition a "To do" list can be created from a combination of trials, sequences and protocols. A compact view of the GUI hides all but the trial controls.

Protocol *CleanOlfactometerStim* is designed to clean the olfactometer automatically.

For more specialized uses, new and arbitrarily complex protocols can be created.

3.8 Scripting

olfStim can also be scripted, i. e. controlled without recourse to the GUI. This can be practical in several use cases, e. g. for stereotypical stimulation sessions or if it is necessary to control odor presentations from other software packages.

Before running a scripted odor presentation session, one has to personalize an initiation script, which sets all necessary variables and paths and will, when called, trigger the execution of the scripting protocol.

Start scripting by executing the initiation script and providing some arguments:

```
olfStimScripting(protocol,#OfTrials,scientist,animalID,interTrialInterval)
```

The resulting information of the olfactory stimulation session (the *smell* structure) will be saved automatically.

In addition to the initiation script the scripting protocol defines the odor stimulation. The scripting protocols control the processes governing trial execution in order to optimize the functionality of *olfStim* for certain types of experiments. They set the time course of events (which odor to present at what concentration, when to open which valve, etc.) for every trial and trigger the trials. The user decides which scripting protocol s/he wants to use and provides its name as an argument to the initiation script.

Currently two scripting protocols are provided in *olfStim*:

'randomOdorPresentation' and 'presentPredefinedOdorList'. The randomOdorPresentation protocol will randomly draw one of the odorants listed in the loaded odorant library file (a structure called *olfactometerOdors*) and present it at the defined concentration.

presentPredefinedOdorList will load a predefined *smell* structure and then execute the trials as defined in it.

3.9 For developers

We deliberately followed procedural coding techniques, avoiding object oriented programming. The reason being, that we regarded low entry barriers to extensions and customizations of features such as protocols paramount. In order to shield namespaces (avoiding conflicts from *olfStim* functions having the same name as existing host-computer functions), while using procedural software design, we used MATLAB's functionality of 'packages'.

The most common type of customization to be done in laboratories using *olfStim* is to create new protocols, in case the general default protocols cannot deliver a certain function necessary for the lab's experiments. Components of protocols are programmed in a modular way, so that they can be combined easily. Components are for example the "Olfactometer settings" consisting of a panel with GUI components to edit valve opening and closing times, total flow rates, etc.. But

our design also includes automated consistency checks, extracts information automatically from the configuration files to populate its fields with default numbers, has functions to extract the values in the GUI fields, etc.. This entire functionality can be added to one's own protocol with a few calls to one function. Other such components include a button for every odor loaded to the olfactometer, session settings, I/O features, notes, progress panel, log panel, etc..

olfStim can currently be used in combination with the LASOM 2.0 olfactometer control board. All interactions with the LASOM board are executed from one library of functions and one library of scripts. To replace LASOM with a different control board, such as an Arduino processor, new libraries must be created and the LASOM libraries replaced.

3.10 Conclusions

olfStim is an open-source software package to control odor delivery with an olfactometer. It enables neuroscience researchers to conduct a wide range of experiments requiring odorant presentations. The current package enables users, after a small amount of configuration steps, to perform experiments with olfactometers. For basic olfactory needs, such as presenting up to 100 odors with a precise time course at defined concentrations, no programming skills are required. For more specialized uses the flexibility of the design and its reliance on Matlab functions, should enable users with limited Matlab programming skills to adapt *olfStim*.

Chapter 4

Genetic tools in reptiles: Results

The last 20 years have seen two remarkable trends in neuroscience. One is the development of genetic tools, such as genetically encoded calcium indicators, optogenetics, transsynaptic retrograde tracers, etc. (Luo et al., 2008). The second is the increasing focus on a handful of experimental model species (mouse, drosophila, zebrafish,...), all of which are based on genetic accessibility. A problem is that genetic methods are to a large extent limited to the species in which they were developed. None of the commonly used model systems originate from the reptile family and, to the best of our knowledge, none of the tools in the contemporary genetic toolset have been used in reptiles.

To gain a cellular, mechanistic understanding of circuits, we need to control and perturb network activity. Today, this is best done with optogenetic methods, thus one of my goals was to explore the usability of such approaches in reptiles. This proved challenging. (1) Like all reptiles, turtles are ectotherms and their body temperature is thus typically lower than that of mammals. (2) Even though our animals come from turtle breeders, they originate from, and thus form a wild type population, with highly variable immune status. (3) The particular anatomical features of the turtle cortex – a thin cortical sheet protected by a particularly tough pia mater, resting on a CSF-filled ventricle – make tissue penetration challenging and thus injections more variable. Bringing genetic tools to the turtle thus required solving a number of unexpected hurdles. This included extensive efforts to develop a viral injection surgery protocol for turtles as the first step.

4.1 Gene delivery

Gene delivery can in principle be achieved with several methods. One is the generation of transgenic animals with recombination, recombinant viral vectors, electroporation, etc. Due to the long generation times of turtles, transgenesis was not explored as a viable option. Of the remaining methods, recombinant viral vectors offer the greatest range of gene delivery possibilities. Viral coating allows for cell-type- and subcellular-component-specific docking and infection, potentially giving rise to tropisms specific to neurons or axonal terminals for retrograde infection.

We thus set out to test in turtles the viruses used in the mammalian neuroscience community, with the goal of achieving two main objectives: (1) Efficient and reliable infection of local populations of neurons and (2) retrograde infection of neurons with axonal terminals in the region of injection.

4.1.1 Viral injection surgeries

Twelve hours prior to surgery, turtles were injected with Baytril/Enrofloxacin 2.5 % (0.2 ml kg^{-1} , SC) and Rimadyl/Caprofen (2 mg kg^{-1} , SC). On the day of the surgery turtles were anaesthetized using Ketamine hydrochloride (23 mg kg^{-1} , IM) and Dexmedetomidin hydrochloride ($75 \text{ } \mu\text{g kg}^{-1}$, IM). After loss of the corneal reflex (after about 20 min), turtles were intubated and mechanically ventilated with a mixture of vaporized Isoflurane and air. Isoflurane concentration was 4 % for the first 30 to 40 min, and 1 to 2 % subsequently. Seven to 10 ml of saline were administered IP at the begin of the surgery to avoid dehydration. Body temperature was kept around $30 \text{ }^\circ\text{C}$ with a heating lamp until the animal awoke. Eyes were protected from desiccation with Vidisic gel (Bausch+Lomb).

Post-op: we injected the Medetomidin antidote Antisedan (0.4 mg kg^{-1}), Baytril and Rimadyl (as before) and ventilated the animals with air until they extubated themselves. Animals were kept isolated in separate tanks with shallow water and a drying platform, heated with a heating lamp, for 48 h after surgery. Baytril was administered daily for 7 d, Rimadyl daily for 3 d.

Animals were transferred to a stereotactic apparatus (David Kopf Instruments, USA) and their heads and necks disinfected with iodine tincture (Braun, Germany). The top of the skull was locally anaesthetized with Lidocaine; a trapezoidal patch of skin was removed above the skull in an area limited caudally by the insertion the head-retraction muscles and anteriorly by an imaginary line connecting the pos-

terior orbitae. We covered the exposed area with IndiSpense (Ultradent Products, USA) to stop all bleeding and hardened the dry bone using Copalite. A craniotomy was opened above the brain region of interest (usually both hemispheres of dorsal cortex and/or olfactory bulb) using a dental drill (W&H, Austria) while continually rinsing with saline. Above the midline we left a narrow strip of thinned bone, to protect the prominent medial vasculature and to reduce post-operative brain movement. We cut small holes (typically 500 μm diameter) into the dura mater and arachnoid using fine iridectomy scissors (Fine Science Tools, Germany). As the pia mater is inseparably connected to brain tissue, cutting the pia with scissors results in some superficial brain damage. However the pia had to be severed in some manner to allow needle-penetration of the brain; of all the methods tested, a fine cut with iridectomy scissors seems preferable.

Piercing any one or all of the turtle meninges with a needle failed, because it required great mechanical pressure and invariably severely damaged the brain. We tested an Excimer Laser as a potential means to open the pia mater in a more controlled fashion, but without consistent results. Precise targeting of the laser to areas devoid of blood vessels proved very difficult. Indeed, excimer-laser action lasts several seconds, during which heart beat and ventilation caused movement. Keeping the surface of the brains dry during laser action also proved difficult. These problems resulted in blood-vessel damage, bleeding (blood coagulation is weak in turtles (Dorst and Mills, 1923; Hackett and Hann, 1967; Jacques, 1963)) and severe inflammation in the period after the surgery.

Viral loads were backfilled in a microinjection syringe (NanoFil, World Precision Instruments, USA) with a pulled quartz pipette as a needle; dead volume was filled with silicone oil. Needles were custom made with a P-2000, Sutter Instruments, USA, as long shank quartz micropipettes. Their tips were stained with a fetal bovine serum-ink mixture (typically 1:1) and then beveled at 45° to a diameter of 30 to 50 μm .

For injections into dorsal cortex and olfactory bulb we penetrated 500 μm into the tissue at an angle of 45° oriented posteriorly with the Kopf stereotactic manipulator. For lateral cortex injections, we penetrated 1500 μm into the tissue at an angle of 40° towards lateral. We then typically injected 40 to 250 nl at a rate of 200 nl min^{-1} using a micropump (UMP3, World Precision Instruments, USA). We retracted the needle by 200 μm for a second injection and waited for 10 min after the end of the injection before retracting the needle. After injection, rinsing with saline was avoided as much as possible.

A small glass coverslip (diameter 5 to 6 mm) was placed over the saline-filled crani-

otomy, ideally resting within the craniotomy on the bone bridge over the midline and sealed in place with silicone (KwikSil, World Precision Instruments, USA). Filling the craniotomy with silicone resulted in macroscopic deformations of the cortex, apparently due to the brain pressing against the cured silicone plug over weeks of incubation. A gold screw was inserted into the skull lateral of the border between cortex and olfactory bulb to allow firm attachment of the head cap. The skull was cleaned, roughened with a scalpel and dried. The whole exposed area and the screw was covered with a thin layer Optibond Solo Plus (Kerr, Italy) and cured with UV light. For mechanical protection a layer of Transbond XT (3M Unitek, USA) was added on top and also cured with UV.

We waited for 4-6 weeks after surgery before starting experiments for AAV incubation. *Rabies virus* incubation ranged from 1 week to 4 weeks. Injections of *lentivirus* were done in cultured slabs (see 4.3). Injections of *rabies virus* in 2 mice were performed similarly to the turtle injections described above, without opening the meninges we penetrated 600 μm with an angle of 60° towards posterior and injected 500 nl of *rabies virus* suspension.

4.1.2 Adeno Associated Virus

Adeno associated virus (AAV), a member of the Parvovirus family, is a widely used recombinant viral vector capable of infecting both dividing and non-dividing cells such as neurons while not integrating into the host genome. It has a carrying capacity of 5 kilobases (Dong et al., 1996). AAVs have never been used in reptiles; I thus set out to test the infectious properties of different AAV serotypes currently in use in the neuroscience community.

It was first necessary to develop and optimize the surgery and AAV injection procedure (chapter 4.1.1). After this optimization the infectious properties of seven different serotypes were compared - AAV2/1, AAV2/2, AAV2/5, AAV2/6, AAV2/7, AAV2/8 and AAV2/9. To that end a total of 28 injections were delivered to 7 animals (2 *Chrysemys picta bellii* and 5 *Trachemys scripta elegans*, ranging from 248 to 481 g).

In each hemisphere, virus was injected into the mediolateral middle of anterior dorsal cortex and posterior dorsal cortex, thus 4 injections per animal (always in the same fashion, as described in section 4.1.1). Along the anteroposterior axis the anterior injection was located at the posterior end of the dorsoventricular ridge and the posterior injection below the anterior attachment point of the

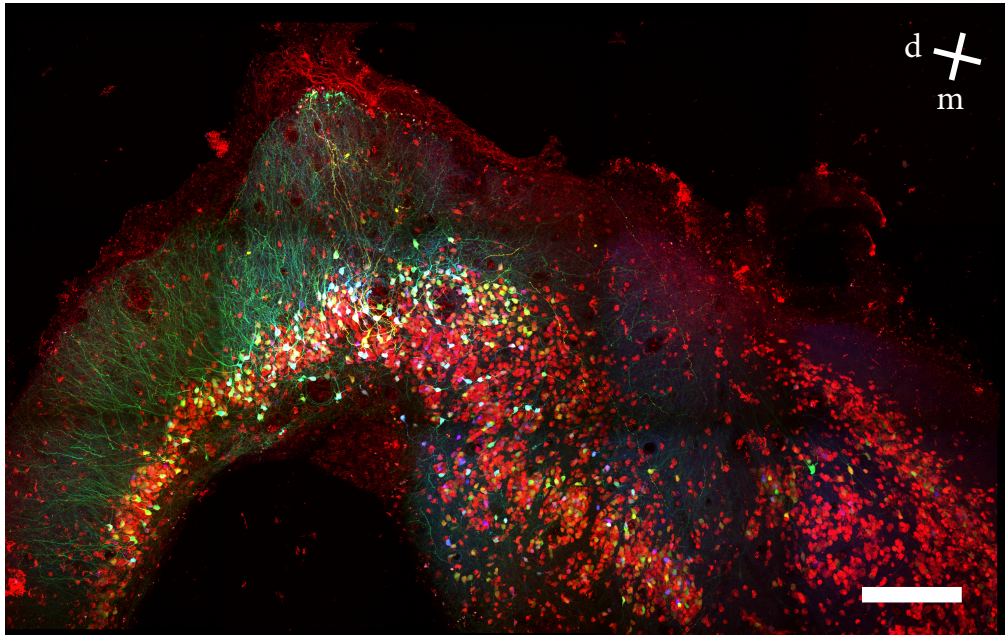


Figure 4.1: Triple infection of AAV after injection of a 3-AAV-serotype mixture in the anterior dorsal cortex. Maximum intensity projection of the dorsal part of a 70 μ m thick frontal section. Background staining NeuN antibody (red). AAV2/1-CB7-mCerulean (blue), AAV2/5-CB7-EGFP (green), AAV2/8-CMV-turboRFP (yellow). Scale bar 250 μ m. Dorsal towards upper left, lateral towards upper right.

neck retraction muscle. Despite a lack of precise stereotactic coordinates in turtle, this strategy guaranteed targeting of roughly the same anatomical positions. Four weeks after injection the animal was sacrificed and the brain processed for histology as described in chapter 2.5.

Every serotype was tested repeatedly in multiple injections ($n=4-27$, table 4.1). For every serotype virus of the same viral production batch was used, to rule out inter-batch differences. Ideally the promoters and regulatory elements in the genomes of the different serotypes are equal, so that they only differ in their protein coat. AAV2/1, AAV2/5 and AAV2/9 viruses had genomes of the kind AAV2/*-CB7-CI-XFP-WPRE-rBG; AAV2/2 and AAV2/7 of the kind AAV2/*-CB7-CI-XFP-rBG, missing the WPRE (Woodchuck Hepatitis Virus Posttranscriptional Regulatory Element). Furthermore two serotypes with a CMV promoter were used: AAV2/6-CMV-PI-eGFP-WPRE-bGH and AAV2/8-CMV-TurboRFP-WPRE-rBG. Thus differences exist, but CMV and CB7 are both high yield viral promoters. Regulatory elements such as WPRE are reported to result in expression rates increased by five to eightfold (Zufferey et al., 1999).

Three serotypes were mixed, and the mixture injected (Figure 4.1). Mixing was

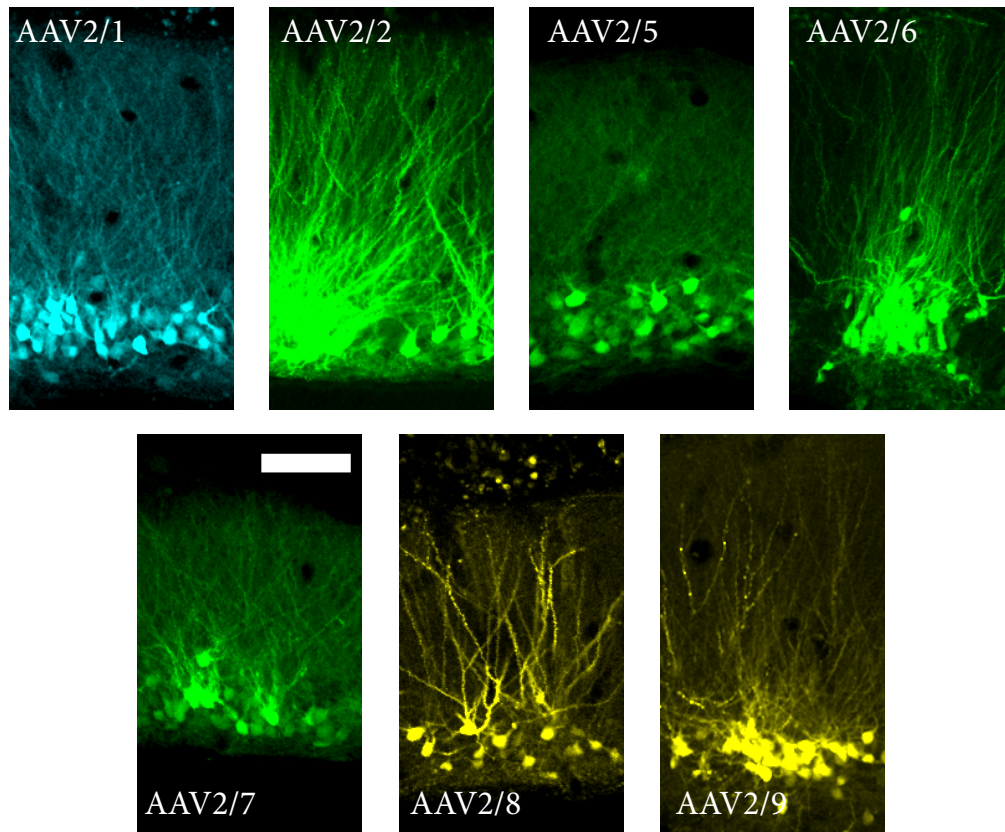


Figure 4.2: All tested AAV serotypes can infect cortical neurons of the turtle. AAV2/1-CB7-*mCerulean*, AAV2/2-CB7-EGFP, AAV2/5-CB7-EGFP, AAV2/6-CMV-EGFP, AAV2/7-CB7-EGFP, AAV2/8-CMV-*turboRFP*, AAV2/9-CB7-*mCherry*. Scale bar for all images 100 μm . Dorsal top.

done such, that final concentration of each virus was 3×10^{12} GC ml^{-1} (genome copy numbers). The mixtures always contained AAV2/1 serotype as a standard for normalization.

To characterize the reliability of infection of each serotype (Figure 4.2), I quantified the failures and successes of infection. Of the 28 injections of AAV2/1 25 gave expression, one was lost due to of bad histology and two resulted in no visible protein expression. For AAV2/2 three out of four were successful, AAV2/5 eight out of ten successful, one of ten were uninterpretable. For AAV2/6 four out of four were successful, AAV2/7 ten of ten successful, AAV2/8 nine of ten successful, one of ten uninterpretable, AAV2/9 fourteen of eighteen were successful. These results are summarized in table 4.1.

I then assessed expression and its variability. The anteroposterior extent of expression was quantified by measuring the distance between the first and last

-	AAV2/1	AAV2/2	AAV2/5	AAV2/6	AAV2/7	AAV2/8	AAV2/9
%	93%	75%	88%	100%	100%	100%	82%
n	27	4	9	4	10	9	17

Table 4.1: The number of assessable injections and the percentage of success (a measure for the reliability of the viral infection method) is provided for each serotype. Fluorescent protein expression discernible with confocal microscopy in at least one cell is defined as success. Expression success in one animal was indeterminable due to bad histology, the injection was thus omitted from these numbers.

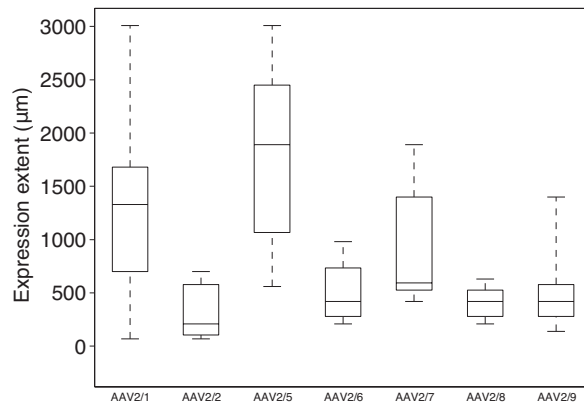


Figure 4.3: Boxplot of expression extent in μm . For each serotype the median value is indicated by the horizontal line in the box, edges of each box are the 25th and 75th percentiles, and whiskers the most extreme values.

sections with visibly stained neurons (Table 4.2, Figure 4.3).

-	AAV2/1	AAV2/2	AAV2/5	AAV2/6	AAV2/7	AAV2/8	AAV2/9
n	22	3	7	4	8	8	13
mean	1272	327	1830	508	919	411	517
median	1330	210	1820	420	840	420	420
std	736	331	879	335	578	152	349

Table 4.2: Spatial extent of AAV expression. n is the number of quantifiable injections, mean, median and standard deviation (values in μm) describe the extent of expression for each AAV serotype. Injections where expression failed are excluded.

AAV2/1 and AAV2/5 infected statistically significantly larger areas than AAV2/2, AAV2/6, AAV2/8, AAV2/9. AAV2/7 lay in between of these two groups (two-sample t-test, Table 4.3).

The variability of the extent of expression for each individual serotype is considerable (Figure 4.3, Table 4.2). For AAV2/1 over 22 interpretable injections, the median was 1330 μm , ranging from 70 μm to 3010 μm with a SD of 736 μm . This variability may be due to inter-individual differences. The mean of the standard deviations of AAV2/1 expression extent calculated over the 4 injection sites of

-	AAV2/1	AAV2/2	AAV2/5	AAV2/6	AAV2/7	AAV2/8	AAV2/9
AAV2/1	-	4.1	10.7	5.5	23.1	0.3	0.2
AAV2/2	4.1	-	2.3	50.9	13.5	55.8	40.6
AAV2/5	10.7	2.3	-	2.0	3.2	0.1	0
AAV2/6	5.5	50.9	2.0	-	22.3	49.7	96.3
AAV2/7	23.1	13.5	3.2	22.3	-	3.1	6.0
AAV2/8	0.3	55.8	0.1	49.7	3.1	-	43.2
AAV2/9	0.2	40.6	0	96.3	6.0	43.2	-

Table 4.3: p-values resulting from two sample t-tests comparing the extent of protein expression of each serotype-pair. All values are in %. Injections where expression failed are excluded.

each animal was 556 μm , lower than the standard deviation calculated over all AAV2/1 injections (736 μm). When normalized to the mean spread, the standard deviation was 45 % when calculated over each animal individually, but 58 % when calculated over all injections pooled over animals. The increased variability across animals could have been due to differing immune status and genetic variability in our population of wild-caught, wild-type turtles.

The spatial extent of infection was also correlated positively with staining density as illustrated in Figure 4.4. No obvious tropism towards cellular subtypes was noticed: AAV infected both excitatory and inhibitory neurons, as confirmed in experiments, where infected neurons were patched (see Chapter 6).

4.1.3 Lentivirus

Lentivirus, a member of the Retrovirus family, is another widely used recombinant viral vector. *Lentivirus* is advantageous because of its shorter delay to expression (compared to AAV) and larger carrying capacity (9 kilobases) (Kumar et al., 2004; Zhang et al., 2010; Luo et al., 2008). Like AAV, it can infect both dividing and non-dividing cells such as neurons. For administrative reasons, *lentivirus* could not be injected into live animals. We thus developed an organotypic slab culture protocol (see chapter 4.3).

After establishing viable organotypic slab cultures, the infection properties of *lentivirus* were tested. For one animal the entire cortical sheath of every hemisphere was used, including dorsal and medial cortex. For two further animals the entire cortical sheath was divided into three smaller slabs by sectioning with iridec-tomy scissors. Eight injections of 1 μl of virus (1:1 mixture of VSVG.HIV.CaMKII α -hChR2(H134R)-EYFP-WPRE and VSVG.HIV.SIN.Synapsin-hChR2(H134R)-EYFP-WPRE) were placed into the resulting 8 slabs.

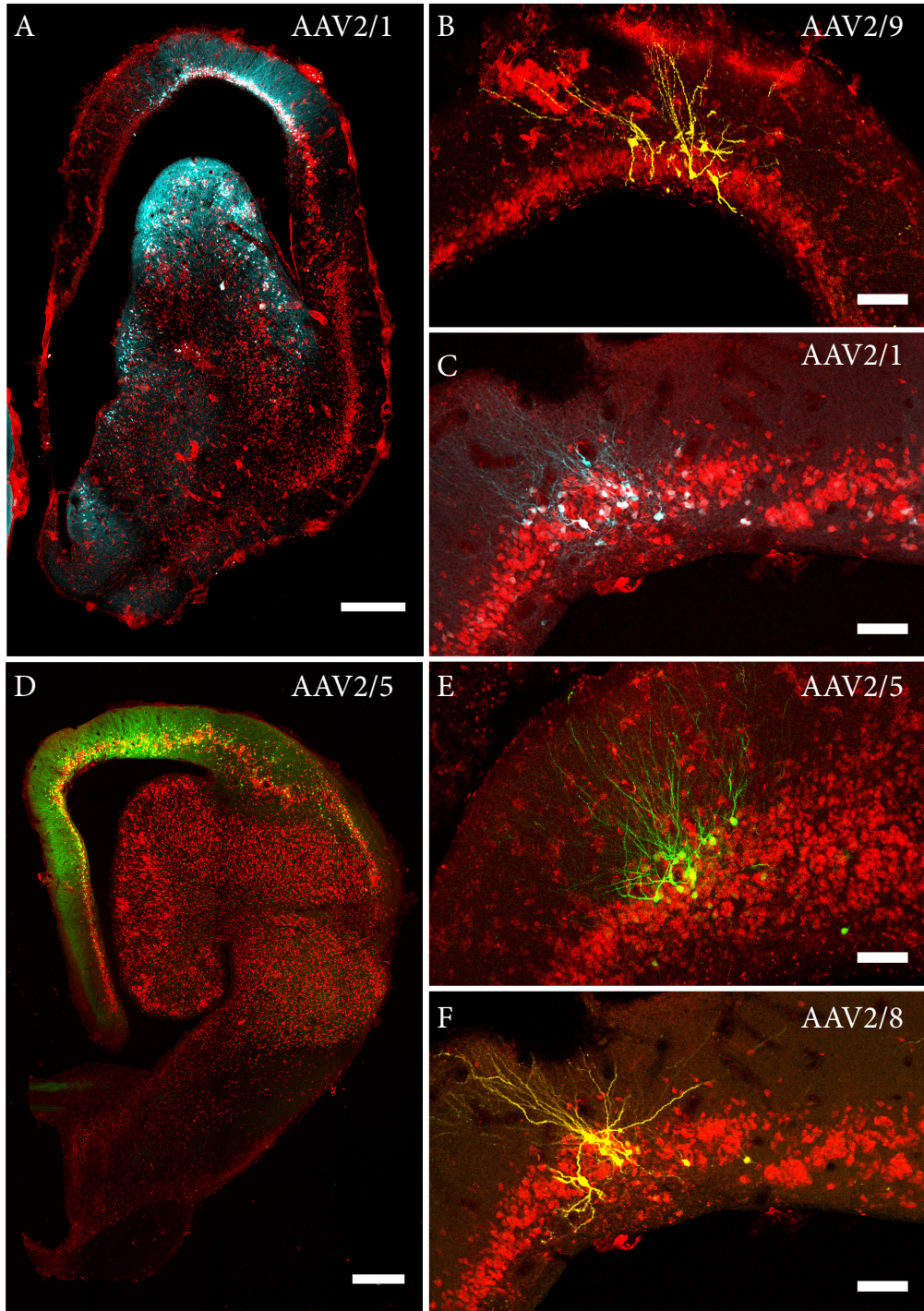


Figure 4.4: Infection of AAV2/1 (A) and AAV2/5 (D) over an a-p extent of more than 1.5 mm. To exemplify variability of infections compare A to C, where AAV2/1 was injected under identical conditions in two animals. The small infection in C is not due to a failed injection (from the same injection shown in image D). Also D and E show variability of AAV2/5 infections under identical conditions in two animals. Images B and F depict the same injection as A and D but for AAV2/9 and AAV2/8. Scale bar for A & D 500 μm , for the rest 100 μm .

After 7-14 days of organotypic culturing, slabs were removed, fixed in 4% PFA and imaged. None of the slabs showed any EYFP expression.

Six further injections of 1 μ l of viral mixture were delivered in slabs taken from third turtle. This time the mixture included *lentivirus* and AAV (1:1 mixture of VSVG.HIV.CaMKII α -hChr2(H134R)-EYFP-WPRE and AAV2/1-hSyn1-mCherry). Both viruses were mixed in the same injection pipette. After 14 days of incubation, imaging of the fixed slabs revealed clear expression of mCherry (AAV) but no EYFP (*lentivirus*). Despite the fact that *lentivirus* has a shorter expression latency than AAV (Luo et al., 2008). In conclusion *lentivirus* has at best poor infectivity for turtle cortical neurons, and in my limited number of injections (n=14 in 3 turtles) I failed to detect any.

4.1.4 Rabies virus

Transsynaptic retrograde tracing using recombinant *rabies virus* (SAD Δ G) relies on several prerequisites (Ugolini et al., 1987; Ugolini, 1995b; Ugolini, 1995a; Wickersham et al., 2006; Wickersham et al., 2007). First TVA (EnvA receptor) must not be endogenously expressed in the host organism. Only after transfection of a local cell population with TVA can *rabies virus* pseudotyped with the EnvA envelope protein (SAD Δ G(EnvA)) infect the transfected local population. Once injected, *rabies* particles with *rabies*' natural envelope glycoprotein (SAD Δ G(SAD G)) can be assembled in the cells cytoplasm, be retrogradely transported and exit the cell from its postsynaptic (dendritic) sites, enabling trans-synaptic retrograde tracing. In the synaptic cleft, viruses must bind to presynaptic axonal sites, enter the presynaptic cell and see their genetic material expressed. All of these mechanisms are operational in mammals, but it is not known whether they are so in reptiles (Wickersham et al., 2006; Wickersham et al., 2007). Reptiles including avians, for example do not express clinical rabies nor is there any evidence that they carry the virus.

I first tested whether *rabies*' natural envelope glycoprotein binds to turtle neurons, and enables infection, i. e. whether the virus can dock onto and infect turtle neurons at their axonal terminals as it does in mice (Clark and Kritchevsky, 1972). Replication deficient *rabies virus* (SAD- Δ G-eGFP(SAD G) and SAD- Δ G-mCherry(SAD G)) was injected into turtle brains. In a total of 4 turtles (3 *Chrysemys picta bellii*, 1 *Trachemys scripta elegans*) 17 injections of 500 to 1000 nl of virus (n=9 in dorsal cortex, n=4 in olfactory bulb, n=4 in lateral cortex) were delivered as described

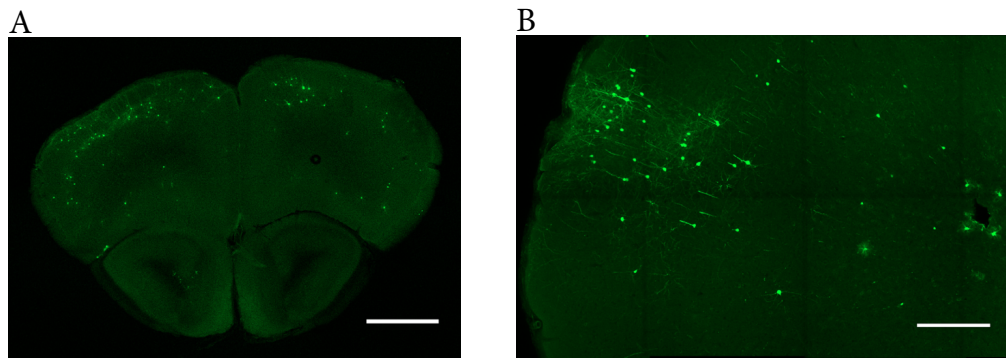


Figure 4.5: Frontal sections of the brains of two mice expressing EGFP after injecting *rabies virus* (SAD- Δ G-eGFP(SAD G)). **A.** Overview image of both hemispheres of one mouse with sparsely distributed neurons expressing EGFP in both hemispheres. Scale bar = 1 mm. **B.** More detailed image of another mouse brain, with sparsely distributed but clearly visible neurons expressing EGFP. Scale bar = 250 μ m.

in 4.1.1. Incubation time was 10 days for one animal, 14 days for another animal and 4 weeks for two animals. After incubation, the animals were sacrificed, perfused and sectioned as described in 2.5 and the brain sections analyzed on a confocal microscope. None of the animals showed any EGFP or mCherry expression, either in cell bodies or in processes.

To test the functionality of the used batch of *rabies virus*, control injections of 500 nl of *rabies virus* (SAD- Δ G-eGFP(SAD G)) were delivered to the somatosensory cortices of two adult C57BL/6 mice. After 7 days of incubation the mice were sacrificed, perfused with 4% PFA, their brains sectioned for histology and examined on a confocal microscope (Figure 4.5). In both mice clear EGFP expression was visible in both hemispheres. I thus conclude, that the batch of *rabies virus* was functional and that the lack of expression seen in turtles is due to the inability of *rabies virus* to infect (or express in) turtle neurons.

4.1.5 AAV-SL1

AAV-SL1 is a recombinant *adeno-associated virus* with a genetically engineered capsid protein (Teruo et al., 2016). This particular protein was one of the hits from a modification effort of AAV2/2's capsid gene. Assembling engineered capsid proteins into a functional viral particle results in novel viral serotypes, which were subsequently screened to select the ones exhibiting retrograde infection properties in mammals. This effort was carried out in the laboratories of Dr. Alla Karpova, Dr. Loren Looger in Janelia farm and Dr. David Schaffer at UC Berkeley, who kindly provided us with several aliquots of AAV-SL1.

Rabies is a transsynaptic retrograde virus: it can jump directly from one infected cell to presynaptically connected cells. AAV-SL1 works differently: its new capsid protein appears to allow it to dock more or less specifically to axons and use them as an entry point to the cells. It lacks the machinery of *rabies virus* necessary for moving retrogradely within the host cell's dendrites as well as for the transsynaptic transfer.

Nonetheless I used AAV-SL1 with the goal of assessing alternatives to *rabies virus*. The pattern of expected cell labelling is comparable to existing molecular retrograde tracers such as fluorophore-conjugated Cholera Toxin's B subunit (CTB), but with the ability to carry genetic material. This means that AAV-SL1 should infect cells which project axons to the region of the injection.

A total of thirteen injections were carried out into the cortices of three turtles (2 *Trachemys scripta elegans*, 1 *Chrysemys picta bellii*). In every hemisphere one of the following sets of injection were delivered:

In one hemisphere of one animal three injections and two injections in each hemisphere of another animal were administered into the pallial thickening (45° towards lateral, penetration distance of 1 mm and subsequent retraction to 500 µm, injection at each depth). In the other three hemispheres one injection was placed along the anteroposterior axis of dorsal cortex in the anterior third and the other in the middle third (n=3).

In every location I injected between 200 nl (n=5) or 500 nl (n=8) of solution. This solution was pure virus (AAV-SL1-CAG-EGFP, AAV-SL1-CAG-tdTomato) for two of the turtles and a mixture for the third (AAV-SL1-CAG-EGFP, AAV2/1-CAG-mCerulean and 1 % CTB-Alexa555. Viral concentration 3×10^{12} GC). This mixture allowed the comparison of AAV-SL1 mediated EGFP expression patterns with labelling patterns from two other sources: AAV2/1 which should infect neuronal cell bodies around the site of injection and CTB-Alexa555, which gets taken up by axons and thus labels the cell bodies of cells, that project to the site of injection (Dederen et al., 1994; Trojanowski, 1983; Trojanowski et al., 1982; Wan et al., 1982). The virus was incubated for four weeks before sacrificing the animals.

Anecdotally, of all AAV serotypes I have tried so far AAV-SL1 gave the infection with most intense expression and greatest spatial extent. Every injection led to intense expression over an anterior-posterior extent of at least 910 µm. 4 of 6

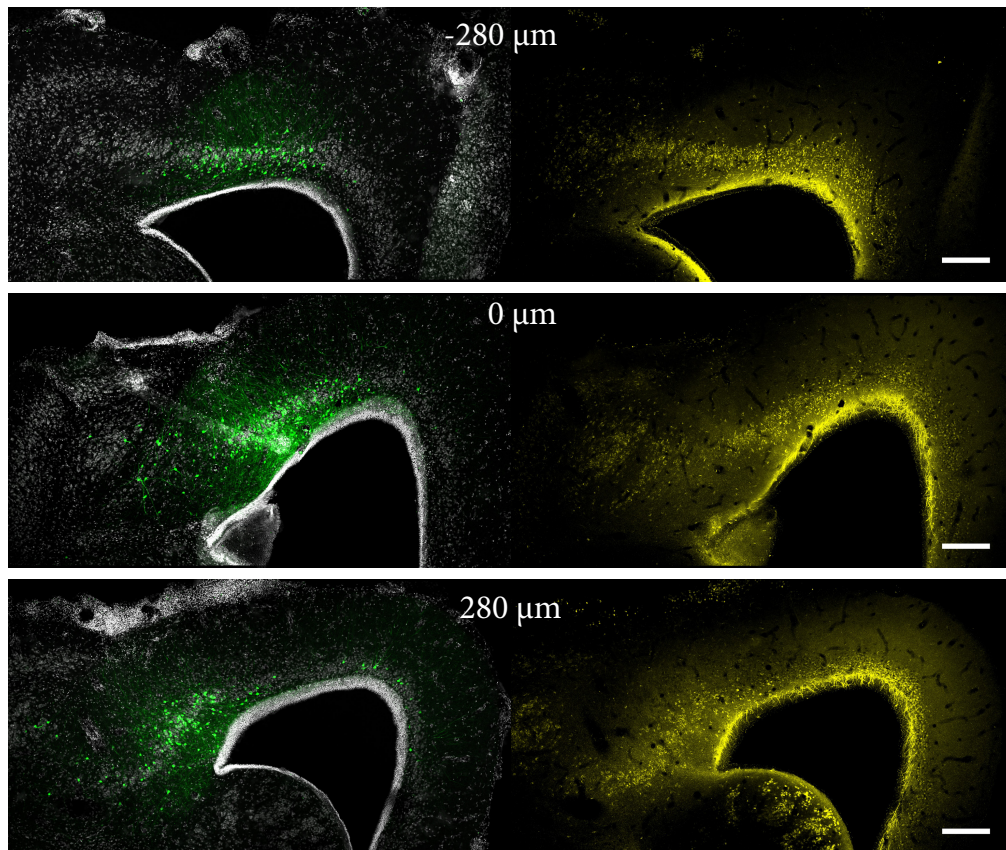


Figure 4.6: Frontal sections of an AAV-SL1 infected cortex of one turtle. Vertical succession of frontal sections. 2nd row from top is the injection site, surrounded by a section 280 μm anterior (top) and one 280 μm posterior (bottom) to the injection. Left column - DAPI counterstained (white) and AAV-SL1 infected neurons, expressing EGFP. Notice in the posterior section the distribution of EGFP expressing neurons posterior from the injection, with a cluster medial and one cluster lateral, which can not be easily explained by diffusion of viral particles. Right column - Same images as on the left, but showing the optical channel of CTB-Alexa555 (yellow). Notice that the distribution of CTB-Alexa555 positive cells posterior of the injection site matches that of AAV-SL1 infected cells. Scale bars, 250 μm .

injected hemispheres had infected cells over the entire extent of cortex. The distribution of expression argues for partially (non-transsynaptic) retrograde infectious properties, meaning that some but not all cell types can be retrogradely infected. The observed distribution is described in the next paragraphs.

AAV2/1 and AAV-SL1 exhibit differences in spatial pattern of expression which argue for a partially retrograde infection by AAV-SL1. Whereas AAV2/1 has a pattern consistent with viral particle diffusion around the site of injection (Figure 4.7), AAV-SL1's infection pattern cannot be explained easily by diffusion: Injections into anterior dorsal cortex ($n=3$) gave the following expression pattern. Anterior to the site of the injection AAV-SL1 infected cells are located in

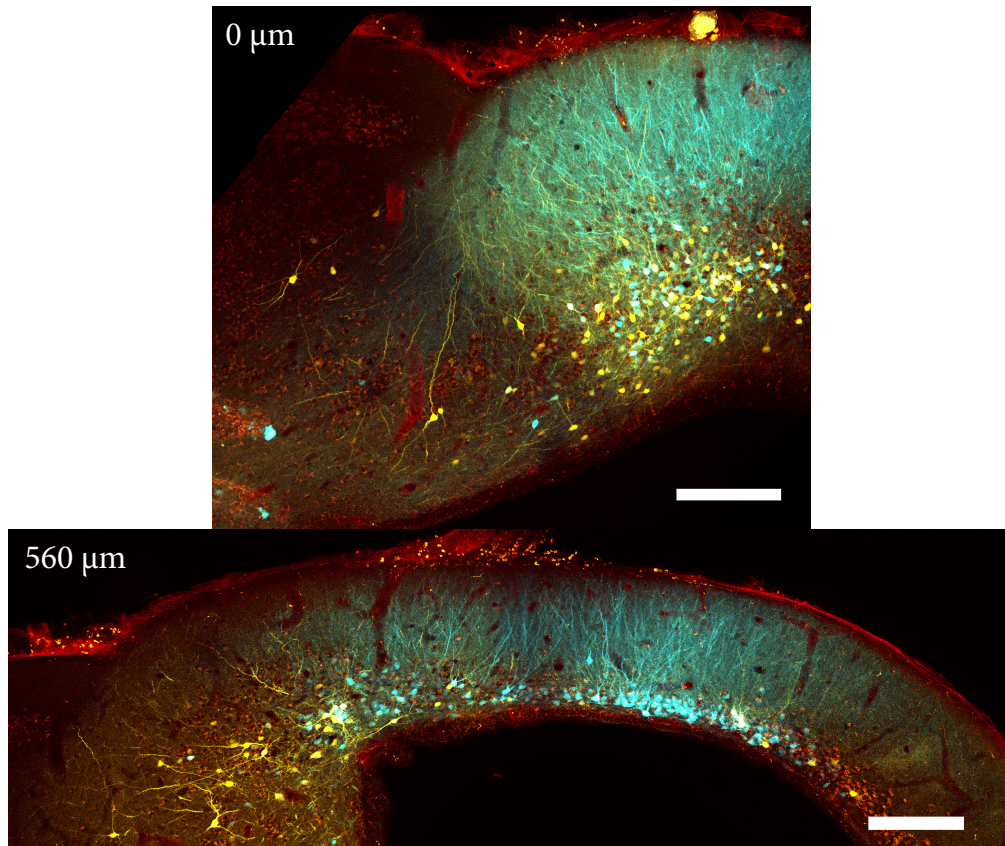


Figure 4.7: Frontal sections of an AAV-SL1 infected cortex of another turtle. NeuN counterstained (red), AAV-SL1 infected neurons expressing tdTomato (yellow) and AAV2/1 mediated EGFP (cyan). Same observation as in Figure 4.6. Infected cells spread around injection site (top section), both for AAV2/1 and AAV-SL1. 560 μm farther posterior medial and lateral clustering of AAV-SL1 infected cells, whereas AAV2/1 infected cells are located in the middle of dorsal cortex. Scale bars, 250 μm . Dorsal top, medial right.

the mediolateral center of dorsal cortex. Posterior to the injection site however, expressing cells are located in the very lateral portion of dorsal cortex and the pallial thickening as well as in the border region between dorsal cortex and medial cortex. The middle of dorsal cortex however has fewer infected cells (Figure 4.6 and 4.7). This pattern can be observed from roughly 150 μm to 600 μm posterior to the injection site and was present in 3 of 3 injections into the anterior dorsal cortex of 2 turtles. The position of injection was defined to be the section (thickness, 70 μm) where expressing cells were densest.

If AAV-SL1 is indeed retrogradely infective, the observed pattern would suggest that neurons of more posterior PT and the medial-dorsal cortical border region project anteriorly to the center of dorsal cortex. Are these neuroanatomical projection patterns expected? To test, a coinjection of AAV-SL1 with the well charac-

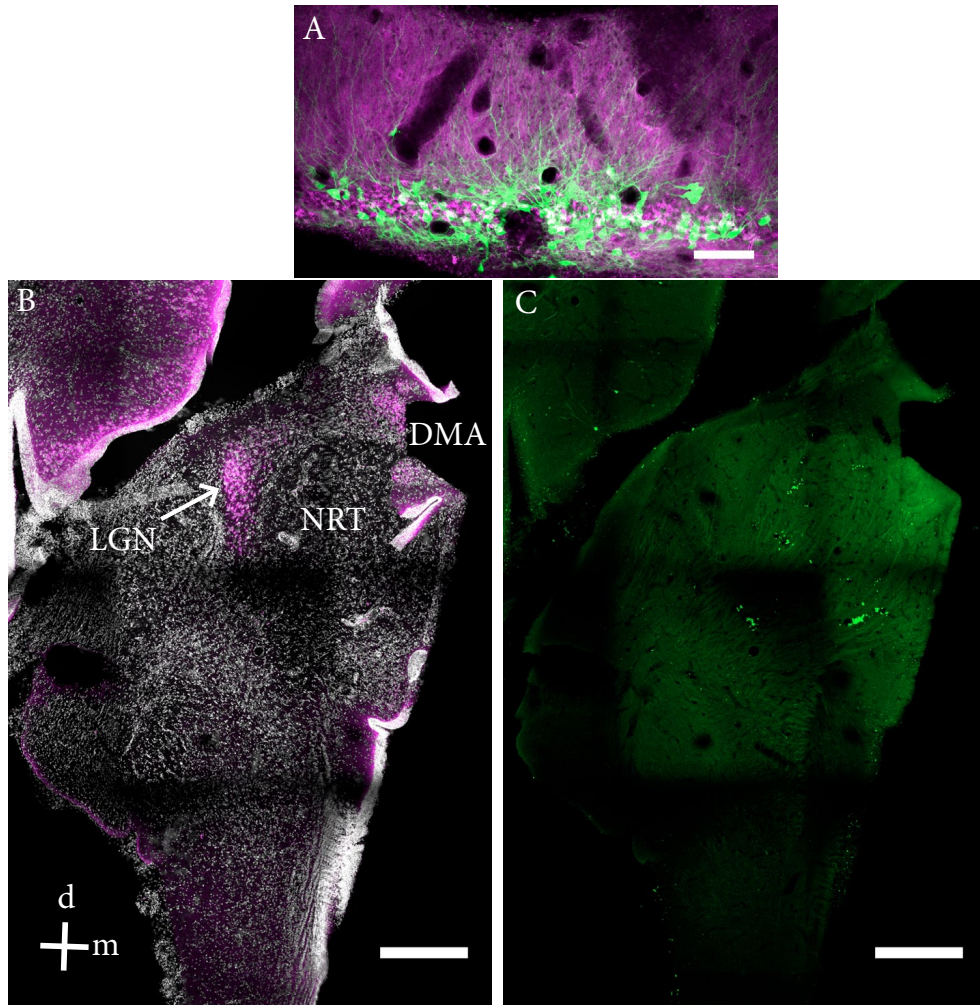


Figure 4.8: Frontal section of the brain of one turtle infected with AAV-SL1. Dorsal top, medial right. **A.** Turtle 4 weeks after coinjection of AAV-SL1-CAG-EGFP, AAV2/1-CB7-mCerulean and CTB-Alexa555 into dorsal cortex. Frontal section of the dorsal cortex with AAV-SL1 infected neurons expressing EGFP (green) and CTB-Alexa555 staining (magenta). Scale bar, 100 μm . **B.** The ventral part of the same frontal section as in A., DAPI counterstained (white) including the thalamus. CTB-Alexa555 (magenta) injection into dorsal cortex results in retrogradely labeled neuronal somata in the lateral geniculate nucleus (LGN) and in what is most likely nucleus dorsomedialis anterior (DMA) (Powers and Reiner, 1980). Scale bar, 500 μm . **C.** Same image as in B. showing EGFP (green). Despite CTB-labeled cells no AAV-SL1 infected EGFP expressing neurons are visible. Scale bar, 500 μm .

terized retrograde tracer cholera toxin subunit-B (CTB-Alexa555) was performed, which revealed the same distribution pattern of labeled cells (Figure 4.6). This evidence suggests that AAV-SL1 infects cortical neurons at least also through their axons.

Can AAV-SL1 also infect non-cortical neurons through their axons? It is known that neurons of the LGN (lateral geniculate nucleus) send axons to the dorsal

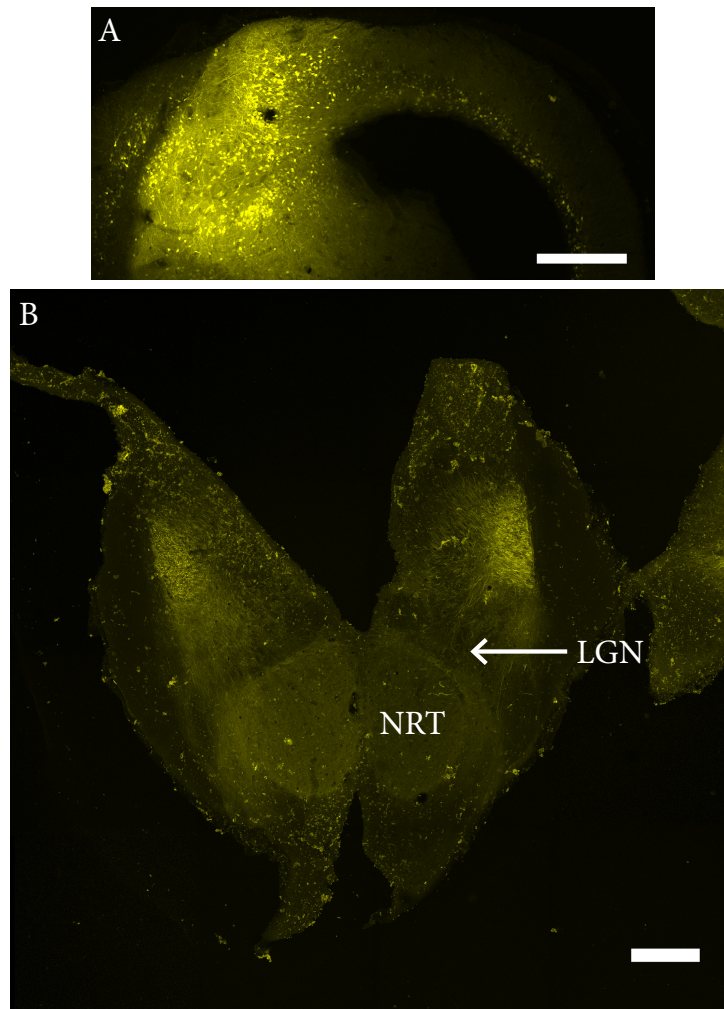


Figure 4.9: Frontal sections of another turtle 4 weeks after injection of AAV-SL1-CAG-tdTomato into the pallial thickening (PT). **A.** Lateral cortex, PT, dorsal cortex and some medial cortex with AAV-SL1 infected neurons expressing tdTomato (yellow). Scale bar, 500 μ m. Dorsal top, medial right. **B.** Thalamus with the nucleus rotundus (NRT) and LGN of the same brain as in A. No AAV-SL1 infected neurons expressing tdTomato (yellow) detectable in any of the thalamic slices. Scale bar, 500 μ m. Dorsal top.

cortex (Desan, 1984) and we thus expected to see infected neurons in thalamus. However despite 12 successful injections in dorsal cortex and pallial thickening no labeled neurons were found in the LGN (Figure 4.9). As described above AAV-SL1 was coinjected with CTB-Alexa555, and CTB-Alexa555 labeled cells were present as predicted in the LGN and a second superficial thalamic nucleus, most likely nucleus dorsomedialis anterior (DMA) (Figure 4.8) (Powers and Reiner, 1980). This reproduces previous neuroanatomical findings (Desan, 1984) and confirms that the lack of AAV-SL1 infection was not due to targeting the injection to the wrong area, but rather an incapacity to infect LGN axons. If AAV-SL1 infects axons, as

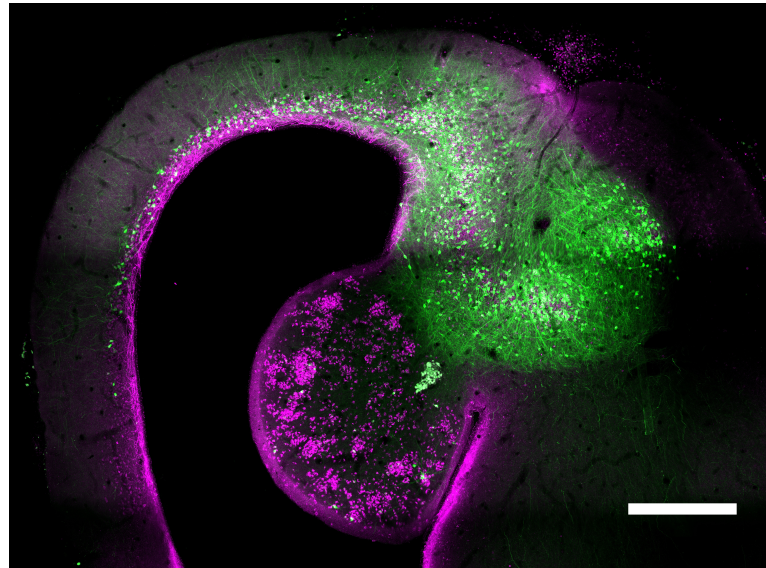


Figure 4.10: Frontal brain section of one turtle 4 weeks after coinjection of AAV-SL1-CAG-EGFP, AAV2/1-CB7-mCerulean and CTB-Alexa555 into pallial thickening. AAV-SL1 infected neurons expressing EGFP (green) and CTB-Alexa555 staining (magenta). CTB retrogradely labels cells in the DVR, while only very sparse EGFP expression by AAV-SL1 infected neurons in DVR. Scale bar, 500 μ m.

shown with cortical neurons 4.10, this property is thus not a general one and does not apply to LGN axons.

Cells located in the dorsoventricular ridge (DVR) are also known to project to the dorsal cortex (Desan, 1984). This was confirmed by coinjection of CTB-Alexa555 and AAV-SL1 into dorsal cortex, which resulted in dense CTB-staining of cells in the DVR. Labelled cells are enriched in the cell clusters of the ventricle lining regions of the DVR and absent in the dispersed cells between clusters. AAV-SL1 infected cells in DVR were sparse in comparison or completely absent. I conclude from the CTB staining that the cells in the DVR clusters rather than the interspersed cells do indeed project to dorsal cortex, and that AAV-SL1 lacks the capacity to efficiently infect the cortex-projecting axons of DVR cells (Figure 4.10).

In conclusion the evidence suggests, that AAV-SL1 can infect the axons of intracortically projecting turtle neurons, but not the afferents of subcortical regions DVR and thalamus.

4.2 Gene expression

I showed that viral infections are possible in turtles using viruses commonly used in the mammalian neuroscience community. The next step was to develop tools to reach two goals in regard to gene expression: high expression rates and restriction of expression to cellular subtypes.

For the first goal, I started by testing commonly used high-yield promoters. These are usually derived from viruses and include promoters such as CB7, CAG and CMV (Miyazaki et al., 1989; Niwa et al., 1991; Yizhar et al., 2011). They all gave high expression rates in turtles.

The other goal, of restricting genetic expression to neuronal subtypes, turned out to be more difficult. In common model organisms this restriction is achieved typically by creating transgenic animals with a strategy called enhancer trapping, thereby exploiting endogenous regulatory systems. Because this strategy is not available in turtles, one is compelled to use virally transfected (short) promoters to achieve cell type specific expression. Finding isolatable promoters with these properties is notoriously difficult (Nathanson et al., 2009). It is why neuroscientists working with mice focus almost exclusively on developing transgenic strains.

Of the published neuronal-subset-specific promoters, the most widely used is α -Ca²⁺/Calmodulin dependent protein Kinase II (CaMKIIa). The CaMKIIa promoter restricts expression to excitatory neurons (Liu and Jones, 1996; Zhang et al., 2010). I tested the CaMKIIa promoter in turtles (Yizhar et al., 2011).

For inhibitory interneurons several promoters derived from the pufferfish *Takifugu rubripes* (*Fugu*) genome have been published (Nathanson et al., 2009). The *Fugu* genome lends itself to promoter isolation, because of its compactness, meaning relatively short intergenic regions with a dense arrangement of regulatory elements (Nathanson et al., 2009). The preceding genomic regions of several interneuron-related genes were cloned into replication-deficient AAV genomes, and recombinant AAV vectors were produced. These genes were somatostatin (fSST), neuropeptide-Y (fNPY) and parvalbumin (fPV), see the methods section 2.2.1 for a detailed description of the vectors. All of these vectors were tested in turtles.

The Cre-Lox system is another tool to control genetic transcription. This method allows deletions, translocations, inversions and insertions of genetic material at specific sites in the DNA of cells. The system consists of a single enzyme, the Cre recombinase, which recombines a pair of short target sequences called the Lox

sequences. The Cre-enzyme and the original Lox site called the LoxP sequence are derived from bacteriophage P1. It is now used extensively in the mammalian neuroscientific community to restrict gene of interest expression to neuronal subtypes (Xue et al., 2014).

It is also used in combinatorial infection strategies, where a mixture of two viruses is delivered (Economo et al., 2016). One virus carries the gene for the Cre recombinase, the other a gene of interest blocked for transcription by a "floxed" stop. This describes a situation where a stop codon, flanked by two Lox sites, is placed directly upstream of the gene. Thus double infection is required for expression and one can influence the sparseness of expression by changing the ratio of the two viruses.

Cre recombinase activity has been reported to be optimally active at a temperature of 37 °C and significantly decreased at 23 °C (Buchholz et al., 1996). Our turtles were typically held at water temperatures of 25 °C. We wondered whether, despite Cre's thermosensitivity, this combinatorial viral strategy might be possible in turtles.

4.2.1 High yield promoters

The three promoters most commonly used to achieve high levels of gene expression in host cells are CB7, CAG and CMV. CB7 and CAG are chicken β -actin promoters with *Cytomegalovirus* enhancer elements. The CAG however is not a promoter in a strict sense as it includes a part of the transcribed chicken β -actin sequence (two exons and an intron) and furthermore contains a chicken β -actin enhancer element (Miyazaki et al., 1989; Niwa et al., 1991). CMV (around 650bp) contains the promoter and immediate-early enhancer from *human Cytomegalovirus* (Yizhar et al., 2011).

The human cytomegalovirus (CMV) immediate-early enhancer and promoter is

Initial tests of injecting AAV2/1-CAG/CB7-EGFP virus into turtle brains showed the capacity of these promoters to express genes of interest in turtle cortical neurons with expression rates high enough to allow visualization of individual axons (Figure 4.11A). Viruses carrying genes under CAG or CB7 control were subsequently used routinely with injections into the brain of a total of more than 40 turtles. The results in chapters 4.1.2, 4.1.5 and 4.2.3 were all obtained using viruses carrying fluorescent protein genes under the control of CAG, CB7 and CMV promoters.

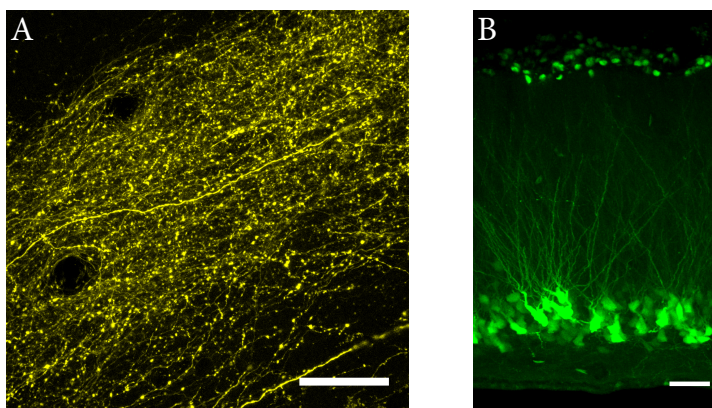


Figure 4.11: A. Maximum intensity projection of an image stack acquired in a frontal section (thickness, 70 μm) of a turtle brain infected with mixture of AAV2/1-CAG-Cre and AAV2/1-CAG-Flex-tdTomato. Axons with boutons projecting to LI of medial cortex can be seen at high magnification. Scale bar, 50 μm .

B. Maximum intensity projection of an image stack acquired in a frontal brain section (thickness, 150 μm) of one turtle 5 weeks after injection of AAV2/1-hSyn1-EGFP-RBG into the anterior dorsal cortex. Scale bar, 50 μm .

4.2.2 Cell type-specific promoters

hSyn

The human synapsin-1 promoter is widely used in mammalian neuroscience because its expression is restricted to neurons and because of its short length (about 470bp) (Kügler et al., 2003; Kügler et al., 2001). This, and its more modest expression rate when compared with CAG/CB7/CMV, make it particularly well suited for genetically encoded calcium indicators where high expression can lead to detrimental calcium buffering (Tian et al., 2009).

Tests of injecting AAV2/1-hSyn-EGFP virus into turtle brains showed the capacity of the hSyn promoter to express genes of interest in turtle cortical neurons with expression rates sufficient for visualization (Figure 4.11 B). Viruses carrying genes under hSyn control were routinely used with injections into the brain of a total of 27 turtles. In none of these animals did we observe expression in radial glial cells.

CaMKIIa promoter

A fragment of the promoter region of CaMKIIa is typically used in a number of vertebrate species to label, probe and perturb a subclass of excitatory neurons. With it, one can visualize, target patching or target expression of effector proteins such as calcium indicators, ChR2, etc. The promoter is also short enough (around 370bp) to be used with AAV. It could thus be a valuable tool for non-

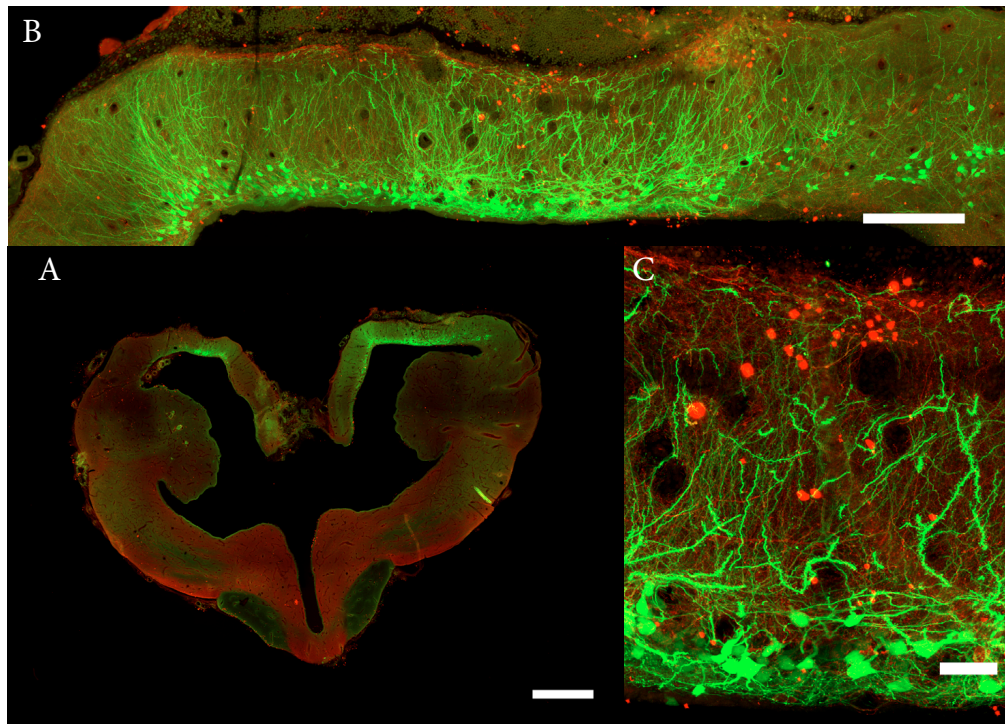


Figure 4.12: Frontal section of a turtle brain infected with AAV2/1-CaMKII α -EGFP shows that CaMKII α promoter results in high expression rates in turtle cortical neurons. **A.** 40 μ m thick frontal section with bilateral expression of EGFP under the CaMKII α promoter (green), antibody counterstaining against GABA. Scale bar, 1 mm **B.** Higher magnification image showing dorsal cortex. Scale bar, 250 μ m **C.** High magnification of the central region of dorsal cortex. Scale bar, 50 μ m

transgenic model systems, especially to probe properties of neuronal networks in turtle dorsal cortex.

Initial tests of injecting AAV2/1-CaMKII α -EGFP virus into turtle brains showed the capacity of the CaMKII α promoter to express genes of interest in turtle cortical neurons with useful expression rates (Figure 4.12). Throughout this thesis viruses carrying genes under CaMKII α control were routinely used with injections into the brain of a total of more than 30 infected turtles (see chapter 6).

An experiment was designed to characterize whether CaMKII α promoter fragment driven expression is restricted to the excitatory population. Two turtles (*Trachemys scripta elegans*) were transfected with AAV2/1-CaMKII α -EGFP. Injections were placed into the dorsal cortex as described in section 4.1.1. Two injections were made in each hemisphere, each with a volume of 1 μ l, one in the anterior, the other in the posterior dorsal cortex. After six and eight weeks the turtles were

sacrificed and perfused with 4 % PFA and 0.5 % glutaraldehyde. Frontal 40 μm sections of the brain were performed with a cryotome, followed by antibody staining against GABA and DAPI counterstaining (chapter 2.5).

Nineteen and 24 sections of the two turtles were then imaged respectively with an automated microscopy scanning robot (3D Histech). The resulting images were used to count GABA-positive neurons (2514 and 2182 respectively) and GABA+CaMKIIa+ double-positive neurons (38 and 31 neurons respectively) in the dorsal cortex. These two populations were sparse enough to be counted from non optically sectioned images. A subset of the sections was furthermore scanned with an LSM confocal microscope. These confocal data were then used to manually count the number of CaMKIIa positive cells. CaMKIIa positive neurons cluster densely in layer II of cortex, which necessitated matching dense optical sectioning (thickness optical section 0.9 μm , z step size 0.7 μm) for single cell resolution.

Turtle	counted slices	# GABA+ cells	# CaMKIIa+ cells	Double+ cells
M32	19	2514	5.0x GABA+	38 (0.3 %)
M36	24	2182	2.1x GABA+	31 (0.7 %)
Total	43	4696	16700	69 (0.4 %)

Table 4.4: Results of manual cell counting.

The ratio between the number of CaMKIIa+ neurons and GABA+ neurons in these two sections was used for a rough estimate of the total number of CaMKIIa+ cells in all 43 counted slices. The results suggest that about 0.4 % of CaMKIIa+ cells are also GABA+ (see table 4.4). This is compared to the 7 % GABAergic interneurons of the total cortical population (Christian Müller, unpublished data). The estimate of double positive cells likely represents an upper limit. Double positive was assigned during counting each time when in doubt and I never found a cell that was both GABA+ and strongly CaMKIIa+. From the sections scanned with the confocal microscope I determined the fluorescence intensity for different cell types and structures, to compare the intensity of CaMKIIa mediated expression in GABA+ cells. The normalized fluorescence intensity in the CaMKIIa channel of an average double positive neuron was 0.10, where the average cell classified as CaMKIIa+ was 0.5 and a typical bright CaMKIIa+ cell was 0.95. Also the background fluorescence measured in LI was 0.11 (see table 4.5).

I thus conclude, that while there seems to be slight leakage of CaMKIIa expression in GABA+ interneurons (at most 6 % of the GABAergic interneurons), the intensity of CaMKIIa expression in these cells is weak. Thus the CaMKIIa promoter can serve as a promoter to restrict expression to excitatory cells in turtle cortex.

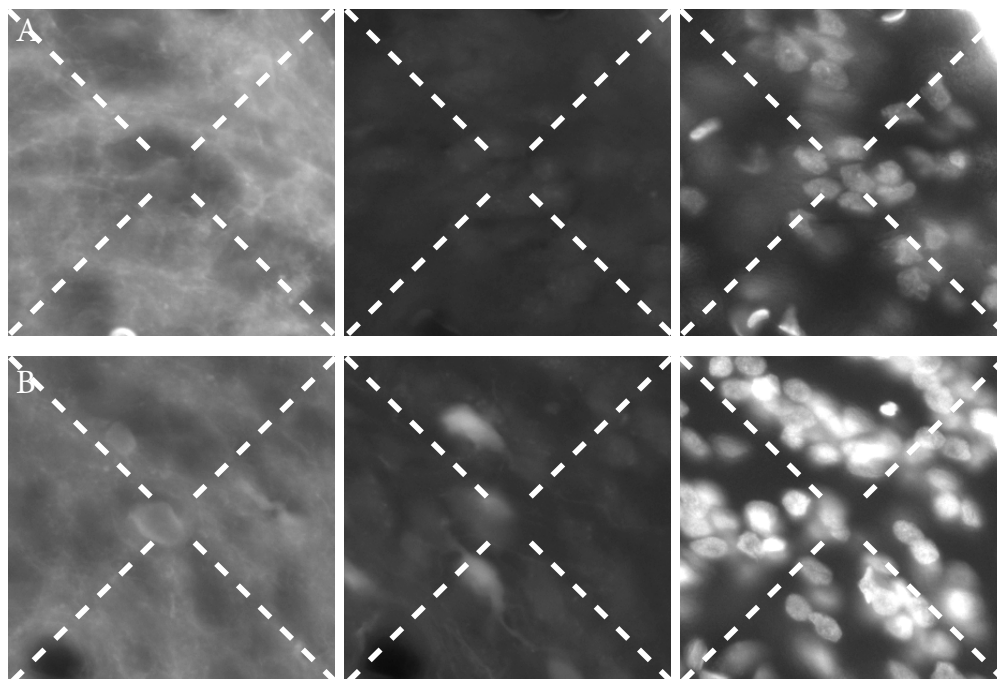


Figure 4.13: Examples of two cells (rows A & B) scored as double positive, for staining with a GABA antibody (left image) and expressing EGFP under a CaMKII α promoter (center). DAPI counterstaining (right). All images are centered on the cell. Cells are located in the dorsal cortex of one 40 μ m thick frontal section of a turtle brain infected with AAV2/1-CaMKII α -EGFP.

Type	Fluorescence intensity (0-255)
Double+	26
Bright CamKII+	244
Average CamKII+	129
GABA+ CamKII-	17
Blood vessel	5
Background	28

Table 4.5: Fluorescence intensities of structures in an AAV2/1-CaMKII α -EGFP infected dorsal cortex.

Fugu derived promoters

In mammalian cortex, different interneuron populations are frequently classified based on marker expression (Klausberger and Somogyi, 2008; Petilla Interneuron Nomenclature Group et al., 2008; DeFelipe et al., 2013; Jiang et al., 2015; Cadwell et al., 2016). Such markers include somatostatin (SST), calbindin (Cal), 5HT3A, parvalbumin (PV), neuropeptide Y (NPY). In turtles all of these markers

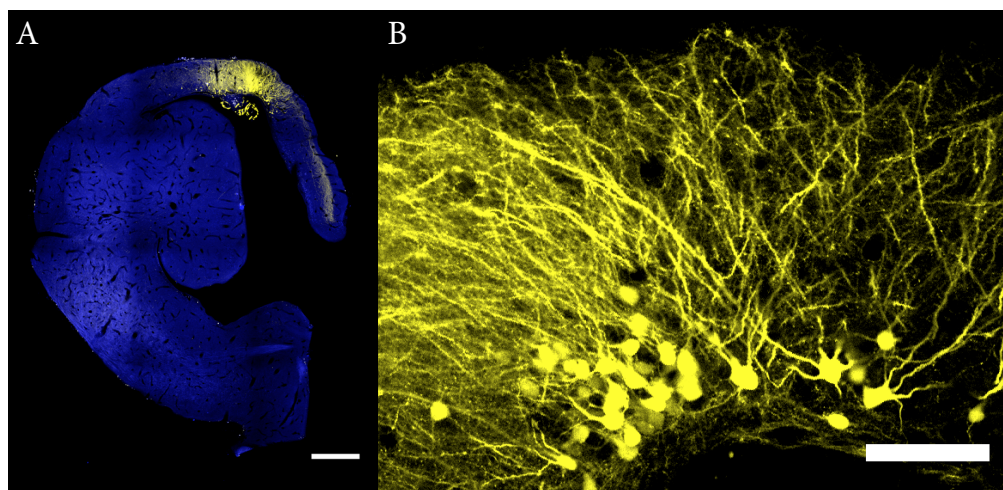


Figure 4.14: Frontal section (thickness, $70\ \mu\text{m}$) of a turtle brain infected with mixture of AAV2/1-CAG-Cre and AAV2/1-CAG-Flex-tdTomato. **A.** Overview of one hemisphere with tdTomato expression in the medial part of dorsal cortex. Axonal projection to LI of medial cortex can be seen. Scale bar, $500\ \mu\text{m}$. **B.** Higher magnification of the medial region of dorsal cortex of the same section, individual transfected cells visible. Scale bar, $100\ \mu\text{m}$.

are expressed in cortical interneurons as well. Only PV is not present (Christian Müller, unpublished data), although PV-type interneurons exist, as identified from their transcriptome (Tosches et al., submitted).

As described in section 4.2, published promoters derived from the Fugu genome restrict gene expression to inhibitory interneurons in the mouse (Nathanson et al., 2009). Of these published promoters, fPV, fSST and fNPY were investigated in turtle neurons by injecting AAV carrying fluorescent protein genes (GFP, RFP) under the control of each promoter. A total of 15 AAV injections ($1\ \mu\text{l}$ of viral solution) were administered into the olfactory bulbs and dorsal and lateral cortices of 4 *Chrysemys picta bellii* (fPV $n=5$, fSST $n=6$, fNPY=4). The brains of these animals were perfused 4 weeks after injection and processed for histology. None of the brains showed any expression. I thus conclude, that the Fugu-derived inhibitory-interneuron specific promoters do not express in turtle neurons.

4.2.3 Cre lox system

As mentioned in the introduction to this chapter 4.2 the Cre-Lox system is of interest because of the possibility to titrate the density of expressing neurons by changing the ratio of two viruses (Xue et al., 2014). Thus in one turtle (male *Chrysemys picta bellii*, 250 g) three viral injections were placed in the dorsal cortex of each hemisphere. Two viruses AAV2/1-CAG-Cre and AAV2/1-CAG-Flex-tdTomato were

mixed in a 1:1 ratio and this mixture was injected (500 nl per injection site) at two depths in cortex (as described in 4.1.1).

The turtle was sacrificed after 10 weeks of incubation, perfused (4 % PFA) and sectioned (thickness, 70 μ m). Sections were imaged on a confocal microscope. High level of tdTomato expression was observed in the cortex of both hemispheres (4.14). Expression levels were high enough, to visualize axonal projection patterns from the medial section of dorsal cortex to medial cortex. I conclude that the Cre recombinase is functional also in the ectothermic species *Chrysemys picta bellii* (Buchholz et al., 1996), and that the Cre-Lox system is available as a tool for gene expression strategies in turtles.

Promoter	Excitatory cells	Inhibitory cells
CB7/CAG/CMV	yes	yes
hSyn	yes	yes
CaMKII	yes	no
fPV	no	no
fSST	no	no
fNPY	no	no
Cre/Lox	yes	yes

Table 4.6: Summary of expression results under tested promoters and the Cre/Lox recombinase.

4.3 Organotypic cortical slab preparation

We developed a novel type of organotypic culturing protocol to screen viruses and promoters for their capacity to respectively infect neurons and control the expression of genes in different neuronal populations of the turtle. For initial tests, we reasoned that organotypic cultures would be more efficient than *in vivo* injections, allowing more injections to be tested per animal. One reason was that *in vivo* injections would be made only in the anterior half of dorsal cortex, posterior areas not being accessible for surgery. Given the limited thickness of the turtle cortical sheath (250 to 500 μ m) and the lower oxygen requirements of turtle nervous tissue, we opted for a slab rather than a slice culture.

To prepare organotypic slab cultures, we followed the procedure of slab preparation (see chapter 2.3.1) with some adaptations. The skin of the turtle's head and neck was thoroughly disinfected with iodine tincture (Braun, Germany) be-

fore and after decapitation. All Ringer was sterilized by filtration and instruments and equipment were autoclaved prior to preparation. These steps were essential. Once the slabs were isolated, the rest of the preparation was performed under a cell-culture hood. The slabs were washed four times in sterile-filtered Ringer and transferred onto 30 mm diameter Millicell cell culture inserts, a PTFE membrane with 0.4 μm diameter pores (Merck Millipore, Germany), and placed in multi-well plates containing an adapted organotypic slice culture medium (Neurobasal-A, 0.5 mmol L-glutamine, 25 % chicken serum, 50 U ml⁻¹ Penicillin-Streptomycin) (Gähwiler et al., 1997).

Viral injections. Pure *lentivirus* or a 1:1 mixture of *lentivirus* and AAV were injected, using the same hardware as described in chapter 4.1.1. We penetrated (depth, 300 μm ; angle, 50°) into the tissue from the ventricular side, making surface incision unnecessary. We injected 1 μl of the virus suspension at a rate of 200 nl min⁻¹ and waited for 10 min before retracting the needle.

Slabs were kept in cooled incubators (Galaxy 170 R with cooling system, New Brunswick at 20°, 5 % CO₂); medium was exchanged every second day.

In a first test run, we compared several media in their capacity to maintain turtle cortical tissue over a period of 10 days. A Neurobasal-A based medium with 25 % chicken serum gave the best results when evaluating survival with a live-dead stain (Live/Dead Kit, Molecular probes).

We did a second round of cultures to evaluate whether health of tissue and cell metabolism suffices for viral infection. Furthermore whether significant gene expression levels can be obtained and whether electrophysiological and synaptic properties were still intact. Cortical slabs of two turtles were injected with 1 μl of AAV (AAV2/1-hSyn1-EGFP) and cultured at 20°C for 12, 15 and 18 days.

The two slabs that were cultured for 18 days were contaminated and dissolved. The other two (cultured for 12 and 15 days) were transferred into Ringer solution and probed electrophysiologically. Pulses of 100 μA current were delivered via a bipolar stimulation electrode. We recorded extracellular field potentials 1 mm posterior to the stimulation site with a low impedance patch pipette (0.5 M Ω). Clear field responses could be detected following the stimulation (Figure 4.15D), that were abolished after superfusing for 10 min with Ringer solution containing 5 μmol tetrodotoxin (TTX) (Figure 4.15E). We conclude that at least some elec-

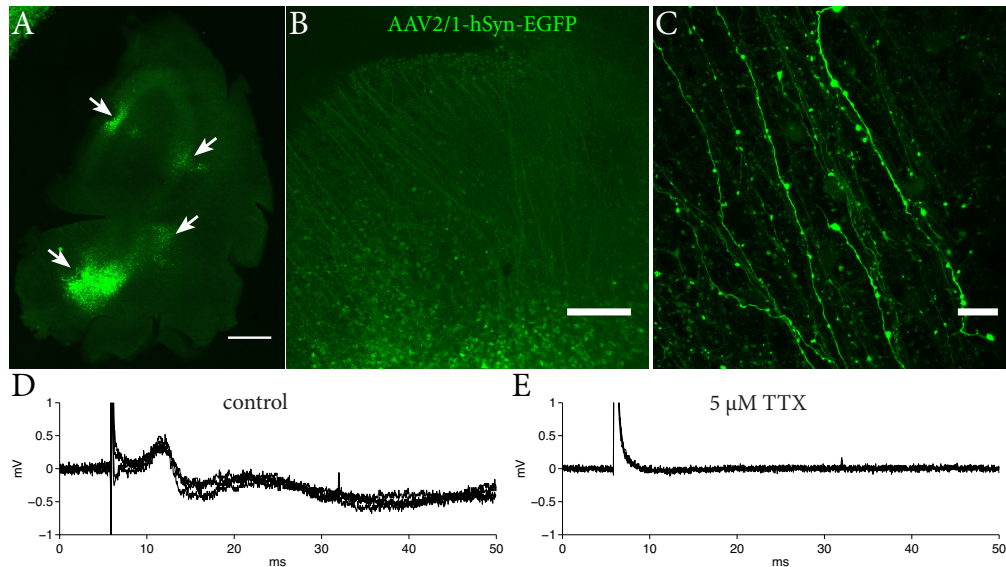


Figure 4.15: Example of one slab after 15 days of organotypic culture. **A.** Overview image of the entire slab showing 4 viral injection sites with EGFP expression (white arrows). AAV2/1-hSyn1-EGFP. Scale bar = 1 mm **B.** One of the injection sites at higher magnification, EGFP expressing cells and processes can be seen. Scale bar = 250 μm **C.** High magnification image with individual axons of EGFP expressing cells. Scale bar = 25 μm . **D.** Extracellular field recording after 100 μA stimulations (at timepoint 5.8 ms) 1 mm anterior to the recording site. **E.** Same as in D. but 10 minutes after wash-in of 5 μM TTX. Field potential response is abolished.

trophysiological function and synaptic activity is intact after 15 days of culture. Results are shown for one slab, but were qualitatively similar with the second slab.

Slabs were fixed in 4% Paraformaldehyde (PFA) and imaged. Imaging the slabs revealed significant EGFP expression levels (Figure 4.15A-C). The limited quality of imaging (due to depth-limitations of confocal imaging in a whole cortical sheath, we could identify individual cells expressing EGFP (Figure 4.15 B), and even EGFP-labeled axons (Figure 4.15C). Results with the second slab were qualitatively similar. We thus conclude that organotypic cortical slabs in turtles are viable for at least 15 days, and constitute an adequate tool for testing viral vector infection and promoter expression qualitatively.

4.4 Immediate early genes

Immediate early genes are genes that are rapidly expressed in response to increased levels of neural activity and some of them are thought to play a role in synaptic plasticity (Lanahan and Worley, 1998; Guzowski, 2002). The visualization of the products of these genes can thus serve as a means to identify cells and

brain regions involved in certain tasks or functions. This visualization is usually done using antibodies or in situ hybridization and has been used with success in mammals and in birds (Bischof et al., 2006; Mayer et al., 2010). The possibility to identify active brain regions involved in a particular task is of interest in reptiles, because of our limited knowledge of the functional specialization of their brain. I thus set out to test whether these tools can be used in turtles, with three antibodies against the gene products of c-Fos, Egr1/Zenk and Arc, exploiting the fact that c-Fos and Egr1/Zenk had been employed successfully in zebrafinch (Mayer et al., 2010).

The right eye of one animal was covered with opaque cement. Thirty six hours later the animal was transferred for 2 h to a novel aquarium with pond scenes on the interior walls and a temperature gradient of 10 °C. A second animal (without perturbation) was placed in a novel aquarium, enriched with olfactory cues (isoamyl acetate, cineole) and temperature gradients, as for the first animal for 2 h. Following these periods of enriched environment, the animals were isolated for 1 h, anaesthetized with Ketamine hydrochloride (23 mg kg⁻¹, IM) and Dexmedetomidine hypochloride (75 µg kg⁻¹, IM), and, after the loss of the corneal reflex (after 20 min), sacrificed and perfused. Their brains were sectioned and processed for immunohistochemistry and HRP staining (section 2.5). The sections then were scanned on an imaging robot (section 2.5.4).

c-Fos (sc-52 by Santa Cruz Biotechnology) staining did not result in sufficient signal to be informative. Arc staining appeared to be broadly unspecific and thus without use for identifying regions of interest. Egr1 / Zenk, however, gave sparser but high contrast staining of neurons. Furthermore in the monocularly deprived animal, staining in anterior dorsal cortex and tectum contralateral to the covered eye was sparser than in the ipsilateral hemisphere. This difference was not present in the control animal (Figure 4.3). We thus conclude that the zinc-finger transcription factor Egr1 / Zenk may be a promising immediate early gene to reveal functional biases in the turtle brain.

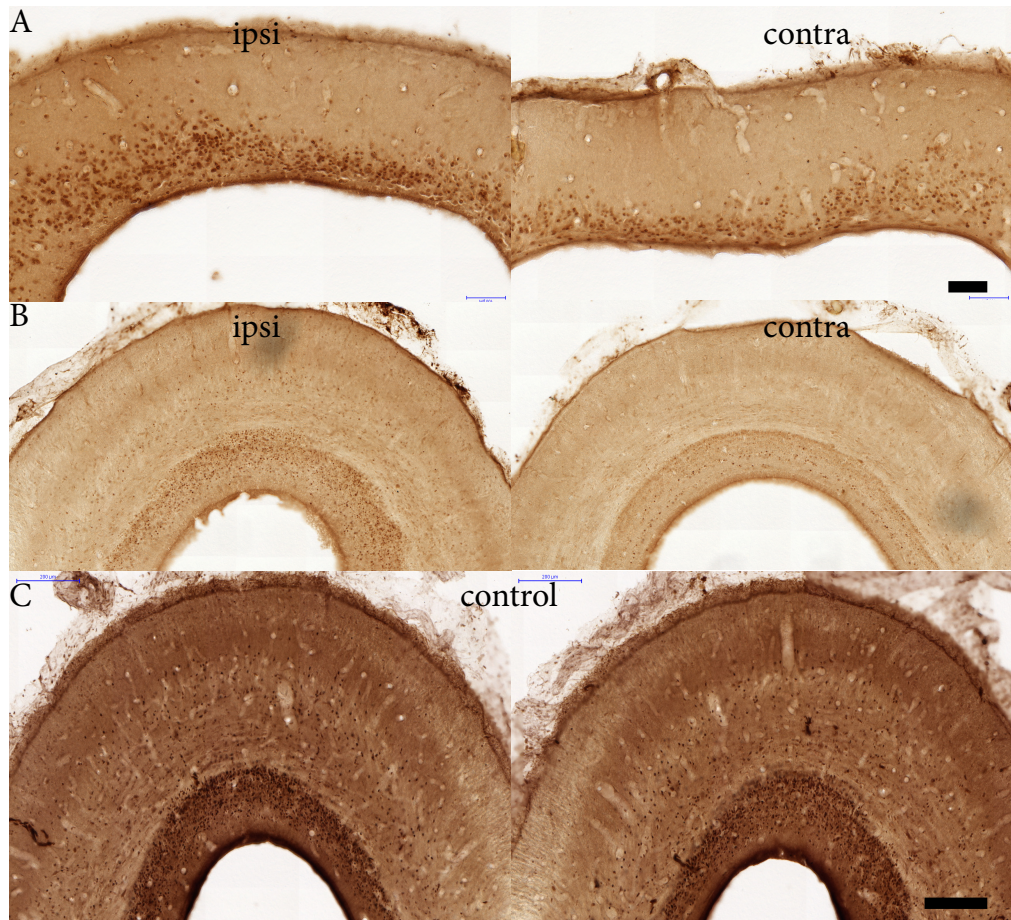


Figure 4.16: Sixty μm frontal sections of a turtle brain stained with an Egr1/Zenk antibody 39 h after functional monocular deprivation (see text). For anterior dorsal cortex (**A**), and tectum (**B**) both the hemisphere ipsilateral (left) and contralateral (right) to the covered eye are shown: note the sparser staining of the contralateral hemisphere. Scale bar = 100 μm . **C.** Sixty μm frontal sections of the tectum of a control turtle, stained for Egr1/Zenk. Scale bar = 200 μm .

Chapter 5

Neurophysiology in the cortical slab

The multiplicity of spatial and temporal scales over which important operations occur in the brain presents a tough challenge for systems neuroscientists. Neurons are single cells, but they often communicate with hundreds to thousands of other neurons spread non-isotropically over comparatively vast regions. Important computations may occur at the scale of synapses, dendrites, neurons or populations of neurons and over time windows ranging from tens of microseconds to seconds, making the choice of appropriate sampling techniques often difficult: the competing demands for high spatial and temporal resolution, high S/N, lack of signal ambiguity (e. g. , linked to inferring voltage from calcium signals), together with very large sample sizes, are a great challenge with any single technique.

The recent development of optical methods (microscopy and sensors) offers much promise on the 'mesoscale'. Yet, optical signals are usually indirect estimates of voltage or AP forming currents (e. g. , via cytoplasmic calcium), and the physical constraints of optical sampling present their own limitations, especially over large imaging volumes.

Older techniques such as electrical extracellular recordings have for decades been - and continue to be - essential tools in systems neuroscience. Recent developments in micro- and nano-fabrication technology now promise potentially massive improvements in sampling density and reproducibility. But what improvements can we expect to obtain, in the way of signals and information, from such electrical recordings? What are reasonable limits on what we can expect with the best possible electrical recording probes at optimal densities? These are some of the questions we address in this study, exploiting the advantages of planar multi-electrode arrays (MEAs) and the simple cerebral cortex of the turtle.

Planar electrode arrays were first developed by Jerry Pine (1980) and soon became instrumental for investigations of light-evoked activity in the vertebrate retina, a thin two-dimensional neuronal network whose output, a population of retinal ganglion cells (RGCs), lies close to the surface. Recent improvements in fabrication technology have led to very dense arrays, enabling nearly saturating sampling of RGC activity over significant areas in the isolated macaque retina (Perry and Cowey, 1985; Pillow et al., 2008; Li et al., 2015). These approaches enable the sampling of action potentials from tens of RGCs simultaneously, and the monitoring of single cells' action potential propagation over large swaths of the retina.

These techniques have, to our knowledge, not been fully explored yet to study central brain networks, in which neuronal projections and synaptic interactions are spread over three dimensions. Our goal here was to test the limits of such an approach, in which easy-to-use surface recordings are used to infer activity distributed over some volume of cortex. Taking advantage of the simpler, thinner and sturdier cerebral cortex of turtles, we explored the value of MEAs for the study of cortical activity in an *ex vivo* preparation.

We found that MEAs, covering an area of 2.25 mm^2 , enable the monitoring of hundreds of neurons (often over 1,000) simultaneously; that in addition to action potentials, synaptic potentials could be detected and separated, enabling the classification of the recorded cells into inhibitory or excitatory neurons; that the spatial distribution of detectable synaptic signals triggered on each unit's action potential maps out a useful fraction of each neuron's axonal projections, thus providing an estimate of each neuron's output projections in x, y and within definable limits, also in z .

These results indicate that in addition to spike times - easily extracted in parallel from hundreds of neurons, precious information about the isolated units' identity, approximate soma position and axonal projections can be extracted relatively easily and in parallel from hundreds if not thousands of neurons using extracellular electrodes. By extrapolating to dense and appropriately designed three-dimensional arrays, one can foresee combining the clarity and high temporal resolution of electrophysiological signals with structural information about many thousands of neurons recorded simultaneously in large brain volumes with very little effort, other than computational.

This work has been done in collaboration with two colleagues, Dr. Mark Shein-

Idelson (M.SI.) and M.Sc. Mike Hemberger (M.H.) (Shein-Idelson et al., 2017). I will acknowledge their contribution at data acquisition and analysis in the text.

5.1 Whole cortex preparation

The experimental potential and advantages of the turtle brain-linked to its resistance to anoxia - was well known to early investigators of sensory and motor systems (Mori et al., 1981a; Mori et al., 1981b; Mori et al., 1984; Mori et al., 1982; Nowycky et al., 1981a; Nowycky et al., 1981b; Greer et al., 1981). In the mid 80s, Arnold Kriegstein, Barry Connors and collaborators developed an *ex vivo* turtle brain preparation in which individual cortical cells could be recorded using intracellular electrodes while the retina was stimulated with light flashes (Connors and Kriegstein, 1986; Kriegstein and Connors, 1986; Kriegstein, 1987). While this work was discontinued, the *ex vivo* preparation was later used in combination with VSD and calcium imaging techniques, providing important data about spontaneous and visually evoked cortical oscillations and propagating waves (Pechtl, 1994; Pechtl et al., 1997; Pechtl, 1995; Senseman, 1999; Senseman and Robbins, 2002). In our laboratory we have adapted this preparation and combined it with more recent techniques (biophysical and molecular) to investigate cortical computation and evolution. To test the sensory viability of this preparation, we carried out recordings from the optic tectum, the lateral forebrain bundle of thalamo-cortical axons, and the dorsal cortex (M.SI.). All revealed reliable responsiveness to images or movies projected onto the retina. All the results below were obtained in dorsal cortex.

The turtle forebrain's pallium is composed of a cortical sheet (Figure 5.1A and B) that extends from the lateral (piriform) cortex (LC, recipient of OB input) to the medial cortex (MC, often called hippocampus) medially. Between LC and MC (starting laterally at the rhinal fissure) lies the smooth dorsal cortex (DC), with direct visual input from the thalamic dorsal geniculate nucleus (Ulinski and Nautiyal, 1988; Desan, 1984; Mulligan and Ulinski, 1990). The dorsal cortical sheet rests not on top of white matter as it does in mammals, but rather directly over large lateral ventricles. Protruding from the lateral pallial wall and extending medially into the lateral ventricle is a region called the dorsal ventricular ridge (DVR, also prominent in avians), whose mammalian equivalent remains debated (Montiel et al., 2016; Shein-Idelson et al., 2016).

The cortical sheet, which overlays the entire forebrain, is composed of one main

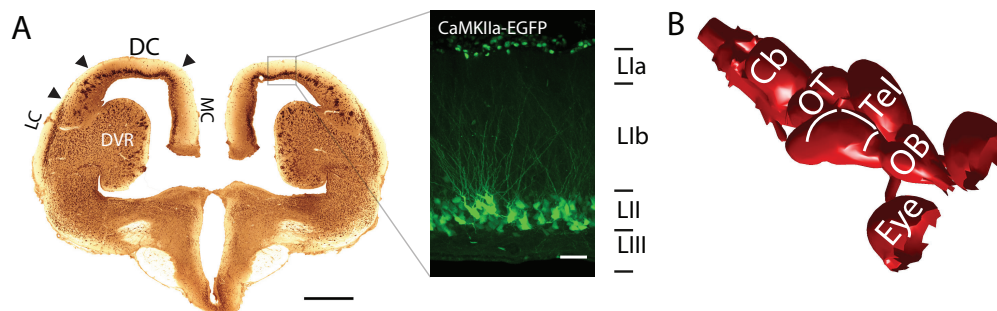


Figure 5.1: **A.** Turtle cortex. Left, NeuN staining of a turtle brain frontal section. Turtle cortex is subdivided into the lateral cortex (LC), medial cortex (MC) and dorsal cortex (DC), receiving multimodal inputs, among them inputs from visual thalamus (lateral geniculate nucleus). Scale bar, 1 mm. Right, frontal section of a turtle brain infected with AAV2/1-CaMKIIa-EGFP, expressing EGFP under the excitatory-neuron specific CaMKIIa promoter. Dorsal cortex consists of one main cell layer (LII) containing mostly glutamatergic excitatory pyramidal cells, while inhibitory neurons and neuropil primarily make up the remaining layers (LI and LIII). Cell-sparse layer I with thalamic fibers running from lateral to medial in LLa. Scale bar, 50 μm. **B.** Turtle brain. Rendering of a 3D volume model of a freshwater turtle brain acquired with MRI. From posterior to anterior - cerebellum (Cb), optic tectum (OT), telencephalon (Tel), olfactory bulb (OB). The depicted structures can be isolated in toto (ex vivo preparation) with attached sensory organs and typically remain functional for 2 days.

cell layer (L2) flanked by two neuropilar layers (L1 dorsally, L3 ventrally). Layer 1 can be subdivided in a superficial L1a in which afferent axons terminate (from LGN in DC), and a deeper and thicker L1b, containing associational fibers from local and distant cortical neurons. The great majority of the excitatory neurons are in L2, while inhibitory interneurons are scattered throughout all three layers, with increased density along the ependymal layer in ventral L3. Excitatory neurons in L2 can be infected with a variety of gene constructs developed for mammalian brains using the CaMKIIa promoter and adeno-associated viral tools (Figure 5.1A, inset; Chapter 4), and thus be both visualized (e. g. , with eGFP) or manipulated optically (e. g. , Chr2).

Following deep anaesthesia of an adult turtle, the brain can be carefully extracted after brainstem and cranial-nerve trans-sections together with intact sensory structures such as the eyes or the nasal epithelium. Because dorsal and medial cortices overlay the ventricular cavity directly, the cortical sheet on one side of the brain can be flattened (after a couple of anterior and posterior transverse incisions) and placed, layer 3 down, on a multi-electrode recording array (Figure 5.2A), mounted on a microscope platform. Because LGN inputs reach cortex from the lateral margin, visual inputs to cortex are intact and the preparation can be stimulated by direct projection of images and movies to the contralateral retina. The preparation can then be studied using a combination of modern techniques such

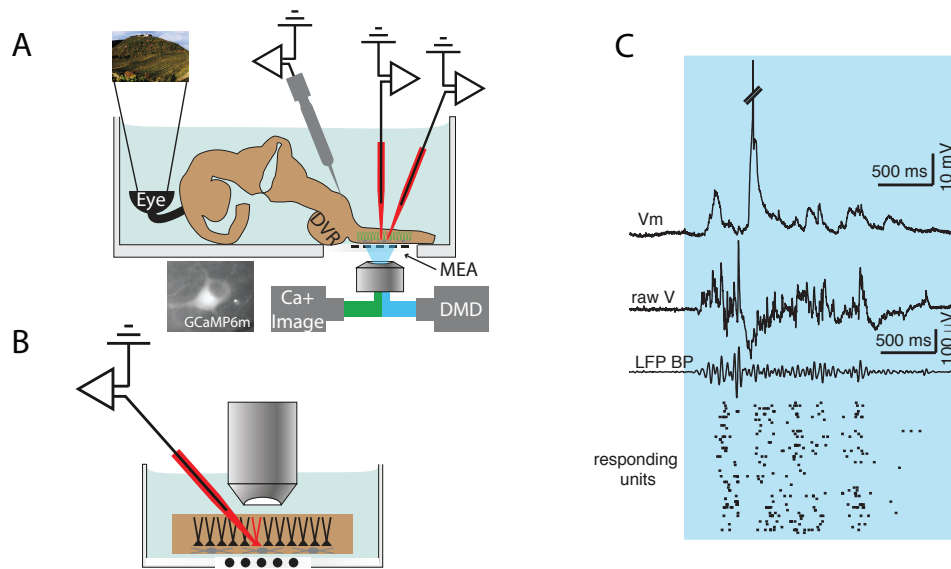


Figure 5.2: **A.** Experimental Preparation. Schematic depicting an imaginary frontal section of a turtle whole-brain ex vivo preparation. The brain is continuously superfused with oxygenated Ringer. Left cortical hemisphere is flapped open (via two sections of the cortical sheet, see white lines in B) and its ventricular side is placed on a multi electrode array (MEA) for extracellular recordings. Accessibility and stability of this *in vitro* preparation allows simultaneous extracellular depth electrode- (e. g. silicon probes) and whole cell patch-clamp recordings. Recombinant viral vector techniques allow gene delivery to turtle cortical neurons. All of the above can be combined with calcium imaging and spatio-temporal patterning of light (e. g. optogenetic excitation) due to the transparency of the MEA base material. These techniques are combined in a brain preparation, where visual stimuli are presented to the eyes and the entire processing cascade from the periphery to the higher cortical areas remains intact (with the exception of the two mentioned sections). Initial explant preparations developed in collaboration with Stephan Junek and Viola Prieseman. M.SI. developed the preparation as presented here on the MEA. DMD setup in collaboration with M.SI.. Combined patching and calcium imaging in collaboration with M.SI. and M.H. **B.** Cortical Slab Preparation. A slab of the dorsal cortical sheet isolated from the rest of the brain by sections and placed with the ventricular side on the MEA. Developed primarily by M.H., adaptations in collaboration. **C.** Example traces of simultaneous intra- and extracellular recordings in the ex vivo whole-brain preparation during visual stimulation. From top to bottom: (1) whole cell patch-clamp recording of a pyramidal cell (35mV clipped from action potential); (2) raw data from one MEA channel and the same data bandpass filtered in the LFP band, spike raster ($n = 47$ single units) pooled over all electrodes of the MEA. Blue shading indicates onset and duration of the light stimulus. Data acquisition by M.H. and Samuel Reiter.

as optogenetic activation or inactivation, calcium imaging, multiple patch-clamp recordings, depth silicon probe recordings, and MEA recordings (Figure 5.2A). The slab preparation constitutes a comparatively reduced preparation, where a part of the dorsal cortical sheet is isolated from the rest of the brain by transverse and sagittal sections (see methods 2.3.1). The resulting isolated cortical preparation is placed with the ventricular side on the MEA (Figure 5.2B). Developed primarily by M.H., adaptations in collaboration.

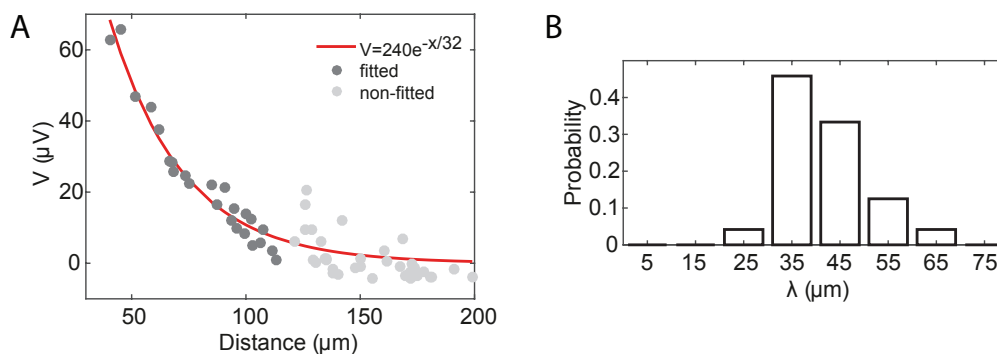


Figure 5.3: **A.** Extracellular action potential amplitude (μV) on each recording electrode of a 60 channel hexagonal MEA ($10\ \mu\text{m}$ diameter electrodes and $40\ \mu\text{m}$ spacing) as a function of distance from the known position of the patched neuronal cell body. In red the fitted exponential function with a space constant of $32\ \mu\text{m}$. (M.H., M.SI.) **B.** Histogram of space constants (λ) for all sorted single units from one experiment using the same 60 channel hexagonal MEA. (M.H., M.SI.)

Figure 5.2C shows a recording from the *ex vivo* preparation performed by M.H. and Samuel Reiter. A whole-cell patch-clamp (WCPC) recording was made from a L2 pyramidal neuron soma (top trace, V_m) while a 120-electrode MEA was used to extract local field potentials (LFPs) and spiking activity from other neurons (47 sorted units shown), evoked by a simple visual stimulus (blue shading). This approach typically enables one to record spontaneous and stimulus-evoked activity from large numbers of neurons over a few mm^2 and over 48 h. After spike sorting, in typical experiments hundreds to more than one thousand units can be unambiguously isolated.

5.2 Extracellular spread of action potential

Data gathering and analysis for the results of this section have been performed by M.SI. and M.H. For the demonstrating the overarching goals of this project it should still be presented here.

Because MEA recordings can be combined with patch-clamp recordings, the spikes of one extracellular unit from the MEA can be driven by direct current injection of one neuron through the patch pipette; the extracellular spread of the spike signal through the tissue can then be examined in the MEA plane (x,y). An example of individual intracellular action potentials and the corresponding extracellular waveform voltage are shown in Figure 5.3. Because the position of the WCPC recording site was known (pipette tip), the relationship between signal amplitude at each MEA electrode position and distance from the soma could be examined (Fig-

ure 5.3A). In this example, this distribution is well described by a single exponential with a space constant of 32 μm . The distribution of decay space constants (λ) for $n > 300$ neurons is shown in Figure 5.3B. From this we established that decay constants are quite narrowly distributed with a mode of about 35 μm . We could thus decide on an appropriate MEA electrode size and spacing. With values of 30 μm diameter and 100 μm pitch, for example, the extracellular spike from each unit could be detected from several contiguous electrodes in the array, increasing the separating power of spike sorting. At the same time, the inter-electrode spacing was large enough that a large area of cortex could be covered with a fixed number of channels (60, 120 or 250), imposed by the design of the amplifier array. With 250-electrode MEAs, we could routinely record simultaneously, over more than 2 mm^2 and during 48 h, from over 1,000 units. The estimated total number of cortical cells in this area is about 50,000 cells (Christian Müller).

With the assumptions that action potentials (APs) originate from a point source (soma or spike initiation zone) and decrement exponentially and isotropically in the extracellular medium we could, by triangulation of each unit's waveform over the MEA, determine the most likely location of the source for each sorted unit's AP. In a typical recording session, we could thus assign a probable position in x, y, z of each point source for which a signal had been detected. Interpretation of MEA data could thus assign a position in x, y and z to each AP source, and thus define a coarse map of presumed soma positions.

5.3 Extracellular detection of synaptic potentials

Upon close observation, unfiltered MEA traces often revealed slow signals associated with single action potential waveforms. These slower signals were not visible from traces that had been high-pass filtered for spike sorting and thus initially escaped our attention (Figure 5.4A and B). They had time courses similar to synaptic potentials with time-to-peak of a few ms and a total duration of a few tens of ms, and tended to follow action potentials with a very short latency (1 ms or less), consistent with delays at chemical synapses. The amplitude of these events varied from a few μV (only detected upon spike-triggered averaging) to over 100 μV (i. e. sometimes considerably larger than the extracellular action potential peak amplitude). We call these events spike-induced fields or SIFs. SIFs were associated equally with spikes caused by current injection in a specific neuron via a patch pipette, or with spontaneous spikes isolated by spike sorting. To facilitate their

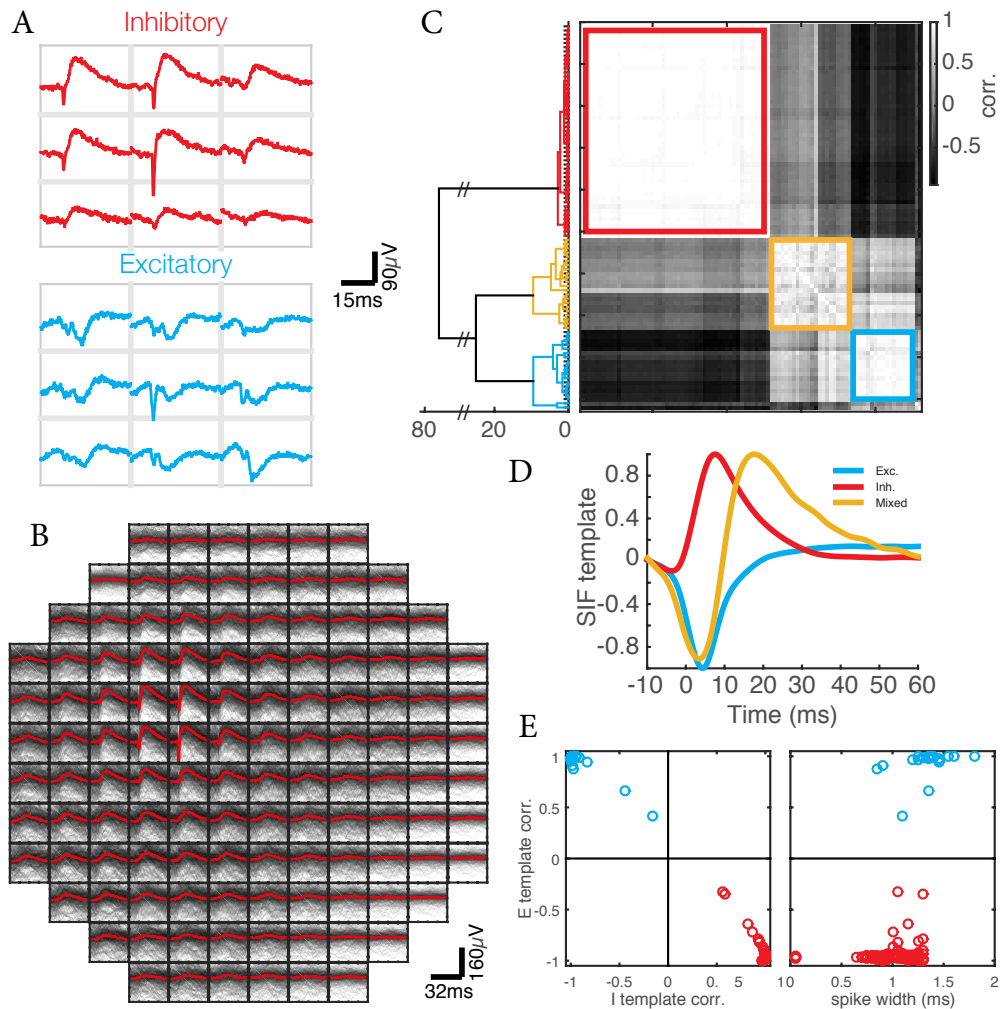


Figure 5.4: **A.** We observed that slow fields follow the AP (termed spike induced fields, SIF) in broad band spike waveforms of single spikes. SIFs come in two flavors. Top, spatial distribution of a positive SIF waveform (red, putative inhibitory neuron, SIF_{in}). Each grey rectangle corresponds to a MEA recording electrode. Fast downward deflection is the spike. Note the spread of the SIF to surrounding electrodes. Lower panel shows the spatial distribution of a negative SIF waveform (blue, putative excitatory neuron, SIF_{ex}). **B.** Broad band spike waveforms averaged (red traces) over all spikes of a single unit on all electrodes arranged according to the physical layout of the MEA. In black, probability density plot in logarithmic scale. Averaged over a large number of detected spikes most sorted units show SIFs. **C.** SIFs triggered by unambiguously sorted units from two recording sessions were selected and their pairwise correlations (Pearson correlation) measured. The plot shows the output of an unsupervised clustering algorithm on these correlations in the form of an ordered correlation matrix. Three unambiguous clusters could be identified (red, yellow, blue) (M.SI.). **D.** These identified clusters allowed extraction of three average waveform templates. Two matched the E (blue) and I (red) waveforms initially identified by eye as in panel A. The third template (yellow) was biphasic, with an initial negative peak coinciding approximately with that for E, and a positive waveform similar to the I template, with roughly 10 ms delay (M.SI.). **E.** Using the obtained average waveforms to assign units based on highest correlation to one of the three templates, we classify neuron type (left panel). SIFs as a measure of cell-type classification are superior to the traditional one using action potential half-width (right panel) (M.SI.).

detection, we examined the SIFs associated with single isolated units. By triggering the unfiltered voltage of each electrode from the time of the corresponding unit's spike, we could observe the variance and spatial distribution of SIFs over the entire MEA and signal average them at each location (Figure 5.4B). This re-

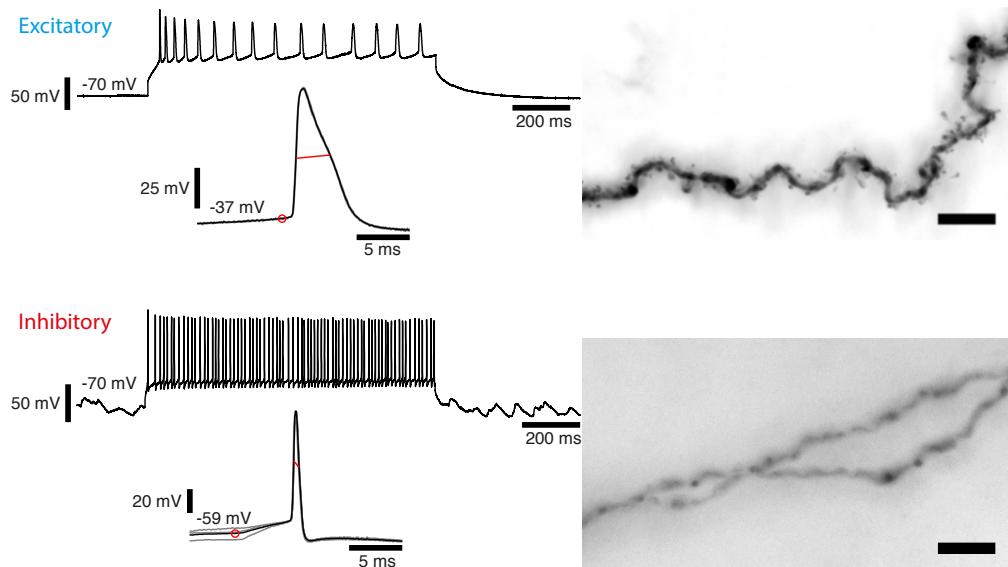


Figure 5.5: Top row shows the electrophysiological and morphological characterization of the patched LII cell shown in this chapter. Cell shows clear excitatory cell characteristics. High current injection (400 pA) leads to a spike train with increasing interspike interval (adaptation ration 0.25). Action potential shape analysis shows a AP half width of 3.2 ms. Biocytin staining reveals densely spiny dendrites. Scale bar 10 μ m.

Bottom row shows the electrophysiological and morphological characterization of the patched LI cell shown in this chapter. Cell shows clear inhibitory cell characteristics. High current injection (325 pA) leads to a high frequency spike train with decreasing interspike interval (adaptation ration 2.4). Action potential shape analysis shows a AP half width of 0.5 ms. Biocytin staining reveals smooth aspiny dendrites. Scale bar 10 μ m.

vealed that amplitudes (and sometimes shapes, see below) varied over space, and that electrodes in the array with detectable SIFs (corresponding to a specific unit spike) were not randomly distributed, but rather usually formed a contiguous field.

By analyzing SIFs associated with hundreds of isolated units, we identified by eye two broad classes defined by SIF polarity (5.4A). We will show below that each originates from either inhibitory or excitatory neurons. We will thus call positive and negative SIFs I and E respectively. To assess the range of SIF waveforms more systematically, we selected SIFs triggered by unambiguously sorted units from the same recording session, and measured their pairwise correlations (Pearson correlation). We ran an unsupervised clustering algorithm on these correlations. The resulting, ordered correlation matrix for a dataset combining two recording sessions (92 units, based on high SNR) is shown in Figure 5.4C. Three unambiguous clusters could be identified, from which three average templates could be extracted (normalized waveforms, Figure 5.4D). Two matched the E and I waveforms initially identified by eye (red, blue; compare to Figure 5.4A). The third template (yellow) was biphasic, with an initial negative peak coinciding

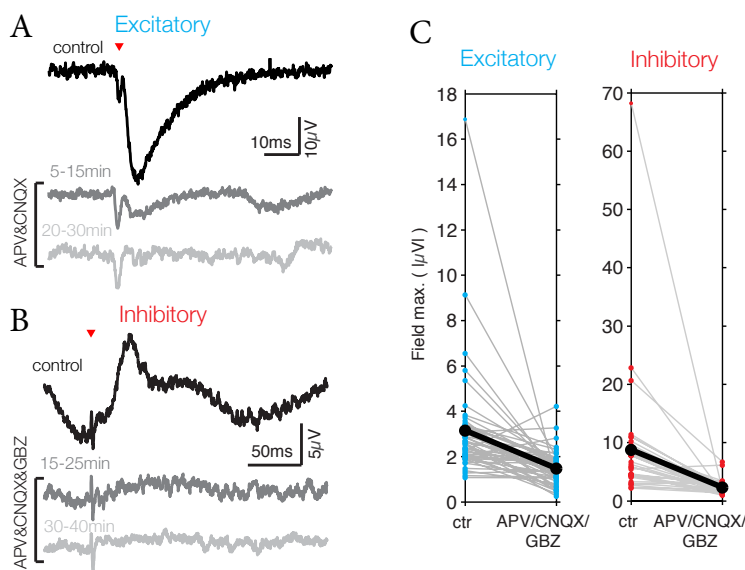


Figure 5.6: **A.** Trace of one MEA electrode averaged over spikes induced by current injection in a patched pyramidal cell. Alignment to peak of intracellular spike (red triangle). Top trace (black, $n=30$ spikes) in control conditions, with large negative SIF. Middle trace (dark grey, $n=50$ spikes) 5 to 15 min after bath application of APV ($75\ \mu\text{M}$) and CNQX ($20\ \mu\text{M}$) with reduced SIF. Bottom trace (light grey, $n=38$ spikes) 30 to 40 min after bath application of APV and CNQX. SIF is abolished while action potentials are unaffected, demonstrating that SIFs are extracellular signatures of postsynaptic currents. **B.** Same as in D but for a LI inhibitory neuron, additionally including $5\ \mu\text{M}$ gabazine in the bath. **C.** Population data showing SIF dependence on pharmacological blocking in sorted units of one experiment. Every unit was categorized as either excitatory (left plot) or inhibitory (right plot). Maximum SIF amplitude for every unit before (ctr) and after blocking postsynaptic receptors with APV ($75\ \mu\text{M}$), CNQX ($20\ \mu\text{M}$) and Gabazine ($5\ \mu\text{M}$).

approximately with that for E, and a positive waveform similar to the I template, with a 10 ms delay. One can easily see that the biphasic waveform is well fitted by the sum of the E and I waveforms with a short delay between them, thus corresponding to a putative excitatory neuron whose APs trigger the firing of postsynaptically connected interneurons (M.SI.).

If as we suspected, SIF polarity indicates neuron type (E or I), we wanted to compare the potential reliability of this measure to the action potential half-width, a common electrophysiological index to estimate neuron type. Although spike widths were, as for mammals shorter on average for interneurons than for principal cells, there was considerable overlap between the distributions. Classification using SIFs by testing this on units with unipolar SIFs, we observed that SIF templates allowed unambiguous cluster separation, which thus confers a significant advantage (Figure 5.4E). A second advantage of SIFs is that, by virtue of their lower frequency content, their spatial decay should be less than for action

potentials (M.SI).

To test that the polarity and shape of SIFs indeed reflected synaptic release in the proximity of each extracellular electrode, we patched individual excitatory and inhibitory neurons (identified electrophysiologically and post hoc by staining and morphological analysis, see Figure 5.5) in a cortical slab preparation and assessed the effects of pharmacological blockers on the spike-triggered events (see methods 2.3.4). Within 20 minutes (note that the cortex is intact and not sliced), superfused NMDA and AMPA receptor blockers (APV, CNQX) entirely abolished the negative SIF caused by identified pyramidal neurons, and gabazine abolished the positive SIF caused by identified inhibitory interneurons (Figure 5.6A and B). The same effect is visible on all channels of the MEA, where the pharmacological block of synaptic receptors abolished the fields, while the high frequency spikes remained unchanged (Figure 5.7 and 5.8). In total I patched 8 LII excitatory cells and 5 LI inhibitory cells. All of the excitatory cells showed negative deflecting SIFs. Of the LI cells 2 showed SIFs, both deflecting positively. The failure of 3 LI inhibitory neurons to show SIFs is probably explained by the distance of these cells from the MEA.

In a subset of these patched cells (4 excitatory and 2 inhibitory) APV+CNQX and Gabazine were added respectively abolishing the fields of all tested cells. Population data for both excitation (APV+CNQX) and inhibition (gabazine) are shown in Figure 5.6C.

neuron type	SIF	spike	drugs
LII pyramid	8/8	6/8	4/4
LI interneuron	2/5	3/5	2/2

Table 5.1: Numbers indicate the total number of excitatory and inhibitory cells patched in an effort to substantiate claims with SIFs of known origins. Furthermore the number of experiments with pharmacological blocking of synapses. For each also the experiments where SIFs and spikes induced in the patched cells were visible and pharmacology abolished the fields.

We conclude that SIFs are the expression of postsynaptic currents caused by spikes travelling along each neuron's axon and thus that they could reflect the path of these axons in the tissue. Because the nature of these potentials makes them often easier to detect than axonal action potentials, they might allow one to estimate the axonal projection field of individual neurons, and this in parallel with all sortable units. This hypothesis will be tested below. Because some

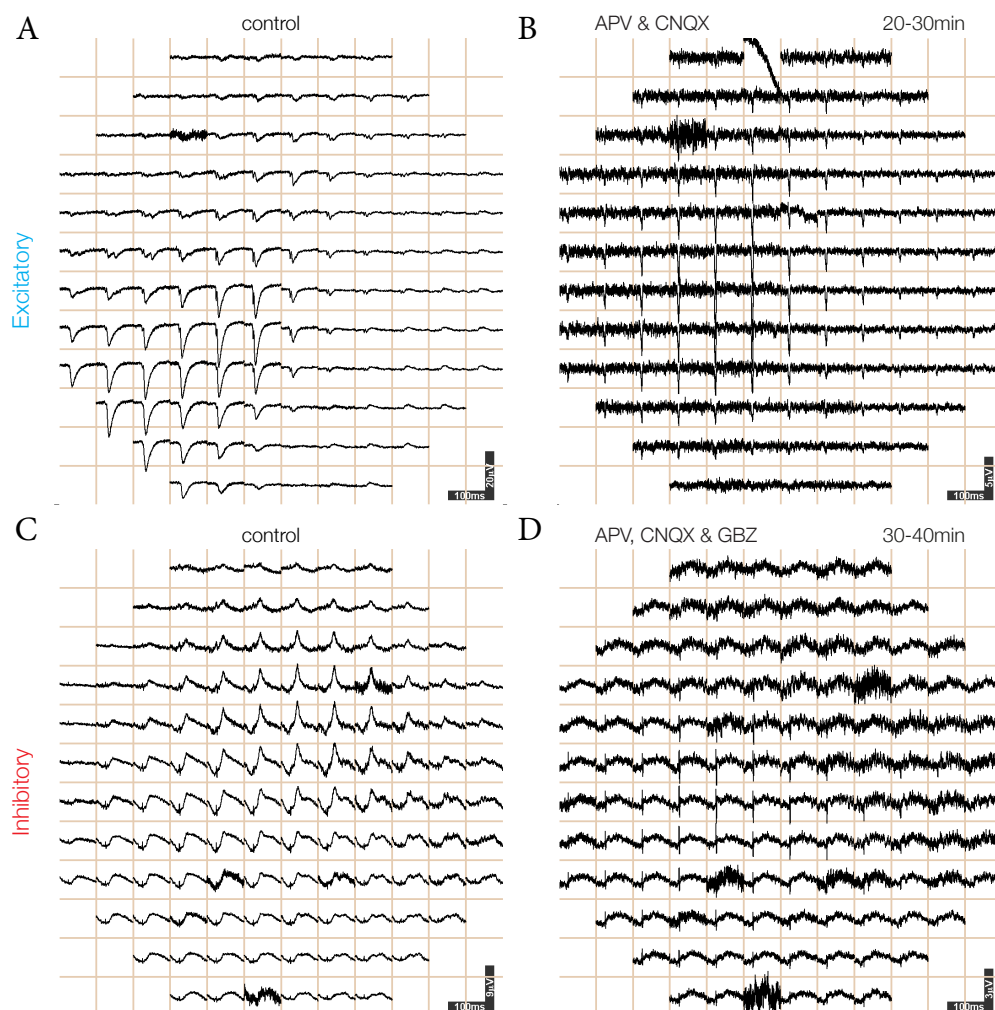


Figure 5.7: Broad band 120-channel MEA traces averaged over all current induced spikes of two cells in WPCP. Traces arranged to reflect the physical arrangement of MEA recording electrodes. **A.** Patched LII excitatory cell in control conditions. Notice the large negative amplitude slow field (SIF) following the induced spike at 20 ms of each contact's trace. **B.** Same cell as in A. but 20 to 30 min after application of APV ($75 \mu\text{M}$) and CNQX ($20 \mu\text{M}$). Spike is still visible, but the field is abolished confirming that SIFs are signals of postsynaptic currents induced by the spike in the presynaptic cell. **C.** Same as in A but a patched LI inhibitory cell in control conditions with a SIF of positive polarity. **D.** Same cell as in C. but 30 to 40 min after application of APV ($75 \mu\text{M}$), CNQX ($20 \mu\text{M}$) and Gabazine ($5 \mu\text{M}$). Spike is still visible, field abolished.

units triggered reliable biphasic SIFs (by temporal summation of an EPSP and a delayed IPSP), we infer that single action potentials from some excitatory neurons are often sufficient to evoke an action potential in one or more postsynaptic interneurons. This has been confirmed from patch recordings (M.H., not shown).

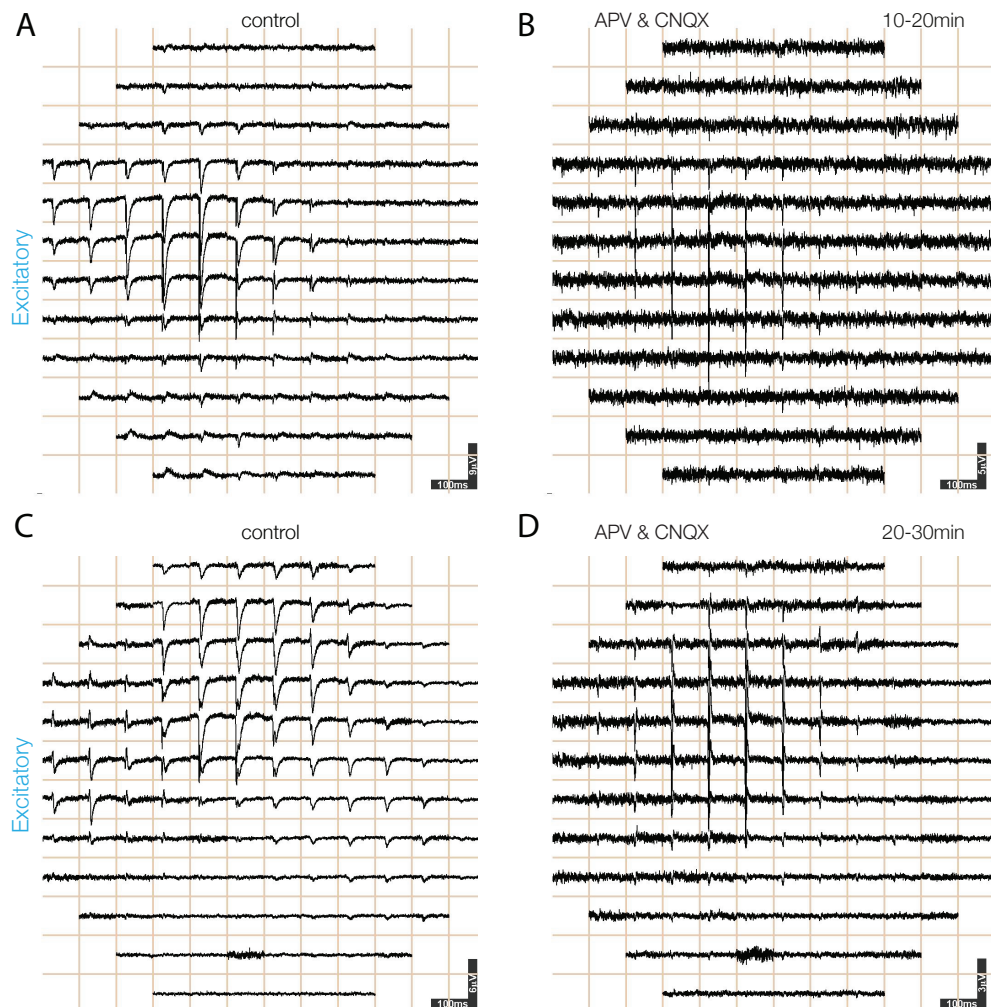


Figure 5.8: As Figure 5.7 for two further patched LII excitatory cells (spike count: A, 558; B, 318; C, 640), D 1031 spikes). All in control conditions and after adding superfusion of APV (75 μ m) and CNQX (20 μ m).

5.4 Estimating neuronal morphology from SIFs

The observations that SIFs are signatures of currents caused by synaptic release and that their spatial distribution is broad and largely contiguous suggested that SIFs might reflect functional axonal architecture. They might thus enable one to track some aspects of a neuron's anatomical projections. While spike signals could in principle be used for the same purpose, as in the retina (Litke et al., 2003; Li et al., 2014; Li et al., 2015), extracellular detection of axonal spikes in cortex, a thicker and electrically noisier structure, fails for the majority of sorted units (M.SI., data not shown). In addition, SIFs indicate the existence of post-synaptic currents rather than action potential transit, and thus reflect connectivity.

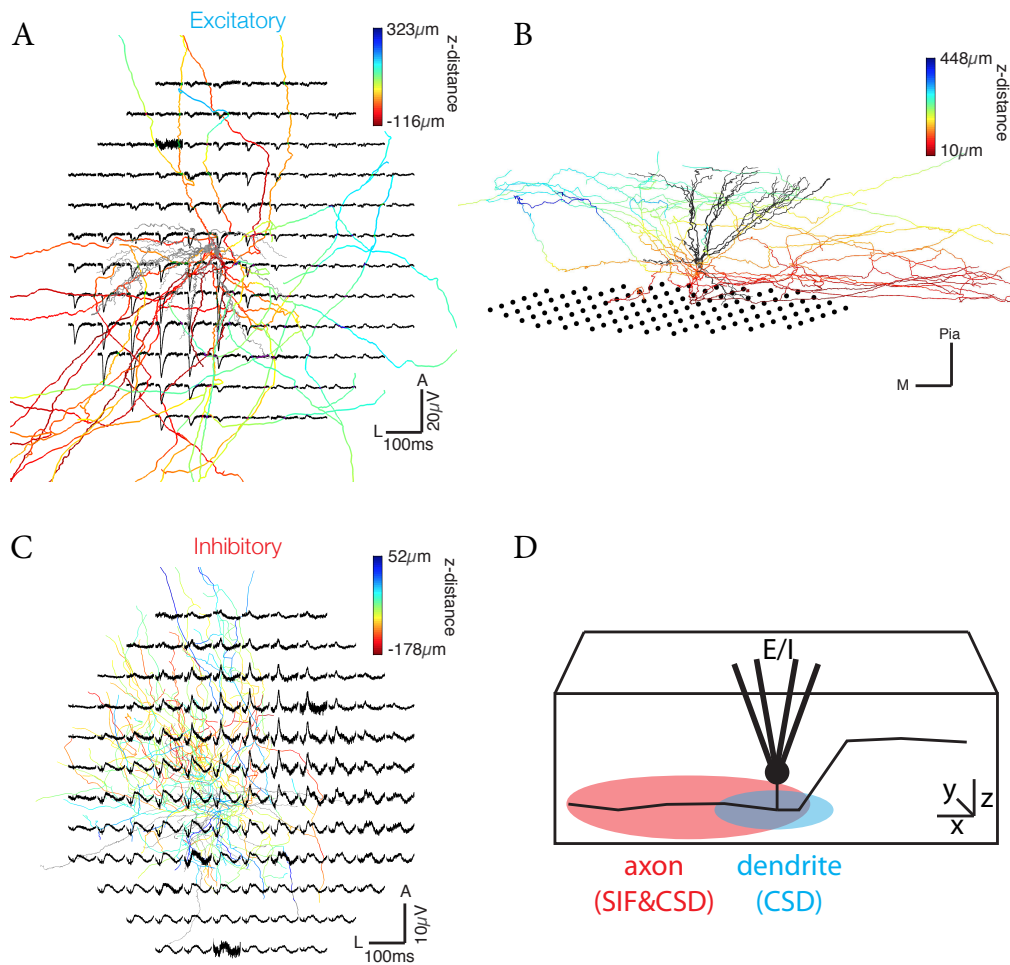


Figure 5.9: **A.** Reconstruction of a biocytin stained pyramidal cell overlaid with the broad band MEA traces averaged over all current induced spikes of that cell. The reconstruction was placed and morphed so that its cell body (grey), dendrites (grey) and axonal arbor (colored) are positioned as during the experiment (see section 2.5.6). The axon is color-coded for z-distance from the cell body (0 is in the middle of LII, negative values towards ventricle, positive towards pia). Note how the SIF amplitude correlates with the density and z-position of axonal projections. **B.** Same reconstructed pyramidal cell (black cell body and dendrites, colored axon) overlaid on the MEA as in A, seen from the side with a slightly elevated (towards pial side) point of view. Medially projecting axonal branches (towards the left) are located in layer I several hundred micrometers from the electrodes, the presumed reason, why no SIFs can be seen medial of the cell in A. **C.** Same data as in A. but for an interneuron of Layer I. **D.** Available information about each individual unit sorted from extracellular electrophysiological data. Soma position by spike amplitude triangulation, cell class classification (E or I) based on SIF polarity, deep layer axonal projection based on SIF distribution, dendrite location based on current source density analysis (CSD) of pre-spike signal distribution.

To examine this issue, I recorded from and stained individual neurons (Figure 5.5) with a WCPC and aligned their reconstructed 3D anatomy (reconstruction by M.H.) with the electrical footprint they had left on the MEA array during record-

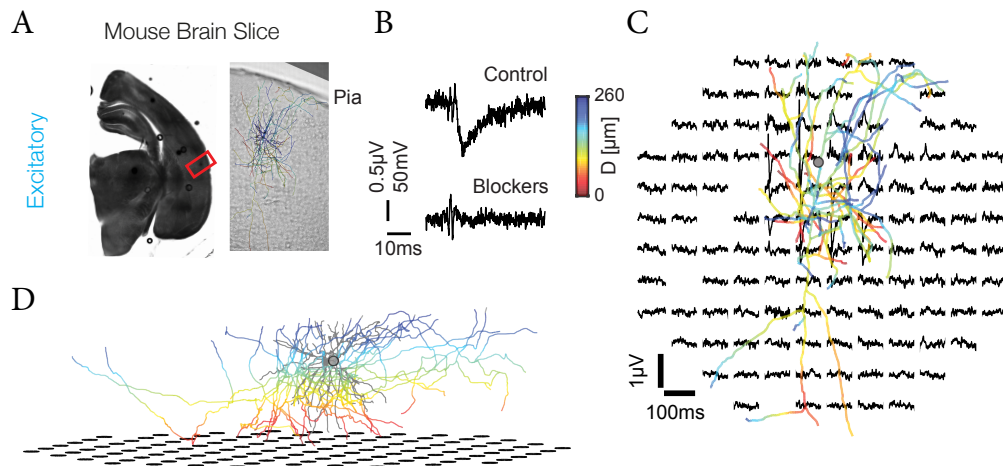


Figure 5.10: Planar perforated MEA and patch-clamp recording of excitatory cell in slice of mouse temporal association cortex. **A.** Bright-field image of frontal brain slice (dorsal to top, lateral to right). On right, zoom-in of red box. Note soma in L2 and axonal arborizations. Color corresponds to depth in the slice (red, close to MEA). **B.** SIF from one electrode before and after application of synaptic blockers. **C. & D.** Overlay as in Figure 5.9A.

ing. The precise post hoc physical registration of anatomical reconstructions was carried out after tissue fixation and histological processing and imposed several additional steps. These are detailed in section 2.5.6. An example of such an alignment is shown in Figure 5.9A for a pyramidal neuron with soma in L2 (soma and dendrites are depicted in grey; axons are color-coded by depth). We focus on this particular neuron because its 3-dimensional axonal structure was particularly favorable to a clear interpretation. An example of a LI interneuron is shown in Figure 5.9C. We observed a good qualitative agreement between axon density and SIFs in the bottom left quadrant of the MEA (Figure 5.9A), where the axon collaterals lay closest to the MEA, i. e. , within layer 3 (red). Axon collaterals located towards the middle of layer 1, however, were not matched by expected SIFs on the MEA. This suggested that the value of SIFs for estimating axonal territories might depend critically on source depth within cortex. Could this be quantified?

The analysis of local dendritic or axonal field potentials in nervous tissue is complex because axons trace complicated paths in space, because synapse distribution and synaptic current density along each axon collateral is unknown, and because accurate models for the spatial distribution of associated currents do not exist for this cortex. We thus examined the issue by generating three plausible models, applied them to a reconstructed neuron, and compared the estimated SIFs to those recorded experimentally. In all three models, we assumed that postsynaptic receptor distribution is continuous along all axon collaterals, and segmented

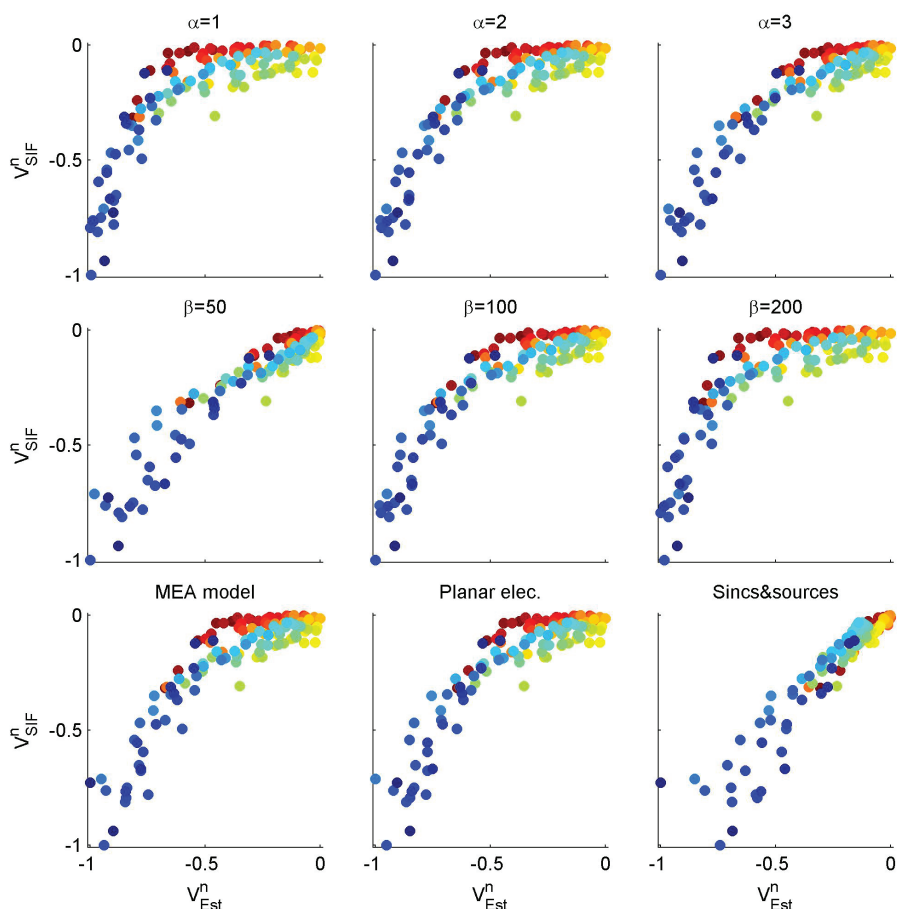


Figure 5.11: Volume conduction models. Data from 5.9A, modeling by M.SI..

the axons into short compartments ($10\ \mu\text{m}$), each treated as a point source. The three models differed in their assumptions about isotropy and uniformity of conductances, boundary conditions, and electrode model (point or plane). Plots of estimated vs. measured peak SIF amplitude for the three models (Figure 5.11) indicated good fit (M.SI.).

To test whether these results are general and not specific to reptilian cortex, I repeated the experiments with frontal slices of P31 mouse cortex (Figure 5.10). I identified SIFs in mouse L2/3 pyramidal neurons in temporal association cortex that disappeared following synaptic block (Figure 5.10B) and matched axonal arborizations near the MEA (Figure 5.10C&D). I also observed return currents consistent with the orientation of layer 2/3.

5.5 Cellular features from MEA signals

The previous sections showed the possibility to use the SIF to extract information about the deep axonal projections of a neuron. We thus combined the analysis of axonal projections over the MEA surface with the estimate of soma position to define for each recorded neuron a mean axonal projection vector in the x,y plane. After fitting a best-fit envelope (polynomial) to the recorded SIFs and calculating soma position from the AP waveforms, this vector was calculated by linking soma to the center of the projection envelope. The recorded pyramidal cell of Figures 5.7A and 5.9A illustrates well the bias of the SIFs in comparison to the action potential. It would have a vector towards postero-lateral (bottom-left quadrant on the recording array). This is however not limited to single patched neurons but can be extracted for every neuron recorded with extracellular electrophysiology and sorted in an isolatable unit.

If we now review all the results of this section, what answer can we give to our initial question? Namely how much information can we extract about each individual neuron we record with extracellular electrophysiology (Figure 5.9D)?

1. Soma position. The distribution of the spike amplitude on the recording electrodes of the two-dimensional electrode arrays allows to triangulate the absolute location of the spike source in x and y and relatively also in z. The high-frequency spike amplitude undergoes an exponential decay with an experimentally determined spatial decay constant of 35 μm (section 5.2).
2. Neuron identity. We found slow fields following spikes (SIFs). These SIFs are extracellular signatures of postsynaptic currents induced by the spike. Thus excitatory cells and inhibitory cells evoke SIFs of opposing polarity, allowing one to classify the recorded units into excitatory and inhibitory neurons (section 5.3).
3. Axonal projection. Because the SIF reflects postsynaptic currents and because postsynaptic currents are evoked at sites where the axon of a sorted cell makes synaptic contact, the distribution of SIFs on the recording electrodes of the two-dimensional electrode array allows one to track the deep-layer axonal projections of each isolated unit (section 5.5).
4. Dendritic tree. In addition to the slow fields following an action potential one can often also observe slow fields preceding a spontaneous action potential. Preliminary data indicate that these fields originate from EPSCs in

the dendrite of the sorted unit, depolarizing the cell over spike threshold. Current source density analysis of the signal distribution on the MEA thus also allows one to estimate the location (xy projection) of the cell's dendrite (not shown).

In a typical 48 h recording session with a 250-channel MEA covering 2 mm² of dorsal cortical tissue more than 1000 units can be isolated. For the majority of these cells we can assign soma position, identify whether the unit is excitatory or inhibitory, extract its deep-layer axonal projections and the position of its dendrite. We can thus record responses of hundreds of well characterized neurons to realistic sensory stimulation in an *ex vivo* preparation with attached sensory organs and an intact neuronal network from the sensory organs to the hippocampus-like medial cortex.

Chapter 6

Dynamical activity in cortical circuits

Periodic brain activity also called neuronal oscillations and spatiotemporal brain activity such as wave-like propagation of neuronal activity are ubiquitous phenomena in neural systems (see sections 1.3.4, 1.2.4). Oscillations are inherent to recurrent neural networks and observed in a wide range of frequencies, brain states, species, and brain regions (Adrian, 1950; Vanderwolf, 1969; Gray and Singer, 1989; Gelperin and Tank, 1990; Kreiter and Singer, 1992; Laurent and Naraghi, 1994; Fries et al., 2001). Similarly travelling waves are an emergent property known in various sensory systems as well as in hippocampus (Ermentrout and Kleinfeld, 2001; Lubenov and Siapas, 2008; Massimini et al., 2004; Sato et al., 2012; Lubenov and Siapas, 2008). The abundance of the two phenomena suggests physiological significance. Accordingly the effort of the neuroscience community to uncover functional significance, algorithmic utility or mechanistic implementation of these intriguing activity patterns has been substantial (Klausberger and Somogyi, 2008; Lasztozci and Klausberger, 2014; Hu et al., 2014). Still we lack a clear understanding, especially so in cortical circuits.

The work described in the previous chapters established methods and tools to investigate neurophysiology in isolated brain preparations of turtles. These include *ex vivo* whole-brain preparations with attached sensory organs and the cortical slab preparation, the first keeping intact the processing cascade from sensory periphery to central circuits, the other the intra-cortical network. I also described the experimental strategy of combining high density MEA recordings and the parallel whole-cell patch-clamp technique (WCPC) to monitor activity in these intact preparations (chapter 5). The possibility to use recombinant viral vectors to deliver genes of interest allows shaping of neuronal activity using optogenetics (chapter 4). All of these advances were combined to elucidate neuronal oscilla-

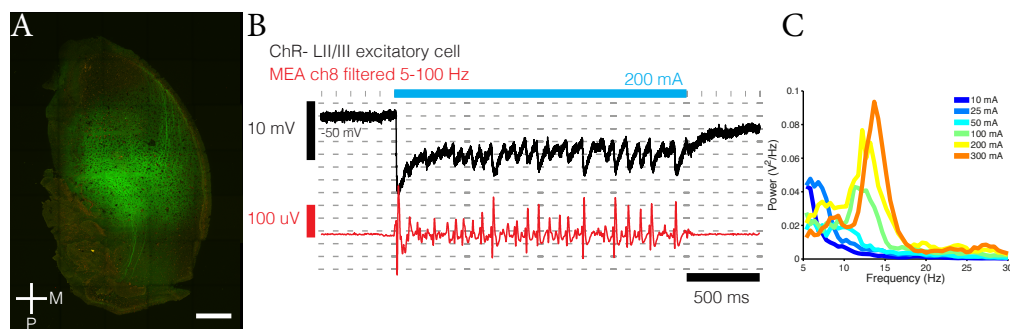


Figure 6.1: **A** Ventral side of a cortical slab (anterior up, lateral left) with visible Chr2(H134R)-GFP (green) expression under a CaMKIIa promoter. Scale bar 1 mm. **B** Upon light stimulation (200 mA, blue bar) temporally patterned activity can be observed in single trials by extracellular LFP recording from the pial side (red trace) and in the subthreshold activity of a patched Chr2- LII/III pyramidal cell (black trace). Temperature 25 °C. **C** Power spectra of the intracellular trace of the Chr2-negative LII/III pyramidal cell upon light stimulation with different light intensities (calculated between 0.5 to 2 s of the stimulus, 10 to 300 mA). Both peak frequency and power increase with increasing light intensities. At peak light intensity of 300 mA the oscillatory frequency peaks around 13.7 Hz.

tions and travelling waves, which are also observed in the turtle dorsal cortex (Prechtl, 1994; Prechtl et al., 1997; Prechtl et al., 2000; Senseman and Robbins, 2002; Schneider, 2015): upon visual stimulation, a frontal region of dorsal cortex exhibits 20 Hz oscillation both in awake animals and *in vitro* preparations (Figure 1.9). In *ex vivo* preparations visual stimulation also elicits travelling waves in the same area. This chapter describes an early effort to investigate the mechanistic implementation of these dynamics in a simpler cortical structure.

I placed injections of AAV carrying Chr2(H134R) under a CaMKIIa or CAG promoter in the dorsal cortex of turtles and 4 - 6 weeks later carried out experiments in cortical slab preparations isolated from these animals (*Trachemys scripta elegans*, *Chrysemys picta bellii*; see methods 4.1.1, 4.1.5 and 2.4). Intact networks are a prerequisite to allow network phenomena such as oscillations to arise. Recordings with MEAs and multiple parallel whole-cell-patch-clamp were performed, while controlling activity of the Chr2-expressing neurons with light stimulation (section 2.4.1). This allowed for precision in monitoring neuronal activity together with reproducible induction of neuronal dynamics. Optogenetic stimulation is evidently not a natural stimulus, but the resulting activity was nonetheless a useful starting point to investigate this activity.

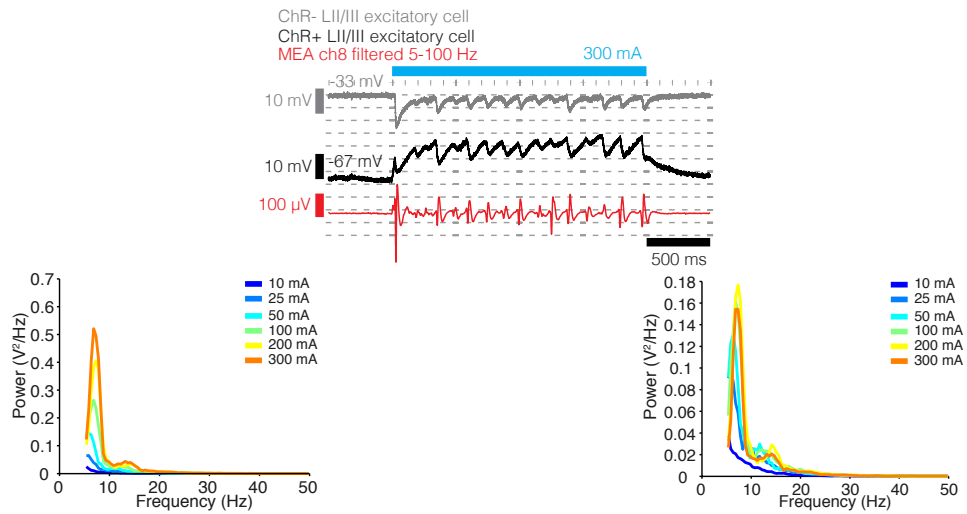


Figure 6.2: Parallel double WPCP recording of one ChR2- (grey) and one weakly ChR2+ excitatory cell (black) in the same configuration and in the same cortical slab as in Figure 6.1. Cooling the preparation to 16 °C resulted in a reduction of peak frequency to around 7 Hz. Notice the difference in peak power between the weakly ChR+ (lower left) and the ChR2- (lower right) excitatory cell.

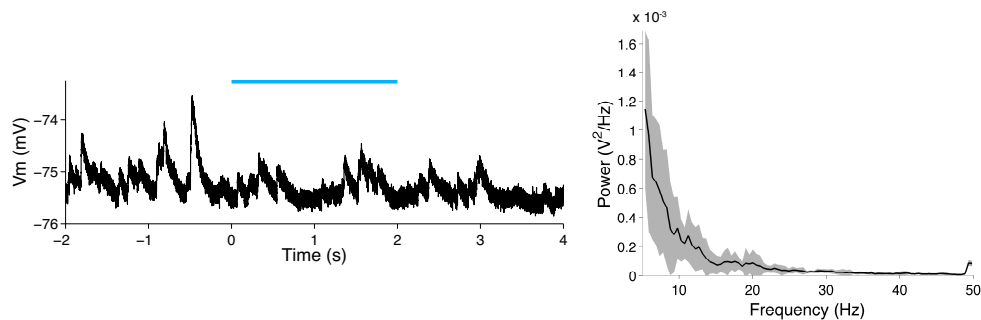


Figure 6.3: WPCP recording in the same configuration as above in a cortical slab after the same injection and preparation procedure as in Figure 6.1 but with a virus carrying EGFP instead of ChR2. Left panel, intracellular activity (black trace) is not impacted by light stimulation (blue bar). Right panel, power spectrum of the intracellular activity during light stimulation shows no peaks.

6.1 Controlling activity with light

Can we optogenetically induce neuronal oscillations in the isolated turtle cortex? When shining light on a cortical slab which expresses ChR2 under CaMKIIa promoter (hence in the excitatory neurons), both the LFP and intracellular sub-threshold activity in a channelrhodopsin-negative cell show time-locked rhythmic activity (Figure 6.1 A, B). The frequency and power of these oscillations increased with increasing light intensity and oscillation frequency at maximal light intensities (driven with 300 mA, see Figure 2.2) typically peaked around 14 Hz (Figure

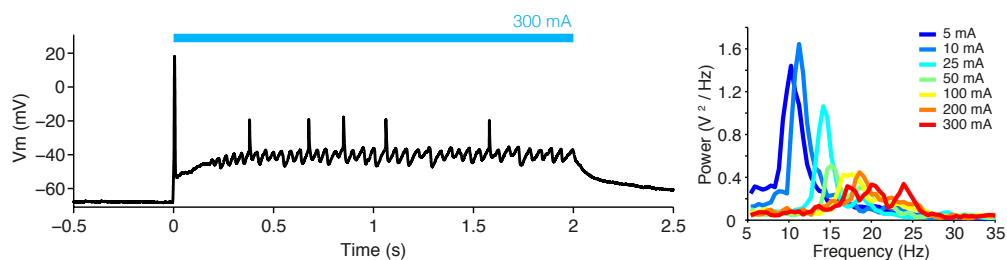


Figure 6.4: Left: Example voltage trace of a Chr2-positive excitatory cell in a slab expressing Chr2 under the CAG promoter during 300 mA light stimulation (blue bar). Right: Frequency spectra of the V_m of the patched cell at different stimulation light intensities. Notice the peak frequencies around 20 Hz in the range of natural cortical oscillations upon visual stimulation.

6.1C). Oscillation power of sub-threshold activity was greater in Chr2-expressing cells. This is due to the depolarizing effect of Chr2-current resulting in greater driving force for GABA-mediated chloride influx (Figure 6.2). The frequency of oscillations also depended on temperature. Cooling the slab of Figure 6.1 to 16 °C, 300 mA light resulted in oscillations with a peak frequency at around 7 Hz (Figure 6.2).

To rule out light-related artifacts, the same experiment was performed in the cortical slab of a turtle infected with AAV carrying EGFP instead of channelrhodopsin. Here the light has no effect on the activity of the network (Figure 6.3). Oscillations also occurred if channelrhodopsin was expressed in all cell types by using an ubiquitous CAG promoter (Figure 6.4 shows one such example of a slab with Chr2 expression under the CAG promoter, with 20 Hz oscillations). The network thus exhibits robust oscillatory activity irrespective of the precise depolarizing drive to inhibitory interneurons.

6.2 Activity by cell type

We next tried to assess the role of the different cell types in these oscillations. To this end a total of 42 neurons (29 pyramidal neurons, 13 interneurons) in 13 slabs expressing Chr2(H134R) under the CaMKIIa and CAG promoter of 7 turtles were patched and responses to light stimulation were analyzed. MEA recordings from the pial or ventricular side of the slab were performed in parallel with patch recordings. The results reported below concern both experimental situations, slabs expressing under CaMKIIa or CAG promoter, unless otherwise indicated.

6.2.1 LII/III Pyramidal cells

The membrane potential (V_m) of ChR2-negative (ChR2⁻) excitatory cells hyperpolarizes about 20 ms after the onset of a 2 s light stimulus. After 100 to 300 ms V_m begins to oscillate (section 6.1, Figures 6.1, 6.2, 6.4), with sharper hyperpolarization than depolarization, suggesting periodic IPSPs. The majority of ChR2⁻ pyramidal cells ($n = 8/9$) lacked initial depolarization at the onset of the stimulus, which would be expected were they to receive inputs from ChR2⁺ cells firing APs at the onset of the stimulus.

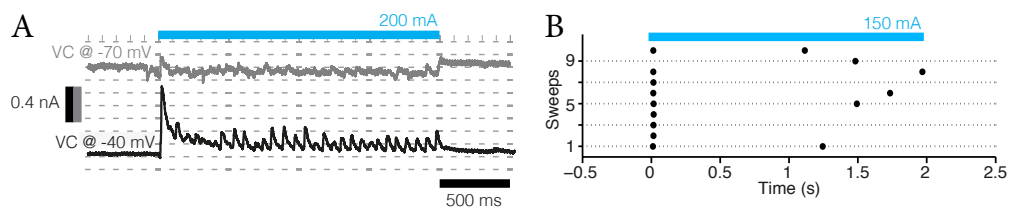


Figure 6.5: **A** An exemplary ChR2⁻ excitatory cell from the LII/III border recorded in voltage-clamp mode during light stimulation (blue bar). The V_m is clamped to -70 mV (the reversal potential for chloride, grey trace) and to -40 mV (black trace) to differentiate EPSCs from IPSCs. No clear EPSCs are visible in this cell as in all other tested excitatory cells. **B** Spike raster of a typical ChR2⁺ pyramidal cell. Cell fires at the onset of the light stimulation and in sparsely in a subset of oscillation cycles.

The membrane potential of ChR2-positive (ChR2⁺) excitatory cells was depolarized immediately after onset of the light stimulus, followed by sharp hyperpolarization about 10 ms later. A sustained oscillation, consisting of periodic IPSPs, has the same characteristics as for ChR2⁻ cells but with higher oscillatory power in the 10 to 15 Hz range (section 6.1, Figure 6.2). Cells which express ChR2(H134R) strongly (assessed from fluorescence intensity) fired a few action potentials after light onset (15.7 ms, std = 1.4 ms) and in a fraction of cycles of the sustained oscillations ($n = 13/17$) as seen in Figure 6.5B.

Voltage-clamp recordings allowed me to distinguish better excitatory post-synaptic currents (EPSC) from inhibitory ones (IPSC). During successful patching IPSCs were typically invisible when keeping the membrane potential between -70 to -75 mV, I thus chose -70 mV as an approximative reversal potential for chloride. Holding the cell at this potential allows to isolate EPSCs, whereas holding the cell at $V_m = -40$ mV results in a compound PSC. Due to the reduced access resistance in ChR2⁺ cells during light stimulation caused by the open ChR2-ion channels, however, space clamp issues made it difficult to hold the cell at the desired V_m .

Interestingly of the 9 ChR2- pyramidal cells which were recorded in VC, 6 lacked any EPSCs during oscillations, 2 received sparse and weak EPSCs, and one only received significant rhythmic excitation. Thus V_m oscillations seemed to be caused primarily or exclusively by the rhythmic IPSCs, time-locked to the global oscillation, measured as a field potential.

Together the voltage-clamp data, the lack of initial depolarization in ChR2- cells and the observed dominance of I over EPSC(P)s suggest the dominant drive to pyramidal cells is from inhibition during light-induced oscillations.

Parallel patching of pairs of pyramidal cells showed that these inhibitory events are highly correlated across pyramidal cells (cross correlation peak at 0.9) with 0 ms time lag (see below in section 6.3 and Fig6.12).

6.2.2 LIII Interneurons

Interneurons in layer III ($n = 8$) showed a different pattern of light-evoked activity. Fifteen to 22 ms after light onset (200 mA, 2 s), a LIII interneuron V_m depolarizes strongly and typically fires an action potential (Figures 6.6, 6.8). This AP is followed by periodic depolarizing potentials, synchronized to the LFP (MEA recording) (Figure 6.7). Voltage-clamp data showed that some neurons receive only rhythmic EPSCs ($n = 4$, Figure 6.6), while others receive both rhythmic EPSCs and IPSCs ($n=2$, Figure 6.7).

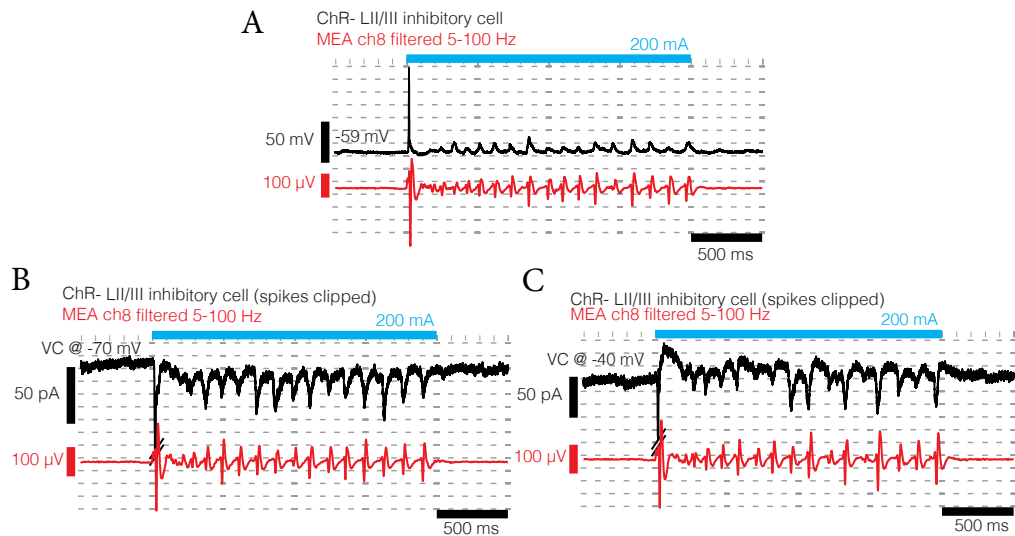


Figure 6.6: **A** Black trace shows a current-clamp patch recording of a LIII interneuron, red trace the extracellular LFP recording of one electrode of the MEA from the pial side of the slab. Blue bar denotes 200 mA light stimulation. Upon light stimulation the interneuron fires an action potential at short latency, and when the LFP shows steady oscillatory activity the interneuron's subthreshold V_m depolarizes rhythmically. **B** Same interneuron and configuration, recording in voltage-clamp mode. The V_m is clamped to -70 mV, the reversal potential for chloride, allowing to isolate EPSCs. The trace shows clear temporally patterned EPSCs. **C** As in B, but the V_m is clamped at -40 mV. Temporally patterned EPSCs but no IPSCs visible.

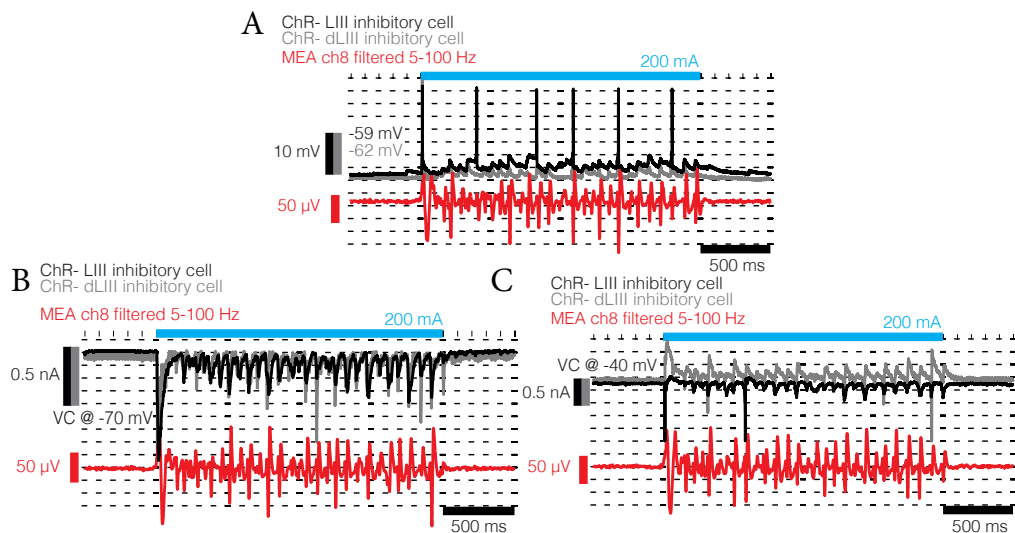


Figure 6.7: Parallel patch-clamp recordings of two LIII interneurons. **A** Current-clamp recording shows both cells firing an initial action potential after 12 ms, then depolarizing rhythmically with one cell (black trace) firing action potentials in a fraction of cycles. LFP recording from the pial side of one MEA channel (red trace). **B** Parallel voltage-clamp recording, where the cells' V_m is clamped at the reversal potential for chloride (-70 mV), shows both cells receiving rhythmic EPSCs. **C** Same as in B, but V_m clamped at -40 mV shows one cell (black trace) receiving no significant IPSCs, whereas the other (grey trace) does receive inhibition following the EPSCs.

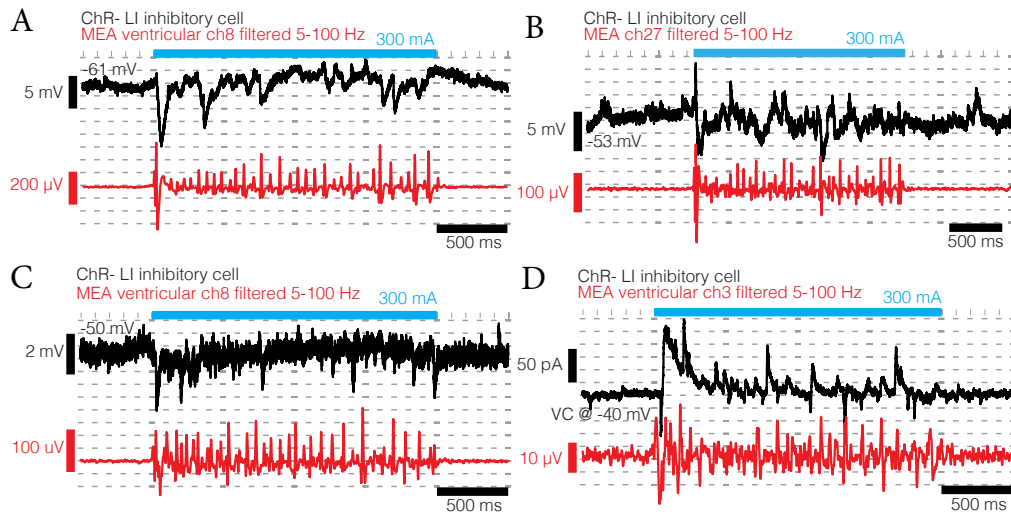


Figure 6.9: Patch-clamp recordings of three LI interneurons (in 3 slabs of 2 turtles) and parallel MEA recording from the ventricular side of the slab. **A-C** Current-clamp recording shows increased activity during light stimulation (blue bar) but no clear oscillations in the subthreshold V_m of the three cells. This is despite the strong oscillatory activity in the LFP measured by the MEA (red traces). **D** Recording from another neuron in the same slab as in C. Voltage-clamp recording, with the V_m clamped to -40 mV. Activity correlated with LFP trace from MEA, but weaker than for the cells of LII/III (see for example Figure 6.7).

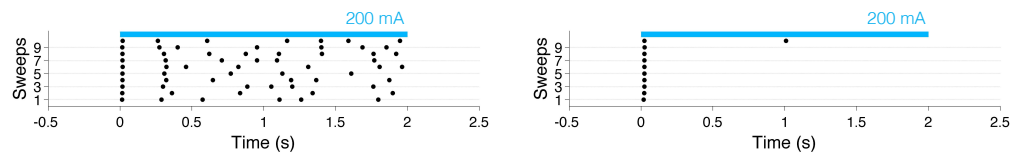


Figure 6.8: Two exemplary LIII interneurons during 10 repetitions of light stimulation trials (blue bar). Some cells as the one on the left fire in a fraction of oscillation cycles. All patched LIII interneurons however fire a spike at the onset of light (after 15 to 22 ms).

6.2.3 LI Interneurons

In a few experiments I managed to patch inhibitory interneurons of Layer I ($n = 5$, 4 slabs of 2 turtles) while recording the field potential from the ventricular side of the slabs with a MEA. Despite the LFP showing strong oscillations in 4 of the 5 cases upon light stimulation, none of the LI interneurons exhibited clear oscillations of the V_m (Figure 6.9). Only one cell showed correlations but significantly weaker than LII/III excitatory or inhibitory cells (Figure 6.10).

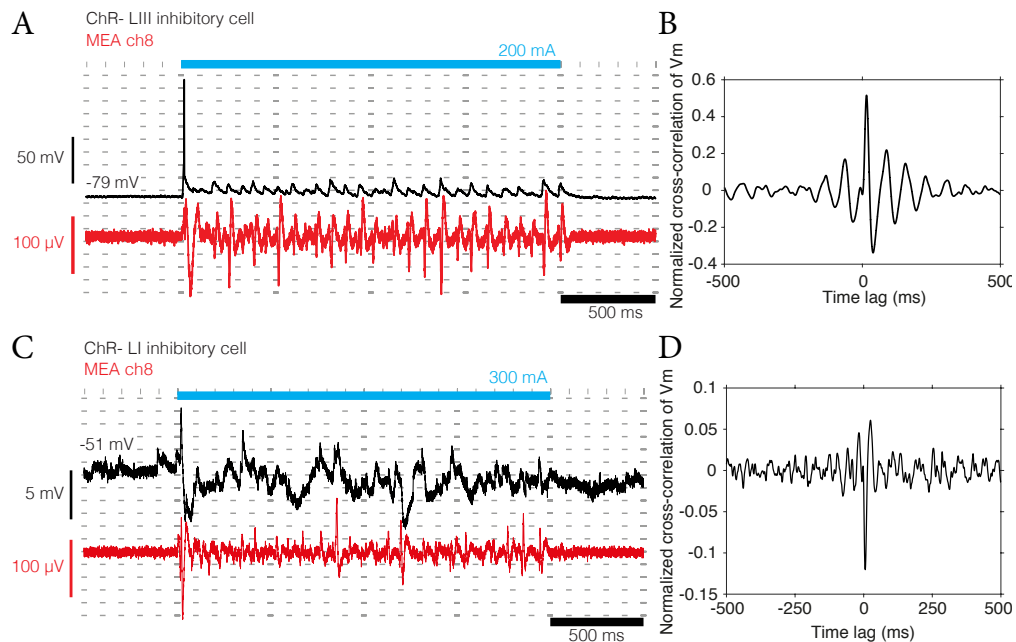


Figure 6.10: Example trials and cross correlations of intracellular and MEA recordings. Data were recorded in two slabs of two animals infected with AAV2/1-CaMKII α -Chr2(H134R). **A** Current-clamp (-80 mV) patch recording of a LIII interneuron (black trace) with parallel MEA recording (red trace) from the pial side of the slab during one stimulation with light (driving current 200 mA). **B** Normalized cross correlation of parallel intracellular V_m and MEA recordings of experiment seen in A. Correlation with a peak of 0.52 at 15 ms. **C** As in A, but intracellular recording of a LI interneuron during light stimulation (200 mA). **D** Cross correlation between cell and MEA seen in C of -0.12 at 11 ms. (6.10).

6.3 Potential circuit mechanism for oscillations

What can we say about the circuit mechanism generating the observed oscillations? As shown in the previous section (6.2) the oscillations of V_m in excitatory cells is primarily caused by rhythmic inhibition. In the majority of LIII interneurons, oscillations were mainly caused by periodic excitation, but some cells also received temporally patterned inhibition. LI interneurons by contrast, did not seem to participate in this light-evoked oscillatory activity.

Simultaneous recordings were made from pairs of LII-III pyramidal cells and from pairs of LIII interneurons in slabs expressing Chr2 under the CamKII α promoter. Membrane potential oscillations were positively correlated with no phase lag if the two neurons were held at the same V_m (Figure 6.12A, B, D). From this I conclude that populations of LII/III excitatory and inhibitory neurons are respectively activated and inactivated simultaneously. To probe the relative timing of these two populations I patched in parallel an excitatory cell at the border of

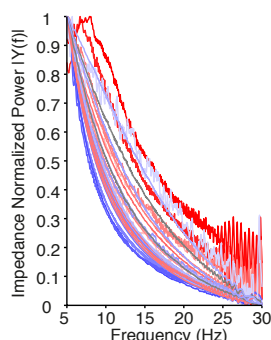


Figure 6.11: Figure shows the power of V_m oscillation in response to frequency sweeps of sinusoidal current injections in 39 patched neurons of 5 turtles (excitatory neurons blue, inhibitory interneurons red). Intrinsic frequency preference of the neurons would be visible by peaks in the frequency response curve. No intrinsic frequency preference can be observed.

LII/III and a deep LIII interneuron. The cross correlation of their V_m during light stimulation was negative around $d_t = 0$, oscillatory, and showed a time lag of -10 ms (Figure 6.12E). The temporal relationship between activity of different neuron classes can be illustrated by calculating an average oscillation cycle (Figure 6.12F). It shows the average V_m of an interneuron (IN) and a pyramidal cell (PC) together with the average LFP, each calculated over all cycles in a total of 20 s of light evoked oscillations: PC depolarization precedes that in the interneurons, which in turn occurs during the phasic PC hyperpolarization- the two phases of this cycle can be seen in the LFP.

Taken together these results suggest a recurrent architecture between the excitatory and inhibitory neuronal populations of LII/III. I showed that during sustained oscillations the ChR+ excitatory neurons and some inhibitory interneurons fire an action potential on the peak of depolarization in a fraction of oscillation cycles (Figures 6.5 and 6.8). The timing of these respective de- and hyperpolarization suggests that a ChR+ subset of the LII/III excitatory cell population is driven over AP threshold with the light stimulation; their APs excite LIII interneurons, of which some are in turn driven over threshold, resulting in a phasic hyperpolarization of the excitatory cell population. LI interneurons though affected occasionally by light-evoked oscillatory activity, do not appear to be involved in the oscillatory activity seen in the lower layers.

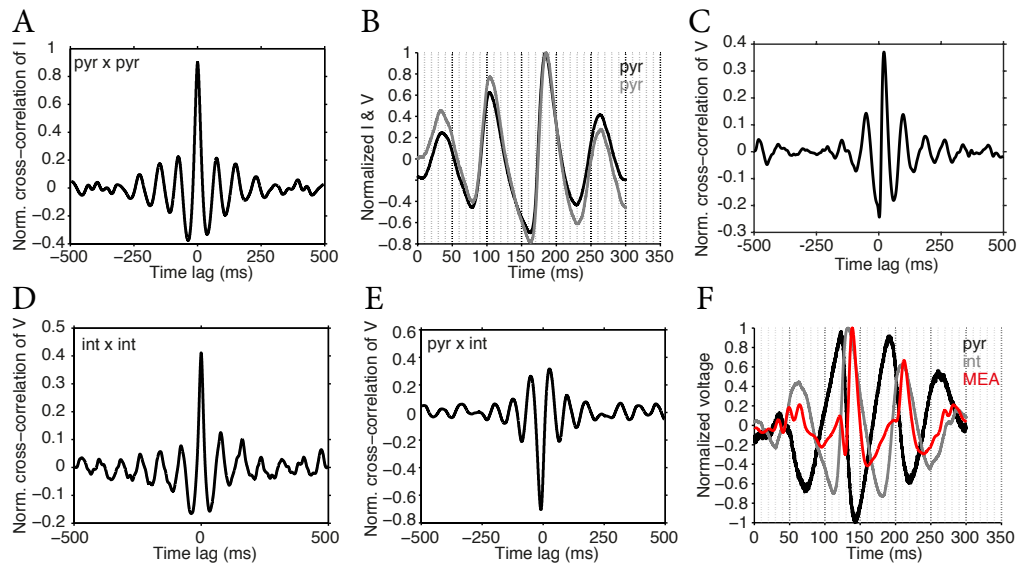


Figure 6.12: Cross correlations of parallel intracellular recordings of cell pairs during 200 to 300 mA light stimulation. All data were recorded in two slabs of one animal infected with AAV2/1-CaMKII α -Chr2(H134R). **A.** Normalized cross correlation of the currents measured in the parallel voltage-clamp (-40 mV) of two excitatory cells. The two cells show almost perfect correlation with a peak of 0.9 at 0.5 ms. **B.** Mean oscillation cycle (see methods 2.3.10 of the same voltage-clamp data as shown in A. **C.** Cross correlation between the V_m of one pyramidal cell and the voltage recorded with one MEA trace, shows correlation of intracellular voltage with LFP. Negative peak of -0.24 at 0 ms, positive peak of 0.37 at 20 ms. Same cell as in A and B. **D.** Parallel current-clamp recording of two LIII interneurons both resting at a V_m of -60 mV. Peak of 0.4 at 0 ms. **E.** Parallel current-clamp recording of one LII pyramidal cell (resting V_m , -50 mV) and one LIII interneuron (resting V_m , -55 mV). The two cells are negatively correlated with a peak value of -0.7 at -10 ms. **F.** Mean oscillation cycle as in B for data shown in E. Excitatory cell (black), inhibitory cell (grey) and MEA recording (red).

6.4 Controlling oscillatory phase & frequency

The previous sections showed that it is possible to induce oscillations optogenetically in turtle dorsal cortex. In this section I describe the effort to control phase and frequency of this oscillation. To this end turtle dorsal cortical slabs expressing channelrhodopsin were stimulated by pulsing light while simultaneously recording LFPs with MEAs and the membrane potential of individual or pairs of neurons with WCPC.

The V_m of a Chr2- cell reflects the ongoing activity in the network rather than the direct effects of light on ChR ion-channel opening. Chr2- cells were thus current-clamped during a stimulation with a constant light (1.5 s) followed by a period (1.5 s) of repetitive short light pulses (duration 10 ms, frequency 10 Hz) superimposed on steady illumination. Pulse intensity and steady illumination were adjusted so that the integral of light intensity was the same over both phases of the light protocol. The superimposed traces of 10 stimulation trials with one recor-

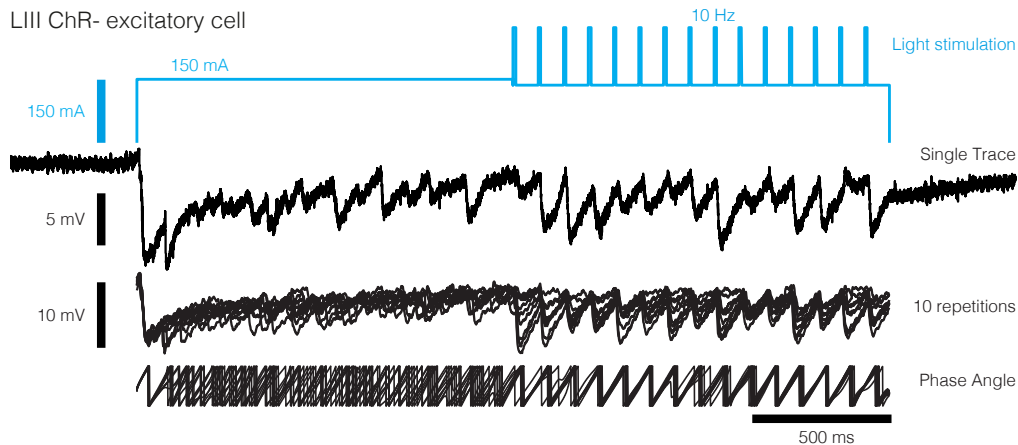


Figure 6.13: Recording of a ChR2- excitatory neuron located in LIII during light stimulation (blue trace). After shining light with constant intensity (150 mA) for 1.5 s, pulses of light (intensity 150 mA, duration 10 ms) were delivered on top with a rate of 10 Hz. To keep the integral of light intensity constant throughout the entire stimulation a scaling factor was applied to the second half of the stimulus. From top to bottom. Top trace: Current-clamp recording during a single stimulation trial. With light onset the V_m of the cell starts to oscillate after the initial activity burst. The oscillations become more pronounced when the light is pulsed. Middle trace: The cell's V_m during ten light stimulation trials superimposed. With the onset of light pulses the phase of the oscillation locks to them. Bottom trace: Phase angle calculated for each of the 10 repetitions and superimposed show phase locking.

ded neuron (Figure 6.13) show that the phase of the oscillation can be controlled by pulsing light. The phase locking value calculated over 10 repetitions of the stimulus has a median of 0.26 during the first 1.5 s of steady illumination, against 0.77 during the second period.

Following my earlier observation that the oscillation frequency upon illumination depends (to some extent) on light intensity (Figure 6.1C), I examined the interaction of continuous and pulsed illumination on the oscillation. The results proved to be interesting. The frequency of light pulses to which the cortex could be locked always corresponded to the "natural" frequency corresponding to the underlying constant illumination. If light pulse frequency exceeded this natural frequency, the network oscillated only at integer fractions of this frequency. Figure 6.14 shows illustrative examples from two slabs in two turtles. In these cases oscillations were phase locked to the light pulses but to every second (oscillating at half the control frequency) or third cycle (at a third of the control frequency). The subset of pulses to which the network phase-locked varied (Figure 6.15).

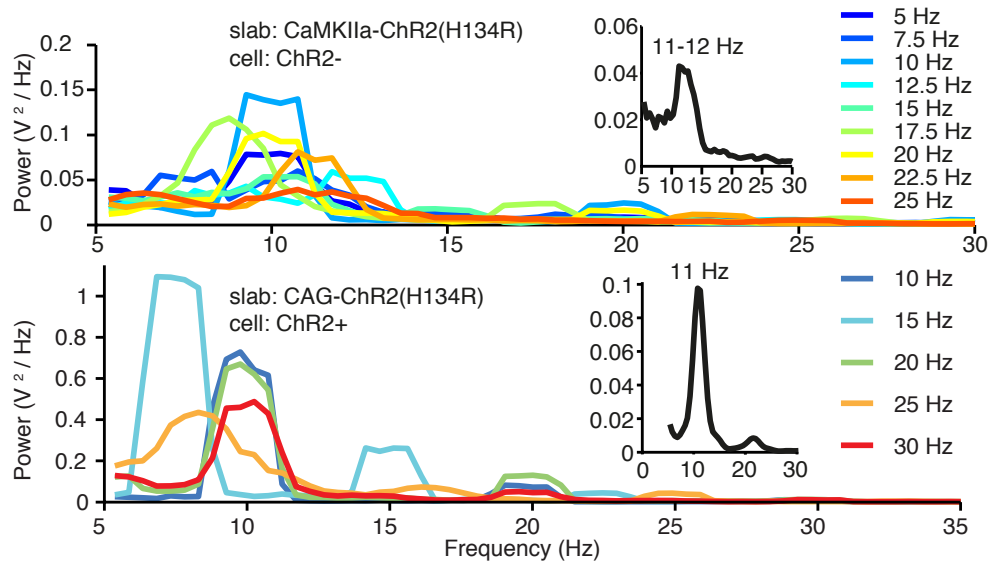


Figure 6.14: Top row. Nine frequency power spectra of intracellular V_m of a patched ChR2-excitatory neuron during attempts to control oscillation frequency. V_m reflects network input to the patched cell in a dorsal cortical slab expressing ChR2 under a CaMKIIa promoter. Each line of varying color corresponds to one spectrum calculated over 10 repetitions of pulsing light (as in Figure 6.13) at different frequencies (see color code). Inset graph shows the spectrum during a 2 s light stimulation with the same intensity (100 mW) as during pulsing. Notice how the network's oscillation frequency is at a fraction of the stimulus frequency, when the latter exceeds the preferred oscillation frequency at the given light intensity. Bottom row. As above, but for a ChR2+ excitatory neuron in a slab transfected with CAG-ChR2 during light stimulation (100 mW). Same result as above, with higher power. Also in a ChR2+ cell, the network effects dominate the V_m .

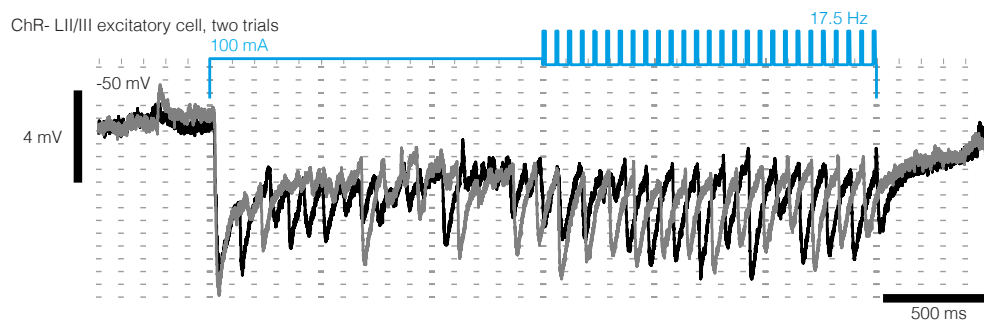


Figure 6.15: Experiment in a dorsal cortical slab expressing ChR2 under a CaMKIIa promoter. Shown is the recorded V_m of a ChR2- pyramidal cell during two trials (grey and black trace) of stimulating with a constant light stimulation followed by pulsing light with 17.5 Hz (blue trace). The integral of light intensity during the entire stimulus is constant. Note the V_m phase locking to every second pulse, and how the two trials follow shifted frames of pulses.

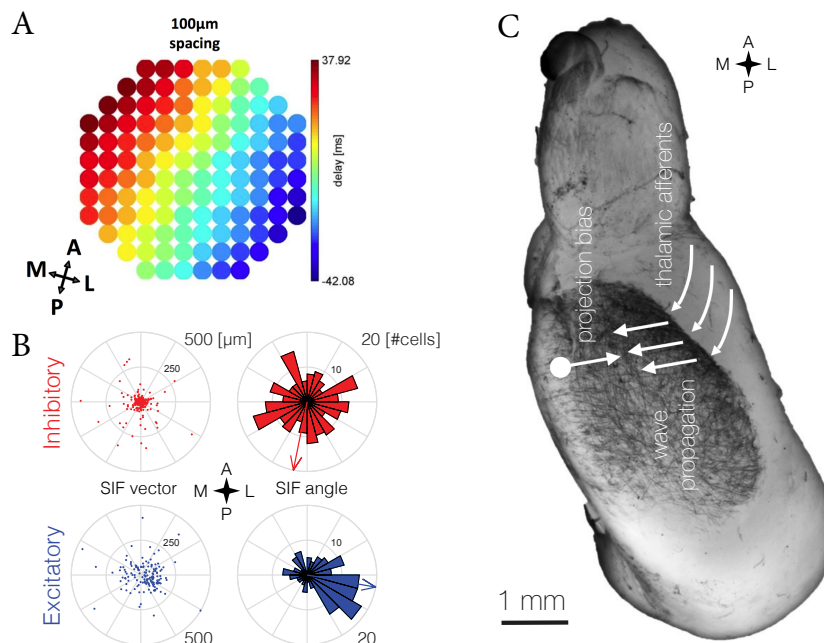


Figure 6.16: **A.** Spatial representation of a 120-channel MEA recording in turtle dorsal cortex, where the color of each electrode represents the time delay of the cross correlation peak between the local channel and an average over all channels. The wave of activity propagates from lateral towards medial (from MSI). **B.** Left row: Frequency distribution (polar plot) of SIF angles relative to brain's cardinal axes (Ant.-Post., Med.-Lat.), as indicated in inset. All recorded simultaneously in one cortical slab. Right row: Polar plots of vectors for I and E neurons as derived from SIF polarity. Note strong bias in mediolateral projections only among the principal neuron population (from MSI). **C.** Schematic showing the orientation of thalamo-cortical afferents, the direction of wave propagation and the projection bias of principal cells in dorsal cortex. Overlaid on an image of one hemisphere of the turtle brain. Myelin staining visualizes the extent of dorsal cortex (Robert Naumann, unpublished).

6.5 Spatiotemporal control of oscillations

As shown using VSD recordings in the past (Prechtl et al., 1997; Prechtl et al., 2000; Senseman and Robbins, 1999; Senseman, 1999; Senseman and Robbins, 2002), turtle dorsal cortex exhibits travelling waves upon visual stimulation (see also Figure 1.5). Colleagues in the Laurent laboratory have replicated this result while recording activity with MEAs (Figure 6.16A, Mark Shein-Idelson). This visual-stimulation-induced activity propagates from the lateral towards the medial edges of cortex following the main axis of thalamo-cortical projections from LGN. The propagation, however, can not be explained by simple thalamo-cortical axonal propagation because the visually evoked wave travels considerably more slowly (around $10 \mu\text{m ms}^{-1}$ vs. $150 \mu\text{m ms}^{-1}$, see introduction 1.2.4). MEA recordings using the methods developed in chapter 5 enabled us to extract the axonal projection patterns of pyramidal cells and interneurons using SIFs (see Figure 5.9).

Excitatory cells showed an axonal projection bias in the medial to lateral direction, i. e. , colinear with but opposite visual wave propagation. This bias was absent in interneurons (Figure 6.16B, C, MSI). This selective spatial anisotropy led me to explore its potential consequences using spatiotemporal optogenetic stimulation.

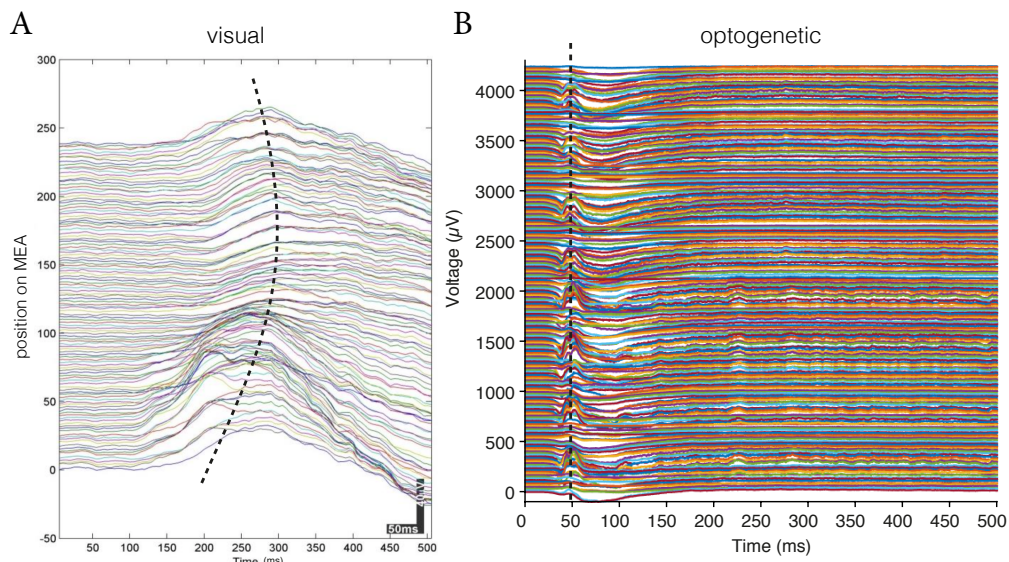


Figure 6.17: **A.** All 120 channels of a MEA LFP recording during visual stimulation by flashing light (at timepoint 0). Note the relative time delays in onset and peak of activity (indicated by broken line). **B.** All 250 channels of a MEA LFP recording during optogenetic stimulation of a dorsal cortical slab expressing Chr2(H134R) under the CaMKIIa promoter. Note the simultaneous activity onset across the active channels.

Can these travelling waves be triggered by optogenetic stimulation? For this I carried out a series of experiments optogenetically stimulating dorsal cortex expressing Chr2(H134R) under the CaMKIIa promoter while recording with MEAs. Stimulating the entire cortex with a flash of light (2 s) resulted in simultaneous activation and phase locked oscillations across the entire recorded area, distinct from the time shifted activity profiles caused by visual stimulation of the retina (Figure 6.17, 6.19A). Thus simultaneous activation of the excitatory neuronal population does not result in propagating activity. To refine stimulus delivery we adapted an inverted microscope to allow stimulation of the sample with a digital micro-mirror device (DMD). This allowed us to control light delivery both in time and space (see methods section 2.4.1).

Subregions of cortex were first stimulated with $400\ \mu\text{m} \times 400\ \mu\text{m}$ squares (Figure 6.18A). Synchronous oscillations could be evoked locally, but no propagation was observed outside of the area of stimulation (Figure 6.19B).

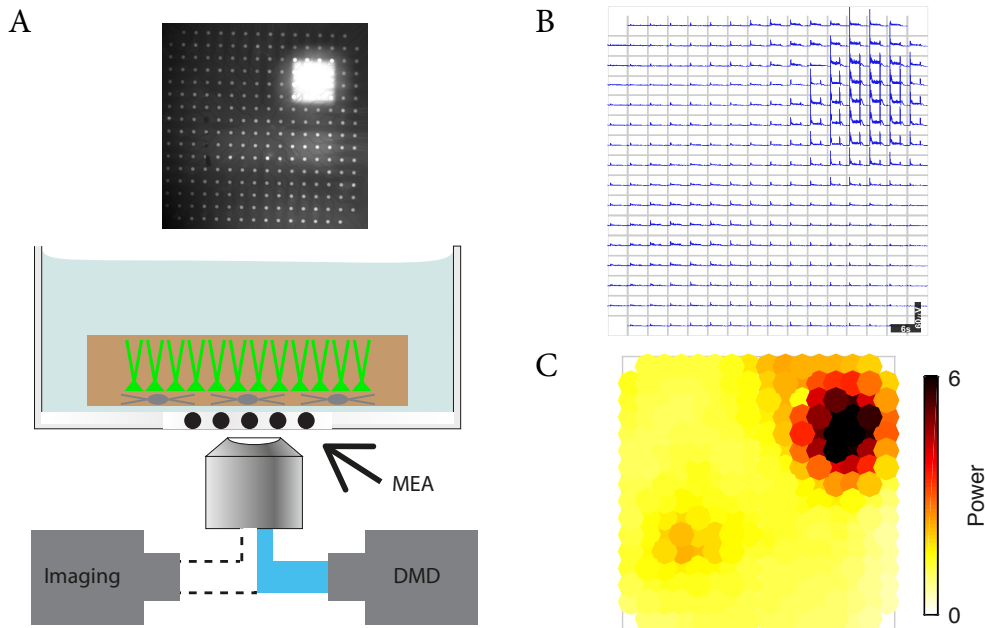


Figure 6.18: **A.** Bottom: Schematic of the experiment in an inverted microscopy setup. Dorsal cortical slab preparation with the ventricular side placed on the MEA. The MEA's glass substrate allows spatially confined light stimulation through an objective (912 × 1140 pixels in the field of view, corresponding to submicron resolution with a 20x objective) with a temporal precision of 17 ms. A 50/50 mirror allows parallel imaging through the objective with a camera. Top: Image of a square stimulus with a side length of 400 μm. **B.** Spatial representation of a 250-channel MEA recording in dorsal cortex of a whole brain explant expressing Chr2(H134R) under a CaMKIIa promoter. For each electrode the recorded electrophysiological trace is shown during one DMD-optogenetic stimulation trial with a 2 s 400 μm square of light (same stimulation location as shown in A.). Note the spatially confined oscillations. Scale bar 6 s, 60 μV. **C.** Same as B, each point shows local oscillatory power in the 5 to 15 Hz range averaged over trials.

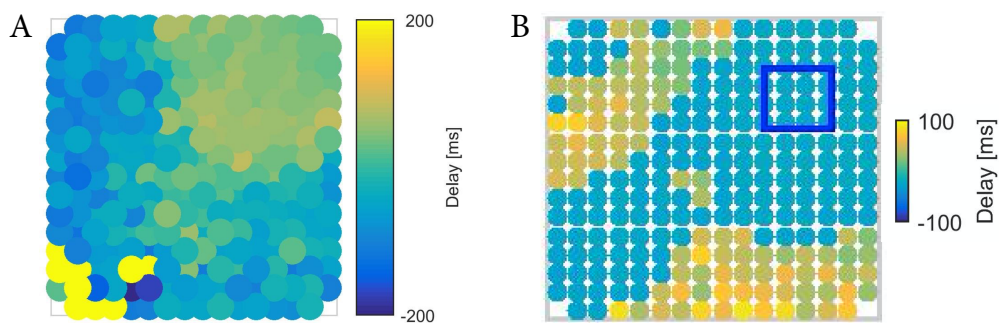


Figure 6.19: **A.** Spatial representation of a 250-channel MEA recording of a dorsal cortical slab expressing Chr2(H134R) under a CaMKIIa promoter during stimulation with a 2 s full field light flash. The color of each electrode represents the time delay of the cross correlation peak between the local channel and an average over all channels. No propagating activity can be seen (compare to Figure 6.16A). **B.** As in **A** only with a 2 s 400 μm square of light (blue box) using the DMD for light stimulation.

Chapter 7

Discussion

7.1 Genetic Tools

Genetic targeting of neurons and neuronal subtypes underlies a host of new techniques in neuroscience such as imaging with genetically encoded calcium indicators, genetic neuroanatomy, electrophysiology from genetically defined cell types, optogenetic manipulation of neuronal activity with channelrhodopsins, halorhodopsins or archaerhodopsins. The results shown in chapter 4 now allow us to perform a basic set of genetic manipulations to aid neuroscientific experiments also in reptilian brains.

7.1.1 Viruses

My results demonstrate that our primary goal, namely to find a technique for efficient gene transfer to a local population of neurons, can be met with AAV2/1, AAV2/5 or AAV-SL1 serotypes. To label neuron populations more selectively AAV2/8 or AAV2/9 can be used. Given my lack of success with *lentivirus* infection and expression, the limitations of AAV- a long delay of several weeks to expression and limited packaging capacity (9 kilobases) (Kumar et al., 2004; Zhang et al., 2010; Luo et al., 2008) - could not be overcome. Out of 14 injections in organotypic slabs taken from 3 turtles, none generated detectable *lentivirus* infection, even as simultaneous AAV injections with the same needle did result in significant expression. This argues against failures of injection, and suggests that *lentivirus* can simply not infect turtle cortical neurons. Thus AAV is at present the only proven recombinant viral vector in turtles. Another recombinant viral vector with large packaging capacity (150 kilobases) used in the neuroscientific community is *Herpes Simplex Virus* (Lilley et al., 2001; Zhang et al., 2010). It is a good candidate for further viral screening.

The most pressing issue is to find a technique to achieve transsynaptic retrograde tracing; no positive results were obtained with *rabies virus*, a commonly used tracer virus (Ugolini et al., 1987; Ugolini, 1995b; Ugolini, 1995a). Failure of *rabies* expression could have been seen due to methodological problems during the injections or a dysfunctional viral batch. This seems unlikely with a success rate of 0 out of 17 injections in turtles but 4 out of 4 in mice. We also tested a range of incubation periods after injection (28 d, 2 turtles; 14 d, 1 turtle; 10 d 1 turtle). It seems unlikely that we somehow missed the period of expression. The literature indicates that some reptilian cell lines are highly susceptible to *rabies* infection (*Viper*) while others not (*Iguana*) (Clark and Kritchevsky, 1972). Thus our failure to infect turtles probably stems from genuine antigenic and molecular incompatibilities. Considering the infectious mechanism of the *rabies virus*, with its precise affinity for presynaptic membrane receptors (Callaway, 2008; Wickersham et al., 2007), I conclude that this targeted neuronal surface structure is either missing or modified in turtles.

Transsynaptic retrograde tracing with viral methods is of particular interest in the turtle as it concerns long-range connectivity. Physiological characterization of long-range connections is extremely challenging and would be greatly aided by the availability of trans-synaptic tracers. Marking a single neuron locally and its distant presynaptic partners with fluorescent proteins would enable long-range, targeted, paired whole cell patch-clamp recordings. In an eye-attached whole-brain *ex vivo* preparation, such physiological characterizations of distantly connected neuronal pairs during sensory processing could, for the first time, be undertaken efficiently.

Another promising transsynaptic retrograde virus, *Pseudorabies virus (PRV)*, should be tested in future experiments (Ugolini, 1995b). *PRV* is a member of the alpha-herpes viruses (as is *HSV*) and despite its name, has no relation to *rabies virus*. An attenuated strain of *PRV* allows retrograde transsynaptic infection and spread while ensuring the health of the host animal. This has been achieved by genetically engineering the *PRV* genome to allow replication only in neurons which also express the Cre-recombinase (DeFalco et al., 2001).

After further work to confirm that *rabies* infection-failure results from an incapacity to bind presynaptic axonal terminals, one could imagine engineering the *rabies* glycoprotein so as to be compatible with turtle presynaptic proteins. A candidate for the outset of such an approach might be found in the capsid protein of *AAV-SL1*. In section 4.1.5 I presented evidence that *AAV-SL1* can indeed infect the axonal terminals of turtle neurons. Even though *AAV-SL1* does not seem to

cross synapses and infect thalamic cells, intracortical retrograde tracing was possible, judged from the similarity of its infection pattern to parallel cholera-toxin staining. For now AAV-SL1 with a non-transsynaptic but simple retrograde infection capacity constitutes the only such tool in reptiles. The *canine adeno virus* (CAV) (Peltékian et al., 2002) might also be worth testing in turtles. If successful its surface proteins could also serve as a basis from which to engineer *rabies virus*.

7.1.2 Promoters

The results presented in section 4.2 lay the ground-work to establish a set of promoters suitable to control the expression of selected and introduced genes in turtle neurons. Promoters were tested to fulfill two desired properties: high yield and neuronal specificity.

The search for high yield promoters that work in turtles was straightforward and successful. All tested viral-derived promoters worked. These included CB7, CAG and CMV (Yizhar et al., 2011). They were used successfully in dozens of injections and now constitute standard tools in the laboratory. The same applies to the h-Syn promoter, which restricts gene expression to neurons. Note however, that infection with CB7, CAG or CMV did not appear to result in non-neuronal cell expression; cortical radial glia cells, for example, have a distinct morphology and would have been readily identified if they had been infected. This suggests that AAV has a tropism towards neurons rather than non-neuronal cells in the turtle brain.

Further restricting gene expression to a subclass of neurons was of paramount interest to this laboratory. In mammalian genetics this is now done by integrating in the host's genome a gene of interest or the Cre-recombinase behind the promoter of a target gene which is expressed in the desired pattern (Meyer et al., 2002; Luo et al., 2008; Kelsch et al., 2012). This strategy, called enhancer trapping, exploits endogenous regulatory systems and does not require the precise knowledge of the involved enhancer elements. Transgenic methods however are not available in turtles (with a generation time of several years) making this strategy not viable. We thus opted to test promoters small enough to be delivered with AAV, and known from the mammalian literature to result in cell-type specific expression. The outcome of these tests provided us with one such promoter - of the gene α -Ca²⁺/Calmodulin dependent protein Kinase II (CaMKIIa) (Liu and Jones, 1996; Zhang et al., 2010; Yizhar et al., 2011). The CaMKIIa promoter suc-

cessfully restricted expression to excitatory neurons of turtle cortex (see chapter 4.2.2).

I failed to identify promoters resulting in gene-expression restricted to inhibitory interneurons (Monyer and Markram, 2004). Three promoters of this kind derived from the genome of the pufferfish *Takifugu rubripes* have been shown in mammals to result in interneuron-specific expression (Nathanson et al., 2009). These promoters were cloned from the preceding genomic regions of three interneuron-related genes - somatostatin (fSST), neuropeptide-Y (fNPY) and parvalbumin (fPV). The three promoters were tested in turtles, but none led to expression. Thus it is currently not possible to target expression only in inhibitory interneurons in the turtle.

Further work by Dr. Tracy Yamawaki (this lab), focused on isolating from the turtle genome candidate promoters for interneuron-specific expression. This effort also was not successful (unpublished). Recent work by Dr. Maria Tosches and Dr. Tracy Yamawaki on single cell RNA sequencing and in-situ hybridization will hopefully lead to identification of further candidate genes with interesting expression patterns, and eventually, to promoter discovery (Tosches et al., submitted).

7.2 Neurophysiology

The results obtained in a joint effort (together with Dr. Mark Shein-Idelson and M.Sc. Mike Hemberger) indicate that the activity of many hundreds of neurons can be recorded simultaneously for days in an *ex vivo* simple cortical preparation, using planar electrode arrays similar to those widely used for retinal recordings (Shein-Idelson et al., 2017; Stafford et al., 2009; Li et al., 2014). Increasing the size of a recorded sample to many thousands of neurons is thus simply a function of increasing the size of the recording arrays. This opens up the possibility to sample neural activity at spike-time resolution over thousands of neurons simultaneously in a cortical preparation. More importantly, we observed that extracellular recordings also enabled the detection of elementary synaptic events, locked in time to the action potentials of single neurons. The practical implications of this finding are discussed below.

7.2.1 Detecting synaptic events with extracellular electrodes

Field potential recordings have a long history in neuroscience (Berger, 1929; Adrian, 1950) but their biophysical underpinning, though in great part agreed upon, remains incompletely understood (Riera et al., 2012; Buzsáki et al., 2012). What seems clear is that local field potentials (LFPs), that is, ones recorded directly from within inter-neuronal extracellular space, are dominated by low-frequency events, due to the steeper attenuation of high-frequency signals (e.g., spikes) over space (Bédard et al., 2010; Pettersen and Einevoll, 2008; Lindén et al., 2011). (Conversely, the low-pass filtering property of extracellular space is useful for spike waveform isolation, because it limits the number of overlapping waveforms at each recording site.) Hence, LFPs preferentially represent local synaptic activity and other slow currents. Due to the small amplitude of unitary synaptic potentials (about 1 mV vs. 100 mV for action potentials), however, LFPs have generally been used to gather information about bulk synaptic activity (stimulus induced or spontaneous; (Creutzfeldt et al., 1966a; Creutzfeldt et al., 1966b; Elul, 1971; Andersen et al., 1971; Kreiman et al., 2006; Trevelyan, 2009; Li et al., 2009), neural synchronization (Buzsáki and Draguhn, 2004; Engel et al., 2001) and, in artificial stimulation conditions, synaptic plasticity (as with field EPSPs for example (Bliss and Lomo, 1973; Kang and Schuman, 1995)). The finding that individual synaptic events caused by single units and spikes could be detected in an intact cortical structure was a surprise. While we detected them initially from spike-triggered averages of broad-band signals, we could often detect them clearly from single events (see Figure 5.4A for example). In retrospect, this observation should not be surprising once one realizes that the propagation of an action potential along the axon collaterals of a cortical neuron must activate, within one or a few milliseconds, hundreds to thousands of synaptic release sites (e.g., (Johnson et al., 2000; Houweling and Brecht, 2008; Oberlaender et al., 2011)). Provided that transmitter release generates a non-zero postsynaptic current at those synapses, many unitary synaptic LFPs will be generated approximately simultaneously and combine additively. By using an isolated (high-passed) unit's waveform at the most favorable recording site as a trigger for the raw recordings from all recording sites, one can retrieve synaptic signals even at sites where no spike can be detected. This is what enables the tracking of an axonal field over many hundreds of micrometers away from the site of spike generation (and travel).

Our study complements that of Haider et al. (2016) in which the authors triggered LFP recordings in cortex from the spikes of an intracellularly recorded neuron. With this operation (and appropriate elimination of contamination by slow auto-

correlation), Haider et al. could show that the LFP is a good predictor of the membrane potential of the recorded unit around spike time (Haider et al., 2016). Comparable results were obtained in the insect olfactory system by this laboratory (Jortner et al., 2007). These results linked spiking in a recorded unit with synaptic drive to that unit. Our present results illuminate the converse relationship: one can reveal, via extracellular recordings, the synaptic influence of an individual neuron on the cortical tissue that it innervates, and thereby track its functional projection domain.

7.2.2 Extensions

Our use of MEAs on turtle cortex was, in retrospect, particularly favorable to extracting spike-triggered “morphological imprints” of single neurons: MEA recordings from intact tissue provided high SNR and dense sampling over space; cortical activity was relatively sparse, minimizing contamination by correlated activity. Finally, a three-layered cortex provided relatively simple and homogeneous source and sink distributions, facilitating data interpretation. Could our approach be extended to other, a priori less favorable structures and non-planar electrode arrays?

Recent advances in the design and fabrication of high-density arrays of multi-shank linear probes (Berényi et al., 2014; Xie et al., 2015; Jeong et al., 2015; Buzsáki et al., 2015; Rossant et al., 2016; Rios et al., 2016; Scholvin et al., 2016) make our approach entirely realizable in three dimensions and in deeper or thicker brain structures, as recent linear-probe recordings from our laboratory indicate (data not shown in the results section). The synaptic innervation zones of each isolated unit can be delineated, provided that enough recording sites are located within a sphere of 100 to 200 μm radius of those synaptic sites. To deal with contamination due to synchronization, demodulation can be used as recently demonstrated with the extraction of hippocampal place field sequences from LFP recordings (Agarwal et al., 2014). Other approaches (Taxidis et al., 2015) were suggested to estimate ripple spike sequences from LFP data. New CSD analysis methods, taking advantage of increased electrode density, could also facilitate synaptic source localization by eliminating spatial filtering due to volume conductance (Potworowski et al., 2012). Finally, modeling strategies have been developed to separate the contribution of lamination and return currents to LFP in six-layered structures (Hagen et al., 2016).

7.2.3 Advantages & applications

A significant advantage of our approach is that it is purely analytical and thus requires no additional hardware or equipment; it can be used on the same datasets as conventionally acquired with electrode arrays for chronic extracellular electrophysiology and requires no additional technical adjustment on data acquisition or formatting, other than the capture and storage of the broadband data, and adequate spatial sampling of the tissue. We emphasize two immediate advantages of our analysis.

The first is cell-type (E-I) identification. In the absence of prior knowledge or of molecular markers (and associated technical overhead), the only approaches so far used to separate putative interneurons from excitatory neurons have been based on spike width and firing statistics (Barthó et al., 2004; Henze et al., 2000). We add a new method, based on direct measurements of extracellular synaptic events. In our preparation, this method provided a dramatic improvement over classification using spike width alone, which failed for a wide range of intermediate values shared by both neuron types.

The second advantage was our ability to track axonal innervation territories of individual neurons. Our approach was mostly focused on using 2-D electrode arrays (due to our interest in reptilian cortex) and thus, sampled mostly the 100 to 150 μm thick region of ventral cortex (layers 2-3), due to signal attenuation from more distal regions of the neuropil. Recently SIFs were obtained with linear probes as well, indicating that the method can be extended to dense arrays of linear probes, with appropriate inter-shank and inter-recording site spacings (Shein-Idelson et al., 2017; Rossant et al., 2016). One could then, from each sorted unit, estimate an axonal projection territory without need for staining. Again, because this analysis relies on sorted spikes as references, it can be carried out in parallel on all sorted units, and thus provide useful morphological and functional information about all recorded units. One should note, however, that a proper interpretation of the data requires both good unit isolation and reasonably low inter-neuronal spike correlations around $dt = 0$, so as to avoid misattribution of SIFs.

In conditions of high signal-to-noise ratio, we could detect local synaptic events generated by single action potentials (i. e. , without signal averaging). This indicates that one could use this technique to monitor release fidelity (and potentially even functional influence) simultaneously at a variety of postsynaptic territories visited by a single cortical neuron. With the recent development of high-density electrophysiological recording probes (Fiscella et al., 2012; Berényi et al., 2014;

Xie et al., 2015; Jeong et al., 2015; Buzsáki et al., 2015; Rios et al., 2016; Rossant et al., 2016; Scholvin et al., 2016; Lopez et al., 2016), analysis techniques such as the one we propose will gain in power and accuracy due to increased sampling density.

One great advantage of the approach is that it can be applied en masse over all sorted units in a recording. Examining such data in reptilian cortex, we could detect a subtle projection bias in the axonal projection fields of populations of excitatory but not inhibitory neurons. This population bias may be important to explain wave propagation in this cortex (Prechtl et al., 1997), for propagation runs along the same orientation as the projection bias. Spontaneous, ongoing and stimulus-evoked waves of neural activity exist in a number of neural systems and animal species (Ermentrout and Kleinfeld, 2001; Massimini et al., 2004; Lubenov and Siapas, 2009; Sato et al., 2012), but their mechanistic underpinnings are poorly understood (Hemberger et al., 2016). The following chapter discusses the first attempts to probe mechanical aspects of cortical waves using optogenetics.

7.3 Optogenetic manipulation of neural dynamics

To understand the function of biological systems, observational together with perturbational techniques are important (Marr, 1982). While observational techniques have advanced greatly over the past decades, perturbation experiments remain difficult. Cooling, pharmacological intervention, electrical stimulation have been used successfully (Long and Fee, 2008), but are often not sufficiently specific. The development of optogenetics represents a step towards realizing perturbational techniques adequate for neural systems (Nagel et al., 2002; Nagel et al., 2003; Boyden et al., 2005; Han and Boyden, 2007). Optogenetics means the integration of optics and genetics to allow gain- or loss-of-function of well-defined events within specific neurons. The optogenetic toolset by now includes dozens of single-component effector proteins which allow such perturbations. The most widely used comprise the families of channelrhodopsin2 (ChR2) for activation and Halorhodopsin (NpHR), and Archaeorhodopsin (Arch) derived proteins for photoinhibition. (Deisseroth, 2011; Yizhar et al., 2011). Optogenetics has two strengths which represent significant advancement for neural perturbations. First, it allows perturbations on the timescale of neuronal signaling, i. e. milliseconds, in intact nervous systems. Second, while electrical stimulation also acts on en-passant

fibers, optogenetics effects a more precisely defined neuronal population: ChR2 is typically coupled to a fluorescent protein and can be expressed in neuronal subpopulations by genetic driver lines.

To reach a mechanistic understanding of cortical dynamics, these tools are particularly important. While not necessarily able to mimic natural activity patterns, optogenetics is the state of the art for the manipulation of neuronal activity. In an *in vitro* system, such as the cortical slab, they allow to induce neuronal activity in a controllable way. The resulting reproducible network phenomena can be monitored with observational tools (MEAs, WCPC), which makes a powerful experimental setup to probe and characterize cortical dynamics. After the demonstration of viral gene delivery capacity and promoter operation, and after initial tests to insure ChR2 function in turtle cortical neurons these experiments could be performed.

7.3.1 Dissection of cortical oscillations

As described in detail in the introduction, periodic signals of brain activity, also referred to as neuronal oscillations, are ubiquitous phenomena in neural systems (section 1.3.4). Despite being ubiquitous there is only scarce empirical evidence for their functional importance (Cassenaer and Laurent, 2007; Cassenaer and Laurent, 2012). Their existence in mammals has been associated with numerous hypothetical functions, among them synchronization (local and over large distances), input selection, representation by phase information and memory consolidation (Buzsáki and Draguhn, 2004). Upon visual stimulation, turtle dorsal cortex, both *in vivo* and *ex vivo*, responds with coherent oscillations in the beta range (19 to 25 Hz) with a peak at 20 Hz and an apparent rostrocaudal phase gradient (Precht, 1994; Schneider, 2015; Fournier et al., *in press*). Oscillation frequency usually results from cellular and network properties with particular dynamics (Klausberger and Somogyi, 2008). An ancient primary sensory cortex, such as turtle dorsal cortex, offers the opportunity to uncover principal functions and core mechanisms of cortical oscillations. The experiments in chapter 6 explore some mechanisms of how oscillations are generated in this structure.

My results show that oscillations can be reproducibly induced optogenetically in the dorsal cortex of turtles. I also started to characterize the involvement and role of the major cell classes in shaping these oscillations. The results suggest a predominant involvement of the excitatory-inhibitory neuron-network of layer

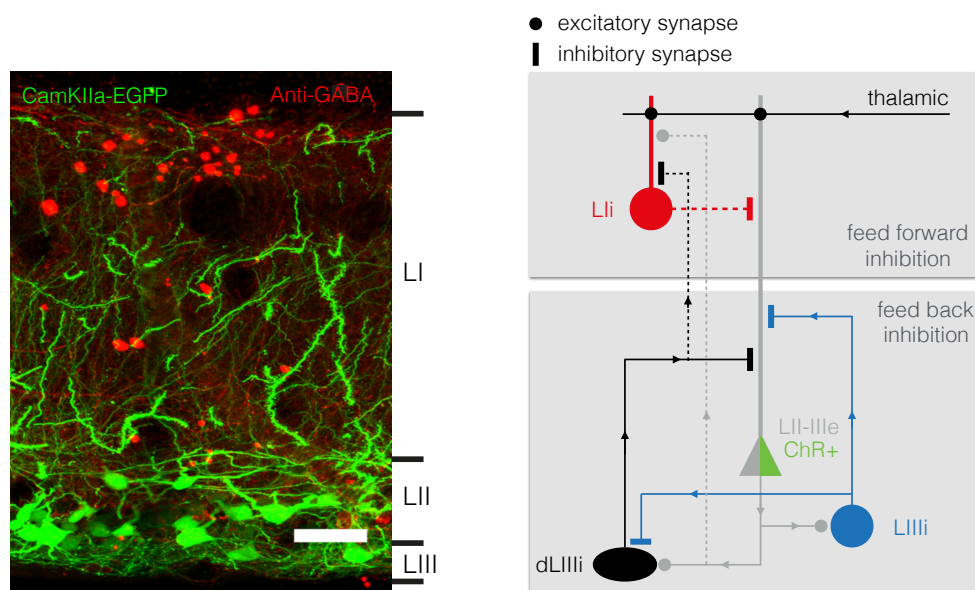


Figure 7.1: Left: Confocal image of a coronal slice of cortex with marked layer boundaries. Cortex was infected with AAV2/1-CaMKII α -EGFP several weeks prior to histology. EGFP expressing cells are excitatory (green), slices were counterstained with an Anti-GABA antibody to reveal inhibitory interneurons (red). Scale bar 50 μ m. Right: Schematic of the functional cortical circuit model resulting from the optogenetic experiments, showing excitatory (circle) and inhibitory (bar) connections between the major cell classes (excitatory, e; inhibitory, i) of cortex.

II/III. Upon light stimulation excitatory neurons expressing channelrhodopsin under a CaMKII α promoter are depolarized in the first 20 ms above action potential threshold, fire an AP, which drives nearly all LII/III inhibitory interneurons to fire in response. This in turn results in strong network-wide inhibition. After this hyperpolarization ChR $^{+}$ cells gradually, and in a more loosely synchronized manner, reach spike threshold again, and recruit inhibitory interneurons. This periodic alternation of "e" and "i", present as long as the light stimulus is on, results in a cortical oscillation, typically in the range of 10 to 15 Hz determined by light power. LI interneurons, despite showing increased subthreshold activity during the LII/III oscillations, did not participate substantially in these oscillations. Their V_m showed, if at all, very weak locking to the oscillations measured in LII/III. This suggests much weaker connectivity from LII/III to LI than within LII/III. Taken together the results suggest that oscillations, caused by pyramidal cell tonic depolarization, result from local negative feedback between PCs and LII/III interneurons with no LI interneuron involvement. For a schematic summary of this preliminary model circuit see Figure 7.1.

What are the reasons for the frequency discrepancy between oscillations evoked

by sensory versus optogenetic stimulation? While this question is best addressed by a modeling effort, two ideas come to mind.

One reason for the lower frequency of optogenetically evoked oscillations could be the apparent lack of recruitment of LI interneurons (Figure 6.9). Upon visually induced afferent activity from thalamus, LI interneurons are active (Fournier et al., in press) and in extracellular depth-recordings by Prechtl and colleagues the strongest oscillations were in fact measured in the dorsal-most 100 μm of cortex (Prechtl et al., 2000). The inputs from thalamic afferents themselves don't seem to be temporally modulated (Shein-Idelson, personal communication). LI interneurons could thus have an additional clocking function in the cortical network, resulting in overall higher frequency oscillations. At the moment little is known of LI interneuron activity. Some hints come from silicon probe recordings where oscillations showed almost no gradient of phase across depth, but a rapid phase reversal superficially, at a level corresponding approximately to the transition between layers 1a (containing LGN axon terminals) and 1b (Fournier et al., in press).

It should be noted that in rare examples, where ChR2 was expressed under the high yield CAG promoter, peak oscillatory power was at 20 Hz (such as in Figure 6.4). This suggests a second possible explanation for the frequency discrepancy. That frequency is simply a function of excitatory drive to the network and that the recurrent LII/III interneuron-pyramidal cell network by itself is capable of generating 20 Hz oscillations. However the mentioned observation alone doesn't refute the LI hypothesis, because under the global CAG promoter, LI interneurons also express CHR2, thus potentially participating and shaping oscillations.

How do these results compare to what is known from mammalian cortical oscillations? During sensory processing in mammalian cortex gamma oscillations, typically around and above 40 Hz, are the dominant frequency band (Gray and Singer, 1989). I will thus compare the two respective dominant visually evoked cortical oscillations - gamma in mammals with beta of turtles. Recent results in mice indicate that the 20 Hz band dominates when PV-interneuron development is artificially arrested (Takada et al., 2014). Cortical interneurons in turtles express parvalbumin at very low levels, but still PV-like interneurons do exist (Tosches et al., submitted) (see below). Therefore it seems unlikely that the difference in frequencies can be explained by a simple lack of one interneuron class.

In mammals two mechanisms "PING" (pyramidal-interneuron network gamma oscillations) and "ING" (interneuron network gamma oscillations) have been pro-

posed for the role of inhibitory neurons in generating gamma oscillations (Tiesinga and Sejnowski, 2009; Isaacson and Scanziani, 2011). In the PING model feedback connectivity between pyramidal cells and interneurons generates oscillations via alternate firing, where the decay time constant of pyramidal cells sets the frequency of the oscillation. In the alternative ING model inhibitory interneurons generate oscillations via reciprocal interconnections without excitatory cell involvement being necessary for their generation (van Vreeswijk et al., 1994). In hippocampal gamma oscillations the inhibitory component of oscillations is delayed 1 to 2 ms compared to the excitation (Klausberger and Somogyi, 2008; Isaacson and Scanziani, 2011). This phase difference is suggestive of a PING predominance in this circuit mechanism. As mentioned above, my data suggests a comparable situation in turtle cortex. Also here the inhibitory component of the oscillations is delayed a couple of milliseconds compared to the excitation (Figure 6.12F), and e-i/i-e connectivity is dominant over i-i/e-e. Thus both LIII interneurons and LII/III pyramidal cells are involved.

Two properties of interneurons are generally thought to be crucial to generate and set the pace of oscillations in mammalian cortex. First, interneurons are electrically coupled via gap junctions, enabling synchronization of large populations with millisecond precision (Beierlein et al., 2000; Galarreta and Hestrin, 1999). Second interneurons synapse reciprocally onto each other which stabilizes oscillations (Bartos et al., 2007; Galarreta and Hestrin, 2002). While reciprocal chemical synapses between interneuron pairs do exist in turtle cortex (Figure 6.7), no electrical coupling between cells could be detected (Mike Hemberger, unpublished), which argues that electrical coupling is not required for the generation of cortical oscillations.

In the last years numerous studies have focussed on the role of different subclasses of interneurons in mammalian cortical dynamics (Klausberger and Somogyi, 2008; Isaacson and Scanziani, 2011; Wilson et al., 2012). Among the diverse types of inhibitory neurons of mammalian neocortex, Parvalbumin positive (PV+) interneurons (basket cells) are thought to play a crucial role in inducing gamma oscillations (Cobb et al., 1995; Cardin et al., 2009; Sohal et al., 2009). This view is based upon the observation, that single or populations of PV+ cells can induce gamma oscillations in pyramidal V_m or LFP respectively, when stimulated at the appropriate frequencies. Driving PV+ interneurons at frequencies below gamma (e. g. 8 Hz) had no effect on LFP power (Cardin et al., 2009). Recent research also pointed to Somatostatin positive (SOM+) interneurons to be a crucial

interneuron class in at least one mechanism of generating gamma oscillations in V1. Upon their optogenetic silencing, visually induced gamma oscillations were suppressed. Further complicating simple narratives on the generation of oscillations, silencing PV+ interneurons had no significant effect on gamma power (Veit et al., 2017). It could be that the exact mechanisms underlying oscillations differ across brain regions, spectral bands, behavioral states and contexts.

It is in this regard that turtle cortex may offer an opportunity to understand a simpler system. Molecular markers allow to track homologous cell types across evolutionarily distant species. To understand the role and evolution of circuit motifs, cortical dynamics and function, functional comparisons of molecularly defined cells in turtles and mammals are of particular interest.

A large scale study in this laboratory combining single cell mRNA sequencing with in-situ hybridization by Dr. Maria Tosches and Dr. Tracy Yamawaki addressed these issues (Tosches et al., submitted), by comparing cortices of two reptile species (*Trachemys scripta elegans*, *Pogona vitticeps*) to mouse neocortex. The study shows that glutamatergic neurons exist in anterior dorsal cortex of turtles with a genetic signature corresponding to upper-layer (UL) and deep-layer (DL) mammalian pyramidal cells, but one-to-one homologies of these excitatory cell types and individual mammalian layer-types don't seem to exist. Rather neocortical and aDC neurons seem to be related at the level of developmental progenitors, without homology of differentiated neuronal types. This and several other observations in the study suggested that new mammalian glutamatergic types might have evolved from the diversification of UL-like and DL-like neurons already present in amniote ancestors.

When the authors compared expression of transcription factors known to define mammalian GABAergic classes, it was found that the same classes of cortical GABAergic neurons are also present in reptiles, and thus existed already in their common amniote ancestor. Conserved combinations of transcription factors were found in distinct clusters of turtle cortical GABAergic neurons, which were classified as putatively MGE-derived and CGE-derived.

Turtle MGE and CGE-derived interneurons seem to be further subdivided into four classes matching the classification in mammals (Tasic et al., 2016; Wamsley and Fishell, 2017). (1) "SST" cells, expressing SST+ NPY+ RELN+ and in some subsets, CALB1+ and the marker of upper-layer Martinotti cells CBLN4. (2) "PV-like" cells, expressing PLAU+, ETV1+, higher expression of the Kv3 channel subunits KCNC1 and KCNC2, but only low PVALB and in one subset, basket-cell marker BCAN. (3) "HTR3A Reln" cells, expressing ADARB2+ HTR3A+ CNR1+ RELN+ TNFAIP8L3+

SST- and in one subset, neurogliaform-cell marker NDNF. (4) "HTR3A VIP-like", expressing ADARB2+ HTR3A+ CNR1+ RELN-. These results suggest that species-specific subtypes of interneurons diversified independently in mammals and reptiles, starting from ancestral PV-like, SST and HTR3A (possibly VIP-like and Reln) cell classes. How these molecularly defined classes of neurons relate to the recorded cells, reported here, is currently unknown, as we lack promoters for genetic access to specific interneurons (see chapter 4.2.2).

My results argue for further exploration of LI interneuron activity during visually evoked oscillations. Simulations could then clarify the mechanistic interplay between LI and the LII/III network during cortical dynamics. To obtain a more detailed understanding of the roles of different cell types in shaping these oscillations and computations, and their relation to mammalian cortical cells and dynamics, targeting of genetically defined cell classes is important (Wilson et al., 2012). The mentioned single cell profiling effort uncovered several interesting candidate genes, some of whom were only expressed in LI interneurons (Tosches et al., submitted). The challenge remains to engineer promoters replicating these expression patterns. Alternatively, mapping recorded cells of the described functional classes onto molecularly defined cell types can help to integrate these two lines of research (Klausberger et al., 2003), which might allow comparisons between reptiles and mammals by proceeding from the emergent functional property - oscillations - towards underlying mechanisms to uncover principles of cortical computations (Konishi, 1991; Borst and Helmstaedter, 2015).

7.3.2 Controlling cortical dynamics

Beyond driving the cortical network to oscillate, the ability to modulate and control different parameters of these dynamics allowed me to address two further topics. One was to define the range of frequencies within which the network can oscillate. The other was to test whether cortical waves, as seen during visual processing, could be triggered by optogenetic stimulation.

To address these questions some technical developments had to be undertaken. The turtle *ex vivo* preparation allows unprecedented experimental accessibility to an intact vertebrate central nervous system which retains sensory-input. The developments described in the previous chapters allow for detailed extracellular electrophysiological monitoring, together with parallel paired patch-recordings and extracellular depth recordings with silicone probes or tetrodes. This setup had to be expanded to allow for precise light stimulation of the sample. A high power

LED with computer controlled driver unit allowed to pulse the stimulating light with sub-millisecond temporal precision. And delivery of light in the microscope-setup with a digital micromirror device (DMD) allowed a further refinement - spatio-temporal control of the light stimulus with submicron precision and 60 Hz temporal resolution (section 2.4, Figure 5.2).

In experiments of section 6.1 the LII/III cortical network was oscillating between 10 to 15 Hz upon sustained optogenetic activation of excitatory cells. By pulsing the stimulating light at different frequencies I tested whether the network can be entrained to oscillate at higher frequencies (section 6.4). In mouse cortex driving PV+ interneurons optogenetically at frequencies above 20 Hz induced network oscillations following the stimulation frequency, with maximum effect around 45 Hz (Cardin et al., 2009). In the same study driving excitatory neurons had a different outcome. Effects on oscillations of the LFP were largest at lower frequencies around 8 Hz with continuously diminishing effects at higher frequencies. A similar effect was seen in turtles. With ChR2 expression restricted to excitatory cells of turtle cortex, pulsed light allows to control frequency and phase of these oscillations, but only about 2 Hz around the "natural" oscillation frequency at a given intensity of stimulating light. If the pulse frequency was increased beyond this range, the network would oscillate at a fraction of the pulse frequency. That is if the network oscillated naturally at 11 Hz upon sustained stimulation, it would oscillate at 7.5 Hz when pulsing light at 15 Hz (Figure 6.14). Thus pulsing the light at 20 Hz could not replicate the visually evoked frequencies, but rather resulted in 10 Hz oscillations of the network. The effect of driving an interneuron population with different frequencies could not be tested, due to a lack of genetic targeting.

Last I tried to trigger one particular type of cortical dynamic, a travelling wave, with spatio-temporal optogenetic stimulation using a DMD based stimulator. Under natural conditions visual stimuli elicit travelling waves in turtle cortex (Prechtl et al., 1997; Prechtl et al., 2000). Despite the fact that these activity patterns are omnipresent in neural systems, we do not yet know how they are generated in any neural system (Ermentrout and Kleinfeld, 2001; Massimini et al., 2004; Benucci et al., 2007; Lubenov and Siapas, 2008; Sato et al., 2012). Manipulating these dynamics in a controlled way could help to form an understanding (Richardson et al., 2005). The turtle *ex vivo* preparation is well suited to study the mechanisms of wave generation. To test whether travelling waves are generated by the cortical network alone, I optogenetically introduced tonic activation either to ChR+ excitatory neurons or a combined excitatory and inhibitory cortical population

and analyzed the resulting LFP for wave-like activity propagation (section 6.5). Stimulating the entire cortex resulted in simultaneous activation and phase locked oscillations across the entire recorded area (2.6 mm²), distinctly different from the phase gradient upon visual stimulation of the retina. Second I activated only a subregion of the recorded area and analyzed whether activity would propagate from the activated region in form of a travelling wave. Likewise this stimulation paradigm resulted in simultaneous activation and phase locked oscillations also outside the stimulated region, where activity attenuated within 200 μ m. The results were the same whether only excitatory or a mixed population of neurons was optogenetically activated.

Axonal projections of excitatory neurons show a bias from the medial to the lateral pole of the cortex, that is aligned with but against the direction of wave propagation (Figure 6.16). But activation of these cortical populations shows that these biases alone do not suffice for the intracortical network to exhibit wave-like activity propagation. Thalamic afferents enter dorsal cortex laterally and project medially (Desan, 1984). They synapse mainly on the distal dendrites of LII principal cells and smooth dendrites of subpial LI interneurons. Interneurons receive - on average - six times more thalamic inputs than pyramidal cells (Smith et al., 1980). What properties of this wiring matter for wave initiation remains to be determined.

Optogenetics offers exciting opportunities to investigate neural networks, to probe the interplay between neuronal types and to uncover the functional significance of network phenomena, such as oscillations and waves (Deisseroth, 2011; Yizhar et al., 2011). Applying this technology with the precision demanded by the complexity of neural processing remains challenging however (Peron and Svoboda, 2011). These difficulties were evident in the experiments described here. New developments might help to overcome these challenges. One is to improve genetic targeting based on recent gene expression data (Tosches et al., submitted). But cell type is only a crude description of any one neuron. In complex vertebrate circuits, sparse subsets of neurons have distinct task-related activity patterns and presumably carry different types of information to guide the animal's behavior. Neurons relevant to a particular aspect of sensation and behavior are intermingled with anatomically and molecularly indistinguishable cells with other functions. In one of the most advanced uses of optogenetics to date, Wilson and colleagues demonstrated, that the operations of subtraction and division are performed by genetically distinct interneuron classes (Wilson et al., 2012). Clearly ensembles of cortical neurons perform far more complex operations. To understand these more sophisticated computations, stimulating unknown numbers of

cells belonging to the same genetic class will not be sufficient. But other advances promise to further refine optogenetic intervention, among them activity dependent genetic switches (Reijmers et al., 2007; Kennedy et al., 2010) and sculpting light in 3D with digital holographic patterns (Papagiakoumou et al., 2010; Vaziri and Emiliani, 2012; Hernandez et al., 2016). The accessibility of the turtle *ex vivo* preparation, with the relative simplicity of its cortex, makes it an excellent model system to exploit these technical refinements.

7.4 Conclusion

This thesis deals with my contributions to establishing the turtle as a useful model system in neuroscience. While neuroscience used to be performed in a range of model systems, research has recently converged to a reduced set of model systems - *C. elegans*, *Drosophila*, zebrafish, mouse, rat, macaque. The reasons for this shift are mostly technical, and thus easily understood. Bringing new systems into play is hard work. Overcoming technical challenges, however trivial, takes a lot of effort. Yet, we believe that general principles of brain function emerge in great part from comparison (Hemberger et al., 2016). For a model system which can help us to separate implementation details from computational and algorithmic principles of the cerebral cortex, it is an effort worth making.

Despite being the most scientifically scrutinized area of brain tissue the mammalian cortex remains enigmatic. Its six layers, modular architecture, canonical circuits (Douglas and Martin, 2004), very many cell types (Petilla Interneuron Nomenclature Group et al., 2008), and computational complexity (Fregnac et al., 2016), result in countless observations but few principles from which to derive a vertically integrative theory. The field's techno-optimism tends to hope for technical solutions, but despite remarkable technical advances the challenges remain. Reductionism and comparison can prove revealing.

Mammalian neocortex seems to have emerged via expansion of an ancestral small dorsal pallial region, homologous to the anterior dorsal cortex of reptiles. (Aboitiz and Zamorano, 2013; Naumann et al., 2015; Montiel et al., 2016; Laurent et al., 2016; Tosches et al., submitted). In reptiles, the entire cerebral cortex remains composed of only three layers and dorsal cortex is a primary sensory area with direct input from thalamus. Genetic profiling of single cells suggests that while no one-to-one homologies between the three layers of reptilian cortex to layers of mammalian neocortex exist, turtle pyramidal cells with genetic profiles of upper-layer and deep-layer mammalian pyramidal cells do (Tosches et al.,

submitted). Besides sharing ancestral pallial modules, single cell transcriptome sequencing shows mammals and reptiles sharing cortical cell classes (Tosches et al., submitted).

Following from this view reptilian cortex offers a relatively simple model system suited for this reductionist and comparative strategy and to probe general cortical network questions: Its reduced division in specialized territories could provide insights into the relationship between high-order associative cortical areas and primary sensory areas. Functions such as sleep (Shein-Idelson et al., 2016), olfactory (Fournier et al., 2015) and visual processing (Schneider, 2015; Fournier et al., in press) can be addressed. And its range of cortical network dynamics, can, as I have shown, offer insights into mechanisms and functions of oscillations and traveling waves. Turtle dorsal cortex could thus give fundamental insights to the primordial organizational, computational and functional principles of cortical networks. These insights are relevant to our understanding of mammalian brains and ultimately of ourselves.

Bibliography

- Aboitiz, F., Montiel, J., and López, J. (2002a). Critical steps in the early evolution of the isocortex: insights from developmental biology. *Brazilian journal of medical and biological research*, 35(12):1455–1472.
- Aboitiz, F., Montiel, J., Morales, D., and Concha, M. (2002b). Evolutionary divergence of the reptilian and the mammalian brains: considerations on connectivity and development. *Brain research. Brain research reviews*, 39(2-3):141–153.
- Aboitiz, F. and Zamorano, F. (2013). Neural progenitors, patterning and ecology in neocortical origins. *Frontiers in Neuroanatomy*, 7:38.
- Adrian, E. D. (1950). The electrical activity of the mammalian olfactory bulb. *Electroencephalography and Clinical Neurophysiology*, 2(1-4):377–388.
- Agarwal, G., Stevenson, I. H., Berényi, A., Mizuseki, K., Buzsáki, G., and Sommer, F. T. (2014). Spatially distributed local fields in the hippocampus encode rat position. *Science (New York, NY)*, 344(6184):626–630.
- Albrecht, D. G. and Hamilton, D. B. (1982). Striate cortex of monkey and cat: contrast response function. *Journal of neurophysiology*, 48(1):217–237.
- Ammermüller, J. and Kolb, H. (1996). Functional architecture of the turtle retina. *Progress in Retinal and Eye Research*, 15(2):393–433.
- Andersen, P., Bliss, T. V., and Skrede, K. K. (1971). Unit analysis of hippocampal population spikes. *Experimental brain research*, 13(2):208–221.
- Ariel, M. (2005). Latencies of climbing fiber inputs to turtle cerebellar cortex. *Journal of neurophysiology*, 93(2):1042–1054.
- Asahina, K., Louis, M., Piccinotti, S., and Vosshall, L. B. (2009). A circuit supporting concentration-invariant odor perception in *Drosophila*. *Journal of biology*, 8(1):9.
- Atallah, B. V. and Scanziani, M. (2009). Instantaneous modulation of gamma oscillation frequency by balancing excitation with inhibition. *Neuron*, 62(4):566–577.
- Bair, W., Cavanaugh, J. R., and Movshon, J. A. (2003). Time course and time-distance relationships for surround suppression in macaque V1 neurons. *23(20):7690–7701*.
- Barry, C., Bush, D., O’Keefe, J., and Burgess, N. (2012). Models of grid cells and theta oscillations. *Nature*, 488(7409):E1–2– discussion E2–3.
- Barthó, P., Hirase, H., Monconduit, L., Zugaro, M., Harris, K. D., and Buzsáki, G. (2004). Characterization of neocortical principal cells and interneurons by network interactions and extracellular features. *Journal of neurophysiology*, 92(1):600–608.
- Bartos, M., Vida, I., and Jonas, P. (2007). Synaptic mechanisms of synchronized gamma oscillations in inhibitory interneuron networks. *Nature reviews Neuroscience*, 8(1):45–56.

- Bass, A. H. and Northcutt, R. G. (1981). Retinal recipient nuclei in the painted turtle, *Chrysemys picta*: an autoradiographic and HRP study. *The Journal of Comparative Neurology*, 199(1):97–112.
- Bédard, C., Rodrigues, S., Roy, N., Contreras, D., and Destexhe, A. (2010). Evidence for frequency-dependent extracellular impedance from the transfer function between extracellular and intracellular potentials: intracellular-LFP transfer function. *Journal of computational neuroscience*, 29(3):389–403.
- Beierlein, M., Gibson, J. R., and Connors, B. W. (2000). A network of electrically coupled interneurons drives synchronized inhibition in neocortex. *Nature neuroscience*, 3(9):904–910.
- Belkin, D. A. (1963). Anoxia: tolerance in reptiles. *Science (New York, NY)*, 139(3554):492–493.
- Bell, C. C., Han, V. Z., Sugawara, Y., and Grant, K. (1997). Synaptic plasticity in a cerebellum-like structure depends on temporal order. *Nature*, 387(6630):278–281.
- Benucci, A., Frazor, R. A., and Carandini, M. (2007). Standing waves and traveling waves distinguish two circuits in visual cortex. *Neuron*, 55(1):103–117.
- Berényi, A., Somogyvári, Z., Nagy, A. J., Roux, L., Long, J. D., Fujisawa, S., Stark, E., Leonardo, A., Harris, T. D., and Buzsáki, G. (2014). Large-scale, high-density (up to 512 channels) recording of local circuits in behaving animals. *Journal of neurophysiology*, 111(5):1132–1149.
- Berger, H. (1929). Über das Elektrenkephalogramm des Menschen. *Archiv für Psychiatrie und Nervenkrankheiten*, 87(1):527–570.
- Bi, G. Q. and Poo, M. M. (1998). Synaptic modifications in cultured hippocampal neurons: dependence on spike timing, synaptic strength, and postsynaptic cell type. *Journal of Neuroscience*, 18(24):10464–10472.
- Bickler, P. E. and Buck, L. T. (2007). Hypoxia tolerance in reptiles, amphibians, and fishes: life with variable oxygen availability. *Annual review of physiology*, 69:145–170.
- Bischof, H.-J., Lieshoff, C., and Watanabe, S. (2006). Spatial memory and hippocampal function in a non-foodstoring songbird, the zebra finch (*Taeniopygia guttata*). *Reviews in the neurosciences*, 17(1-2):43–52.
- Blair, H. T., Wolday, A. C., and Zhang, K. (2007). Scale-invariant memory representations emerge from moiré interference between grid fields that produce theta oscillations: a computational model. 27(12):3211–3229.
- Bliss, T. V. and Lomo, T. (1973). Long-lasting potentiation of synaptic transmission in the dentate area of the anaesthetized rabbit following stimulation of the perforant path. *The Journal of physiology*, 232(2):331–356.
- Borst, A. and Helmstaedter, M. (2015). Common circuit design in fly and mammalian motion vision. 18(8):1067–1076.
- Bortone, D. S., Olsen, S. R., and Scanziani, M. (2014). Translaminar inhibitory cells recruited by layer 6 corticothalamic neurons suppress visual cortex. *Neuron*, 82(2):474–485.
- Boyden, E. S., Zhang, F., Bamberg, E., Nagel, G., and Deisseroth, K. (2005). Millisecond-timescale, genetically targeted optical control of neural activity. 8(9):1263–1268.
- Brainard, D. H. (1997). The Psychophysics Toolbox. *Spatial vision*, 10(4):433–436.
- Bruce, L. L. (2006). Evolution of the nervous system in reptiles. In Kaas, J. H., editor, *Evolution of Nervous Systems*, pages 125–156. Academic Press.

- Buchholz, F., Ringrose, L., Angrand, P. O., Rossi, F., and Stewart, A. F. (1996). Different thermostabilities of FLP and Cre recombinases: implications for applied site-specific recombination. *Nucleic acids research*, 24(21):4256–4262.
- Burgess, N., Barry, C., and O'Keefe, J. (2007). An oscillatory interference model of grid cell firing. *Hippocampus*, 17(9):801–812.
- Busse, L., Wade, A. R., and Carandini, M. (2009). Representation of concurrent stimuli by population activity in visual cortex. *Neuron*, 64(6):931–942.
- Butler, A. B. and Hodos, W. (2005). *Comparative Vertebrate Neuroanatomy: Evolution and Adaptation*. John Wiley & Sons, 2 edition.
- Buzsáki, G. (2002). Theta oscillations in the hippocampus. *Neuron*, 33(3):325–340.
- Buzsáki, G. (2006). *Rhythms of the Brain*. Oxford University Press.
- Buzsáki, G., Anastassiou, C. A., and Koch, C. (2012). The origin of extracellular fields and currents—EEG, ECoG, LFP and spikes. *Nature reviews Neuroscience*, 13(6):407–420.
- Buzsáki, G. and Draguhn, A. (2004). Neuronal oscillations in cortical networks. *Science (New York, NY)*, 304(5679):1926–1929.
- Buzsáki, G., Horváth, Z., Urioste, R., Hetke, J., and Wise, K. (1992). High-frequency network oscillation in the hippocampus. *Science (New York, NY)*, 256(5059):1025–1027.
- Buzsáki, G., Stark, E., Berényi, A., Khodagholy, D., Kipke, D. R., Yoon, E., and Wise, K. D. (2015). Tools for probing local circuits: high-density silicon probes combined with optogenetics. *Neuron*, 86(1):92–105.
- Cadwell, C. R., Palasantza, A., Jiang, X., Berens, P., Deng, Q., Yilmaz, M., Reimer, J., Shen, S., Bethge, M., Tolias, K. F., Sandberg, R., and Tolias, A. S. (2016). Electrophysiological, transcriptomic and morphologic profiling of single neurons using Patch-seq. *Nature biotechnology*, 34(2):199–203.
- Callaway, E. M. (2008). Transneuronal circuit tracing with neurotropic viruses. *Current opinion in neurobiology*, 18(6):617–623.
- Carandini, M. and Heeger, D. J. (2012). Normalization as a canonical neural computation. *Nature reviews Neuroscience*, 13(1):51–62.
- Carandini, M., Heeger, D. J., and Movshon, J. A. (1997). Linearity and normalization in simple cells of the macaque primary visual cortex. *Journal of Neuroscience*, 17(21):8621–8644.
- Cardin, J. A., Carlén, M., Meletis, K., Knoblich, U., Zhang, F., Deisseroth, K., Tsai, L.-H., and Moore, C. I. (2009). Driving fast-spiking cells induces gamma rhythm and controls sensory responses. *Nature*, 459(7247):663–667.
- Cassenaer, S. and Laurent, G. (2007). Hebbian STDP in mushroom bodies facilitates the synchronous flow of olfactory information in locusts. *Nature*, 448(7154):709–713.
- Cassenaer, S. and Laurent, G. (2012). Conditional modulation of spike-timing-dependent plasticity for olfactory learning. *Nature*, 482(7383):47–52.
- Cavanaugh, J. R., Bair, W., and Movshon, J. A. (2002). Nature and interaction of signals from the receptive field center and surround in macaque V1 neurons. *Journal of neurophysiology*, 88(5):2530–2546.
- Churchland, M. M., Cunningham, J. P., Kaufman, M. T., Foster, J. D., Nuyujukian, P., Ryu, S. I., and Shenoy, K. V. (2012). Neural population dynamics during reaching. *Nature*, 487(7405):51–56.

- Cirelli, C. (2009). The genetic and molecular regulation of sleep: from fruit flies to humans. *Nature reviews Neuroscience*, 10(8):549–560.
- Clark, H. F. and Kritchevsky, D. (1972). Growth and attenuation of rabies virus in cell cultures of reptilian origin. *Proceedings of the Society for Experimental Biology and Medicine. Society for Experimental Biology and Medicine (New York, N.Y.)*, 139(4):1317–1325.
- Cobb, S. R., Buhl, E. H., Halasy, K., Paulsen, O., and Somogyi, P. (1995). Synchronization of neuronal activity in hippocampus by individual GABAergic interneurons. *Nature*, 378(6552):75–78.
- Colombe, J. B., Sylvester, J., Block, J., and Ulinski, P. S. (2004). Subpial and stellate cells: two populations of interneurons in turtle visual cortex. *The Journal of Comparative Neurology*, 471(3):333–351.
- Connors, B. W. and Kriegstein, A. R. (1986). Cellular physiology of the turtle visual cortex: distinctive properties of pyramidal and stellate neurons. 6(1):164–177.
- Crawford, N. G., Faircloth, B. C., McCormack, J. E., Brumfield, R. T., Winker, K., and Glenn, T. C. (2012). More than 1000 ultraconserved elements provide evidence that turtles are the sister group of archosaurs. *Biology letters*, 8(5):783–786.
- Crawford, N. G., Parham, J. F., Sellas, A. B., Faircloth, B. C., Glenn, T. C., Papenfuss, T. J., Henderson, J. B., Hansen, M. H., and Simison, W. B. (2015). A phylogenomic analysis of turtles. *Molecular phylogenetics and evolution*, 83:250–257.
- Creutzfeldt, O. D., Watanabe, S., and Lux, H. D. (1966a). Relations between EEG phenomena and potentials of single cortical cells. I. Evoked responses after thalamic and epicortical stimulation. *Electroencephalography and Clinical Neurophysiology*, 20(1):1–18.
- Creutzfeldt, O. D., Watanabe, S., and Lux, H. D. (1966b). Relations between EEG phenomena and potentials of single cortical cells. II. Spontaneous and convulsoid activity. *Electroencephalography and Clinical Neurophysiology*, 20(1):19–37.
- Dederen, P. J., Gribnau, A. A., and Curfs, M. H. (1994). Retrograde neuronal tracing with cholera toxin B subunit: comparison of three different visualization methods. *The Histochemical journal*, 26(11):856–862.
- DeFalco, J., Tomishima, M., Liu, H., and Zhao, C. (2001). Virus-assisted mapping of neural inputs to a feeding center in the hypothalamus. *Science (New York, NY)*.
- DeFelipe, J., López-Cruz, P. L., Benavides-Piccione, R., Bielza, C., Larrañaga, P., Anderson, S., Burkhalter, A., Cauli, B., Fairén, A., Feldmeyer, D., Fishell, G., Fitzpatrick, D., Freund, T. F., González-Burgos, G., Hestrin, S., Hill, S., Hof, P. R., Huang, J., Jones, E. G., Kawaguchi, Y., Kisvarday, Z., Kubota, Y., Lewis, D. A., Marín, O., Markram, H., McBain, C. J., Meyer, H. S., Monyer, H., Nelson, S. B., Rockland, K., Rossier, J., Rubenstein, J. L. R., Rudy, B., Scanziani, M., Shepherd, G. M., Sherwood, C. C., Staiger, J. F., Tamás, G., Thomson, A., Wang, Y., Yuste, R., and Ascoli, G. A. (2013). New insights into the classification and nomenclature of cortical GABAergic interneurons. *Nature reviews Neuroscience*, 14(3):202–216.
- Deisseroth, K. (2011). Optogenetics. *Nature methods*, 8(1):26–29.
- Desan, P. H. (1984). The organization of the cerebral cortex of the pond turtle, *Pseudemys Scripta Elegans*. *PhD Thesis, Harvard University*.
- Dodt, H.-U., Leischner, U., Schierloh, A., Jährling, N., Mauch, C. P., Deininger, K., Deussing, J. M., Eder, M., Zieglgänsberger, W., and Becker, K. (2007). Ultramicroscopy: three-dimensional visualization of neuronal networks in the whole mouse brain. *Nature methods*, 4(4):331–336.
- Domnisoru, C., Kinkhabwala, A. A., and Tank, D. W. (2013). Membrane potential dynamics of grid cells. *Nature*, 495(7440):199–204.

- Dong, J. Y., Fan, P. D., and Frizzell, R. A. (1996). Quantitative analysis of the packaging capacity of recombinant adeno-associated virus. *Human gene therapy*, 7(17):2101–2112.
- Dorst, S. E. and Mills, C. A. (1923). Comparative studies on blood clotting in mammals, birds and reptiles. *American Journal of Physiology*, 64(1):167–180.
- Douglas, R. J. and Martin, K. A. C. (2004). Neuronal circuits of the neocortex. *Annual review of neuroscience*, 27:419–451.
- Economo, M. N., Clack, N. G., Lavis, L. D., Gerfen, C. R., Svoboda, K., Myers, E. W., and Chandrashekar, J. (2016). A platform for brain-wide imaging and reconstruction of individual neurons. *eLife*, 5:e10566.
- Elul, R. (1971). The genesis of the EEG. *International review of neurobiology*, 15:227–272.
- Engel, A. K., Fries, P., and Singer, W. (2001). Dynamic predictions: oscillations and synchrony in top-down processing. *Nature reviews Neuroscience*, 2(10):704–716.
- Ermentrout, G. B. and Kleinfeld, D. (2001). Traveling electrical waves in cortex: insights from phase dynamics and speculation on a computational role. *Neuron*, 29(1):33–44.
- Ernst, C. and Christie, B. R. (2006). Isolectin-IB 4 as a vascular stain for the study of adult neurogenesis. *Journal of neuroscience methods*, 150(1):138–142.
- Fernandez, A. S., Pieau, C., Repérant, J., Boncinelli, E., and Wassef, M. (1998). Expression of the Emx-1 and Dlx-1 homeobox genes define three molecularly distinct domains in the telencephalon of mouse, chick, turtle and frog embryos: implications for the evolution of telencephalic subdivisions in amniotes. *Development (Cambridge, England)*, 125(11):2099–2111.
- Fiscella, M., Farrow, K., Jones, I. L., Jäckel, D., Müller, J., Frey, U., Bakkum, D. J., Hantz, P., Roska, B., and Hierlemann, A. (2012). Recording from defined populations of retinal ganglion cells using a high-density CMOS-integrated microelectrode array with real-time switchable electrode selection. *Journal of neuroscience methods*, 211(1):103–113.
- Fournier, J., Müller, C. M., and Laurent, G. (2015). Looking for the roots of cortical sensory computation in three-layered cortices. *Current opinion in neurobiology*, 31:119–126.
- Fournier, J., Müller, C. M., Schneider, I., and Laurent, G. (in press). Visual processing in a non-retinotopic visual cortex.
- Freeman, T. C. B., Durand, S., Kiper, D. C., and Carandini, M. (2002). Suppression without inhibition in visual cortex. *Neuron*, 35(4):759–771.
- Fregnac, Y., Fournier, J., Gérard-Mercier, F., Monier, C., Pananceau, M., Carelli, P., and Troncoso, X. (2016). The Visual Brain: Computing Through Multiscale Complexity. In Buzsáki, G. and Christen, Y., editors, *Micro-, Meso- and Macro-Dynamics of the Brain*, pages 43–57. Springer, Cham (CH).
- Fries, P., Reynolds, J. H., Rorie, A. E., and Desimone, R. (2001). Modulation of oscillatory neuronal synchronization by selective visual attention. *Science (New York, NY)*, 291(5508):1560–1563.
- Gabbiani, F., Krapp, H. G., Koch, C., and Laurent, G. (2002). Multiplicative computation in a visual neuron sensitive to looming. *Nature*, 420(6913):320–324.
- Gähwiler, B. H., Capogna, M., Debanne, D., McKinney, R. A., and Thompson, S. M. (1997). Organotypic slice cultures: a technique has come of age. *Trends in neurosciences*, 20(10):471–477.
- Galarreta, M. and Hestrin, S. (1999). A network of fast-spiking cells in the neocortex connected by electrical synapses. *Nature*, 402(6757):72–75.

- Galarreta, M. and Hestrin, S. (2002). Electrical and chemical synapses among parvalbumin fast-spiking GABAergic interneurons in adult mouse neocortex. *Proceedings of the National Academy of Sciences of the United States of America*, 99(19):12438–12443.
- Gelperin, A. and Tank, D. W. (1990). Odour-modulated collective network oscillations of olfactory interneurons in a terrestrial mollusc. *Nature*, 345(6274):437–440.
- Geva-Sagiv, M., Las, L., Yovel, Y., and Ulanovsky, N. (2015). Spatial cognition in bats and rats: from sensory acquisition to multiscale maps and navigation. *Nature reviews Neuroscience*, 16(2):94–108.
- Ginger, M., Haberl, M., Conzelmann, K.-K., Schwarz, M. K., and Frick, A. (2013). Revealing the secrets of neuronal circuits with recombinant rabies virus technology. *Frontiers in neural circuits*, 7:2.
- Gouwens, N. W. and Wilson, R. I. (2009). Signal propagation in *Drosophila* central neurons. 29(19):6239–6249.
- Gradinaru, V., Thompson, K. R., Zhang, F., Mogri, M., Kay, K., Schneider, M. B., and Deisseroth, K. (2007). Targeting and readout strategies for fast optical neural control in vitro and in vivo. 27(52):14231–14238.
- Granda, A. M. and Dvorak, C. A. (1977). Vision in Turtles. In Crescitelli, F., editor, *The Visual System in Vertebrates*, pages 451–495. Springer.
- Gray, C. M., König, P., Engel, A. K., and Singer, W. (1989). Oscillatory responses in cat visual cortex exhibit inter-columnar synchronization which reflects global stimulus properties. , *Published online: 23 March 1989*; | doi:10.1038/338334a0, 338(6213):334–337.
- Gray, C. M. and Singer, W. (1989). Stimulus-specific neuronal oscillations in orientation columns of cat visual cortex. *Proceedings of the National Academy of Sciences of the United States of America*, 86(5):1698–1702.
- Greer, C. A., Mori, K., and Shepherd, G. M. (1981). Localization of synaptic responses in the in vitro turtle olfactory bulb using the [¹⁴C]2-deoxyglucose method. *Brain research*, 217(2):295–303.
- Guzowski, J. F. (2002). Insights into immediate-early gene function in hippocampal memory consolidation using antisense oligonucleotide and fluorescent imaging approaches. *Hippocampus*, 12(1):86–104.
- Hackett, E. and Hann, C. (1967). Slow clotting of reptile bloods. *Journal of comparative pathology*, 77(2):175–180.
- Hagen, E., Dahmen, D., Stavrinou, M. L., Lindén, H., Tetzlaff, T., van Albada, S. J., Grün, S., Diesmann, M., and Einevoll, G. T. (2016). Hybrid Scheme for Modeling Local Field Potentials from Point-Neuron Networks. *Cerebral cortex (New York, NY : 1991)*.
- Haider, B., Schulz, D. P. A., Häusser, M., and Carandini, M. (2016). Millisecond Coupling of Local Field Potentials to Synaptic Currents in the Awake Visual Cortex. *Neuron*, 90(1):35–42.
- Han, X. and Boyden, E. S. (2007). Multiple-color optical activation, silencing, and desynchronization of neural activity, with single-spike temporal resolution. *PLoS one*, 2(3):e299.
- Harris, K. D. and Thiele, A. (2011). Cortical state and attention. *Nature reviews Neuroscience*, 12(9):509–523.
- Harvey, C. D., Collman, F., Dombeck, D. A., and Tank, D. W. (2009). Intracellular dynamics of hippocampal place cells during virtual navigation. *Nature*, 461(7266):941–946.
- Hasselmo, M. E., Giocomo, L. M., and Zilli, E. A. (2007). Grid cell firing may arise from interference of theta frequency membrane potential oscillations in single neurons. *Hippocampus*, 17(12):1252–1271.
- Hedges, S. B. (2012). Amniote phylogeny and the position of turtles. *BMC Biology*, 10(1):64.

- Hedges, S. B. and Poling, L. L. (1999). A molecular phylogeny of reptiles. *Science (New York, NY)*, 283(5404):998–1001.
- Helmstaedter, M., Staiger, J. F., Sakmann, B., and Feldmeyer, D. (2008). Efficient recruitment of layer 2/3 interneurons by layer 4 input in single columns of rat somatosensory cortex. *28(33):8273–8284*.
- Hemberger, M., Pammer, L., and Laurent, G. (2016). Comparative approaches to cortical microcircuits. *Current opinion in neurobiology*, 41:24–30.
- Henze, D. A., Borhegyi, Z., Csicsvari, J., Mamiya, A., Harris, K. D., and Buzsáki, G. (2000). Intracellular features predicted by extracellular recordings in the hippocampus in vivo. *Journal of neurophysiology*, 84(1):390–400.
- Hernandez, O., Papagiakoumou, E., Tanese, D., Fidelin, K., Wyart, C., and Emiliani, V. (2016). Three-dimensional spatiotemporal focusing of holographic patterns. *Nature communications*, 7:11928.
- Hirsch, J. A. and Gilbert, C. D. (1991). Synaptic physiology of horizontal connections in the cat's visual cortex. *Journal of Neuroscience*, 11(6):1800–1809.
- Holtmaat, A. and Svoboda, K. (2009). Experience-dependent structural synaptic plasticity in the mammalian brain. *Nature reviews Neuroscience*, 10(9):647–658.
- Hong, E. J. and Wilson, R. I. (2013). Olfactory neuroscience: normalization is the norm. *Current biology : CB*, 23(24):R1091–3.
- Hopfield, J. J. (1995). Pattern recognition computation using action potential timing for stimulus representation. *Nature*, 376(6535):33–36.
- Hounsgaard, J. and Nicholson, C. (1990). The Isolated Turtle Brain and the Physiology of Neuronal Circuits. In Jahnsen, H., editor, *Preparations of Vertebrate Central Nervous System In Vitro*, pages 155–181.
- Houweling, A. R. and Brecht, M. (2008). Behavioural report of single neuron stimulation in somatosensory cortex. *Nature*, 451(7174):65–68.
- Hu, H., Gan, J., and Jonas, P. (2014). Interneurons. Fast-spiking, parvalbumin⁺ GABAergic interneurons: from cellular design to microcircuit function. *Science (New York, NY)*, 345(6196):1255–1263.
- Hubel, D. H. and Wiesel, T. N. (1959). Receptive fields of single neurones in the cat's striate cortex. *The Journal of physiology*, 148(3):574–591.
- Huerta, P. T. and Lisman, J. E. (1995). Bidirectional synaptic plasticity induced by a single burst during cholinergic theta oscillation in CA1 in vitro. *Neuron*, 15(5):1053–1063.
- Isaacson, J. S. and Scanziani, M. (2011). How inhibition shapes cortical activity. *Neuron*, 72(2):231–243.
- Jacques, F. A. (1963). Blood coagulation and anticoagulant mechanisms in the turtle *Pseudemys Elegans*. *Comparative biochemistry and physiology*, 16:241–249.
- Jeong, J.-W., Shin, G., Park, S. I., Yu, K. J., Xu, L., and Rogers, J. A. (2015). Soft materials in neuroengineering for hard problems in neuroscience. *Neuron*, 86(1):175–186.
- Jiang, X., Shen, S., Cadwell, C. R., Berens, P., Sinz, F., Ecker, A. S., Patel, S., and Tolias, A. S. (2015). Principles of connectivity among morphologically defined cell types in adult neocortex. *Science (New York, NY)*, 350(6264):aac9462.
- Johnson, D. M., Illig, K. R., Behan, M., and Haberly, L. B. (2000). New features of connectivity in piriform cortex visualized by intracellular injection of pyramidal cells suggest that "primary" olfactory cortex functions like "association" cortex in other sensory systems. *Journal of Neuroscience*, 20(18):6974–6982.

- Jones, E. G. and Peters, A. (1990). *Comparative Structure and Evolution of Cerebral Cortex*. Springer Science & Business Media.
- Jortner, R. A., Farivar, S. S., and Laurent, G. (2007). A simple connectivity scheme for sparse coding in an olfactory system. *27(7):1659–1669*.
- Kaas, J. H. (2008). The evolution of the complex sensory and motor systems of the human brain. *Brain research bulletin, 75(2-4):384–390*.
- Kamondi, A., Acsády, L., Wang, X.-J., and Buzsáki, G. (1998). Theta oscillations in somata and dendrites of hippocampal pyramidal cells in vivo: Activity-dependent phase-precession of action potentials. *Hippocampus, 8(3):244–261*.
- Kang, H. and Schuman, E. M. (1995). Long-lasting neurotrophin-induced enhancement of synaptic transmission in the adult hippocampus. *Science (New York, NY), 267(5204):1658–1662*.
- Kaschube, M., Schnabel, M., Löwel, S., Coppola, D. M., White, L. E., and Wolf, F. (2010). Universality in the evolution of orientation columns in the visual cortex. *Science (New York, NY), 330(6007):1113–1116*.
- Katzner, S., Busse, L., and Carandini, M. (2011). GABAA inhibition controls response gain in visual cortex. *31(16):5931–5941*.
- Kazama, H. and Wilson, R. I. (2008). Homeostatic matching and nonlinear amplification at identified central synapses. *Neuron, 58(3):401–413*.
- Kazama, H. and Wilson, R. I. (2009). Origins of correlated activity in an olfactory circuit. *12(9):1136–1144*.
- Kelsch, W., Stolfi, A., and Lois, C. (2012). Genetic labeling of neuronal subsets through enhancer trapping in mice. *PloS one, 7(6):e38593*.
- Kennedy, M. J., Hughes, R. M., Peteya, L. A., Schwartz, J. W., Ehlers, M. D., and Tucker, C. L. (2010). Rapid blue-light-mediated induction of protein interactions in living cells. *Nature methods, 7(12):973–975*.
- Klausberger, T., Magill, P. J., Márton, L. F., Roberts, J. D. B., Cobden, P. M., Buzsáki, G., and Somogyi, P. (2003). Brain-state- and cell-type-specific firing of hippocampal interneurons in vivo. *Nature, 421(6925):844–848*.
- Klausberger, T. and Somogyi, P. (2008). Neuronal diversity and temporal dynamics: the unity of hippocampal circuit operations. *Science (New York, NY), 321(5885):53–57*.
- Konishi, M. (1991). Deciphering the Brain's Codes. *Neural Computation, 3(1):1–18*.
- Konopacki, J., MacIver, M. B., Bland, B. H., and Roth, S. H. (1987). Carbachol-induced EEG 'theta' activity in hippocampal brain slices. *Brain research, 405(1):196–198*.
- Körding, K. P. and Wolpert, D. M. (2006). Bayesian decision theory in sensorimotor control. *Trends in cognitive sciences, 10(7):319–326*.
- Kosareva, A. A. (1967). Projection of optic fibers to visual centers in a turtle (*Emys orbicularis*). *The Journal of Comparative Neurology, 130(3):263–275*.
- Kreiman, G., Hung, C. P., Kraskov, A., Quiroga, R. Q., Poggio, T., and Dicarlo, J. J. (2006). Object selectivity of local field potentials and spikes in the macaque inferior temporal cortex. *Neuron, 49(3):433–445*.
- Kreiter, A. K. and Singer, W. (1992). Oscillatory Neuronal Responses in the Visual Cortex of the Awake Macaque Monkey. *The European journal of neuroscience, 4(4):369–375*.
- Kriegstein, A. R. (1987). Synaptic responses of cortical pyramidal neurons to light stimulation in the isolated turtle visual system. *Journal of Neuroscience, 7(8):2488–2492*.

- Kriegstein, A. R. and Connors, B. W. (1986). Cellular physiology of the turtle visual cortex: synaptic properties and intrinsic circuitry. *6*(1):178–191.
- Kügler, S., Kilic, E., and Bähr, M. (2003). Human synapsin 1 gene promoter confers highly neuron-specific long-term transgene expression from an adenoviral vector in the adult rat brain depending on the transduced area. *Gene therapy*, *10*(4):337–347.
- Kügler, S., Meyn, L., Holzmüller, H., Gerhardt, E., Isenmann, S., Schulz, J. B., and Bähr, M. (2001). Neuron-specific expression of therapeutic proteins: evaluation of different cellular promoters in recombinant adenoviral vectors. *Molecular and cellular neurosciences*, *17*(1):78–96.
- Kumar, M., Keller, B., Makalou, N., and Sutton, R. E. (2004). Systematic Determination of the Packaging Limit of Lentiviral Vectors. *Human gene therapy*, *12*(15):1893–1905.
- Lagarias, J. C., Reeds, J. A., Wright, M. H., and Wright, P. E. (1998). Convergence properties of the Nelder-Mead simplex method in low dimensions. *Siam Journal on Optimization*, *9*(1):112–147.
- Lanahan, A. and Worley, P. (1998). Immediate-early genes and synaptic function. *Neurobiology of learning and memory*, *70*(1-2):37–43.
- Larkum, M. E., Watanabe, S., Lasser-Ross, N., Rhodes, P., and Ross, W. N. (2008). Dendritic properties of turtle pyramidal neurons. *Journal of neurophysiology*, *99*(2):683–694.
- Lasztozci, B. and Klausberger, T. (2014). Layer-specific GABAergic control of distinct gamma oscillations in the CA1 hippocampus. *Neuron*, *81*(5):1126–1139.
- Laurent, G. (2002). Olfactory network dynamics and the coding of multidimensional signals. *Nature reviews Neuroscience*, *3*(11):884–895.
- Laurent, G., Fournier, J., Hemberger, M., Müller, C., Naumann, R., Ondracek, J. M., Pammer, L., Reiter, S., Shein-Idelson, M., Tosches, M. A., and Yamawaki, T. (2016). Cortical Evolution: Introduction to the Reptilian Cortex. In Buzsáki, G. and Christen, Y., editors, *Micro-, Meso- and Macro-Dynamics of the Brain*, pages 23–33. Springer, Cham (CH).
- Laurent, G. and Naraghi, M. (1994). Odorant-induced oscillations in the mushroom bodies of the locust. *Journal of Neuroscience*, *14*(5 Pt 2):2993–3004.
- Lee, M. S. Y. (1997). Reptile relationships turn turtle. *Nature*, *389*(6648):245–245.
- Lein, E. S., Hawrylycz, M. J., Ao, N., Ayres, M., Bensinger, A., Bernard, A., Boe, A. F., Boguski, M. S., Brockway, K. S., Byrnes, E. J., Chen, L., Chen, L., Chen, T.-M., Chin, M. C., Chong, J., Crook, B. E., Czaplinska, A., Dang, C. N., Datta, S., Dee, N. R., Desaki, A. L., Desta, T., Diep, E., Dolbeare, T. A., Donelan, M. J., Dong, H.-W., Dougherty, J. G., Duncan, B. J., Ebbert, A. J., Eichele, G., Estin, L. K., Faber, C., Facer, B. A., Fields, R., Fischer, S. R., Fliss, T. P., Frensley, C., Gates, S. N., Glatfelter, K. J., Halverson, K. R., Hart, M. R., Hohmann, J. G., Howell, M. P., Jeung, D. P., Johnson, R. A., Karr, P. T., Kawal, R., Kidney, J. M., Knapik, R. H., Kuan, C. L., Lake, J. H., Laramee, A. R., Larsen, K. D., Lau, C., Lemon, T. A., Liang, A. J., Liu, Y., Luong, L. T., Michaels, J., Morgan, J. J., Morgan, R. J., Mortrud, M. T., Mosqueda, N. F., Ng, L. L., Ng, R., Orta, G. J., Overly, C. C., Pak, T. H., Parry, S. E., Pathak, S. D., Pearson, O. C., Puchalski, R. B., Riley, Z. L., Rickett, H. R., Rowland, S. A., Royall, J. J., Ruiz, M. J., Sarno, N. R., Schaffnit, K., Shapovalova, N. V., Sivisay, T., Slaughterbeck, C. R., Smith, S. C., Smith, K. A., Smith, B. I., Sodt, A. J., Stewart, N. N., Stumpf, K.-R., Sunkin, S. M., Sutram, M., Tam, A., Teemer, C. D., Thaller, C., Thompson, C. L., Varnam, L. R., Visel, A., Whitlock, R. M., Wohnotka, P. E., Wolkey, C. K., Wong, V. Y., Wood, M., Yaylaoglu, M. B., Young, R. C., Youngstrom, B. L., Yuan, X. F., Zhang, B., Zwingman, T. A., and Jones, A. R. (2007). Genome-wide atlas of gene expression in the adult mouse brain. *Nature*, *445*(7124):168–176.
- Li, C.-Y. T., Poo, M.-M., and Dan, Y. (2009). Burst spiking of a single cortical neuron modifies global brain state. *Science (New York, NY)*, *324*(5927):643–646.

- Li, P. H., Field, G. D., Greschner, M., Ahn, D., Gunning, D. E., Mathieson, K., Sher, A., Litke, A. M., and Chichilnisky, E. J. (2014). Retinal representation of the elementary visual signal. *Neuron*, 81(1):130–139.
- Li, P. H., Gauthier, J. L., Schiff, M., Sher, A., Ahn, D., Field, G. D., Greschner, M., Callaway, E. M., Litke, A. M., and Chichilnisky, E. J. (2015). Anatomical identification of extracellularly recorded cells in large-scale multielectrode recordings. 35(11):4663–4675.
- Lilley, C. E., Branston, R. H., and Coffin, R. S. (2001). Herpes simplex virus vectors for the nervous system. *Current gene therapy*, 1(4):339–358.
- Lindén, H., Tetzlaff, T., Potjans, T. C., Pettersen, K. H., Grün, S., Diesmann, M., and Einevoll, G. T. (2011). Modeling the spatial reach of the LFP. *Neuron*, 72(5):859–872.
- Litke, A. M., Bezayiff, N., Chichilnisky, E. J., Cunningham, W., Dabrowski, W., Grillo, A. A., Grivich, M., Grybos, P., Hottowy, P., Kachiguine, S., Kalmar, R. S., Mathieson, K., Petrusca, D., Rahman, M., and Sher, A. (2003). What does the eye tell the brain?: Development of a system for the large scale recording of retinal output activity. In *2003 IEEE Nuclear Science Symposium. Conference Record (IEEE Cat. No.03CH37515)*, pages 951–955 Vol.2. IEEE.
- Liu, X. B. and Jones, E. G. (1996). Localization of alpha type II calcium calmodulin-dependent protein kinase at glutamatergic but not gamma-aminobutyric acid (GABAergic) synapses in thalamus and cerebral cortex. *Proceedings of the National Academy of Sciences of the United States of America*, 93(14):7332–7336.
- Lohmann, K. J., Cain, S. D., Dodge, S. A., and Lohmann, C. M. (2001). Regional magnetic fields as navigational markers for sea turtles. *Science (New York, NY)*, 294(5541):364–366.
- London, M., Roth, A., Beeren, L., Häusser, M., and Latham, P. E. (2010). Sensitivity to perturbations in vivo implies high noise and suggests rate coding in cortex. *Nature*, 466(7302):123–127.
- Long, M. A. and Fee, M. S. (2008). Using temperature to analyse temporal dynamics in the songbird motor pathway. *Nature*, 456(7219):189–194.
- Lopez, C. M., Mitra, S., Putzeys, J., Raducanu, B., Ballini, M., Andrei, A., Severi, S., Welkenhuysen, M., Van Hoof, C., Musa, S., and Yazicioglu, R. F. (2016). 22.7 A 966-electrode neural probe with 384 configurable channels in 0.13 μ m SOI CMOS. In *2016 IEEE International Solid-State Circuits Conference (ISSCC)*, pages 392–393. IEEE.
- Louie, K. and Wilson, M. A. (2001). Temporally structured replay of awake hippocampal ensemble activity during rapid eye movement sleep. *Neuron*, 29(1):145–156.
- Lubenov, E. V. and Siapas, A. G. (2008). Decoupling through synchrony in neuronal circuits with propagation delays. *Neuron*, 58(1):118–131.
- Lubenov, E. V. and Siapas, A. G. (2009). Hippocampal theta oscillations are travelling waves. *Nature*, 459(7246):534–539.
- Lübke, J., Roth, A., Feldmeyer, D., and Sakmann, B. (2003). Morphometric analysis of the columnar innervation domain of neurons connecting layer 4 and layer 2/3 of juvenile rat barrel cortex. *Cerebral cortex (New York, NY : 1991)*, 13(10):1051–1063.
- Luo, L., Callaway, E. M., and Svoboda, K. (2008). Genetic Dissection of Neural Circuits. *Neuron*, 57(5):634–660.
- Lyson, T. R., Sperling, E. A., Heimberg, A. M., Gauthier, J. A., King, B. L., and Peterson, K. J. (2012). MicroRNAs support a turtle + lizard clade. *Biology letters*, 8(1):104–107.
- Marder, E. and Taylor, A. L. (2011). Multiple models to capture the variability in biological neurons and networks. 14(2):133–138.

- Markram, H., Lübke, J., Frotscher, M., Roth, A., and Sakmann, B. (1997a). Physiology and anatomy of synaptic connections between thick tufted pyramidal neurones in the developing rat neocortex. *The Journal of physiology*, 500 (Pt 2):409–440.
- Markram, H., Lübke, J., Frotscher, M., and Sakmann, B. (1997b). Regulation of synaptic efficacy by coincidence of postsynaptic APs and EPSPs. *Science (New York, NY)*, 275(5297):213–215.
- Markram, H., Muller, E., Ramaswamy, S., Reimann, M. W., Abdellah, M., Sanchez, C. A., Ailamaki, A., Alonso-Nanclares, L., Antille, N., Arsever, S., Kahou, G. A. A., Berger, T. K., Bilgili, A., Buncic, N., Chalimourda, A., Chindemi, G., Courcol, J.-D., Delalondre, F., Delattre, V., Druckmann, S., Dumusc, R., Dynes, J., Eilemann, S., Gal, E., Gevaert, M. E., Ghobril, J.-P., Gidon, A., Graham, J. W., Gupta, A., Haenel, V., Hay, E., Heinis, T., Hernando, J. B., Hines, M., Kanari, L., Keller, D., Kenyon, J., Khazen, G., Kim, Y., King, J. G., Kisvarday, Z., Kumbhar, P., Lasserre, S., Le Bé, J.-V., Magalhães, B. R. C., Merchán-Pérez, A., Meystre, J., Morrice, B. R., Muller, J., Muñoz-Céspedes, A., Muralidhar, S., Muthurasa, K., Nachbaur, D., Newton, T. H., Nolte, M., Ovcharenko, A., Palacios, J., Pastor, L., Perin, R., Ranjan, R., Riachi, I., Rodríguez, J.-R., Riquelme, J. L., Rössert, C., Sfyarakis, K., Shi, Y., Shillcock, J. C., Silberberg, G., Silva, R., Tauheed, F., Telefont, M., Toledo-Rodriguez, M., Tränkler, T., Van Geit, W., Díaz, J. V., Walker, R., Wang, Y., Zaninetta, S. M., DeFelipe, J., Hill, S. L., Segev, I., and Schürmann, F. (2015). Reconstruction and Simulation of Neocortical Microcircuitry. *Cell*, 163(2):456–492.
- Marr, D. (1982). *Vision*. W. H. Freeman and Company, 1 edition.
- Marr, D. and Poggio, T. (1976). Cooperative computation of stereo disparity. *Science (New York, NY)*, 194(4262):283–287.
- Marre, O., Amodei, D., Deshmukh, N., Sadeghi, K., Soo, F., Holy, T. E., and Berry, M. J. (2012). Mapping a complete neural population in the retina. *32(43):14859–14873*.
- Massimini, M., Huber, R., Ferrarelli, F., Hill, S., and Tononi, G. (2004). The sleep slow oscillation as a traveling wave. *24(31):6862–6870*.
- Mayer, U., Watanabe, S., and Bischof, H.-J. (2010). Hippocampal activation of immediate early genes *Zenk* and *c-Fos* in zebra finches (*Taeniopygia guttata*) during learning and recall of a spatial memory task. *Neurobiology of learning and memory*, 93(3):322–329.
- Mazor, O. and Laurent, G. (2005). Transient dynamics versus fixed points in odor representations by locust antennal lobe projection neurons. *Neuron*, 48(4):661–673.
- Mazurskaya, P. Z. (1973a). Organization of receptive fields in the forebrain of *Emys orbicularis*. *Neuroscience and behavioral physiology*, 6(4):311–318.
- Mazurskaya, P. Z. (1973b). Retinal projection in the forebrain of *Emys orbicularis*. *Neuroscience and behavioral physiology*, 6(1):75–82.
- Mazurskaya, P. Z., Davydova, T. V., and D, S. G. (1966). Functional organization of exteroceptive projections in the turtle forebrain cortex (in Russian). *Fiziologicheskii zhurnal SSSR imeni I. M. Sechenova*, (52):1049–1057.
- McAlpin, S., Duckett, P., and Stow, A. (2011). Lizards cooperatively tunnel to construct a long-term home for family members. *PLoS one*, 6(5):e19041.
- Medina, L. and Abellán, A. (2009). Development and evolution of the pallium. *Seminars in cell & developmental biology*, 20(6):698–711.
- Medini, P. (2011). Layer- and cell-type-specific subthreshold and suprathreshold effects of long-term monocular deprivation in rat visual cortex. *31(47):17134–17148*.
- Meyer, A. H., Katona, I., Blatow, M., Rozov, A., and Monyer, H. (2002). In vivo labeling of parvalbumin-positive interneurons and analysis of electrical coupling in identified neurons. *22(16):7055–7064*.

- Mischiati, M., Lin, H.-T., Herold, P., Imler, E., Olberg, R., and Leonardo, A. (2015). Internal models direct dragonfly interception steering. *Nature*, 517(7534):333–338.
- Mitzdorf, U. (1985). Current source-density method and application in cat cerebral cortex: investigation of evoked potentials and EEG phenomena. *Physiological reviews*, 65(1):37–100.
- Miyazaki, J., Takaki, S., Araki, K., Tashiro, F., Tominaga, A., Takatsu, K., and Yamamura, K. (1989). Expression vector system based on the chicken beta-actin promoter directs efficient production of interleukin-5. *Gene*, 79(2):269–277.
- Montiel, J. F., Vasistha, N. A., Garcia-Moreno, F., and Molnár, Z. (2016). From sauropsids to mammals and back: New approaches to comparative cortical development. *The Journal of Comparative Neurology*, 524(3):630–645.
- Monyer, H. and Markram, H. (2004). Interneuron Diversity series: Molecular and genetic tools to study GABAergic interneuron diversity and function. *Trends in neurosciences*, 27(2):90–97.
- Moreno, N., Morona, R., López, J. M., and González, A. (2010). Subdivisions of the turtle *Pseudemys scripta* subpallium based on the expression of regulatory genes and neuronal markers. *The Journal of Comparative Neurology*, 518(24):4877–4902.
- Mori, K., Nowycky, M., and Shepherd, G. (1984). ... and inhibitory interactions at distal dendritic sites on mitral cells in the isolated turtle *Journal of Neuroscience*.
- Mori, K., Nowycky, M. C., and Shepherd, G. M. (1981a). Analysis of a long-duration inhibitory potential in mitral cells in the isolated turtle olfactory bulb. *The Journal of physiology*, 314:311–320.
- Mori, K., Nowycky, M. C., and Shepherd, G. M. (1981b). Analysis of synaptic potentials in mitral cells in the isolated turtle olfactory bulb. *The Journal of physiology*, 314:295–309.
- Mori, K., Nowycky, M. C., and Shepherd, G. M. (1981c). Electrophysiological analysis of mitral cells in the isolated turtle olfactory bulb. *The Journal of physiology*, 314:281–294.
- Mori, K., Nowycky, M. C., and Shepherd, G. M. (1982). Impulse activity in presynaptic dendrites: analysis of mitral cells in the isolated turtle olfactory bulb. *Journal of Neuroscience*, 2(4):497–502.
- Mulligan, K. A. and Ulinski, P. S. (1990). Organization of geniculocortical projections in turtles: isoazimuth lamellae in the visual cortex. *The Journal of Comparative Neurology*, 296(4):531–547.
- Nagel, G., Brauner, M., Liewald, J. F., Adeishvili, N., Bamberg, E., and Gottschalk, A. (2005). Light Activation of Channelrhodopsin-2 in Excitable Cells of *Caenorhabditis elegans* Triggers Rapid Behavioral Responses. *Current Biology*, 15(24):2279–2284.
- Nagel, G., Ollig, D., Fuhrmann, M., Kateriya, S., Musti, A. M., Bamberg, E., and Hegemann, P. (2002). Channelrhodopsin-1: a light-gated proton channel in green algae. *Science (New York, NY)*, 296(5577):2395–2398.
- Nagel, G., Szellas, T., Huhn, W., Kateriya, S., Adeishvili, N., Berthold, P., Ollig, D., Hegemann, P., and Bamberg, E. (2003). Channelrhodopsin-2, a directly light-gated cation-selective membrane channel. *Proceedings of the National Academy of Sciences of the United States of America*, 100(24):13940–13945.
- Nase, G., Singer, W., Monyer, H., and Engel, A. K. (2003). Features of neuronal synchrony in mouse visual cortex. *Journal of neurophysiology*, 90(2):1115–1123.
- Nathanson, J. L., Jappelli, R., Scheeff, E. D., Manning, G., Obata, K., Brenner, S., and Callaway, E. M. (2009). Short Promoters in Viral Vectors Drive Selective Expression in Mammalian Inhibitory Neurons, but do not Restrict Activity to Specific Inhibitory Cell-Types. *Frontiers in neural circuits*, 3:19.

- Naumann, R. K., Ondracek, J. M., Reiter, S., Shein-Idelson, M., Tosches, M. A., Yamawaki, T. M., and Laurent, G. (2015). The reptilian brain. *Current biology* : CB, 25(8):R317–21.
- Ness, T. V., Chintaluri, C., Potworowski, J., Łęski, S., Głóbska, H., Wójcik, D. K., and Einevoll, G. T. (2015). Modelling and Analysis of Electrical Potentials Recorded in Microelectrode Arrays (MEAs). *Neuroinformatics*, 13(4):403–426.
- Niedworok, C. J., Schwarz, I., Ledderose, J., Giese, G., Conzelmann, K.-K., and Schwarz, M. K. (2012). Charting monosynaptic connectivity maps by two-color light-sheet fluorescence microscopy. *Cell reports*, 2(5):1375–1386.
- Niwa, H., Yamamura, K., and Miyazaki, J. (1991). Efficient selection for high-expression transfectants with a novel eukaryotic vector. *Gene*, 108(2):193–199.
- Northcutt, R. G. (2013). Variation in reptilian brains and cognition. *Brain, behavior and evolution*, 82(1):45–54.
- Nowycky, M. C., Mori, K., and Shepherd, G. M. (1981a). Blockade of synaptic inhibition reveals long-lasting synaptic excitation in isolated turtle olfactory bulb. *Journal of neurophysiology*, 46(3):649–658.
- Nowycky, M. C., Mori, K., and Shepherd, G. M. (1981b). GABAergic mechanisms of dendrodendritic synapses in isolated turtle olfactory bulb. *Journal of neurophysiology*, 46(3):639–648.
- Oberlaender, M., Boudewijns, Z. S. R. M., Kleele, T., Mansvelder, H. D., Sakmann, B., and de Kock, C. P. J. (2011). Three-dimensional axon morphologies of individual layer 5 neurons indicate cell type-specific intracortical pathways for whisker motion and touch. *Proceedings of the National Academy of Sciences of the United States of America*, 108(10):4188–4193.
- Oh, S. W., Harris, J. A., Ng, L., Winslow, B., Cain, N., Mihalas, S., Wang, Q., Lau, C., Kuan, L., Henry, A. M., Mortrud, M. T., Ouellette, B., Nguyen, T. N., Sorensen, S. A., Slaughterbeck, C. R., Wakeman, W., Li, Y., Feng, D., Ho, A., Nicholas, E., Hirokawa, K. E., Bohn, P., Joines, K. M., Peng, H., Hawrylycz, M. J., Phillips, J. W., Hohmann, J. G., Wohnoutka, P., Gerfen, C. R., Koch, C., Bernard, A., Dang, C., Jones, A. R., and Zeng, H. (2014). A mesoscale connectome of the mouse brain. *Nature*, 508(7495):207–214.
- Ohki, K., Chung, S., Kara, P., Hübener, M., Bonhoeffer, T., and Reid, R. C. (2006). Highly ordered arrangement of single neurons in orientation pinwheels. *Nature*, 442(7105):925–928.
- O'Keefe, J. and Conway, D. H. (1978). Hippocampal place units in the freely moving rat: why they fire where they fire. *Experimental brain research*, 31(4):573–590.
- O'Keefe, J. and Recce, M. L. (1993). Phase relationship between hippocampal place units and the EEG theta rhythm. *Hippocampus*.
- Olsen, S. R., Bhandawat, V., and Wilson, R. I. (2010). Divisive normalization in olfactory population codes. *Neuron*, 66(2):287–299.
- Olsen, S. R., Bortone, D. S., Adesnik, H., and Scanziani, M. (2012). Gain control by layer six in cortical circuits of vision. *Nature*, 483(7387):47–52.
- Olsen, S. R. and Wilson, R. I. (2008). Lateral presynaptic inhibition mediates gain control in an olfactory circuit. *Nature*, 452(7190):956–960.
- Papadopoulou, M., Cassenaer, S., Nowotny, T., and Laurent, G. (2011). Normalization for sparse encoding of odors by a wide-field interneuron. *Science (New York, NY)*, 332(6030):721–725.
- Papagiakoumou, E., Anselmi, F., Bègue, A., de Sars, V., Glückstad, J., Isacoff, E. Y., and Emiliani, V. (2010). Scanless two-photon excitation of channelrhodopsin-2. *Nature methods*, 7(10):848–854.

- Pelli, D. G. (1997). The VideoToolbox software for visual psychophysics: transforming numbers into movies. *Spatial vision*, 10(4):437–442.
- Peltékian, E., Garcia, L., and Danos, O. (2002). Neurotropism and Retrograde Axonal Transport of a Canine Adenoviral Vector: A Tool for Targeting Key Structures Undergoing Neurodegenerative Processes. *Molecular Therapy*, 5(1):25–32.
- Perez-Orive, J., Mazor, O., Turner, G. C., Cassenaer, S., Wilson, R. I., and Laurent, G. (2002). Oscillations and sparsening of odor representations in the mushroom body. *Science (New York, NY)*, 297(5580):359–365.
- Peron, S. and Svoboda, K. (2011). From cudgel to scalpel: toward precise neural control with optogenetics. *Nature methods*, 8(1):30–34.
- Perry, V. H. and Cowey, A. (1985). The ganglion cell and cone distributions in the monkey's retina: implications for central magnification factors. *Vision Research*, 25(12):1795–1810.
- Petersen, C. C. H., Hahn, T. T. G., Mehta, M., Grinvald, A., and Sakmann, B. (2003). Interaction of sensory responses with spontaneous depolarization in layer 2/3 barrel cortex. *Proceedings of the National Academy of Sciences of the United States of America*, 100(23):13638–13643.
- Peterson, E. H. and Ulinski, P. S. (1979). Quantitative studies of retinal ganglion cells in a turtle, *Pseudemys scripta elegans*. I. Number and distribution of ganglion cells. *The Journal of Comparative Neurology*, 186(1):17–42.
- Petilla Interneuron Nomenclature Group, Ascoli, G. A., Alonso-Nanclares, L., Anderson, S. A., Barrionuevo, G., Benavides-Piccione, R., Burkhalter, A., Buzsáki, G., Cauli, B., DeFelipe, J., Fairén, A., Feldmeyer, D., Fishell, G., Fregnac, Y., Freund, T. F., Gardner, D., Gardner, E. P., Goldberg, J. H., Helmstaedter, M., Hestrin, S., Karube, F., Kisvárdy, Z. F., Lambolez, B., Lewis, D. A., Marín, O., Markram, H., Muñoz, A., Packer, A., Petersen, C. C. H., Rockland, K. S., Rossier, J., Rudy, B., Somogyi, P., Staiger, J. F., Tamás, G., Thomson, A. M., Toledo-Rodriguez, M., Wang, Y., West, D. C., and Yuste, R. (2008). Petilla terminology: nomenclature of features of GABAergic interneurons of the cerebral cortex. *Nature reviews Neuroscience*, 9(7):557–568.
- Petersen, K. H. and Einevoll, G. T. (2008). Amplitude variability and extracellular low-pass filtering of neuronal spikes. *Biophysical journal*, 94(3):784–802.
- Pillow, J. W., Shlens, J., Paninski, L., Sher, A., Litke, A. M., Chichilnisky, E. J., and Simoncelli, E. P. (2008). Spatio-temporal correlations and visual signalling in a complete neuronal population. *Nature*, 454(7207):995–999.
- Potworowski, J., Jakuczun, W., Łęski, S., and Wójcik, D. (2012). Kernel current source density method. *Neural Computation*, 24(2):541–575.
- Powers, A. S. and Reiner, A. (1980). A Stereotaxic Atlas of the Forebrain and Midbrain of the Eastern Painted Turtle (*Chrysemys picta picta*). *Journal für Hirnforschung*, (21):125–159.
- Prechtl, J. C. (1994). Visual motion induces synchronous oscillations in turtle visual cortex. *Proceedings of the National Academy of Sciences of the United States of America*, 91(26):12467–12471.
- Prechtl, J. C. (1995). Flutter-like response in visual cortex of the semi-isolated turtle brain. *The Biological Bulletin*, 189(2):215–216.
- Prechtl, J. C., Bullock, T. H., and Kleinfeld, D. (2000). Direct evidence for local oscillatory current sources and intracortical phase gradients in turtle visual cortex. *Proceedings of the National Academy of Sciences of the United States of America*, 97(2):877–882.

- Prechtl, J. C., Cohen, L. B., Pesaran, B., Mitra, P. P., and Kleinfeld, D. (1997). Visual stimuli induce waves of electrical activity in turtle cortex. *Proceedings of the National Academy of Sciences of the United States of America*, 94(14):7621–7626.
- Prinz, A. A., Bucher, D., and Marder, E. (2004). Similar network activity from disparate circuit parameters. 7(12):1345–1352.
- Quiroga, R. Q., Nadasdy, Z., and Ben-Shaul, Y. (2004). Unsupervised spike detection and sorting with wavelets and superparamagnetic clustering. *Neural Computation*, 16(8):1661–1687.
- Rall, W. (1962). Theory of physiological properties of dendrites. *Annals of the New York Academy of Sciences*, 96:1071–1092.
- Reichl, L., Heide, D., Löwel, S., Crowley, J. C., Kaschube, M., and Wolf, F. (2012). Coordinated optimization of visual cortical maps (I) symmetry-based analysis. *PLoS computational biology*, 8(11):e1002466.
- Reijmers, L. G., Perkins, B. L., Matsuo, N., and Mayford, M. (2007). Localization of a stable neural correlate of associative memory. *Science (New York, NY)*, 317(5842):1230–1233.
- Richardson, K. A., Schiff, S. J., and Gluckman, B. J. (2005). Control of traveling waves in the Mammalian cortex. *Physical review letters*, 94(2):028103.
- Rieppel, O. (1999). Turtle origins. *Science (New York, NY)*, 283(5404):945–946.
- Rieppel, O. and deBraga, M. (1996). Turtles as diapsid reptiles. , *Published online: 05 December 1996*; | doi:10.1038/384453a0, 384(6608):453–455.
- Riera, J. J., Ogawa, T., Goto, T., Sumiyoshi, A., Nonaka, H., Evans, A., Miyakawa, H., and Kawashima, R. (2012). Pitfalls in the dipolar model for the neocortical EEG sources. *Journal of neurophysiology*, 108(4):956–975.
- Rios, G., Lubenov, E. V., Chi, D., Roukes, M. L., and Siapas, A. G. (2016). Nanofabricated Neural Probes for Dense 3-D Recordings of Brain Activity. *Nano letters*, 16(11):6857–6862.
- Rodríguez, F., López, J. C., Vargas, J. P., Broglio, C., Gómez, Y., and Salas, C. (2002a). Spatial memory and hippocampal pallium through vertebrate evolution: insights from reptiles and teleost fish. *Brain research bulletin*, 57(3-4):499–503.
- Rodríguez, F., López, J. C., Vargas, J. P., Gómez, Y., Broglio, C., and Salas, C. (2002b). Conservation of spatial memory function in the pallial forebrain of reptiles and ray-finned fishes. 22(7):2894–2903.
- Rossant, C., Kadir, S. N., Goodman, D. F. M., Schulman, J., Hunter, M. L. D., Saleem, A. B., Grosmark, A., Belluscio, M., Denfield, G. H., Ecker, A. S., Tolias, A. S., Solomon, S., Buzsáki, G., Carandini, M., and Harris, K. D. (2016). Spike sorting for large, dense electrode arrays. 19(4):634–641.
- Roth, T. C. and Krochmal, A. R. (2015). The role of age-specific learning and experience for turtles navigating a changing landscape. *Current biology : CB*, 25(3):333–337.
- Rothman, J. S., Cathala, L., Steuber, V., and Silver, R. A. (2009). Synaptic depression enables neuronal gain control. *Nature*, 457(7232):1015–1018.
- Sato, T. K., Nauhaus, I., and Carandini, M. (2012). Traveling waves in visual cortex. *Neuron*, 75(2):218–229.
- Sawada, K. and Sun, X.-Z. (2010). Application of heat-induced antigen retrieval on whole mount immunostaining for adult mouse cerebellum. *Curr Neurobiol*, 1:21–24.
- Schneider, I. (2015). *Visually-evoked dynamics in turtle dorsal cortex examined using large-scale, chronic electrocorticogram recordings*. PhD thesis, Max Planck Institute for Brain Research & Universität Gießen.

- Schoch, R. R. and Sues, H.-D. (2015). A Middle Triassic stem-turtle and the evolution of the turtle body plan. *Nature*, 523(7562):584–587.
- Scholvin, J., Kinney, J. P., Bernstein, J. G., Moore-Kochlacs, C., Kopell, N., Fonstad, C. G., and Boyden, E. S. (2016). Close-Packed Silicon Microelectrodes for Scalable Spatially Oversampled Neural Recording. *IEEE Transactions on Biomedical Engineering*, 63(1):120–130.
- Seelig, J. D. and Jayaraman, V. (2013). Feature detection and orientation tuning in the Drosophila central complex. *Nature*, 503(7475):262–266.
- Seelig, J. D. and Jayaraman, V. (2015). Neural dynamics for landmark orientation and angular path integration. *Nature*, 521(7551):186–191.
- Senseman, D. M. (1999). Spatiotemporal structure of depolarization spread in cortical pyramidal cell populations evoked by diffuse retinal light flashes. *Visual neuroscience*, 16(1):65–79.
- Senseman, D. M. and Robbins, K. A. (1999). Modal behavior of cortical neural networks during visual processing. 19(10):RC3.
- Senseman, D. M. and Robbins, K. A. (2002). High-Speed VSD Imaging of Visually Evoked Cortical Waves: Decomposition Into Intra- and Intercortical Wave Motions. *Journal of neurophysiology*, 87(3):1499–1514.
- Shadlen, M. N. and Movshon, J. A. (1999). Synchrony unbound: a critical evaluation of the temporal binding hypothesis. *Neuron*, 24(1):67–77– 111–25.
- Shadlen, M. N. and Newsome, W. T. (1994). Noise, neural codes and cortical organization. *Current opinion in neurobiology*, 4(4):569–579.
- Sharma, J., Angelucci, A., and Sur, M. (2000). Induction of visual orientation modules in auditory cortex. *Nature*, 404(6780):841–847.
- Shedlock, A. M., Botka, C. W., Zhao, S., Shetty, J., Zhang, T., Liu, J. S., Deschavanne, P. J., and Edwards, S. V. (2007). Phylogenomics of nonavian reptiles and the structure of the ancestral amniote genome. *Proceedings of the National Academy of Sciences of the United States of America*, 104(8):2767–2772.
- Shein-Idelson, M., Ondracek, J. M., Liaw, H.-P., Reiter, S., and Laurent, G. (2016). Slow waves, sharp waves, ripples, and REM in sleeping dragons. *Science (New York, NY)*, 352(6285):590–595.
- Shein-Idelson, M., Pammer, L., Hemberger, M., and Laurent, G. (2017). Large-scale mapping of cortical synaptic projections with extracellular electrode arrays. *Nature methods*, 14(9):882–890.
- Siapas, A. G. and Wilson, M. A. (1998). Coordinated interactions between hippocampal ripples and cortical spindles during slow-wave sleep. *Neuron*, 21(5):1123–1128.
- Silies, M., Gohl, D. M., and Clandinin, T. R. (2014). Motion-detecting circuits in flies: coming into view. *Annual review of neuroscience*, 37:307–327.
- Sillitoe, R. V. and Hawkes, R. (2002). Whole-mount immunohistochemistry: a high-throughput screen for patterning defects in the mouse cerebellum. *The journal of histochemistry and cytochemistry : official journal of the Histochemistry Society*, 50(2):235–244.
- Singer, W. (2013). Cortical dynamics revisited. *Trends in cognitive sciences*, 17(12):616–626.
- Smeets, W. J., Hoogland, P. V., and Lohman, A. H. (1986). A forebrain atlas of the lizard Gekko gekko. *The Journal of Comparative Neurology*, 254(1):1–19.
- Smith, L. M., Ebner, F. F., and Colonnier, M. (1980). The thalamocortical projection in Pseudemys turtles: a quantitative electron microscopic study. *The Journal of Comparative Neurology*, 190(3):445–461.

- Sohal, V. S., Zhang, F., Yizhar, O., and Deisseroth, K. (2009). Parvalbumin neurons and gamma rhythms enhance cortical circuit performance. *Nature*, 459(7247):698–702.
- Stafford, B. K., Sher, A., Litke, A. M., and Feldheim, D. A. (2009). Spatial-temporal patterns of retinal waves underlying activity-dependent refinement of retinofugal projections. *Neuron*, 64(2):200–212.
- Steriade, M. (2004). Neocortical cell classes are flexible entities. *Nature reviews Neuroscience*, 5(2):121–134.
- Stewart, M. and Fox, S. E. (1991). Hippocampal theta activity in monkeys. *Brain research*, 538(1):59–63.
- Stopfer, M., Bhagavan, S., Smith, B. H., and Laurent, G. (1997). Impaired odour discrimination on desynchronization of odour-encoding neural assemblies. *Nature*, 390(6655):70–74.
- Stuart, G. J., Dodt, H. U., and Sakmann, B. (1993). Patch-clamp recordings from the soma and dendrites of neurons in brain slices using infrared video microscopy. *Pflügers Archiv : European journal of physiology*, 423(5-6):511–518.
- Sun, H. and Frost, B. J. (1998). Computation of different optical variables of looming objects in pigeon nucleus rotundus neurons. 1(4):296–303.
- Takada, N., Pi, H. J., Sousa, V. H., Waters, J., Fishell, G., Kepecs, A., and Osten, P. (2014). A developmental cell-type switch in cortical interneurons leads to a selective defect in cortical oscillations. *Nature communications*, 5:5333.
- Tasic, B., Menon, V., Nguyen, T. N., Kim, T. K., Jarsky, T., Yao, Z., Levi, B., Gray, L. T., Sorensen, S. A., Dolbeare, T., Bertagnoli, D., Goldy, J., Shapovalova, N., Parry, S., Lee, C., Smith, K., Bernard, A., Madisen, L., Sunkin, S. M., Hawrylycz, M., Koch, C., and Zeng, H. (2016). Adult mouse cortical cell taxonomy revealed by single cell transcriptomics. *Nature neuroscience*, 19(2):335–346.
- Tateno, T., Jimbo, Y., and Robinson, H. P. C. (2005). Spatio-temporal cholinergic modulation in cultured networks of rat cortical neurons: spontaneous activity. *Neuroscience*, 134(2):425–437.
- Taxidis, J., Anastassiou, C. A., Diba, K., and Koch, C. (2015). Local Field Potentials Encode Place Cell Ensemble Activation during Hippocampal Sharp Wave Ripples. *Neuron*, 87(3):590–604.
- Tervo, D. G. R., Hwang, B.-Y., Viswanathan, S., Gaj, T., Lavzin, M., Ritola, K. D., Lindo, S., Michael, S., Kuleshova, E., Ojala, D., Huang, C.-C., Gerfen, C. R., Schiller, J., Dudman, J. T., Hantman, A. W., Looger, L. L., Schaffer, D. V., and Karpova, A. Y. (2016). A Designer AAV Variant Permits Efficient Retrograde Access to Projection Neurons. *Neuron*, 92(2):372–382.
- Tian, L., Hires, S. A., Mao, T., Huber, D., Chiappe, M. E., Chalasani, S. H., Petreanu, L., Akerboom, J., McKinney, S. A., Schreiner, E. R., Bargmann, C. I., Jayaraman, V., Svoboda, K., and Looger, L. L. (2009). Imaging neural activity in worms, flies and mice with improved GCaMP calcium indicators. *Nature methods*, 6(12):875–881.
- Tiesinga, P. and Sejnowski, T. J. (2009). Cortical enlightenment: are attentional gamma oscillations driven by ING or PING? *Neuron*, 63(6):727–732.
- Torr, P. H. S. and Zisserman, A. (2000). MLESAC: A New Robust Estimator with Application to Estimating Image Geometry. *Computer Vision and Image Understanding*, 78(1):138–156.
- Tosches, M. A., Yamawaki, T. M., Naumann, R. K., Jacobi, A. A., Tushev, G., and Laurent, G. (submitted). Evolution of cortical neuronal diversity from single cell profiling of the reptilian telencephalon.
- Trevelyan, A. J. (2009). The Direct Relationship between Inhibitory Currents and Local Field Potentials. *Journal of Neuroscience*, 29(48):15299–15307.
- Trojanowski, J. Q. (1983). Native and derivatized lectins for in vivo studies of neuronal connectivity and neuronal cell biology. *Journal of neuroscience methods*, 9(3):185–204.

- Trojanowski, J. Q., Gonatas, J. O., and Gonatas, N. K. (1982). Horseradish peroxidase (HRP) conjugates of cholera toxin and lectins are more sensitive retrogradely transported markers than free HRP. *Brain research*, 231(1):33–50.
- Ugolini, G. (1995a). Specificity of rabies virus as a transneuronal tracer of motor networks: transfer from *The Journal of Comparative Neurology*.
- Ugolini, G. (1995b). Transneuronal Tracing with Alpha-herpesviruses: A Review of the Methodology. pages 1–25.
- Ugolini, G., Kuypers, H. G., and Simmons, A. (1987). Retrograde transneuronal transfer of herpes simplex virus type 1 (HSV 1) from motoneurons. *Brain research*, 422(2):242–256.
- Ulanovsky, N. and Moss, C. F. (2007). Hippocampal cellular and network activity in freely moving echolocating bats. 10(2):224–233.
- Uliniski, P. S. and Nautiyal, J. (1988). Organization of retinogeniculate projections in turtles of the genera *Pseudemys* and *Chrysemys*. *The Journal of Comparative Neurology*, 276(1):92–112.
- van Vreeswijk, C., Abbott, L. F., and Ermentrout, G. B. (1994). When inhibition not excitation synchronizes neural firing. *Journal of computational neuroscience*, 1(4):313–321.
- Vanderwolf, C. H. (1969). Hippocampal electrical activity and voluntary movement in the rat. *Electroencephalography and Clinical Neurophysiology*, 26(4):407–418.
- Vaziri, A. and Emiliani, V. (2012). Reshaping the optical dimension in optogenetics. *Current opinion in neurobiology*, 22(1):128–137.
- Veit, J., Hakim, R., Jádí, M. P., Sejnowski, T. J., and Adesnik, H. (2017). Cortical gamma band synchronization through somatostatin interneurons. *Nature neuroscience*, 20(7):951–959.
- Wamsley, B. and Fishell, G. (2017). Genetic and activity-dependent mechanisms underlying interneuron diversity. *Nature reviews Neuroscience*, 18(5):299–309.
- Wan, X. C., Trojanowski, J. Q., and Gonatas, J. O. (1982). Cholera toxin and wheat germ agglutinin conjugates as neuroanatomical probes: their uptake and clearance, transganglionic and retrograde transport and sensitivity. *Brain research*, 243(2):215–224.
- Wang, W. Z., Oeschger, F. M., Montiel, J. F., Garcia-Moreno, F., Hoerder-Suabedissen, A., Krubitzer, L., Ek, C. J., Saunders, N. R., Reim, K., Villalón, A., and Molnár, Z. (2011). Comparative aspects of subplate zone studied with gene expression in sauropsids and mammals. *Cerebral cortex (New York, NY : 1991)*, 21(10):2187–2203.
- Wernet, M. F., Huberman, A. D., and Desplan, C. (2014). So many pieces, one puzzle: cell type specification and visual circuitry in flies and mice. *Genes & development*, 28(23):2565–2584.
- White, L. E., Coppola, D. M., and Fitzpatrick, D. (2001). The contribution of sensory experience to the maturation of orientation selectivity in ferret visual cortex. *Nature*, 411(6841):1049–1052.
- Wickersham, I. R., Finke, S., Conzelmann, K.-K., and Callaway, E. M. (2006). Retrograde neuronal tracing with a deletion-mutant rabies virus. *Nature methods*, 4(1):47–49.
- Wickersham, I. R., Lyon, D. C., Barnard, R. J. O., Mori, T., Finke, S., Conzelmann, K.-K., Young, J. A. T., and Callaway, E. M. (2007). Monosynaptic Restriction of Transsynaptic Tracing from Single, Genetically Targeted Neurons. *Neuron*, 53(5):639–647.
- Wilkinson, A., Coward, S., and Hall, G. (2009). Visual and response-based navigation in the tortoise (*Geochelone carbonaria*). *Animal cognition*, 12(6):779–787.

- Wilson, M. A. (2002). Hippocampal memory formation, plasticity, and the role of sleep. *Neurobiology of learning and memory*, 78(3):565–569.
- Wilson, M. A. and McNaughton, B. L. (1994). Reactivation of hippocampal ensemble memories during sleep. *Science (New York, NY)*, 265(5172):676–679.
- Wilson, N. R., Runyan, C. A., Wang, F. L., and Sur, M. (2012). Division and subtraction by distinct cortical inhibitory networks in vivo. *Nature*, 488(7411):343–348.
- Wilson, R. I. (2011). Understanding the functional consequences of synaptic specialization: insight from the *Drosophila* antennal lobe. *Current opinion in neurobiology*, 21(2):254–260.
- Womelsdorf, T., Schoffelen, J.-M., Oostenveld, R., Singer, W., Desimone, R., Engel, A. K., and Fries, P. (2007). Modulation of neuronal interactions through neuronal synchronization. *Science (New York, NY)*, 316(5831):1609–1612.
- Xie, C., Liu, J., Fu, T.-M., Dai, X., Zhou, W., and Lieber, C. M. (2015). Three-dimensional macroporous nano-electronic networks as minimally invasive brain probes. *Nature materials*, 14(12):1286–1292.
- Xue, M., Atallah, B. V., and Scanziani, M. (2014). Equalizing excitation-inhibition ratios across visual cortical neurons. *Nature*, 511(7511):596–600.
- Yaksi, E. and Wilson, R. I. (2010). Electrical coupling between olfactory glomeruli. *Neuron*, 67(6):1034–1047.
- Yartsev, M. M., Witter, M. P., and Ulanovsky, N. (2011). Grid cells without theta oscillations in the entorhinal cortex of bats. *Nature*, 479(7371):103–107.
- Yizhar, O., Fenno, L. E., Davidson, T. J., Mogri, M., and Deisseroth, K. (2011). Optogenetics in neural systems. *Neuron*, 71(1):9–34.
- Zagorul'ko, T. M. (1968). [The evoked potentials of the general cortex and tectum opticum of the tortoise in relation to the intensity and wave length of photo stimulus]. *Fiziologicheskii zhurnal SSSR imeni I. M. Sechenova*, 54(4):436–446.
- Zardoya, R. and Meyer, A. (1998). Complete mitochondrial genome suggests diapsid affinities of turtles. *Proceedings of the National Academy of Sciences of the United States of America*, 95(24):14226–14231.
- Zhang, F., Gradinaru, V., Adamantidis, A. R., Durand, R., Airan, R. D., de Lecea, L., and Deisseroth, K. (2010). Optogenetic interrogation of neural circuits: technology for probing mammalian brain structures. *Nature protocols*, 5(3):439–456.
- Zhu, P., Frank, T., and Friedrich, R. W. (2013). Equalization of odor representations by a network of electrically coupled inhibitory interneurons. *PLoS ONE*, 16(11):1678–1686.
- Zufferey, R., Donello, J. E., Trono, D., and Hope, T. J. (1999). Woodchuck hepatitis virus posttranscriptional regulatory element enhances expression of transgenes delivered by retroviral vectors. *Journal of virology*, 73(4):2886–2892.

Declaration

I declare that I have written the thesis independently and without any use of resources other than the ones quoted in the thesis. The thesis has not been used as an examination record in another course of studies. This is a true copy of the thesis, including any required final revisions, as accepted by my supervisors.

I understand that my thesis may be made electronically available to the public.

Lorenz Pammer
Frankfurt am Main
December, 2017

Acknowledgments

In the course of this thesis, my work has depended on a large number of people to all of whom I am deeply grateful.

Foremost I want to thank Gilles Laurent, who gave me this great opportunity to pursue my doctorate research in his laboratory at the Max Planck Institute for Brain Research. For working hard to make the institute such an excellent place for us to work in. Who gave me an amount of freedom only matched by the amount of relentless support. His optimistic skepticism, his combination of scientific creativity and rigor and his wisdom have influenced me deeply.

Erin Schuman in my thesis advisory committee and Manfred Kössl my supervisor in Frankfurt University for all their dedicated guidance, support and valuable input on my research.

I want to thank my colleagues and friends Mike Hemberger and Mark Shein-Idelson for the countless shared hours in joint experiments, analyses and discussions, for their help and inspiration. Tracy Yamawaki for our common efforts in virus and promoter testing, Stephan Junek for the early olfaction research projects and his imaging teaching. Andreas Kotowicz and Sina Tootoonian for our discussions and their programming and analysis expertise. All the other colleagues in the laboratory - Christian Müller, Ingmar Schneider, Ueli Rutishauser, Viola Priesemann, Julien Fournier, Robert Naumann, Janie Ondracek, Andres Laan, Dewi Husainie, Sam Reiter, Maria Tosches, Hua-Peng Liaw, Hsing-Hsi Li, Marcel Lauterbach, Alessandro Coatti, Hiroaki Norimoto, Lorenz Fenk.

Our fantastic TAs, Michaela Klinkmann for her outstanding work from the first days, equally Anja Arends, Jenny Ehrnsberger-Knop, Angeles Macias, Theres Manthey, Christina Thum and Eva Scholz. Antje Berken for her constant administrative-scientific support, Anita Wagner and Maren Baier. Heiko Fernau, Andreas Um-minger, Guido Schmalbach, Dettlef Schädler and Oliver Eulitz for their dedicated support and the rest of the institute's administration and technical support teams.

I have immensely profited from the scientific community's adherence to openness and the philosophy of sharing progress among each other. I want to thank Johannes Letzkus for his generous offers to share his laboratory for mouse viral injections, novel viral serotypes and genetic mouse lines. Dima Rinberg from Janelia Farm and NYU for the friendly sharing of his expert olfactometer designs, support during construction and scientific discussions. Ilka Diester, at that time in the Ernst Strüngmann Institute, for allowing me to do mouse experiments with rabies virus in her lab, with Edith Doering helping me with the injections. Boris Zemelman, at the time in Janelia Farm, for sending me the first round of various AAV serotypes to test in reptiles. Alla Karpova and Loren Looger from the same institution for their kind sharing of the then unpublished AAV-SL1 virus. The Callaway laboratory in the Salk Institute and the Fishell lab for AAV viruses with cell type specific promoters. Karl Deisseroth in Stanford University for inviting me to attend a methods workshop and sharing channelrhodopsin-carrying viruses. Adrian Fairhall and Michael Berry for inviting me to the outstanding Methods in Computational Neuroscience course in Woods Hole, Elad Schneidman, Eve Marder, Jakob Macke and Hubert Eichner for their inspirational mentoring.

Finally, the Max Planck Society and European Research Council for funding me and our research.

LORENZ PAMMER

Max Planck Institute for Brain Research
Max-von-Laue Straße 4
60438 - Frankfurt am Main
Germany
tel +49 176 45758561
@ lorenz.pammer@brain.mpg.de
Matriculation # 4150697

PROFILE

Born on May 12th 1985 in Vienna, Austria. Austrian citizenship.
German native, fluent English (IELTS: 8,5/9), intermediate French (B2), beginner Romanian.

EDUCATION

2010-2017 — PHD. MAX PLANCK INSTITUTE FOR BRAIN RESEARCH FRANKFURT, GERMANY

- Set up of Gilles Laurent lab after relocation from CALTECH. Research on cortical neuronal network dynamics.
- MATLAB software package controlling olfactory stimulation hardware.
- Regular presentations, 5 international conferences, invited speaker (ETH, Paris VI, Tübingen Uni, CCU Lisbon).

2011 — SUMMER SCHOOL. MARINE BIOLOGICAL LABS WOODS HOLE, MA, U.S.A.

Computational neuroscience and machine learning. Modelling project with Eve Marder and Elad Schneidman.

2013 — WORKSHOP. DEISSEROTH LAB, STANFORD UNIVERSITY STANFORD, CA, U.S.A.

Workshop in the laboratory of Karl Deisseroth to learn CLARITY, a new neuroanatomical technique.

2004-2009 — DIPLOMA (BSC+MSC) MOLECULAR BIOLOGY. UNIVERSITY OF VIENNA VIENNA, AUSTRIA

Graduated with highest distinction (average 1.15; Austrian grading system ranges from 1.0, best - 5.0, fail).

2008-2009 — MASTER THESIS. SVOBODA LAB, HHMI JANELIA FARM ASHBURN, VA, U.S.A.

- Psychophysical experiments on physical variables of somatosensory perception in mouse (grade 1.0).
- Received the "Prize for outstanding master theses" of the natural sciences club of the University of Vienna.

2008 — ERASMUS. UNIVERSITY OF GENEVA GENEVA, SWITZERLAND

1995-2003 — GYMNASIUM ERLGASSE VIENNA, AUSTRIA

Graduated with distinction (average 1.17). 2001-2003 class representative, 2002/2003 school representative.

2000/2001 — EXCHANGE YEAR. SENATOR GERSHAW HIGH SCHOOL BOW ISLAND, CANADA

WORK EXPERIENCE & INVOLVEMENTS

2013-2017 — ELECTED PHD REPRESENTATIVE. MPI FOR BRAIN RESEARCH FRANKFURT, GERMANY

Initiated and cofounded a career service for PhDs and postdocs in PhDnet, the Max-Planck-wide PhD representation (~4000 PhDs). Strategy development, community building, white paper on science policy.

2010-2015 — FOUNDER & ORGANISER. MPI LECTURE SERIES FRANKFURT, GERMANY

Initiated, organized biweekly talks of leading speakers (i.a. nobel prize winners).

2007-2008 — INTERNSHIP. BARRY DICKSON LAB, IMP VIENNA, AUSTRIA

Two summer internships. Fly behavioral genetic screening. Programming code for fly behavioral quantification.

2008 — INTERNSHIP. FLORIAN WURM LAB, EPFL LAUSANNE, SWITZERLAND

Two months internship on good manufacturing practice compatible transient transfection optimization.

2008 — STARTUP TRAINING. VENTURE.LAB GENEVA, SWITZERLAND

Participated in startup project at Swiss venture.challenge.

2006 — INTERNSHIP. ANA ZENCLUSSEN LAB, CHARITÉ BERLIN, GERMANY

Molecular mechanisms contributing to fetal-maternal tolerance, concentrating on arginase-1 expression patterns.

2005-2007 — EDITOR. PLAY.FM VIENNA, AUSTRIA

2003-2004 — CIVIL SERVICE. LANDLERHILFE SIBIU, ROMANIA

Performed 14 months civil service in Romania. Cared for the elderly of the German-speaking minority in Sibiu.

2002 — INTERNSHIP. FLORIAN RÜCKER LAB, BOKU VIENNA, AUSTRIA

SCHOLARSHIPS & PRIZES (SELECTION)

2010 **Prize for outstanding master's theses** Natural Sciences Club University Vienna (acceptance rate ~5%)

2008/2009 **Academic excellence scholarship** Austrian Ministry of Science & Education (acceptance rate <5%)

2008/2009 **HHMI Janelia Visiting Scientists Scholarship** (3% awarded to master's students, 60% to professors)

PUBLICATIONS (SELECTION)

Pammer, Yamawaki, Laurent - A genetic toolkit for neuroscience in reptilian brains. *in preparation*

Shein-Idelson, Pammer, Hemberger, Laurent - Large-scale mapping of cortical synaptic projections with extracellular electrode arrays. *Nature Methods* 2017

Hemberger*, Pammer*, Laurent - Comparative approaches to cortical microcircuits. *Curr Opin Neurobiol* 2016

Hires, Pammer, Svoboda, Golomb - Tapered whiskers are required for active tactile sensation. *eLIFE* 2013

Pammer*, O'Connor*, Hires, Clack, Huber, Myers, Svoboda - The Mechanical Variables Underlying Object Localization along the Axis of the Whisker. *Journal of Neuroscience* 2013 *first authors